Search for a diffuse cosmic neutrino flux using shower events in the ANTARES neutrino telescope

Suche nach einem diffusen kosmischen Neutrinofluss mit Hilfe von Schauerereignissen im ANTARES Neutrinoteleskop

Der Naturwissenschaftlichen Fakultät
der Friedrich-Alexander-Universität Erlangen-Nürnberg
zur Erlangung des Doktorgrades Dr. rer. nat.

vorgelegt von
Florian Folger
aus Neu-Ulm

Abstract

The ANTARES neutrino telescope [1] is a three-dimensional array of 885 photomultiplier tubes that has been installed in the Mediterranean Sea and that is designed to detect high energy neutrinos from the cosmos. Neutrinos that interact with nucleons in water in deep inelastic scattering processes induce secondary particles, such as muon tracks or hadronic and electromagnetic particle showers, that move faster than the speed of light in water and hence, emit Cherenkov radiation [2]. By measuring the arrival time and the amount of Cherenkov photons at different detector positions the event pattern can be reconstructed, from which conclusions about the energy and the direction of the inducing neutrino can be drawn.

Whereas for along time the charged current interaction of a muon neutrino has been regarded as the golden channel of neutrino astronomy, as the long muon trajectory allows a good angular resolution, it is evident that the study of hadronic showers from neutral current events or electromagnetic showers from charged current interactions of the electron neutrino is a gain of information that must be taken into account, too. Recent results from the IceCube [3] experiment endorse this approach as for the very first time an evidence for a diffuse cosmic neutrino flux was found with the contribution of shower events [4].

Within this work a search for the all-flavour diffuse cosmic neutrino flux using the ANTARES data from 2007 - 2012 is presented. As first step a reconstruction algorithm has been developed that is able to identify shower events and determine their parameters, such as vertex position, interaction time, shower energy and neutrino direction, by performing a maximum likelihood fit. The fit is based on probability density function tables that have been created from extensive Monte-Carlo simulations.

Several approaches have been investigated to distinguish between track-like and shower-like events. Different cuts have been introduced to suppress the background of atmospheric neutrino and muon events. As after the final cuts no significant signal was observed, a $90\,\%$ confidence upper limit on the diffuse cosmic neutrino flux was evaluated using the Feldman-Cousins approach [5] that yields a value per neutrino flavour of

$$E^2 \cdot \Phi_{90\,\%} = 4.9 \cdot 10^{-8}\,\mathrm{GeV/cm^2 \cdot sr \cdot s}$$

A publication of this work is in preparation.

Zusammenfassung

Im Rahmen dieser Arbeit wurde eine Suche nach einem diffusen kosmischen Neutrinofluss mit Hilfe von Schauerereignissen in den ANTARES [1] Daten von 2007 - 2012 durchgeführt. Das ANTARES Neutrinoteleskop besteht aus einer dreidimensionalen Anordnung von 885 Photomultipliern auf 12 vertikalen Trossen (Lines). Diese wurden in der Tiefsee des Mittelmeers installiert um Tscherenkow-Strahlung nachzuweisen, die von Teilchen emittiert wird, welche in Streuprozessen hoch-energetischer Neutrinos mit Nukleonen im Wasser erzeugt wurden. Diese Neutrinoereignisse werden allerdings von einem Untergrund aus atmosphärischen Myonen überlagert, die etwa sechs Größenordnungen häufiger auftreten. Die Herausforderung besteht darin, diesen Untergrund zu unterdrücken und Ereignissignaturen zu finden, die von Neutrinoereignissen stammen. Unter diesen muss weiterhin unterschieden werden zwischen schauerartigen Ereignissen aus hadronischen und elektromagnetischen Teilchenschauern, die im Detektor als punktförmige Lichtquelle erscheinen, und spurartigen Ereignissen, die zum Beispiel bei tief-inelastischen Wechselwirkungen eines Myonneutrinos über den geladenen Strom erzeugt werden.

Hierfür wurde ein Algorithmus, die *Dusj*-Schauerrekonstruktion, entwickelt, mit deren Hilfe Schauerereignisse in den Daten identifiziert und deren Eigenschaften, wie der Interaktionsort und -Zeitpunkt, die Schauerenergie und die Richtung des Neutrinos, rekonstruiert werden können. Das Programm wurde implementiert als Teil der offiziellen Analyse-Software *SeaTray* [6], die in der ANTARES-Kollaboration zur Datenprozessierung verwendet wird. Bereits verfügbare Schauerrekonstruktions-Algorithmen, wie zum Beispiel BBFit [7], sind entwickelt worden, um lediglich den Ort und Zeitpunkt der Schauererzeugung zu rekonstruieren. Da jedoch für die Analyse des diffusen kosmischen Neutrinoflusses auch die Energie der Ereignisse benötigt wird, war es notwendig, einen Algorithmus zur Bestimmung aller Schauereigenschaften zu entwerfen. Mit Hinblick auf dieses Ziel wurden in der Kollaboration im Rahmen zweier zeitgleicher Doktorarbeiten zwei unterschiedliche Methoden entwickelt: Die *Q-Strategy* [8] und diese Arbeit.

Die Q-Strategy bestimmt die Schauerenergie aus der *Gesamtheit aller selektierten Schauersignale* in den Photomultipliern, indem die Energie in Relation zur Gesamtzahl aller nachgewiesenen Photonen im Ereignis gesetzt wird. Mit diesem Ansatz kann allerdings nur dann ein brauchbares Ergebnis erzielt werden, wenn das gesamte Ereignis im instrumentierten Volumen liegt, da für Ereignisse, die am Rand des Detektors statt-

finden, ein Teil der Photonen verloren geht und die Energie daher unterschätzt wird. Der Ansatz, der im Dusj-Algorithmus verfolgt wird, ist ein zweistufiger Maximum-Likelihood-Fit, der auf Wahrscheinlichkeitstabellen beruht, welche aus Monte-Carlo-Simulationen berechnet wurden. In diesen Tabellen wurden die Schauereigenschaften, wie zum Beispiel die Schauerenergie, nicht zur Gesamtanzahl aller Photonen sondern lediglich zur *Anzahl der mit einem Photomultiplier detektierten Photonen* in Beziehung gesetzt. Dies bietet im Vergleich zur Q-Strategy den großen Vorteil, nun auch Ereignisse, die am Rande oder sogar außerhalb des Detektors stattgefunden haben, richtig rekonstruieren zu können. Daher ist die Suche nach Schauerereignissen in dieser Arbeit nicht länger auf vollständig eingeschlossene Ereignisse beschränkt.

Im Energiebereich zwischen $1\,\mathrm{TeV}$ und $1\,\mathrm{PeV}$ Schauerenergie erreicht der entwickelte Algorithmus eine Rekonstruktionsgenauigkeit von $4-6\,\mathrm{m}$ (Median) und $5-9\,\mathrm{m}$ (arithmetisches Mittel) für den Interaktionsort. Die Schauerenergie weist eine leichte Unterschätzung um $0.2-0.3$ Größenordnungen (Median) und $0.3-0.5$ Größenordnungen (arithmetisches Mittel) auf. Die Bestimmung der Neutrinorichtung erreicht einen stabilen Median-Fehler von $6°$ für Schauer unter $100\,\mathrm{TeV}$, verliert aber an Genauigkeit bei höheren Energien. Bei $1\,\mathrm{PeV}$ liegt der Median-Fehler etwa bei $25°$, der entsprechende mittlere Fehler bei $15°-40°$. Fr alle Schauereigenschaften nimmt die Rekonstruktionsgenauigkeit mit steigender Energie ab. Die angegebenen Fehler beziehen sich auf Ereignisse die bereits einen Qualitätsfilter passiert haben, wofür der reduzierte logarithmische Likelihood-Wert, zugehörig zum Fit-Ergebnis der Orts-Rekonstruktion, eine bestimmte Schwelle nicht überschreiten darf. Dieses Kriterium passieren etwa $10\,\%$ (bei $1\,\mathrm{TeV}$) bis $60\,\%$ (bei $1\,\mathrm{PeV}$) aller detektierten Schauerereignisse, wobei gleichzeitig eine Unterdrückung des atmosphärischen Myon-Untergrunds um 5-6 Größenordnungen erzielt wird. Lässt man dieses Qualitätskriterium außer Acht, werden etwa $50\,\%$ (bei $1\,\mathrm{TeV}$) bis $90\,\%$ (bei $1\,\mathrm{PeV}$) aller Schauer erfolgreich rekonstruiert.

Da die Bedingungen zur Datennahme mit ANTARES umweltbedingten Schwankungen unterliegen, die sich zum Beispiel in variablen optischen Untergrundraten und Lichtausbrüchen von biolumineszenten Lebensformen äußern und die sich in Zeitskalen von Tagen ändern können, müssen einzelne Perioden von der Analyse ausgeschlossen werden. Die effektive Datennahmezeit, die für die Analyse verwendet wurde, beträgt 1247 Tage. Aus diesen Daten wurden ausschließlich Ereignisse verwendet, die alle der folgenden Kriterien erfüllen:

- Das Ereignis muss erfolgreich rekonstruiert worden sein.

- Das Ereignis muss das Qualitätskriterium (der Schnitt auf die reduzierte Likelihood) erfüllen.

- Signale, die von der Rekonstruktion dem Schauer zugeordnet wurden, müssen auf mindestens 3 unterschiedlichen Lines angeordnet sein.

- Der rekonstruierte Ort darf nicht näher als 15 m an einem der Photomultiplier liegen.

Letzteres der Kriterien soll gelegentlich auftretende Ereignisse herausfiltern, bei denen die Hochspannung im Photomultiplier einen Funkenbogen erzeugt, der von den umliegenden Photomultipliern als helle punktförmige Lichtquelle gesehen wird. Auf diese Weise kann ein Neutrino-induzierter Teilchenschauer vorgetäuscht werden.

Die Entwicklung des Rekonstruktions-Algorithmus, sowie die Optimierung der finalen Analysestrategie, wurde mit Hilfe der offiziellen, Kollaborations-internen Monte-Carlo-Simulation für Neutrino- und atmosphärische Myonereignisse durchgeführt. Hierzu ist für jede Datennahme-Einheit (Run), die jeweils etwa ein paar Stunden andauert, eine individuelle Simulation angefertigt worden, bei der die zu dieser Zeit vorherrschenden Datennahme-Bedingungen berücksichtigt wurden. Da keine Simulation für Tauneutrino-Ereignisse zur Verfügung stand, wurde der Beitrag von Tauneutrinos anhand der Simulation für Elektronneutrinos abgeschätzt. Weiterhin wurde aufgrund geringer Statistik in der Simulation für atmosphärische Myonen, besonders nach der finalen Datenselektion, eine Extrapolation entwickelt um die Myon-Kontamination abzuschätzen, nachdem alle simulierten Myonereignisse bereits herausgefiltert wurden. Diese Kontamination durch atmosphrische Myonen beträgt etwa 38 % für den Fall, dass kein kosmisches Neutrinosignal mitberücksichtigt wird und alle weiteren Ereignisse von atmosphärischen Neutrinos induziert werden, und 26 % unter Berücksichtigung eines zusätzlichen kosmischen E^{-2}-Neutrinoflusses mit einer Stärke von $1.2 \cdot 10^{-8}\,\text{GeV/cm}^2 \cdot \text{sr} \cdot \text{s}$ und einer oberen Energiegrenze von $2\,\text{PeV}$, also dem Fluss für den kürzlich von IceCube Anzeichen gefunden wurden [4]. Eine zusätzliche Korrektur für die Anzahl der Myonneutrino-Ereignisse durch Wechselwirkung über den geladenen Strom musste eingeführt werden, um eine Vereinfachung in der Simulation zu korrigieren, bei der für hohe Energien aufgrund von Limitierungen in der verfügbaren Rechenleistung der hadronische Schauer am Ort der Interaktion nicht mit-simuliert wurde.

Da in der momentan verfügbaren Version der offiziellen Monte-Carlo-Simulation Photonstreuung in Schauerereignissen nicht simuliert wurde, wurde für eine kleine Anzahl an Runs eine aktualisierte Simulation mit Photonstreuung erzeugt, um die Auswirkung dieser Vereinfachung auf die Analyse zu studieren. Als Konsequenz davon wurde die Strategie zur Unterscheidung zwischen spurartigen und schauerartigen Ereignissen geändert. Der ursprünglich verwendete multivariate Algorithmus wurde durch ein weniger restriktives Kriterium (der Schnitt auf die reduzierte Likelihood) ersetzt, um ein möglichst kompatibles Ergebnis mit der aktuellen und der zukünftigen Simulation zu erhalten.

Systematische Fehler, die in der Analyse auftreten, stammen unter anderem aus der Unsicherheit auf die atmosphärischen Flussmodelle, wofür $\pm 30\,\%$ für den atmo-

sphärischen Myonfluss und den konventionellen Neutrinofluss (Bartol [9]) angenommen wurden. Der Fehler auf die prompte Komponente beträgt etwa $^{+25}_{-40}$ %, einer Modellrechnung von Enberg [10] folgend. Des Weiteren treten systematische Effekte aufgrund der Unsicherheit in den Simulationsparametern, wie der Absorptionslänge von Licht in Wasser, der Streulänge und der Photomultiplier-Effizienz, auf. Diese belaufen sich auf $^{+54}_{-47}$ % für Schauer von atmosphärischen Neutrinos und $^{+17}_{-32}$ % von kosmischen Neutrinos. Dieser Fehler enthält außerdem einen Beitrag, der von der fehlenden Photonstreuung herrührt. Für Spurereignisse liegt der Fehler aus den Simulationsparametern bei $10 - 20$ %.

Die Analyse wurde entwickelt als sogenannte blinde Suche, die nur mit Hilfe von simulierten Ereignissen optimiert wurde und bei der nicht vorab die aufgenommenen Messdaten untersucht wurden. Dies soll verhindern, dass Erwartungen, die von früheren Messungen herrühren, wie zum Beispiel Ergebnisse von IceCube [11] [12] [13], die Analyse in irgendeiner Weise beeinflussen. Da diese ersten Schauer-Analysen von IceCube, die mit den Daten des noch nicht vollständig ausgebauten IceCube-Detektors durchgeführt wurden, kein Signal eines kosmischen Neutrinoflusses messen konnten, auch wenn deren instrumentiertes Volumen das von ANTARES bei Weitem übersteigt, wurde diese Analyse zur Bestimmung einer oberen Grenze auf den diffusen kosmischen Neutrinofluss optimiert. Dazu wurde die Model-Rejection-Factor-Technik [14] verwendet. Eine Kombination aus Schnitten auf eine minimal rekonstruierte Schauerenergie und einen minimal rekonstruierten Zenithwinkel, die sich auf die Anzahl der übrigbleibenden kosmischen Neutrino- und atmosphärischen Myon- und Neutrinoereignisse auswirkt, wurde solange variiert, bis die beste Sensitivität erzielt wurde. Die Sensitivität ist ein Maß für die Stärke eines Flusses der im Mittel mit einem Konfidenzlevel von 90 % mit der Analyse ausgeschlossen werden kann. Diese wurde bestimmt zu:

$$E^2 \cdot \bar{\Phi}_{90\,\%} = 2.21^{+0.87}_{-0.73} \cdot 10^{-8} \,\mathrm{GeV/cm^2 \cdot sr \cdot s}$$

Die vollständig entwickelte Analyse-Methode wurde anhand von 10 % der ANTARES-Daten getestet, wobei keine Probleme auftraten. Ein beobachteter Überschuss an gemessenen Daten bezüglich einer reinen atmosphärischen Untergrund-Annahme lag innerhalb der bestimmten systematischen und statistischen Fehler. Nach einer ausführlichen Begutachtung durch verschiedene Mitglieder der ANTARES-Kollaboration aus unterschiedlichen Instituten wurden die übrigen 90 % der Daten analysiert und offenbarten 8 Ereignisse in 1247 Tagen nach allen Schnitten, wogegen $4.92^{+2.85}_{-2.96}$ aus dem atmosphärischen Untergrund (Myonen, konventionelle Neutrinos nach Bartol [9] und prompte Neutrinos nach Enberg [10]) erwartet wurden. Der Überschuss an Ereignissen gegenüber dem Untergrund weist eine Signifikanz von $1.5\,\sigma$ auf und könnte ein Anzeichen für einen Beitrag aus dem kosmischen Neutrinofluss sein. Der von IceCube gemessene Fluss mit oberer Energiegrenze [4] würde weitere $2.14^{+0.48}_{-0.73}$ kosmische Ereignisse zu den atmosphärischen Erwartungen beitragen. Allerdings sind die gemes-

senen 8 Ereignisse auch mit dem Untergrund verträglich, wenn man die systematischen und statistischen Fehler auf die Simulation und den Poisson-Fehler von $\sqrt{8} = 2.8$ berücksichtigt.

Unter der Annahme eines ungebrochenen kosmischen E^{-2}-Neutrinoflusses mit einem Flavourverhältnis von $\nu_\mu : \nu_e : \nu_\tau = 1 : 1 : 1$ wurde eine obere Grenze auf den diffusen kosmischen Neutrinofluss pro Neutrinoflavour mit einem 90 %-Konfidenzlevel berechnet zu:

$$E^2 \cdot \Phi_{90\,\%} = 4.91 \cdot 10^{-8} \, \text{GeV/cm}^2 \cdot \text{sr} \cdot \text{s}$$

Diese Grenze ist gültig im Energiebereich von 22.7 TeV bis 7.8 PeV und wurde mit der Feldman-Cousins-Methode [5] bestimmt. Systematische Fehler wurden mit Hilfe des Programms **Pole 1.0** [15] [16], das Gauß-Verteilungen für die Fehler auf Signal und Untergrund annimmt, mit einbezogen.

Folgende Abbildung zeigt die bestimmte obere Grenze (als grüne Linie) im Vergleich zu den Ergebnissen anderer Experimente und Analysen. Eine Veröffentlichung dieser Analyse ist in Bearbeitung.
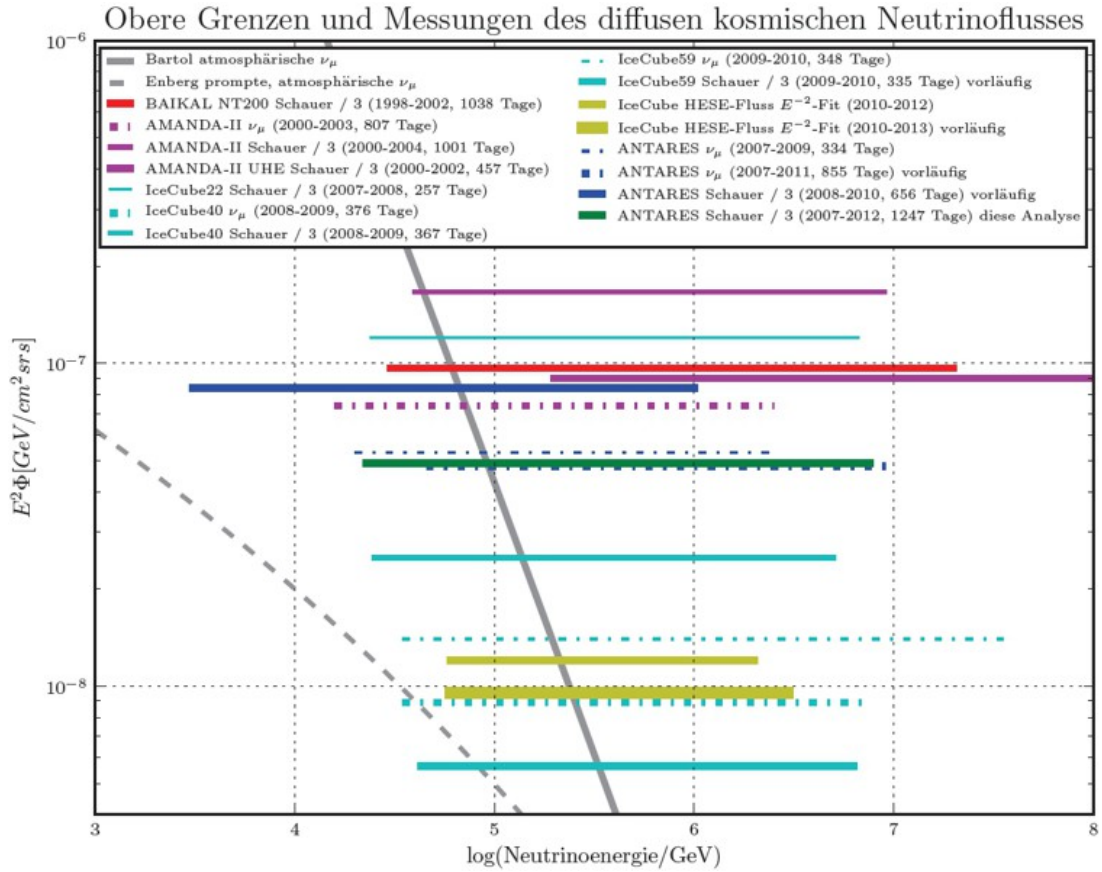
Abbildung 1: *Das Ergebnis dieser Arbeit im Vergleich zu anderen Analysen.* Die Abbildung zeigt die obere Grenze auf den diffusen kosmischen Neutrinofluss, die in dieser Arbeit bestimmt wurde (grün) und vergleicht diese mit anderen Ergebnissen. Grenzen, die sich auf alle drei Neutrinoflavour beziehen, wurden durch 3 geteilt (beziehen sich also nun auf einen Flavour) um sie besser mit Grenzen aus ν_μ-Analysen vergleichen zu können. Lediglich die Analyse der IceCube-Daten seit 2010 konnte bisher einen Fluss aus hoch-energetischen kosmischen Neutrinos nachweisen und rekonstruieren (gelb) [4] [17]. Alle anderen Linien zeigen Grenzen aus ν_μ-Analysen (gestrichelte Linien) und Schaueranalysen mit allen drei Neutrinoflavour (durchgezogene Linien) aus den Experimenten BAIKAL [18], AMANDA [19] [20] [21], IceCube [11] [22] [12] [23] [13] und ANTARES [24] [25] [8]. Zum Vergleich sind die atmosphärischen ν_μ-Flüsse (graue Linien) nach Bartol [9] und Enberg [10] eingezeichnet. Alle Flüsse beziehen sich auf die Summe aus Neutrino und Anti-Neutrino.

Contents

Chapter 1

Introduction

The search for cosmic neutrinos is one of the biggest experimental challenges in modern astronomy. Whereas throughout all times scientists have drawn their conclusions about our universe from observations with optical telescopes, in the last century these observations have been extended to other wavelengths in the electromagnetic spectrum, reaching from low energy infrared wavelengths up to high energy x-rays and gamma rays. Astronomy is no longer limited to visible objects but makes use of the full range of the cosmic rays spectrum. And now, another particle comes into play that could answer fundamental questions about the highest energies in the universe: the neutrino. The existence of this very light uncharged lepton was proven in 1956 by the Cowan-Reines experiment, where, for the first time, the neutrino was directly observed [26]. First observations of extra-terrestrial neutrinos have been made by the Homestake experiment in the late 1960s [27], where solar neutrinos have been detected. The search for extra-terrestrial neutrinos, especially from origins outside our solar system, is called *neutrino astronomy*.

This new field in astronomy has been promoted in the last years by experiments, such as BAIKAL [28], AMANDA [29], ANTARES [1] and IceCube [3]. The neutrino is an excellent information carrier about its origin as, like all uncharged particles, it is not deflected by magnetic fields along its path. Further, with an extremely low scattering cross-section it propagates through space without being absorbed in interstellar matter. This cross-section, on the other hand, is the crucial point for the detection of neutrinos at the earth and forces experiments to have large amounts of target material. Thus, the ANTARES detector is located at the seabed of the Mediterranean Sea and has an instrumented volume of $\approx 0.01\,\mathrm{km}^3$ of sea water. IceCube, with an instrumented volume of $\approx 1\,\mathrm{km}^3$, has been built into the glacial ice at the South Pole.

For many years the detection of high energy muon neutrinos in deep inelastic charged current ν_μ scattering processes has been regarded as the *golden channel* of neutrino astronomy as such reactions induce long muon tracks from which conclusions about the direction and energy of the neutrino can be drawn. The reconstruction of the properties of these muons allows in principle to do astronomy with neutrinos. The

identification of neutrino point sources in the sky and their assignment to known astrophysical objects could give us insights into the processes that take place inside these objects. For instance, the detection of neutrinos from an object also emitting high energy photons could answer the question whether particles inside this object are accelerated in hadronic or electromagnetic processes. In the latter case no neutrino would be observed [3].

The construction of the ANTARES detector was completed in May 2008, IceCube in December 2010, but in both cases data was already taken during earlier periods with smaller detector configurations. However, the analysis of these data up to 2012 did not reveal any statistically significant excess of muon neutrinos from a certain direction in the sky [30] [31] [32].

Another method to look for cosmic neutrinos is the search for the diffuse cosmic neutrino flux. Here the analysis is performed by counting the number of neutrino events averaged over the whole sky, regardless from where they are coming, and measuring their energy spectrum. Several analyses of the diffuse cosmic ν_μ flux exist, but none of them could measure events from such a flux, and therefore set upper limits on its strength [22] [23] [24].

But as for the analysis of the diffuse flux the demand for a good angular resolution of the neutrino reconstruction is less high than for point source analyses, here neutrinos from all three flavours can be taken into account. ν_e and ν_τ produce hadronic and/or electromagnetic particle showers that can be reconstructed as well. Further, neutrinos of all three flavours induce hadronic showers in neutral current reactions. Whereas the standard all-flavour diffuse flux analyses could not measure a neutrino signal either [11] [33] [13] [8], it was a dedicated analysis of ultra-high energy events in IceCube that found two shower events above 1 PeV that are not compatible with a background only hypothesis [34]. The follow-up analysis of two years of data revealed another 26 neutrino events above 30 TeV, compatible with an extra-terrestrial neutrino flux. 20 of them are shower events [4].

Even though it was the ν_μ charged current channel that promised insights into the secrets of our universe in the first place, there are now promising indications that it is may be the shower events that help neutrino astronomy achieve its breakthrough.

Chapter 2

The diffuse cosmic neutrino flux

The diffuse cosmic neutrino flux is understood in the following as the flux of extra-terrestrial neutrinos that arrive at the earth, averaged over all angles of incidence. Compared to analyses that aim at identifying clusters of neutrino emission points in the sky (point sources), here the focus is laid on the determination of the energy spectrum and the normalization N_0, i.e. the strength, of the cumulative neutrino flux. The cosmic neutrino flux is expected to follow a power law with a spectral index γ:

$$\Phi(E) = \frac{\mathrm{d}N}{\mathrm{d}E} = N_0 \cdot E^{-\gamma} \tag{2.1}$$

where $\mathrm{d}N/\mathrm{d}E$ is the number of neutrinos that arrive per energy interval $E + \mathrm{d}E$. The flux is typically given in units $1/(\mathrm{GeV} \cdot \mathrm{cm}^2 \cdot \mathrm{sr} \cdot \mathrm{s})$. From the models introduced in chapter 2.1 the spectral index is expected to have a value of $\gamma \approx 2.0$.

In the following (chapters 2.1 and 2.2) a short outline of the origin of cosmic neutrinos is given, summarizing the explanations in [35] [36], where also a more extensive discussion can be found.

2.1 Neutrino generation processes

In the cosmos neutrinos can be generated in a variety of objects and processes, covering several orders of magnitude in the energy spectrum.

The first observed extra-terrestrial neutrinos were solar neutrinos that were discovered by the Homestake experiment in 1968 [27]. Neutrinos from the sun are produced in nuclear fusion reactions, of which the so-called *pp-chain* gives, with 86 %, the largest contribution to the solar neutrino production. Solar neutrinos have an energy from a few hundred keV up to a few MeV [37].

The first and up to now only proven source of neutrinos from outside our solar system is the supernova 1987A that took place on 23rd of February 1987. Three

neutrino experiments, Kamiokande II [38], IMB [39] and Baksan [40], independently measured altogether 25 neutrinos from that source in the energy range of a few MeV [36].

However, both occurrences wouldn't have been recorded by large volume neutrino telescopes like ANTARES or IceCube as their minimum energy threshold is on the order of $10 - 100\,\mathrm{GeV}$. Neutrinos at this threshold and up to the very highest energies observed in the cosmos $> 10^{11}\,\mathrm{GeV}$ [41] might be produced in any region in the cosmos where protons are accelerated to high energies.

This can happen for example at shock fronts that move through the interstellar gas. Here, charged particles are accelerated by the so-called *First order Fermi mechanism*. In this theory the particle gains a constant fraction of energy by traversing through the shock front from the upstream region (in front of the shock) to the downstream region (the shocked gas behind the front). To achieve such high energies the particle has to repeat this transition many times.

The *Second order Fermi mechanism* describes the acceleration of charged particles as a consequence of multiple deflections at the irregularities of the magnetic field inside a moving plasma cloud. Both Fermi mechanisms are described for instance in [37] [42].

Once protons have been accelerated, neutrinos can be produced in hadronic particle showers when the high energy proton interacts with other particles in the gas. The predominantly charged pions and kaons in these showers decay and thereby create neutrinos. With a probability $> 99.9\,\%$ charged pions decay into muons:

$$\pi^- \to \mu^- + \overline{\nu}_\mu \qquad \pi^+ \to \mu^+ + \nu_\mu \tag{2.2}$$

Decaying charged kaons can either produce pions (in $28\,\%$ of all cases), of which the charged ones decay further into muons, or directly produce muons ($64\,\%$). The induced muon may decay further into an electron producing two more neutrinos

$$\mu^- \to e^- + \nu_\mu + \overline{\nu}_e \qquad \mu^+ \to e^+ + \overline{\nu}_\mu + \nu_e \tag{2.3}$$

Equations and branching ratios are taken from [43]. Following these equations, the ratio of ν_μ/ν_e is 2 at the source, but due to neutrino oscillations a ratio of $\nu_\mu : \nu_e : \nu_\tau = 1 : 1 : 1$ is expected at Earth [44]. The spectral index of the neutrino flux from such a scenario is expected to have a value of $\gamma \approx 2$ [42].

2.2   Cosmic high energy neutrino sources

As shown in the previous chapter all objects that are capable of accelerating protons up to very high energies are also potential neutrino sources. The evidence or

absence of neutrinos in the measured particle flux from such a source can prove or disprove acceleration models. For instance, high energy electrons - also accelerated by the Fermi mechanism - will produce high energy gamma rays via Bremsstrahlung or inverse Compton-scattering when interacting with the matter or radiation fields close to the source. On the other hand high energy mesons may decay into neutral pions that produce gamma rays as well. Therefore measuring high energy gamma rays from a source does not allow to draw conclusions about the acceleration model in the source. Neutrinos, however, can only be created if the primary high energy particles are hadronic. Hence, the detection of gamma rays *and* neutrinos from a source would be a strong evidence for hadronic acceleration. If gamma rays *without* neutrinos are detected, the acceleration is likely more leptonic in that source [35] [3].

Within our galaxy the most promising candidates for neutrino production are **supernova remnants** [36]. The explosion of a massive star typically causes an expanding shell that produces a shock wave when moving through regions that are filled with interstellar gas. Whereas during the supernova explosion only low energy MeV neutrinos are produced, the shock afterwards can create neutrinos up to $100 \, \text{TeV}$ [42], if protons are accelerated. In many cases the relic of the massive star after the explosion is a **pulsar**, an object with a strong magnetic field that can emit high energy gamma rays. The potential detection of neutrinos from a pulsar can help to better understand the acceleration in the magnetosphere [45].

Further, the so-called **Fermi bubbles** [46], two large circular structures above and below the Galactic centre that emit a hard E^{-2} gamma ray spectrum, are a promising galactic candidate for neutrino emission. Their origin is not yet understood, however, the detection of neutrinos from these bubbles could prove attempts to explain the origin using hadronic models [47].

Binary systems, such as **microquasars**, are also a promising candidate for neutrino emission [48]. A black hole is accreting mass from a heavy companion star, where as a consequence a relativistic jet is formed perpendicular to the accretion disk. In these jets protons can be accelerated to very high energies and produce pions in scattering processes. Following equation (2.2) these pions produce high energy neutrinos.

Steady neutrino sources that can produce neutrinos above $100 \, \text{TeV}$ are probably of extra-galactic origin. **Active galactic nuclei (AGN)** are the most powerful long-term persistent objects known in the cosmos and are a collective term for galaxies with a super-massive active black hole. As with microquasars the black hole is surrounded by an accretion disc and, typically, two relativistic jets that are emitted perpendicular to the disk and that can reach the length of $1 \, \text{Mpc}$[1]. As the theoretical models of these objects are still quite speculative, the detection of neutrinos that are expected to be produced in the disk and in the jets can help to better understand the physics in the

---

[1]1 Mega parsec $= 3.26 \cdot 10^6$ light years

AGN. There are even cases, where a dust layer prevents the emission of gamma rays from the disk. Here the only information from the center of the AGN could be obtained from neutrinos [35].

As an example for a transient high energy neutrino source, **gamma ray bursts (GRB)** are to be mentioned. GRBs are the brightest phenomena in the universe, if only for a brief moment. Merging binary systems with a black hole or a neutron star or a so-called hyper-nova, the collapse of a very massive star into a rapidly rotating black hole, cause bright flashes of gamma rays lasting from a few milliseconds up to a few hundred seconds. The mechanisms of particle acceleration inside these bursts are not yet completely understood but a hadronic component, and hence neutrino emission, is naturally expected from such violent phenomena [35]. Recent analyses have searched for neutrinos from known GRBs, but could not find a significant correlation [49] [50] [51].

2.3   Theoretical predictions

Long before experiments, such as IceCube or ANTARES, began searching for neutrinos theoretical predictions came up to give an expectation for the diffuse cosmic neutrino flux. By now several models exist, of which here only those are mentioned that predict a flux that is high enough to be detected or excluded by ANTARES (see chapter 12). Other models, such as GRB neutrino flux models, yield a flux about one order of magnitude lower.

The most famous model might be that by Waxman and Bahcall, firstly introduced in 1998 [52] [53]. It has been developed for optically thin sources, i.e. objects where induced cosmic rays and photons can escape easily. Further, it was assumed that protons are accelerated by the Fermi mechanism (see chapter 2.1) and transfer their entire energy to pions. The normalization N_0 of the resulting E^{-2} spectrum was obtained from cosmic ray measurements at earth and yielded a value of $4.5 \cdot 10^{-8}\,\mathrm{GeV/cm^2 \cdot sr \cdot s}$ for muon neutrinos at the source, which arrives at Earth due to neutrino oscillation [44] with a strength of $2.25 \cdot 10^{-8}\,\mathrm{GeV/cm^2 \cdot sr \cdot s}$ per neutrino flavour.

In the same year Mannheim, Protheroe and Rachen (MPR) [54] extended the flux calculations by taking into account characteristics of the astrophysical objects that have a varying opacity and assuming that they do not necessarily have a fixed E^{-2} spectrum. A wider discussion of these models is also given in [36]. The MPR flux shown in figure 2.1 refers to an optical thin model.

The two models by Mannheim [55] in 1995 and Stecker [56] in 2005 are derived from optically thick AGN sources taking into account measurements of the diffuse gamma ray flux. Becker, Biermann and Rhode (BBR II) [57] calculate the flux using cosmic

ray observations of FR II radio galaxies and blazars[2], here again for an E^{-2} particle spectrum. All three of the last mentioned models assume a neutrino production in the jets.

Figure 2.1 gives an overview of the here introduced theoretical astrophysical flux models, compared to the Bartol [9] atmospheric neutrino flux. A discussion of the atmospheric neutrino flux is given in chapter 4.2
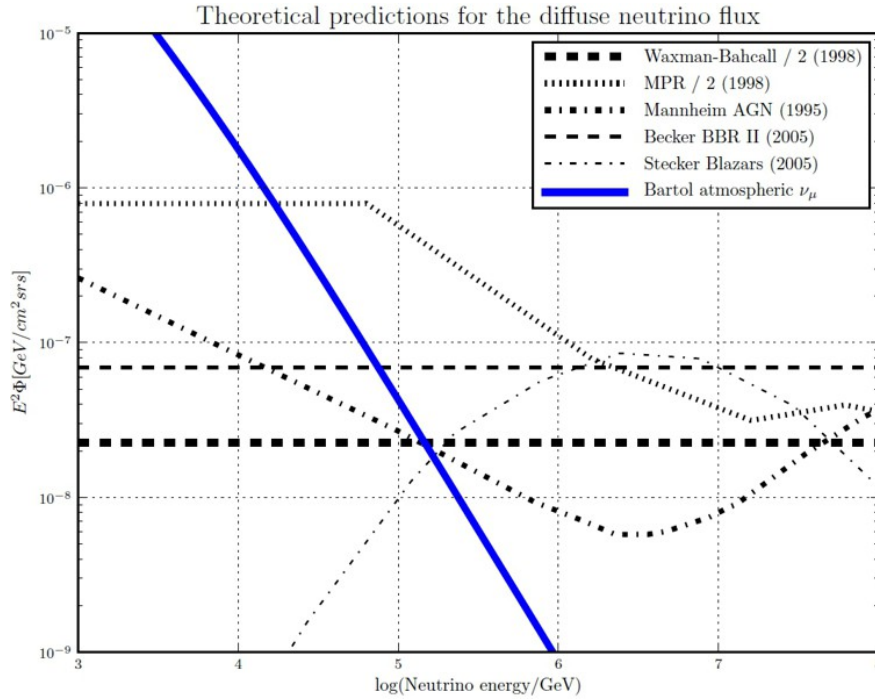
Figure 2.1: *Theoretical predictions for the diffuse cosmic neutrino flux.* The plot shows various models for the diffuse cosmic neutrino flux per flavour. The predictions from Waxman-Bahcall [52] [53] and Mannheim et al. (MPR) [54] have been divided by two to take into account neutrino oscillations. Those models calculate the ν_μ flux at the source assuming a ratio of $\nu_\mu : \nu_e = 2 : 1$. The AGN models by Mannheim [55], Stecker [56] and Becker et al. (BBR II) [57] already give the ν_μ flux as observed at Earth. For comparison the atmospheric ν_μ flux (blue line) as calculated by Bartol [9] has been added. All fluxes represent the sum of neutrino and anti-neutrino.

2.4 Recent measurements

This section gives an overview of experiments and analyses towards the detection of the diffuse cosmic neutrino flux of the last 20 years. As throughout all these years none of the experiments could measure a significant number of cosmic neutrinos above the atmospheric background, upper limits have been set. Only recently, a first evidence for

---

[2]Radio galaxies and blazars are special subtypes of AGN that have a high luminosity at radio wavelengths

cosmic neutrinos was found [34] [4] [17] which can be regarded as a great breakthrough in neutrino astronomy.

As in the following limits from ν_μ diffuse flux analyses, i.e. those that have been sensitive to one flavour only, are compared to shower analyses that include all three neutrino flavours, the results from the latter ones are divided by 3 for comparison. Limits in shower analyses are typically given for the sum of all three flavours. Hence, assuming a flavour ratio of $1:1:1$ the here presented limits always refer to one single flavour.

The pioneer work in neutrino detection with large volume telescopes has been done by the BAIKAL [28] and AMANDA [29] experiments. The first one is located underwater in Lake Baikal, Russia, where 200 photo-multipliers (PMT) have been installed in a three-dimensional array on 8 strings from 1993 to 1998 (see chapter 3.1 for a description of the detection principles). AMANDA, located in the glacial ice of the Antarctic, consists of 677 PMTs on 19 strings that have been deployed between 1995 and 2000.

The best upper limits on the neutrino flux obtained by these prototype experiments are $7.4 \cdot 10^{-8}\,\mathrm{GeV/cm^2 \cdot sr \cdot s}$ on the ν_μ flux (AMANDA-II [19]) and $1.7 \cdot 10^{-7}\,\mathrm{GeV/cm^2 \cdot sr \cdot s}$ (AMANDA-II [20]) as well as $1.0 \cdot 10^{-7}\,\mathrm{GeV/cm^2 \cdot sr \cdot s}$ (BAIKAL [18]) per neutrino flavour, obtained in shower analyses. A dedicated search for high energy neutrinos above $100\,\mathrm{TeV}$ with AMANDA has set an upper limit of $9.0 \cdot 10^{-8}\,\mathrm{GeV/cm^2 \cdot sr \cdot s}$ [21].

Beginning in 2004 the detector array of AMANDA-II was extended gradually towards a detector with $1\,\mathrm{km^3}$ instrumented volume: IceCube [3]. First measurements have been performed with a 22 string configuration (IC22), each carrying 60 PMTs, followed by periods with 40, 59 and 79 strings. The detector with all 86 strings was completed in December 2010. The currently best limit on the ν_μ flux is obtained from the IC40 data and yielded $8.9 \cdot 10^{-9}\,\mathrm{GeV/cm^2 \cdot sr \cdot s}$ [22]. The up to now best published limit from a shower analysis is $2.5 \cdot 10^{-8}\,\mathrm{GeV/cm^2 \cdot sr \cdot s}$ per neutrino flavour (IC40) [12]. However, preliminary results indicate a better limit of $5.7 \cdot 10^{-9}\,\mathrm{GeV/cm^2 \cdot sr \cdot s}$ per flavour (IC59) [13].

The ANTARES [1] telescope, whose data will be analysed in this work, was built in the Mediterranean Sea from 2006 to 2008. A description of the detector is given in chapter 3. Analyses of the diffuse ν_μ flux yielded a best upper limit of $4.8 \cdot 10^{-8}\,\mathrm{GeV/cm^2 \cdot sr \cdot s}$ [25]. The goal of this work is to obtain an all flavour limit from the analysis of showers events in the ANTARES data. A similar study has been developed in parallel as part of another PhD thesis, where a limit of $8.4 \cdot 10^{-8}\,\mathrm{GeV/cm^2 \cdot sr \cdot s}$ per neutrino flavour was obtained [8].

While all experiments have been setting limits up to now, it was an analysis of high energy neutrinos above $30\,\mathrm{TeV}$ measured with the IceCube detector that for the very

first time found an evidence for the existence of a high energy cosmic neutrino flux. The analysis was published in the end of 2013 and obtained a best fit to the data with a normalization $N_0 = (1.2 \pm 0.4) \cdot 10^{-8} \, \mathrm{GeV/cm^2 \cdot sr \cdot s}$ per neutrino flavour in the energy region between $60 \, \mathrm{TeV}$ and $2 \, \mathrm{PeV}$, assuming an E^{-2} spectrum. Further, a cut-off was proposed at a value $< 10 \, \mathrm{PeV}$ [4]. A preliminary, updated version of that analysis, taking into account IceCube data up to 2013, obtained a best fit of $N_0 = (0.95 \pm 0.3) \cdot 10^{-8} \, \mathrm{GeV/cm^2 \cdot sr \cdot s}$ per neutrino flavour [17].

Figure 2.2 gives an overview of the limits and fluxes that have been determined by the experiments, including the energy ranges for which they are valid. As ANTARES is a relatively small-sized detector, comparable to AMANDA-II, the limit for the shower channel is expected to yield a value near the AMANDA results [20] [21].

The future experiment *KM3NeT* [58] is already in preparation. Following the principle of ANTARES it is planned to install a large neutrino telescope in the Mediterranean Sea with a volume of at least $1 \, \mathrm{km^3}$.
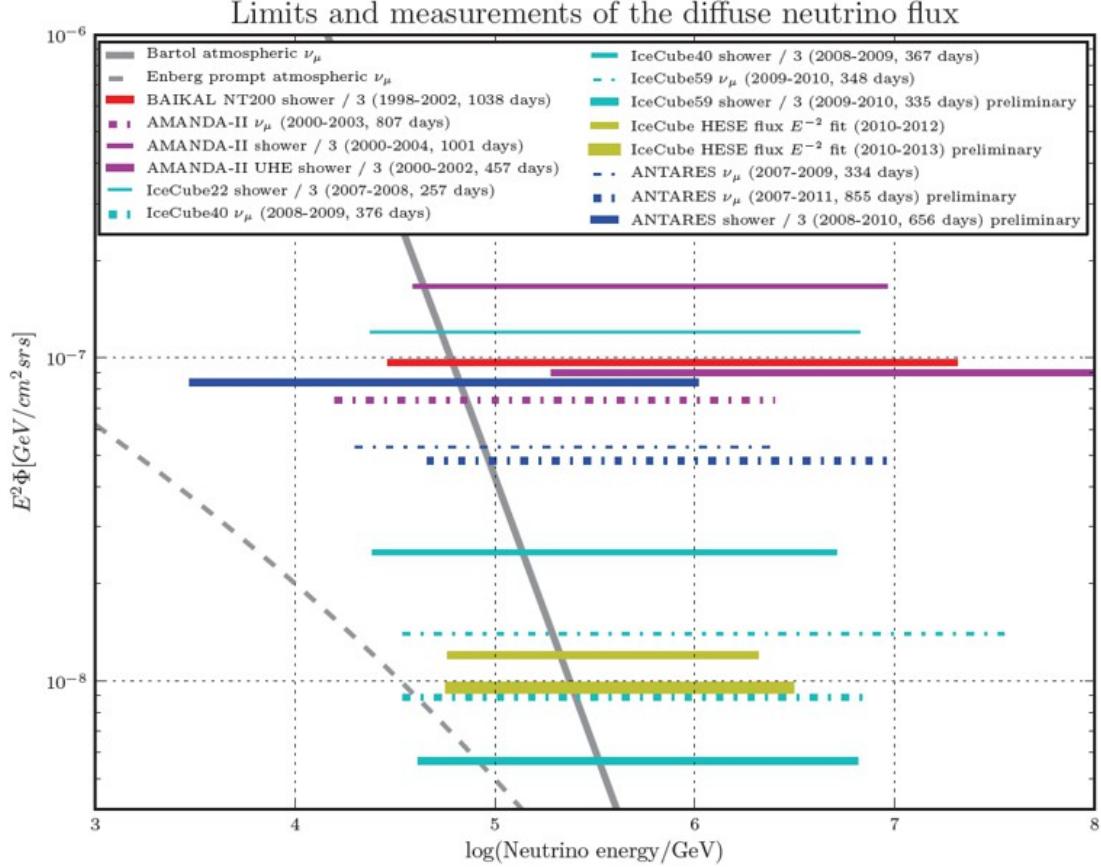
Figure 2.2: *Limits and measurements of the diffuse cosmic neutrino flux.* The plot shows the result of various analyses of the diffuse cosmic neutrino flux. Limits from all flavour shower analyses are divided by 3 (i.e. they are given per flavour now) to be able to compare them to ν_μ limits. Only the analysis of the IceCube data since 2010 could prove the existence of a flux from cosmic high energy neutrinos and fit a flux expectation (yellow) [4] [17]. All other lines mark upper limits from ν_μ analyses (dashed-dotted lines) and all flavour shower analyses (solid lines), sorted by experiment: BAIKAL [18], AMANDA [19] [20] [21], IceCube [11] [22] [12] [23] [13] and ANTARES [24] [25] [8]. For comparison, the atmospheric ν_μ fluxes (grey lines) as calculated by Bartol [9] and Enberg [10] have been added. All fluxes represent the sum of neutrino and anti-neutrino.

Chapter 3

The ANTARES experiment

The ANTARES[1] experiment [1] has been designed to search for cosmic neutrinos by detecting secondary leptons or hadronic particle showers the have been induced in deep inelastic neutrino scattering processes. In a depth of around 2500 m, 40 km offshore from Toulon, a three-dimensional array of 885 photomultiplier tubes (PMT) has been set up by the ANTARES collaboration, an association of 32 institutes from 7 European and one North-African countries (as from December 2013).

The detector consists of string units (lines), each holding 75 optical modules (OM) that are arranged in groups of three on 25 storeys (see figure 3.1), where the distance between two storeys on the string is 14.5 m. Thus, the total instrumented length on a string is about 350 m. Each OM carries a 10" Hamamatsu PMT that points downwards at $45°$ to give the detector, for background suppression reasons, a higher sensitivity to up-going than to down-going events. A detailed description of the OM is given in [59]. Each string is anchored at the seabed and held in an approximately vertical position by a buoy at the top. The true line shape and thus the position of the OMs varies with the sea current and is determined in regular intervals of approximately 2 minutes from triangulating the signals of an acoustic positioning system. Here, an accuracy of < 10 cm is achieved [60].

The detector construction was started in January 2007 with an initial configuration of 5 strings. In December 2007 the setup was expanded to 10 strings and finally the full 12 string detector was completed in May 2008 with an instrumented volume of approximately 0.01 km^3. For this analysis data was taken with each detector configuration since 2007 up to the end 2012. A scheme of the final detector configuration is given in figure 3.2.

---

[1]Astronomy with a Neutrino Telescope and Abyss environmental RESearch
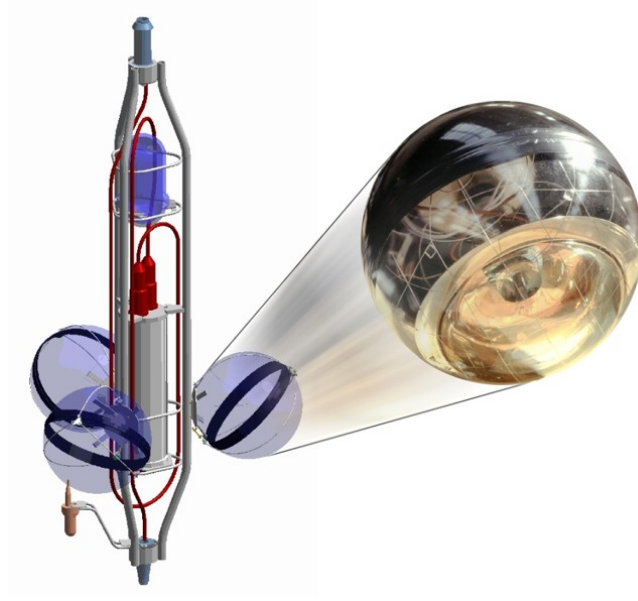
Figure 3.1: *The ANTARES storey and optical module.* An artist's view of a storey [61] and a photograph of an OM [62]. Combined image taken from [63]

.
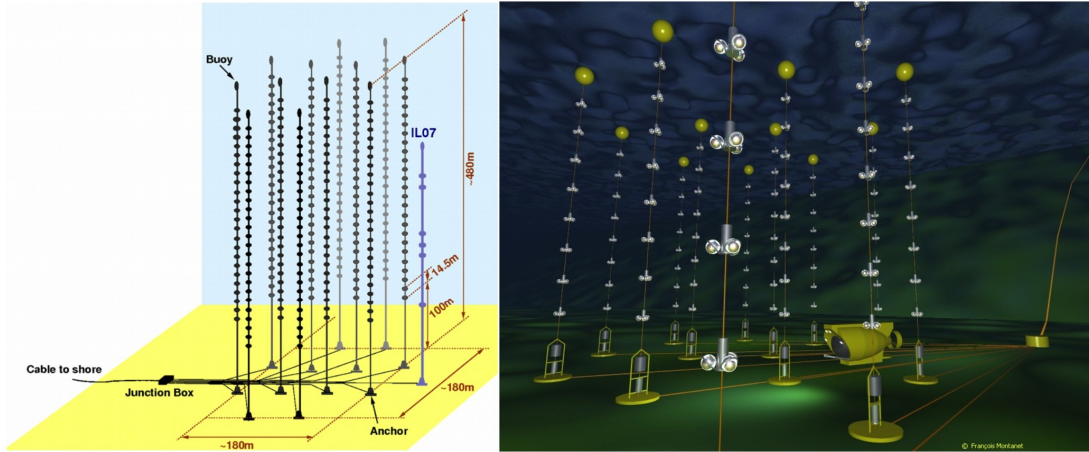
Figure 3.2: *Scheme of the ANTARES detector.* Sketch of the ANTARES detector layout (left) [64] and an artist's view (right) [62]

3.1 Neutrino detection principles

The detection of neutrinos is achieved by reconstructing the position, path and energy of the secondary particles that are created in deep inelastic scattering processes of the neutrino and a nucleon (here typically one of a water atom). ANTARES is designed to detect neutrinos with energies greater than $100\,\text{GeV}$, where the majority of the secondary particles move with a velocity above the Cherenkov threshold, greater than the speed of light in water, and hence emit Cherenkov photons [2]. Figure 3.3 gives an

illustration of the principle of Cherenkov radiation. A charged particle traversing from a point S' to S with a velocity v_s is polarizing its environment along its path. When returning to ground state the surrounding excited atoms emit photons (indicated by wave front circles in the figure) that interfere destructively if v_s is below the phase velocity of light in water v. However, for greater velocities the interference is coherent as the particle propagates a larger distance than the emitted Cherenkov wave fronts in the same time.
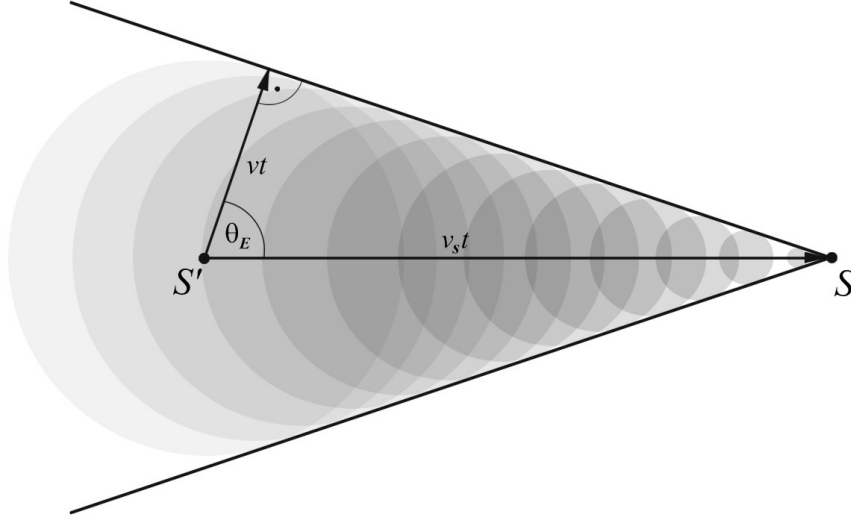
Figure 3.3: *Illustration of the Cherenkov cone.* A charged particle moving through a dielectric matter with a speed greater than that of light in matter emits Cherenkov radiation under a specific angle Θ_E respective to the track.

The so called Cherenkov radiation has a spectral range from $400\,\text{nm}$ to $700\,\text{nm}$ [37] and is emitted at an angle Θ_E with respect to the particle track. From simple geometry one can derive that the angle is a function of the refractive index $n = c/v$ and the velocity of the charged particle $\beta = v_s/c$ (c is the speed of light in vacuum):

$$\Theta_E = \arccos \frac{vt}{v_s t} = \arccos \frac{1}{n\beta} \tag{3.1}$$

The refraction index of water at the ANTARES site is about 1.35 for a wavelength of $450\,\text{nm}$, for which the efficiency of the PMTs and the transparency of water are maximal [35]. Hence, the Cherenkov photons are emitted under an angle of $42°$. By measuring the arrival time and the amount of these photons the properties of the secondary particles, such as energy, trajectory & position, can be reconstructed and hence, conclusions about the inducing neutrino can be drawn.

3.2   Event signatures

Depending on the flavour and type of the incoming neutrino the interaction with the water target material creates different event topologies that are described in this section. Here, the focus is laid on the space-time event topology of the events, as those are relevant for the reconstruction and the discrimination between the different channels. A more detailed particle physics based description, also from a theoretical point of view, can be found in [37] [42].

A charged current interaction of the muon neutrino was always believed to be the golden channel of neutrino astronomy as the induced muon trajectory can be reconstructed with a sufficiently high accuracy to allow the search for cosmic neutrino point sources [30]. However, recent results of the IceCube neutrino observatory, where for the very first time an evidence for high-energy extraterrestrial neutrinos was found [34] [4] [17], showed that also particle shower events, such as electron neutrino charged current or all flavour neutral current reactions, may play a major role in the search for cosmic neutrinos and their sources.

3.2.1   Neutral current interactions

Deep inelastic neutral current (NC) reactions happen, as their name implies without the exchange of electric charge from the primary to the secondary particles. The neutral mediator is the Z_0 boson that couples to the neutrino without changing it. The momentum and energy that is transferred to the nucleon causes a hadronic particle shower, as illustrated in figure 3.4. A fraction of the energy and momentum, however, is carried away by the neutrino and cannot be measured. The energy that is available for the evolution of the hadronic shower is reflected by the Bjorken inelasticity parameter y that is, for high energy neutrinos, the relative energy transfer from the neutrino to the hadronic shower ($y = E_{\text{shower}}/E_\nu$). Values for y as function of the neutrino energies are illustrated in [36] and lie on average between 0.25 and 0.5 for neutrinos and 0.25 and 0.4 for anti-neutrinos at neutrino energies relevant for ANTARES.

The cross-sections for NC neutrino interactions are identical for all three neutrino flavours and yield values of $2 \cdot 10^{-41}\,\mathrm{m}^2$ at $100\,\mathrm{GeV}$ and $2 \cdot 10^{-38}\,\mathrm{m}^2$ at $1\,\mathrm{PeV}$. For anti-neutrinos at $100\,\mathrm{GeV}$ the cross-sections are about a factor 2 lower but converge towards the neutrino cross-sections with increasing energy [36].

A detailed description of the composition and extension of hadronic showers and how the longitudinal and angular profile is parametrized is presented in [36]. As shown in figure 3.6 the showers reach a length of $5\,\mathrm{m}$ up to $10\,\mathrm{m}$ increasing with shower energy. Further, it is shown in [36] that the main hadronic component are pions, but also other particles, like kaons, neutrons, protons and others occur. Emitted electrons,
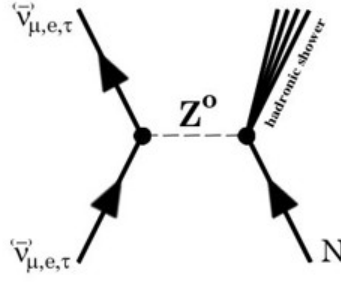
Figure 3.4: *Feynman graph of a deep inelastic neutral current neutrino interaction.* For all three neutrino flavours a neutral current interaction produces a hadronic vertex shower. Image modified from [63].

positrons and hard photons will induce electromagnetic sub-showers, muons leave the shower producing a track signature in the detector. This great variability causes significant event-to-event fluctuations compared to electromagnetic showers, as will be shown below.

3.2.2 Charged current interactions

In deep inelastic charged current (CC) reactions (anti-) neutrinos interact with the target nucleon producing the corresponding (anti-) lepton and a hadronic particle shower at the interaction vertex by exchanging a virtual charged W boson. However, depending on the flavour of the neutrino the event signature in the detector is different, as illustrated in figure 3.5. Compared to NC reactions here, the whole energy of the neutrino will be transferred to the outgoing particles.
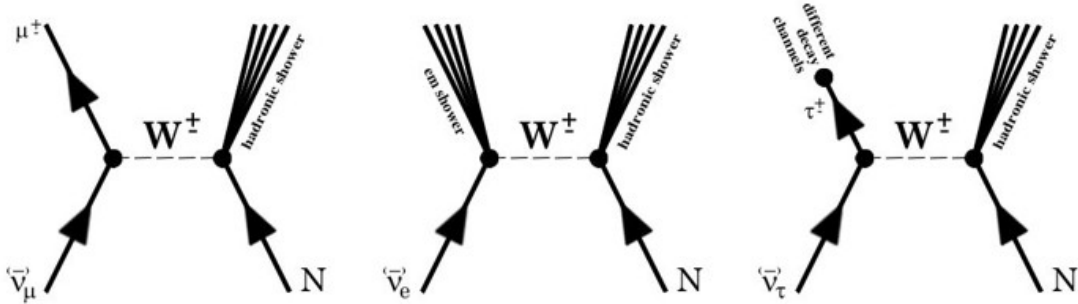
Figure 3.5: *Feynman graphs of deep inelastic charged current neutrino interactions.* Depending on the flavour of the neutrino different event signatures are created in the detector. Image modified from [63].

Again, the cross-sections for CC neutrino interactions are a function of the neutrino energy and yield calculated values of $7 \cdot 10^{-41} \, \mathrm{m}^2$ at $100 \, \mathrm{GeV}$ and $7 \cdot 10^{-38} \, \mathrm{m}^2$ at $1 \, \mathrm{PeV}$. Hence, according to their cross-section compared to NC interaction, CC reactions are about a factor 3 more frequent than NC reactions. For anti-neutrinos at $100 \, \mathrm{GeV}$ the

cross-sections are, similar to NC reactions, about a factor 2 lower, but converge towards the neutrino cross-sections with increasing energy [65] [36].

Muon neutrino CC interactions produce, beside the hadronic vertex shower, a muon that traverses a distance, depending on its energy, from a few hundred up to several thousand meters (as illustrated in figure 3.6) producing Cherenkov emission along its track. Hence, for the majority of high energy events the vertex shower is far outside the detector, where the pure contained muon trajectory is suited for a high precision neutrino direction reconstruction with a resolution better than $1°$ [30].

Electron neutrino CC processes create an electron or positron that produces an electromagnetic shower. Due to its small mass the electron will immediately loose its energy via Bremsstrahlung. As long as the energy of the generated photons is higher than two times the electron rest mass, an electron-positron pair is produced via pair production that itself will suffer from Bremsstrahlung again and hence evolve a cascade of electrons, positrons and photons. As the composition of the electromagnetic showers only contains these three particles much less event-to-event fluctuations compared to multi-particle hadronic showers are observed.

The lateral extension of such a shower is of the order of $10\,\mathrm{cm}$, whereas its length varies with energy from $5\,\mathrm{m}$ up to $10\,\mathrm{m}$ increasing with shower energy (see also figure 3.6). A parametrization of the longitudinal profile and different approaches to determine its constants are presented in [36].

At low energies the extension of an electromagnetic shower is smaller than a hadronic one with the same shower energy, whereas for higher energies the sizes converge. As at the vertex the hadronic shower is always present the event topology is a superposition of both shower types that can not be distinguished. However, both together contain the full energy of the inducing neutrino.

Tau neutrinos in the CC channel interact with the nucleon producing a tau lepton. With a mass of $1.78\,\mathrm{GeV}$ and a mean life time of $2.91 \cdot 10^{-13}\,\mathrm{s}$ [43] the tau lepton traverses a distance of

$$l_\tau = 49\,\mathrm{m} \cdot \frac{E_\tau}{\mathrm{PeV}} \tag{3.2}$$

before it decays. Along this track Cherenkov light is emitted similarly to that from muon tracks, however, with a slightly different energy dependence as the tau lepton is much heavier than the muon. Further, depending on the tau decay channel different event topologies arise. [43] gives the following branching ratios:

- $17.4\,\%$ of all tau leptons decay into muons giving rise to a second starting track.

- $17.9\,\%$ decay into electromagnetic showers and

- $64.7\,\%$ produce hadronic showers.

For the two latter channels thus, two showers (the initial hadronic vertex shower and the tau decay shower) are created within the same event at a distance of the energy dependent tau lepton track length. Whereas this double shower signature can be used to exclusively search for tau neutrinos [66], within this analysis no dedicated strategy was developed to distinguish between single and double shower events, which is mainly due to the fact that tau neutrino events have not been simulated.
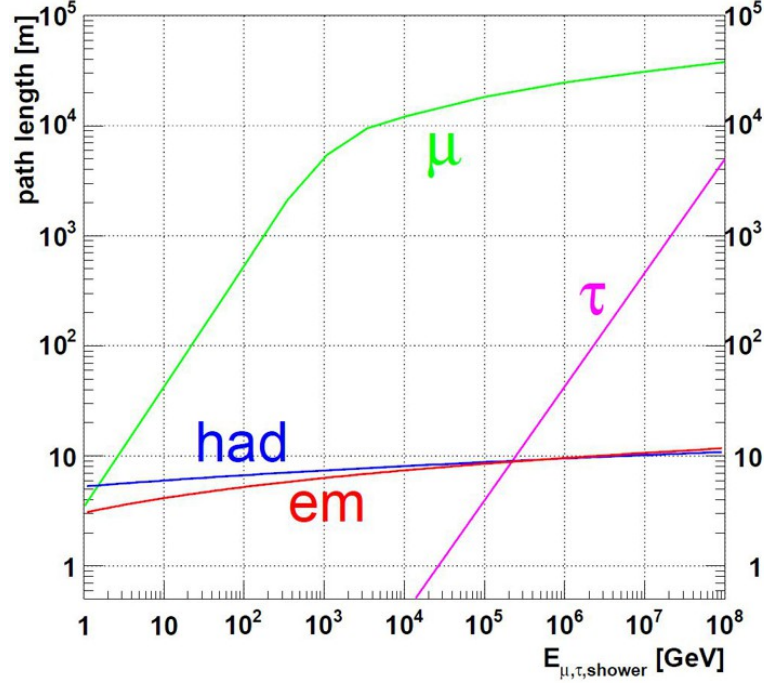
Figure 3.6: *Longitudinal ranges of different event topologies.* The plot shows the range of muon and tau lepton tracks and the length of hadronic and electromagnetic cascades as function of the particle/shower energy. Image taken from [36].

3.2.3 Resonant interactions

Apart from deep inelastic scattering processes also a few rare resonant and quasi-elastic interactions take place of which the Glashow resonance [67] is the most frequent one. Here an electron anti-neutrino interacts resonantly with an electron in the shell of a water molecule and creates a W^- boson at a resonance energy of $6.3\,\mathrm{PeV}$. The cross-section of $5 \cdot 10^{-35}\,\mathrm{m}^2$ is about 360 times higher than the deep inelastic nucleon cross-section for neutrinos at the same energy [68].

The W^- boson decay has multiple branching ratios, so that Glashow resonant events can cause all described event signatures from pure hadronic showers in hadronic decay modes to all flavour lepton events from leptonic decays, of which each creates its characteristic event signature, as described in chapter 3.2.2.

Figure 3.7 shows a Feynman graph of the Glashow resonance with the W^--Boson decaying into a lepton and its corresponding anti neutrino. In figure 3.8 different cross-sections for Glashow resonant and deep inelastic scattering events are compared.
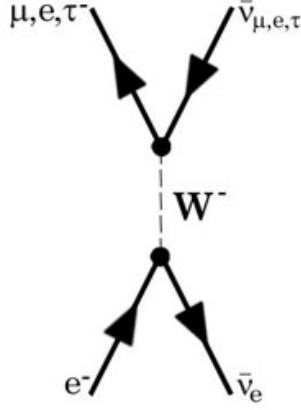
Figure 3.7: *Feynman graph of a Glashow resonance neutrino interaction.* An electron anti-neutrino at 6.3 PeV interacts with an electron producing a W^- boson that can decay, as shown here, into a lepton and its corresponding anti-neutrino.
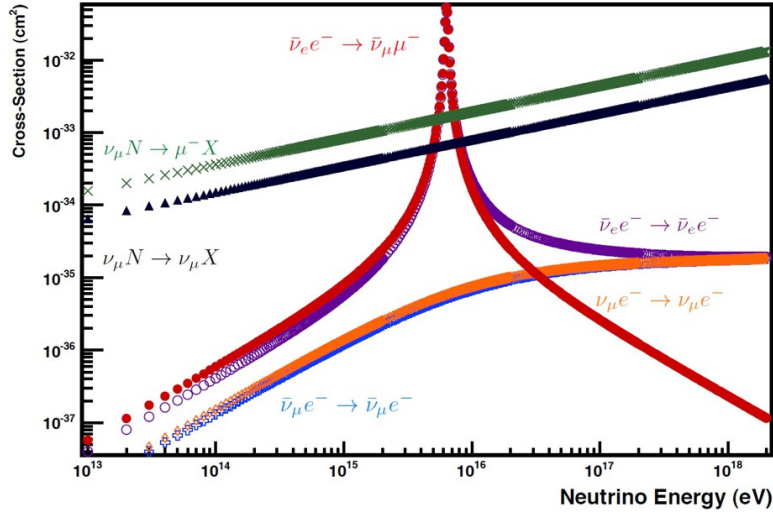
Figure 3.8: *Neutrino interaction cross-sections around the Glashow resonance energy.* The graph shows cross-sections for different neutrino electron and nucleon scattering processes. One can see that the two indicated Glashow resonance channels, where the W^- Boson decays into an electron (violet) or in a muon (red), are at their peak energy about 40 times higher than the deep inelastic charge current nucleon interaction (green) and about 100 times higher than the neutral current interaction (black). Image from [69].

Other resonant and quasi-elastic interactions are also taken into account in the event simulation (see chapter 5.1.1). However, the variety of such events that are explained in detail in [65] are located far below 1 TeV and are therefore of minor interest for a search of cosmic high energy neutrinos in the TeV-PeV scale, where the scattering cross-sections are by far dominated by deep inelastic scattering.

3.3 Data acquisition in ANTARES

The data acquisition system (DAQ) in ANTARES follows the "all-data-to-shore" concept and is described in full detail in [1], [70] and [71]. All recorded signals are sent to the shore station where different trigger algorithms are looking for physics events within the continuous data stream.

A signal is recorded at an OM when the charge threshold, typically 0.3 photo electrons (pe) measured by the PMT, is exceeded. Then an analogue ring sampler (ARS) is acquiring the signal by collecting the charge induced by all incoming photons within an integration time window of 25 ns. The accumulated charge defines the amplitude of the signal hit, the time of the threshold crossing related to the first photon its time. After having closed the integration gate, the ARS is busy with writing and sending the signal information for a dead time of around 250 ns. However, as each OM is equipped with two ARS chips, the second one is ready to take another 25 ns of data at around 40 ns after the threshold of the first ARS was exceeded. Hence, an OM that detected two consecutive hits may be inactive for a certain time, depending on how close the two hits have been detected, but for a maximum time of 225 ns.

The charge and time information of a hit is determined by an amplitude-to-voltage converter (AVC) and a time-to-voltage converter (TVC), respectively, each providing 256 channels. The calibration of these converters is performed at least once a month, for each ARS and OM individually. The resolution of the charge calibration is limited by the difference (in channels) between the pedestal value and the single photo electron peak. For the majority of OMs this difference is between 10 and 13 channels, which yields a calibration resolution of about 0.1 pe. Hence, following a linear extrapolation, the maximum detectable charge in one hit (charge saturation) for those OMs is about $20 - 25$ pe. Figure 3.9 shows the distribution of the calibrated saturation levels for the ANTARES OMs.

The time calibration is performed with an optical beacon system and is described in detail in [72]. For relative time differences between the detected hits, i.e. the relevant information for event reconstruction, the time calibration resolution reaches a level of 0.5 ns. The absolute time calibration is limited by the GPS system and reaches a level of 100 ns, which is still good enough for astronomical research, such as the search for cosmic neutrino point sources. For the analysis of the diffuse cosmic neutrino flux in this work, however, the absolute time information is of minor interest.

3.3.1 Trigger algorithms

Within the time continuous stream of data that is send to shore different trigger algorithms look for correlations in the hits to form potential physics events. Figure 3.10
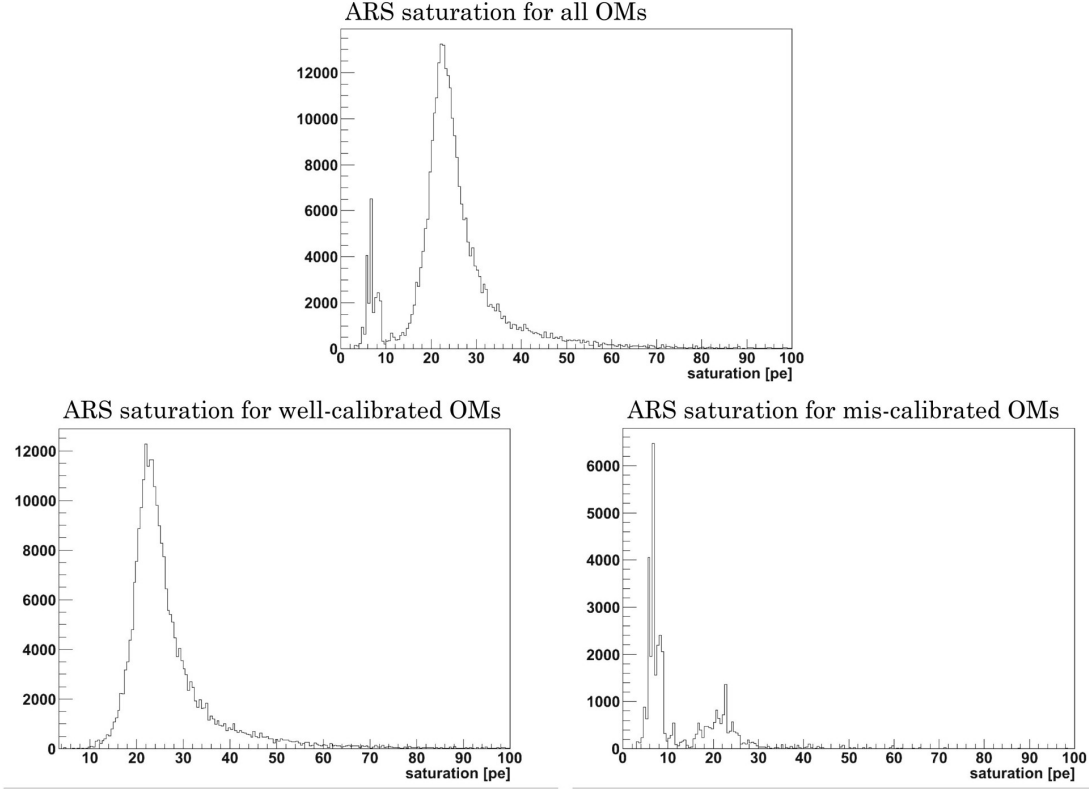
Figure 3.9: *Charge saturation distributions for ANTARES OMs.* The plots show the distributions of the maximum detectable charge per PMT from all ANTARES OMs taken from 250 runs within the run number range between 30000 and 55000 for all calibrated OMs (upper plot), for well calibrated OMs only (lower left) and for OMs where the calibration failed (lower right). The information about a successful or failed OM calibration is obtained from flags holding the information whether the identification of the 0 pe and the 1 pe channels succeeded. The saturation level has been evaluated for each ARS by calculating the charge that is related to AVC channel 255 from the corresponding calibration set.

illustrates the functionality of the ANTARES software trigger that is also described in further detail in [1].

In order not to build physics events based on optical background that is caused by the decay of Potassium-40 or bioluminescent micro lifeforms (see chapter 4.1) a pre-selection on the hits is performed. As this kind of optical background mostly causes single hits from one photon, the hit sample that serves as input for the trigger algorithms are hits with a charge above a certain threshold, typically 3 pe, and coincident hits that occur on the same storey within a time window of 20 ns. All hits that fulfil at least one of the criteria are referred to as *level 1 (L1)* hits, where two hits from a coincidence are represented by only one of them.

Within these L1 hits different trigger algorithms search for correlations. The standard muon triggers, such as the *3D* and *1D* triggers, look for L1 hits that fulfil the

causality condition

$$|t_i - t_j| \leq \frac{d_{ij}}{v_{\text{light}}} \tag{3.3}$$

where for the *3D* triggers the condition is to be understood three-dimensional, for the *1D* triggers one-dimensional along one specific direction. t_i and t_j are the arrival times of two hits i and j, d_{ij} the distance between them and v_{light} the speed of light in water. Only hits that fulfil pairwise this condition can be causally connected and hence be caused by the same event.

Other, more simple trigger codes look for coincidences in two adjacent storeys within 100 ns (*T2* trigger), or in adjacent or next-to-adjacent storeys, within 100 ns or 200 ns, respectively (*T3* trigger). Directional triggers that are meant to detect events from a certain direction, e.g. the galactic center (*GC* trigger), are available but not used within this analysis. Table 3.1 lists all trigger codes that have been used for this analysis. More information about the different implementations is given in [73] [74].

Table 3.1: Used trigger types for this analysis

Trigger name
ANT_TRIGGER_3D_SCAN
ANT_TRIGGER_1D_MIXED
ANT_TRIGGER_1D_MIXED_WITH_PREFIT
ANT_TRIGGER_T3
ANT_TRIGGER_T2
ANT_TRIGGER_TQ

Different trigger types can be used in parallel. The sub-sample of L1 hits that fulfil the specified trigger types is referred to as *L2* hits. Here, for a L1 hit that originates from a coincidence the second coincident hit that was removed from the sample of L1 hits is retrieved again from the full sample and merged into the sample of L2 hits.

To ensure that no data is lost an additional time window of $2.2\,\mu$s, which is the time that a photon takes to traverse the complete detector, is added before the first and after the last L1 hit that fulfilled the specified trigger types. All detected hits within this time window are collected and written to disk as one *event*. In the following the L2 hits are referred to as *triggered hits*, whereas *snapshots hits* denote all hits within the full time window.

Depending on the data taking conditions, i.e. the current background rates, run setup, etc., the choice of the different trigger types varies. Hence, not all trigger types mentioned above have been running during all the time. All triggered events are gathered and stored in *runs*. The effective life time of such a run varies and can last up to a few hours.
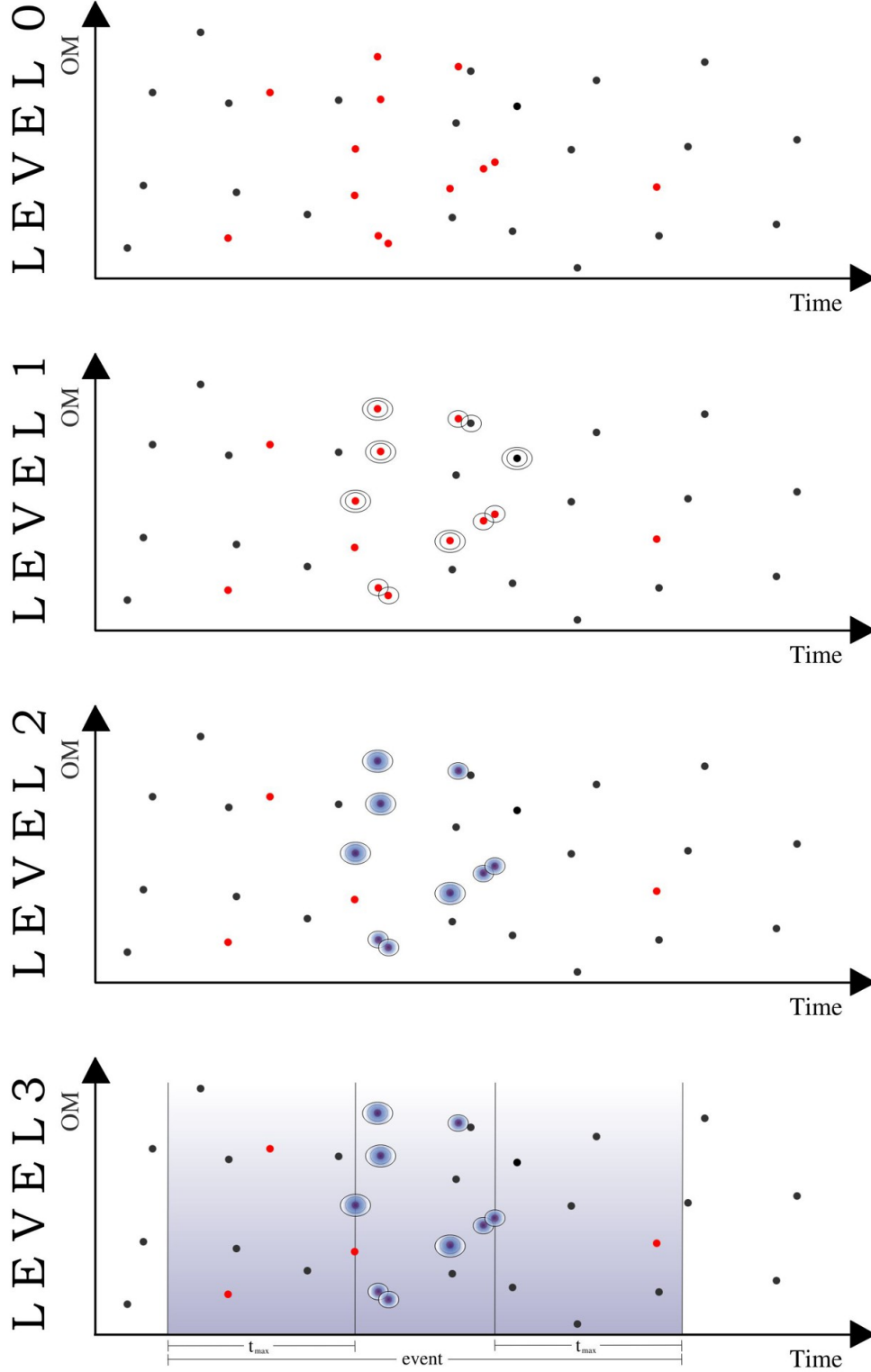
Figure 3.10: *Schematic description of the ANTARES software trigger.* **Level 0:** Illustration of the data stream with hits caused by physics events (red) and background (black). **Level 1:** Large hits are encircled twice, coincident hits once. Here two background hits are also marked as *L1* hits, as one has a high charge and the other is in coincidence with a true hit. **Level 2:** One ore more trigger algorithms look for correlations and causal connections within the *L1* hits to identify the (red) signal hits. The blue coloured circles contain the final *triggered (L2)* hits. **Level 3:** The event is built by adding twice a time window with a length of $2.2\,\mu$s. See text for more informations. Image modified from [63].

Chapter 4

Background sources

The background for the ANTARES experiment can be divided into two types. Firstly, an optical component that is caused by deep sea bioluminescence and the decay of the radioactive Potassium-40 (^{40}K). These sources create photons that are detected by the OMs together with the signal hits and that are present as background hits in each physics event (chapter 4.1). The second type of background for the search of cosmic neutrino events are triggered events that are induced by particles of atmospheric origin, such as atmospheric neutrinos (chapter 4.2) and atmospheric muons (chapter 4.3).

4.1 Optical background in water

Apart from signal hits from physics events, the ANTARES OMs continuously record optical background hits that are caused by two different sources.

The **decay of ^{40}K** that is dissolved in the salt water produces electrons with an energy of $1.3\,\text{MeV}$. This energy is far below the event detection threshold of ANTARES, that is about $10 - 100\,\text{GeV}$, and hence, the emitted Cherenkov photons can not trigger its own event, but create a statistical white noise of single photo electrons with an almost constant rate of $30 \pm 7\,\text{kHz}$ in each OM [75].

Additional background photons are created by **bioluminescent organisms** in the deep sea, such as plankton or shrimps that emit light for the purpose of communication, attracting prey, camouflage, etc... At detailed description of the mechanisms and physical properties of bioluminescence is given in [75]. In contrast to the steady, pervasive background of the ^{40}K decay the bioluminescent background also occurs in local bursts that vary in duration from a few milliseconds up to minutes and can create from 10 up to 10^{11} photons per second.

Both sources together create a highly variable optical background at the level of a few ten kHz per OM in times of good data taking conditions, but can also increase up to a few MHz. Figure 4.1 illustrates the variability of the background rate as function

of time. A constant *base line* is superimposed by occasional *bursts*. To quantify the
data quality of an ANTARES run that typically lasts a few hours three parameters
are evaluated, which are the base line rate, the mean rate and the burst fraction. The
latter one in principle is the fraction of time in the run that is dominated by bursts.
The exact evaluation of base line and burst fraction is explained in [75]. The mean rate
is the averaged background rate including the bursts.
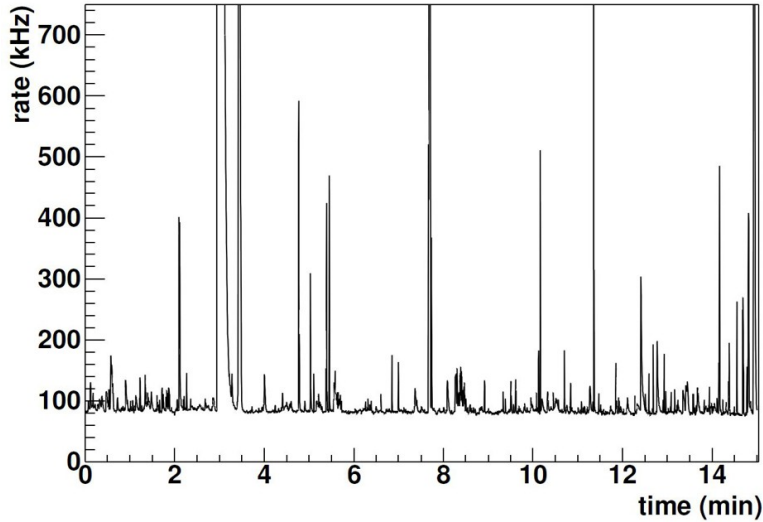
Figure 4.1: *Time profile of the background rate in an ANTARES OM.* The plot shows the time-
dependent background rate measured by an ANTARES OM in good data taking conditions. A constant
base line rate of about 90 kHz is overlaid by some occasional bursts yielding rates up to a few hundred
kHz. Image from [75].

As the sample of *snapshot hits* in a triggered event contains hits from physical
origin as well as these background hits, for each analysis a dedicated algorithm has to
be applied that separates the signal from the background hits. For shower events such
a hit selection has been developed as part of the event reconstruction package that is
described in chapter 6.

4.2   Atmospheric neutrinos

Atmospheric neutrinos are produced when high energy cosmic ray particles scatter with
the matter in the Earth's atmosphere and thereby create charged mesons, mostly pions
and kaons. The main production of neutrinos happens in semi-leptonic decays of these
mesons, which generate the so-called *conventional atmospheric neutrino flux* (chapter
4.2.1). At higher energies, where the lifetimes of pions and kaons are long enough
to make another interaction before they decay, the neutrino spectrum gets dominated
by the decay of short-lived heavier particles, typically charmed mesons. This *prompt
atmospheric neutrino flux* is further described in chapter 4.2.2.

4.2.1 The conventional neutrino flux

Conventional atmospheric neutrinos are produced in the decay of charged pions and kaons, following the same equations (2.2)(2.3) that are responsible for the production of high energy cosmic neutrinos (see chapter 2.1). Assuming that all particles decay one expects a ratio of 2 in favour of ν_μ compared to ν_e, which is true for low energy particles. However, for muons with an energy above 2.5 GeV the decay length, taking into account relativistic time dilation, exceeds the height of the Earth's atmosphere and hence the ν_μ/ν_e ratio quickly increases [42].

The differential spectrum, i.e. the number of events $\mathrm{d}N$ per energy interval $E + \mathrm{d}E$, of the conventional atmospheric neutrino flux can be described by a power law

$$\frac{\mathrm{d}N}{\mathrm{d}E} \sim E^{-\gamma} \tag{4.1}$$

and is derived from the energy spectrum of the primary cosmic rays that hit the Earth's atmosphere. Also the primary spectrum follows a power law with a spectral index γ of 2.7, slightly steeping at energies above 10^6 GeV towards a spectral index of 3.0 [42]. As the pions and kaons often lose some of their energy in collisions before they decay, neutrinos are produced at lower energies which yields a neutrino spectrum that is one power steeper than the primary cosmic spectrum, hence $\gamma_\nu = 3.7$ [76].

Several numerical models exist that calculate the conventional neutrino flux as function of the energy and the inclination angle. Figure 4.2 shows the ν_μ and ν_e fluxes as calculated by Honda [77] and Bartol [9]. In the ν_μ channel both models agree well with each other, whereas for ν_e the Bartol model predicts a higher flux. As the atmospheric neutrino flux is a background source in the search for cosmic neutrinos, the Bartol flux was chosen as conservative model within this work. Both models show good agreement with recent measurements, performed by the IceCube [76] and ANTARES [78] experiments for the ν_μ flux, as well as for the ν_e flux measured by IceCube [79]. Hence, the detector and its background is understood well to proceed with searches for a cosmic signal.

In the analysis of neutrino events with ANTARES one can a priori not distinguish between interactions that are induced by atmospheric and cosmic neutrinos. But as the cosmic neutrino spectrum is expected to be harder with a spectral index of about $\gamma = 2.0$, typically a lower cut on the reconstructed energy is performed as, depending on the intensity of the cosmic neutrino flux, the cosmic flux dominates above a certain neutrino energy.
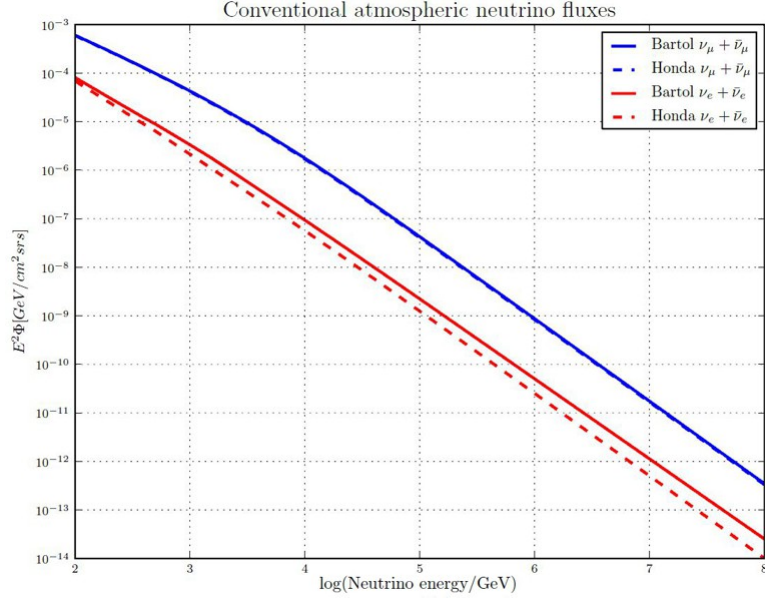
Figure 4.2: *Conventional atmospheric neutrino fluxes.* The plot shows the differential conventional atmospheric neutrino fluxes dN/dE averaged over one hemisphere for muon neutrinos (blue) and electron neutrinos (red) as predicted by two different models Honda [77] (dashed line) and Bartol [9] (solid line). The plot has been generated using the neutrinoflux tool [80] [81] where both parametrizations are implemented.

4.2.2 The prompt neutrino flux

The so called prompt component of the atmospheric neutrino flux is induced by the decay of charmed (and heavier flavoured) mesons in cosmic ray induced particle showers. Due to their very short lifetime of $\approx 10^{-12}$ s [43] $D^{\pm}$ mesons decay promptly after they have been produced, hence, above a certain energy threshold the prompt component dominates over the conventional neutrino flux as here the (relativistic) lifetimes of pions and kaons become long enough to interact again before they can decay and produce neutrinos. This crossover energy is a function of the zenith angle and is between 10^5 and 10^6 GeV for vertical neutrinos and increasing with a more horizontal zenith angle [10].

Again, several theoretical predictions exist for the prompt neutrino flux, of which the parametrization by Enberg [10] is used within this work. Here, also a small contribution from ν_τ is predicted that is however about 17 times lower than that for the two other flavours as only D_s mesons can decay into ν_τ. The prompt fluxes of ν_μ and ν_e are predicted to produce the same flux. Figure 4.3 illustrates the Enberg prompt flux in comparison to the conventional Bartol flux.

As for the analysis of neutrinos using shower events the ν_e CC channel makes the largest contribution to the event sample, also the majority of prompt neutrinos is expected from this channel, especially as the crossover energy is already at 40 TeV,
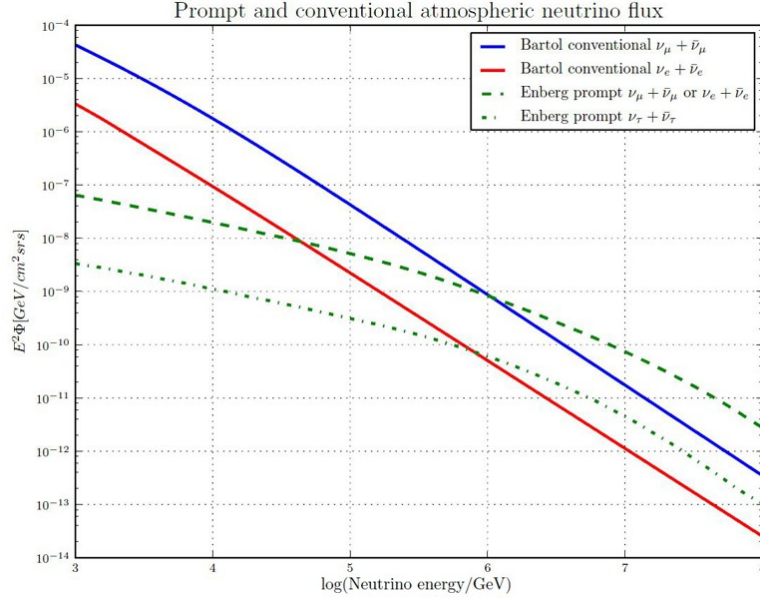
Figure 4.3: *Prompt and conventional atmospheric neutrino flux.* The plot shows the differential prompt atmospheric neutrino flux dN/dE averaged over one hemisphere for muon and electron neutrinos (green dashed line) and tau neutrinos (green dashed-dotted line) as predicted by the Enberg model [10]. For comparison reasons the conventional flux from Bartol [9] for muon neutrinos (blue solid line) and electron neutrinos (red solid line) was added. The fluxes have been generated using the neutrinoflux tool [80] [81].

about 1.4 orders of magnitude lower in energy than the crossover point in the ν_μ channel. As shown later in chapter 12 this is also about the energy region where the lower cut is performed to select the cosmic signal events. Hence, the prompt flux, although it is quite low, must not be neglected within this analysis.

Finally, it should be mentioned that the existence of the prompt neutrino flux has never been proven in experiments. To measure the prompt flux is a challenge, as below the crossover energy it is largely dominated by the conventional flux and above the energy it is expected to be exceeded by the diffuse cosmic neutrino flux. However recently, an upper limit on the prompt flux was presented by the IceCube collaboration that is about 3.8 times higher than the Enberg prediction [82].

4.3 Atmospheric muons

The majority of triggered background events in ANTARES is caused by atmospheric muons that enter the instrumented volume. For the analyses of ν_μ neutrinos atmospheric muons are an insidious background as they have to be separated from muons that have been induced by neutrinos, which is usually done by a cut on the reconstructed zenith. Neutrinos arrive at the detector from all directions whereas atmospheric muons

only come from above. Figure 4.4 shows the angular distribution of the muon fluxes in ANTARES for atmospheric and neutrino induced muons. One can derive that from the upper hemisphere about 10^6 times more atmospheric muons arrive than neutrino signal events.
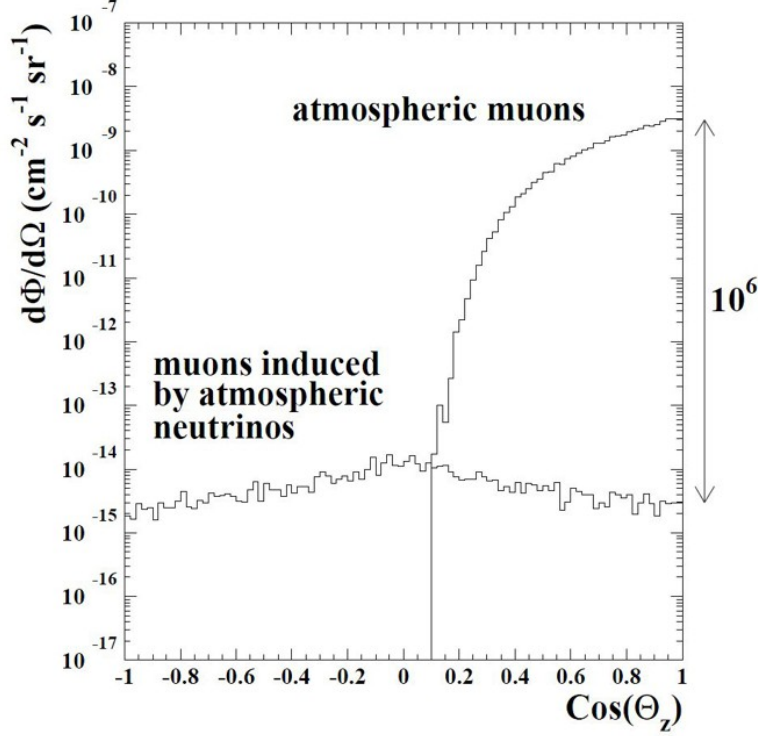
Figure 4.4: *Angular distribution of the muon fluxes in ANTARES.* The plot shows the flux of atmospheric and neutrino induced muons with an energy above 1 TeV arriving at the ANTARES detector. Image from [35].

Also for shower analyses atmospheric muons are a serious background, but as in this case the shower signal events have a completely different (shower-like) signature, compared to muon tracks, it is a priori not necessary to separate them by a cut on the zenith. One could also imagine a cut that is based on the different event topologies. However, as shown later, it is simply the huge amount of atmospheric muon events that makes a cut on the zenith inevitable, also for this shower analysis.

The differential energy spectrum of atmospheric muons follows the one of the primary cosmic rays with a spectral index $\gamma = 2.7$ in the energy range $10^2 - 10^6$ GeV and $\gamma = 3.0$ above [42]. Compared to neutrinos that retain their native energy spectrum on their way down to the deep sea, which is of course due to their small cross-section, atmospheric muons decay or lose parts of their energy until they can reach the detector. Hence, the differential energy spectrum is a function of the water depth and is no longer a power law spectrum when reaching the detector, as shown in figure 4.5.

Further, atmospheric muons can occur in bundles up to a few hundred almost parallel
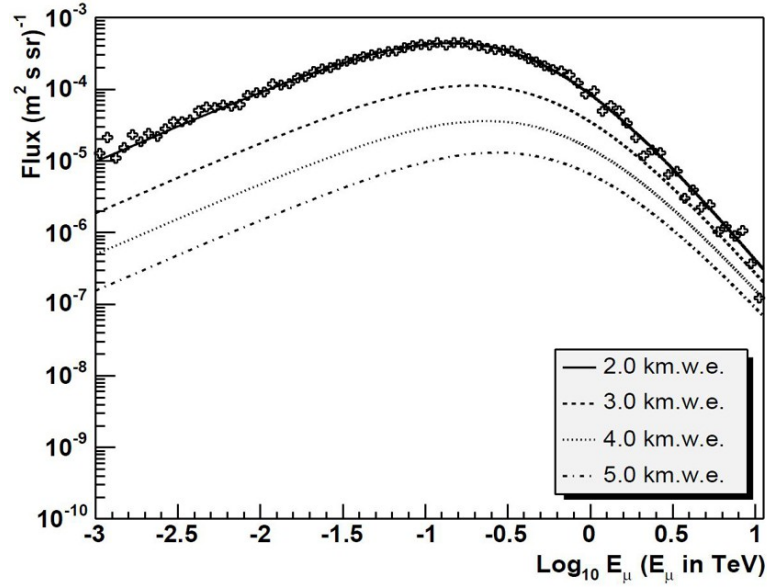
Figure 4.5: *Atmospheric muon flux as function of the water depth.* The plot shows the differential flux $\mathrm{d}N/\mathrm{d}E$ of single atmospheric muons for different water depths (*w.e.* means water equivalent $= 10^6 kg{\cdot}m^2$) as function of the muon energy. The marker points indicate a full Monte-Carlo simulation, the lines follow a parametrization. Image from [83].

traversing muons. The bundles have their origin in huge particle showers that are induced by very high energy cosmic ray particles. The number of muons in such events are called *multiplicity*. The abundance of high multiplicity events is shown in figure 4.6.

Depending on the activated software triggers the rate of recorded atmospheric muon events is between 5 and 10 Hz [1]. The suppression strategy for the atmospheric muon background within this analysis is a combination of a cut on the event topology that is related to the goodness of fit during the event reconstruction (see chapter 6) and cuts on the reconstructed zenith and energy of the event (see chapter 7).
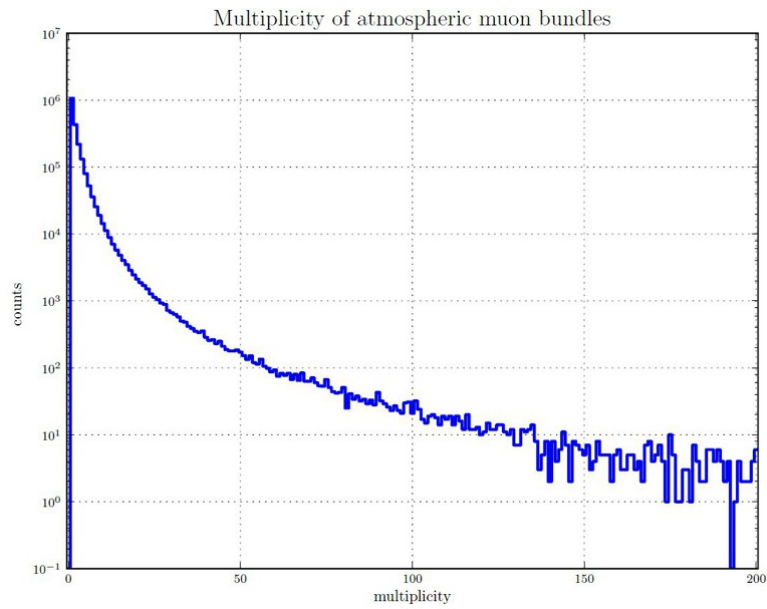
Figure 4.6: *Distribution of the multiplicity in triggered atmospheric muon events.* The plot shows the number of triggered atmospheric muon events as function of the number of simultaneously traversing muons in the bundle (multiplicity). The plot has been generated from run-by-run based simulations (see chapter 5) averaged over the whole active data taking lifetime from 2007-2012.

Chapter 5

Event simulation

For the development of a reconstruction algorithm for shower events and the optimization of the diffuse flux analysis a Monte-Carlo simulation of signal and background events and the detector response was required. Therefore, a run-by-run based simulation (RBR) was used, where for each ANTARES data run an individual set of simulated events was created, taking into account the detector and data taking conditions that have prevailed during that run. As for ANTARES this production is the second of that kind, it is referred to as RBR v2.

As the creation of such a simulation is a huge effort the generation of the RBR simulations is performed by a dedicated Monte-Carlo working group. These simulations are then used for all analyses within the whole collaboration. Simulating representative events for the time period from 2007-2012 consumed about $2.6 \cdot 10^5$ CPU hours (30 years), which is about $20\,\%$ of the computing resources for ANTARES at the computing centre in Lyon [84] (numbers scaled from [85]). The procedure is documented in detail in [85]. A summary is given in the following.

5.1 Simulation software

The simulation of events is performed in three parts. At first, primary particles (neutrinos, muons and first generation shower particles) are simulated. From these particles in a second step the Cherenkov light is generated, followed by a third step where the response of the detector to detected photons is evaluated.

5.1.1 Event generation

For the generation of neutrino events the event generator **GENHEN** [86] [87] [88] was used. This generator simulates ν_μ and ν_e interactions using the LEPTO [89] package for deep inelastic scattering processes and RSQ [90] for resonant and quasi-

elastic processes. The used parton distribution functions are CTEQ6-DIS [91]. The hadronisation is performed using PYTHIA/JETSET [92], the muon propagation using MUSIC [93]. For ν_μ NC and ν_e NC/CC shower events version v6r8 was used, for ν_μ CC events version v6r10. ν_τ events have not been simulated within this production as the simulation software is not sufficiently well tested concerning the propagation of tau leptons. Hence, their contribution is estimated differently, as will be described in chapter 10.1. An event created by GENHEN contains the trajectory of the primary neutrino and all long-lived induced secondary particles of the first generation.

Neutrino events have been generated following a power law energy spectrum with a simulated spectral index between $\gamma = 1.1$ and 1.7, depending on the type of events. The choice of these spectra that are harder than an expected cosmic flux with $\gamma = 2.0$ or than the atmospheric neutrino flux was made to increase the event statistics in the high energy region. An event weighting procedure, however, allows to re-weight the event sample to any kind of required flux for any kind of life time. In the weighting also the interaction cross-sections, the target (water) properties and the neutrino earth transmission probability is included. For this analysis each event weight, internally named *w2* or *generation weight*, is multiplied with the corresponding neutrino flux Φ_ν, so that the number of expected events N_{exp} at a certain step in the analysis is the summation of the weights from all simulated events N_{sim}:

$$N_{\mathrm{exp}} = \frac{t}{N_{\mathrm{gen}}} \sum_{i=1}^{N_{\mathrm{sim}}} w2_i(E, \Theta) \cdot \Phi_\nu(E, \Theta) \tag{5.1}$$

where E is the energy of the event and Θ the zenith direction of the neutrino. Here, it is assumed that flux and weight are independent of the azimuthal direction. N_{gen} is the total number of all generated events in the simulation, not to be confused with N_{sim} that is the number of simulated events that cause hits in the detector and are finally stored. t is the lifetime to which the simulation refers to. More information about this weighting scheme is given in [8] [94].

The generation of atmospheric muon events is performed by **MUPAGE** v3r5 [95] [96]. Where as a full Monte-Carlo simulation of atmospheric particle showers was used earlier for smaller productions, for a mass-production, such as the run-by-run simulation, it is inevitable to have a fast event generator that is capable of simulating the needed amount of atmospheric muon events. Therefore MUPAGE uses parametric formulas from [97] that have been obtained from a full simulation of cosmic ray interactions with the Earth's atmosphere using the HEMAS package [98] and constrained by measurements of the atmospheric muon flux with the MACRO experiment [99] [100]. The propagation of the muons under water is done with the MUSIC code [93].

5.1.2 Cherenkov light generation

The generation of Cherenkov light from the previously created particles is performed by two consecutive programs. **KM3** (here in version v4r2) [101] [102] [103] generates photons from muon tracks using previously built photon tables. Again, the CPU consumption is a crucial point when simulating millions of muons, so that a full tracking of each individual photon including scattering is not feasible. Hence, the photon generation, scattering and propagation has been pre-simulated with a full GEANT 3.21 [104] simulation and stored in lookup tables that are now used to create the photons for the simulated GENHEN events. The muon propagation and energy loss is again handled by the MUSIC code [93].

In a second step the light from all other particles, i.e. the shower particles, is produced by **GEASIM** v4r13 [105]. Based on the first generation particles that have been generated by GENHEN, a full GEANT 3.21 [104] shower simulation is performed for hadronic showers that have been induced by neutrinos with an energy below 100 TeV. From all shower particles the Cherenkov light is produced similarly to the light production in KM3. Electromagnetic showers and their photon emission follow parametrized tables. However, in contrast to muon track events, for the Cherenkov light from showers no photon scattering was included in the simulation. For future Monte-Carlo productions photon scattering will be simulated for all kinds of event types. However, in order to be able to use RBR v2 for this analysis, a hit selection was introduced to select only direct photons (see chapter 6.1.1). Hence, the reconstruction of the events is based on unscattered photons, as the late arriving, scattered photons are removed anyway.

Due to computing time reasons, for high energy events with a neutrino energy above 100 TeV, no full GEANT simulation is performed any more. Here, for pure shower events the so-called One-Particle-Approximation (OPA) is used where all hadronic particles are replaced by an equivalent electron that takes the energy of π^0, γ, e^+ and e^- at 100 %, and that from π^+ and π^- at 20 %. For this equivalent electron the photon tables for electromagnetic showers are used. A detailed description of the OPA is given in [106], however, also further improvements are presented in that thesis that are not yet taken into account in RBR v2.

For ν_μ CC events, where a muon track and the hadronic vertex shower occur in the same event, the muon is ignored by GEASIM and the shower is propagated as described above. However, as the vertex shower in ν_μ CC events is only traceable if the interaction is close to the instrumented volume and as high energy muons are typically generated far outside of the detector, for ν_μ track events no vertex shower photons have been simulated at all if the neutrino energy exceeds 100 TeV. Whereas for common muon analyses this simplification was justified, it turned out that when looking explicitly for showers this assumption causes a deficiency of high-energy events that has to be corrected, as explained later in chapter 10.4.

As for both light generators only those photons are recorded that finally will be detected by one of the OMs, already at this stage some properties of the OM, such as geometry, position and angular acceptance, are used, even though the detector simulation is done in the next step.

5.1.3   Detector simulation

The final step in the simulation of an event is the detector simulation to create *hits* and *events* from the photons in an equivalent way as it is expected from the real detector (described in chapter 3.3). This simulation is done by a program called **Trigger-Efficiency** [107]. Here it is where the different run setups and detector configurations come into play as until now the exact same simulation procedure was applied to each run.

The different data taking conditions in terms of variable background rates are taken into account by simulating a constant random white noise individually for each OM using the currently measured detection rates. By doing so not only the global variability of the baseline is considered but also local bioluminescent bursts that affect only parts of the detector are included in the simulation. However, correlations between background hits that originate from bursts are not included in the white noise simulation.

TriggerEfficiency then simulates the PMT response and the electronics inside the ARS to transform the signal and background photons into hits. Therefore for each OM the currently valid ARS charge calibration and effective charge threshold is used. Further, the time and charge of each hit undergo a Gaussian smearing. Hits on OMs that have not been working during the corresponding run are removed. The positions of the OMs, however, have been kept fixed from a reference detector layout that is used for all runs instead of the triangulated real OM positions, which is due to technical reasons as the previous simulation programs also require a detector layout that has to be consistent with the one used here.

Finally, the same software triggers are applied that have been used during the data taking for that run.

5.2   Event quantities

For each ANTARES run the simulation has to be created with enough statistics to allow physics analyses that have a high statistical significance. Therefore, for each neutrino event type the number of simulated events was chosen in a way that in any case more simulated events pass the trigger conditions than would pass in real ANTARES data. The adjusting to the corresponding run life time is achieved using weights. Within this

analysis every simulated event has been used three times, each time with a different weight to reproduce the Bartol [9] conventional atmospheric spectrum, the Enberg [10] prompt spectrum and an E^{-2} neutrino spectrum, as expected from the cosmic neutrino flux. The parametrization of the atmospheric fluxes that are for the weighting have been taken from the *neutrinoflux* package [80] [81] that has been implemented as part of the analysis framework SeaTray (see appendix A.1).

Table 5.1 lists the input parameters that have been used for the simulation of the neutrino events, where *showers* sum up ν_μ, ν_e NC and ν_e CC events and *muons* stands for ν_μ CC events. For each of these types a separate simulation was produced for neutrinos and anti-neutrinos, hence, all in all 22 neutrino event samples have been generated for each run.

Table 5.1: Input parameters in the RBR v2 neutrino Monte-Carlo simulation

Event type	Number of simulated events per run	Generation volume [km^3]	Spectral index	Neutrino energy [GeV]
high energy showers	200	0.15	1.4 (1.2 for 2012)	$5 \cdot 10^4 - 10^8$
low energy showers	500	0.15	1.4 (1.2 for 2012)	$100 - 10^5$
very low energy showers	500	0.15	1.2	$4 - 300$
high energy muons	$3 \cdot 10^7$	$8 \cdot 10^4$	1.7 (1.2 for 2012)	$2 \cdot 10^4 - 10^8$
low energy muons	$2.5 \cdot 10^8$	$4.9 \cdot 10^3$	1.7	$5 - 2 \cdot 10^4$

The simulations have been created assuming isotropic 4π neutrino directions. The generation volume is a cylindrical can with the detector in its center. Inside this can neutrino interactions are generated. Its size was adjusted to ensure that for each event type all possible events that could occur in the real detector are also simulated. Thus, the generation volume for muon tracks is by far larger, as high-energy muons travel several kilometres before they decay, whereas showers have a lengths of only a few meters (see also figure 3.6).

For the huge amount of atmospheric muons only one third of the effective run life time was simulated due to computing limitations. As the event sample provided by MUPAGE refers directly to a given life time no event-wise weighting is necessary for atmospheric muon simulations. All MUPAGE events are weighted with 3.

Within this analysis all 23 simulated event samples per run are used from all runs that fulfilled the quality requirements. The final run selection is given in chapter 8.

Chapter 6

Event reconstruction

The reconstruction of the events from a set of hits is performed by the **Dusj shower reconstruction project**[1] that is a collection of algorithms for full shower identification and reconstruction, implemented in C++ [108] and Python [109]. The tool has been developed as part of this thesis and is now, together with another shower reconstruction project called *Q-Strategy* [8] the standard reconstruction algorithm for showers in ANTARES.

The reconstruction strategy has been implemented as part of the software framework *SeaTray* [6] that is the official tool used for event processing and reconstruction in ANTARES. In this framework the single tasks of a complete event reconstruction, such as a hit selection, a fit routine or a calibration tool, are performed by independent exchangeable *modules* and *services*. Modules serving the same purpose are gathered in *projects* that can be connected individually to the framework. For example, all modules and services of the Dusj reconstruction belong to the project *antares-shower-reco-dusj*. See also appendix A.1 for more information about the implementation of the framework.

A sub-framework called *Gulliver* [110] that is a software package within SeaTray, dedicated to maximum likelihood fits, was used to design the single parts of the Dusj reconstruction chain modularly. Therefore, generic tools for a maximum likelihood shower reconstruction, such as a seed generator and a shower parametrization, have been developed within this work. A detailed description of these tools and the functionality of Gulliver, also from a technical point of view, is given in appendix A.2.

In the following the functionality of the Dusj reconstruction chain is presented. The algorithm is capable of reconstructing hadronic showers from neutral current interactions as well as electromagnetic showers from ν_e charged current interactions. In the following, whenever the word *shower* is mentioned, both event types are meant. As

---

[1]The word *"Dusj"* is the Norwegian word for shower, however, in the sense of shower in a bathroom. The word for shower in the sense of cascade is *"kaskade"*, which would have been the more correct but also more boring choice as a name...

the SeaTray framework denotes *hits* also as *pulses* (due to its IceCube origin), some configuration parameters have the term *pulse* in their name. But within this context *hit* and *pulse* have the same meaning.

For the processing of the complete RBR Monte-Carlo simulations and ANTARES data the SeaTray version with the revision number[2] 10926 was used (see also appendix A). Here, the Python function **addDusjShowerReconstruction** was used in its default configuration. The function gathers all SeaTray modules and services that are necessary for a complete reconstruction and event classification with the Dusj project and is further explained in appendix B.1.

The Dusj algorithm was applied to all events, also muon track events, without any further analysis-based pre-selection. The event selection to separate shower events from muon track events is done later and is described further in chapter 7. The reconstruction of an event is done in four parts (see also illustration in figure 6.1):

- A two-part hit selection, where at first hits from direct photons are selected using the **I3RemovePulsesAfterARSDeadTime** hit selection module that is part of the project *hit-selector*, followed by the module **I3DusjShowerIdentifier** that identifies signal hits from the shower among background hits from bioluminescence and ^{40}K. The input hit sample is the full *snapshot* as it was introduced in chapter 3.3.1. It is also possible to use this module as preceding event selection to suppress muon track events to a certain extent before the data is passed to the actual shower reconstruction. However, for this analysis no event pre-selection was performed.

- The main shower parameter reconstruction is performed by a maximum likelihood fit in two steps. First the vertex and interaction time is reconstructed from a Monte-Carlo based probability density function (PDF) table that is provided by the service **I3DusjShowerVertexPDF** (see chapter 6.2.1). Then, using the reconstructed vertex as input, the shower energy and neutrino direction is reconstructed from the PDF table of a second service **I3DusjShowerEnergyDirectionPDF** (see chapter 6.2.2). Both services are implemented as likelihood services in the Gulliver framework (see appendix A.2).

- An additional module **I3DusjShowerCutValuesCollector** collects and evaluates potential cut parameters that can later be used to remove badly reconstructed events and to suppress muon track events. Those parameters are for example final log-likelihood values, chi-squares of time residuals, etc... (see chapter 6.3)

- Finally an event classification using random decision forests (RDF) that have been trained from the RBR Monte-Carlo simulation is performed to separate

---

[2]Here, the SVN (Subversion) [111] revision control package was used.

showers from muon track events. The training and classification is based on some selection of the collected Dusj cut parameters (see chapter 6.4). However, in the course of this analysis some issues concerning the RBR have been encountered that in the end led to the decision not to use the result of the RDF classification in this work.
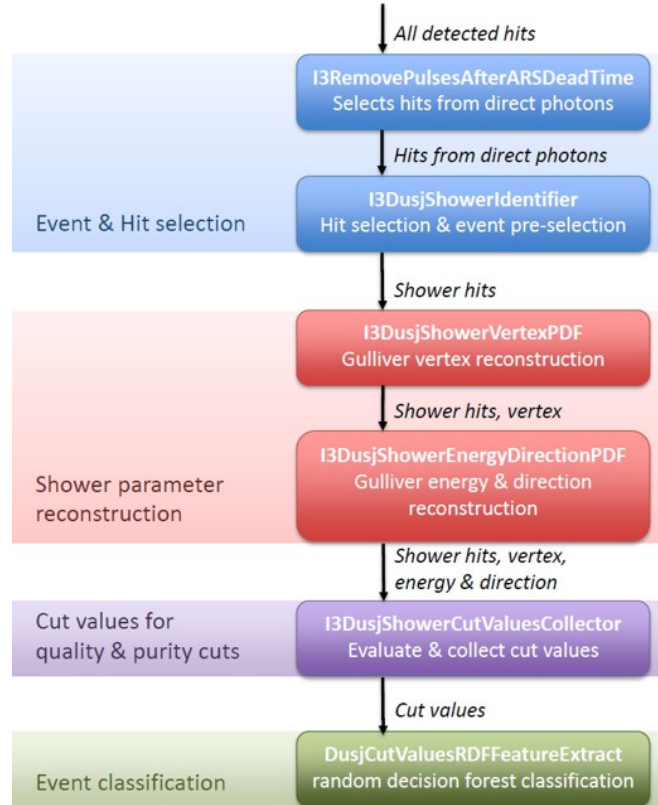
Figure 6.1: *Scheme of the work flow of a shower reconstruction with the Dusj project.* The figure illustrates how the shower is reconstructed from a set of hits (signal and background) as input.

The main output of the Dusj shower reconstruction using the function **addDusj-ShowerReconstruction** is the set of shower hits that were used for the reconstruction, a set of potential cut parameters for further quality and purity cuts, the output of the RDF classification and, of course, the fit result.

6.1 Hit selection

The first step in the reconstruction of the shower is the identification of signal hits that are caused by the shower. A two-part hit selection is used to identify those signal hits among the background hits that are caused by the decay of ^{40}K or arise from

bioluminescence in the deep sea. In the following the two steps are explained in further detail.

6.1.1   Selecting hits from direct photons

This part of the hit selection was introduced to the Dusj reconstruction chain when studies on the upcoming RBR *version 3* Monte-Carlo simulation showed that for simulations where photon scattering in water is included (and this is going to be the case for the very first time for shower events in RBR v3) lots of late hits will be detected after the dead time interval of both ARS chips on one OM in very high energy events. As the PDF tables for the following shower reconstruction that will be performed on the selected hits have been created from a Monte-Carlo simulation without photon scattering, it is necessary to introduce a hit selection that only selects hits that are caused by direct photons.

The module **I3RemovePulsesAfterARSDeadTime** selects only hits that are detected by the first fired ARS on every optical module. Hits that are recorded from the second ARS (which fires around 40 ns after the first one) or very late hits that occur even after both ARS have been in dead time (≈ 250 ns later) will be removed from the sample. Figure 6.2 shows the distribution of time residuals once before and once after the ARS hit selection has been performed on a simulation with photon scattering included. The time residual is defined as the difference between the measured (simulated) hit time and the expected arrival time from the assumption of a point like light emission from the Monte-Carlo vertex position without photon scattering.

$$t_{\mathrm{res}} = t_{\mathrm{measured/simulated}} - t_{\mathrm{expected}} \tag{6.1}$$

One can clearly see the main peak of direct hits at 0 ns, the peak of the second fired ARS at around 40 ns and the very late hits after the ARS dead time. The two latter peaks will be successfully removed by the hit selection, whereas the peak from direct photons is reduced only marginally. The probability of having late photons in the event increases with the shower energy and hence, in the simulation with photon scattering, the ARS hit filter reduces the number of shower hits by $\approx 40\,\%$ in events with a shower energy of 10 TeV up to $\approx 75\,\%$ at 10 PeV shower energy. Hits with $t_{\mathrm{res}} < 0$ are either optical background hits or are caused by photons that have been emitted from a particle in the shower that had travelled a certain distance from the interaction vertex with the speed of light in vacuum.

For the current RBR simulation this hit selection is not absolutely necessary as due to the missing photon scattering late hits are less frequent and hence, cannot lead to a wrong vertex estimation and shower hit identification in the following hit selection routine (see chapter 6.1.2) as easily as in simulations with photon scattering. The

reduction of shower hits in the current RBR simulation is about $\approx 15\,\%$ in events with a shower energy of $10\,\text{TeV}$ up to $\approx 35\,\%$ at $10\,\text{PeV}$ shower energy, where late hits after the ARS dead time would have been removed by the following shower hit selection as well.

But as during the generation of the PDF tables that have been built from a Monte-Carlo simulation for which photon scattering was not available this filter was yet applied, it is recommended to keep it in the reconstruction chain as well. Table C.9 in appendix C.2 lists the configuration parameters of this hit selection. Note that the given default values are the ones that are implemented in the module and not those that are used for this analysis, where by default also the hits from the second ARS are removed. The configuration that was used for the reconstruction within this analysis is given in appendix B.6.
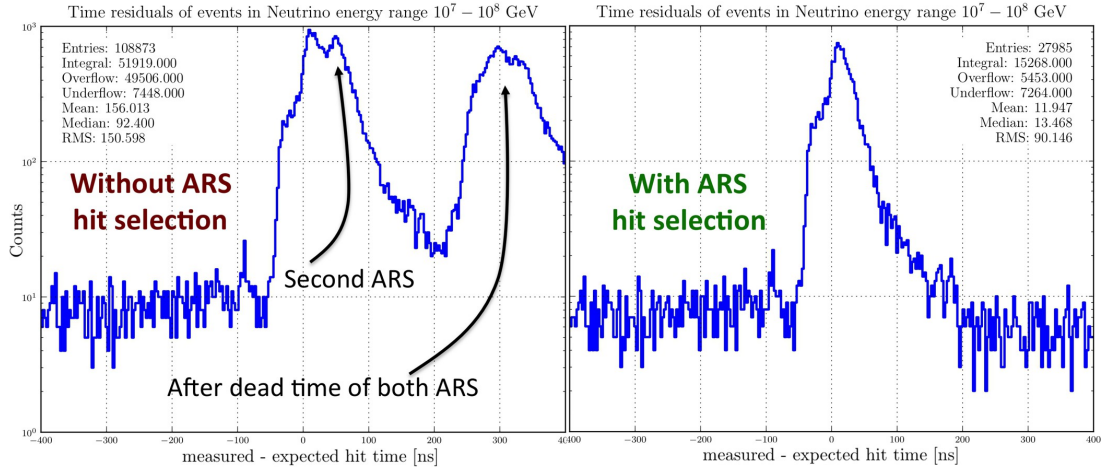
Figure 6.2: *Effect of the ARS dead time hit selection on high energy events.* The figure shows time residuals (following equation (6.1)) of all hits from shower events induced by high energy neutrinos in the neutrino energy interval $10^7 - 10^8$ GeV. Without the ARS hit selection late hits fire the second ARS and even arrive after the dead time of both ARS (left plot). With the hit selection included only hits from direct photons are selected (right plot). A preliminary RBR v3 CC ν_e simulation for run 53119 including photon scattering served as input for these plots.

6.1.2 Selecting shower signal hits

After having selected the hits from direct photons, now they are passed to the main part of the hit selection. The **I3DusjShowerIdentifier** is a SeaTray module that can identify shower events among track events and select - in events that have been identified as showers - the shower signal hits among optical noise hits. As input it requires all hits (or in this case: better the pre-selected direct photon hits) in the event. The module then provides:

- A set of identified shower signal hits

- A rough estimation of the vertex position and interaction time as pre-fit

- A reduced chi-square of time residuals with respect to the vertex estimation that can be used for quality and purity cuts later on

Optionally a cut on the evaluated reduced chi-square can be performed by the module itself to suppress muon track events to a certain extent even before the main reconstruction is done. The reduced chi-square is evaluated from the time residuals (as defined in equation (6.1)) of the hits respective to the vertex estimation:

$$\chi^2_{\text{reduced}} = \frac{\sum_{i=1}^{N_{\text{hits}}} t^2_{\text{res},i}}{N_{\text{hits}} - 4} \tag{6.2}$$

The denominator contains the number of degrees of freedom that is the number of hits reduced by the number of fit parameters, which are 4 for the vertex fit: x, y, z and *time*. In the default configuration of this module the cut would be done at a chi-square value of 1000.0 which would yield an atmospheric muon suppression of 80 % from all RBR events that would have successfully passed the whole reconstruction chain. On the other hand also about 20 % of shower events would be removed by this cut. Thus, for this analysis no cut is performed at this stage, but the reduced chi-square is stored for later stages of the analysis.

The module identifies shower hits by performing a rough fit of the interaction time and vertex position and afterwards looking which hits among all input hits could be caused by a shower at this vertex and that time. The vertex position of this pre-fit reaches a mean distance of around 40 m (for shower energies around 100 GeV) up to 90 m (at 10 TeV) from the true Monte-Carlo vertex in the RBR. The corresponding interaction time yields a mean error of 100 ns (at 100 GeV) up to 350 ns (at 10 TeV). In principle the module is capable of finding more than one vertex in the same event. However, this feature has not been tested so far as all available Monte-Carlo simulations provide single vertex events only.

To obtain the rough vertex estimation a simple scan fit is performed based on coincidences of hits with a charge higher than 1.2 photo electrons (pe) (value is a configurable parameter). Optical background hits (as introduced in chapter 4.1) are typically caused by single photons [1], thus using coincidences with a charge cut at 1.2 pe per hit ensures that the pre-fit is performed on a hit sample with a sufficiently high purity. Figure 6.3 illustrates in detail how this vertex estimation is obtained.

In a second step for each of the found vertices (those could be more in the same event) the best fitting hits among all input hits are selected. Therefore, the time residual is evaluated for each hit. A hit is regarded as signal hit if the time residual does not exceed a limit of ±80 ns (see figure 6.4), and its position is closer than 50 m to one of the coincidences or the estimated vertex position. The latter criterion prevents very far
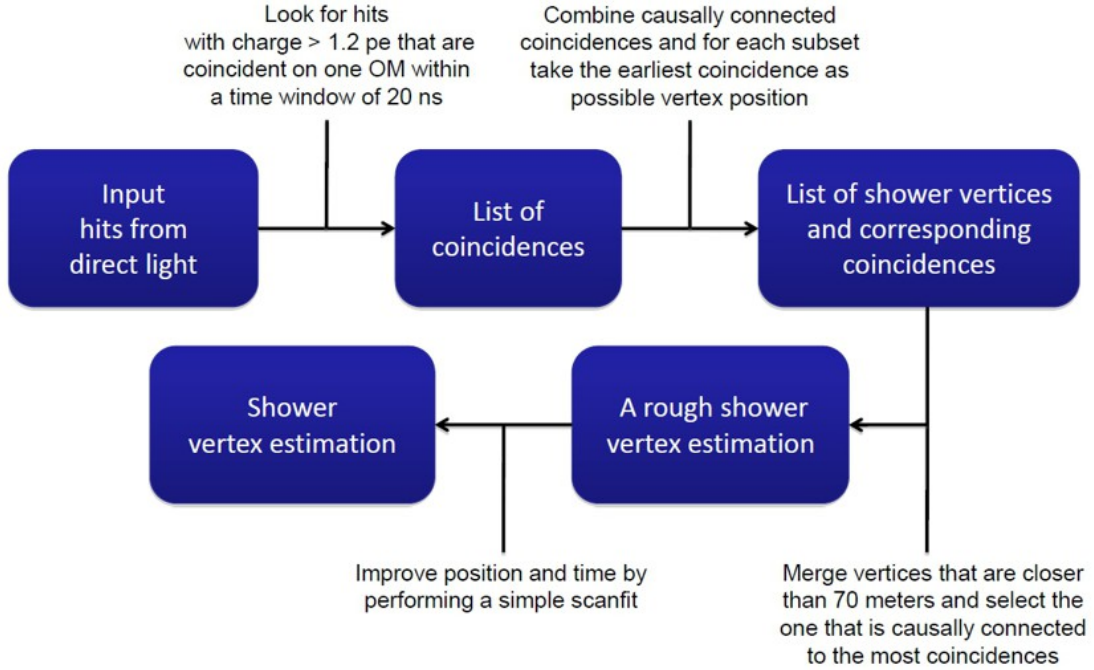
Figure 6.3: *Scheme of the vertex estimation in the I3DusjShowerIdentifier pre-fit.* In the sample of all input hits the module looks for coincidences of pair-wise hits on one ANTARES storey where each hit has a charge higher than 1.2 pe. Then, the list of such coincidences is divided into sub-lists where each sub-list contains coincidences that could be causally connected when taking the speed of light in water into account. Sub-lists where the earliest coincidence of one is located closer than 70 m (on a nearby string) to earliest of another sub-list are merged to one. Within this work that sub-list that contains the most coincidences is taken as the shower vertex where as first estimation the position and time is set to the optical module, where the earliest coincidence occurs. A rough scan fit improves this position and interaction time. All numbers in this plot are configurable parameters. The given values are those that have been used for this analysis.

background hits that occasionally fit to the point-like light emission hypothesis from being falsely selected as signal hit. Of course, both values are configurable parameters.

Figure 6.4 shows the time residual distribution of all input hits with respect to the most significant vertex estimation (the one based on the largest number of coincidences) and the applied selection window. Figure 6.5 illustrates a scheme of the work flow of the hit selection.

In the end a reduced chi-square (as defined in equation (6.13)) is evaluated for each vertex from the time residuals of its hits that can be used later on for purity and quality cuts or optionally as muon pre-suppression by removing all vertices where this reduced chi-square exceeds a certain limit. Optionally, this hit selection procedure can also be applied to an external vertex estimation from a preceding pre-fit routine. In this case the module will evaluate the reduced chi-square for both, the external seed vertex and the internally determined one, and select the one with the lower chi-square value. However, in the following reconstruction chain no external vertex seed is used.
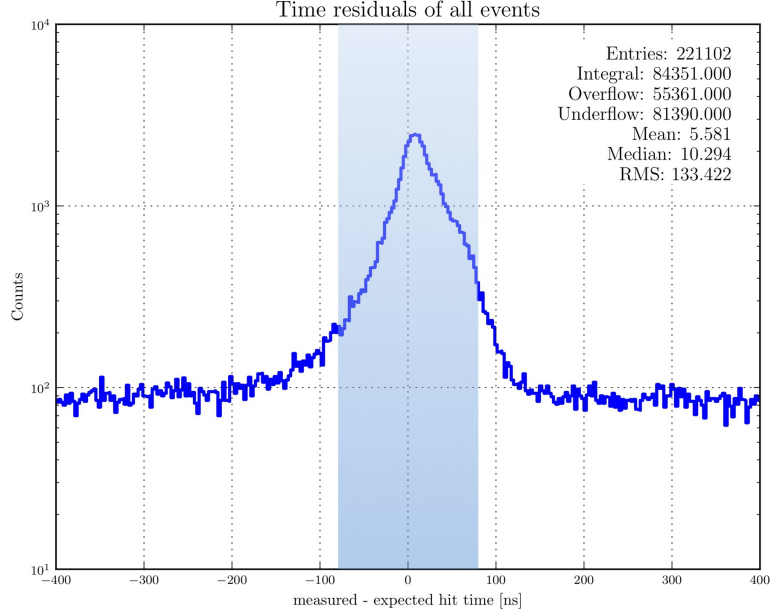
Figure 6.4: *Time residuals of all hits with respect to the internal vertex estimation.* The figure shows time residuals (following equation (6.1)) of all hits where the expected hit time is calculated from the internal vertex estimation of the I3DusjShowerIdentifier. The blue window marks the allowed range for the time residual of a hit to be regarded as signal hit. The plot was created from all shower Monte-Carlo events in run 50990 of the RBR.

The tables C.10 - C.12 in appendix C.2 give a list of all configuration parameters of the module. Appendix B.6 holds the configuration that was used for this analysis.
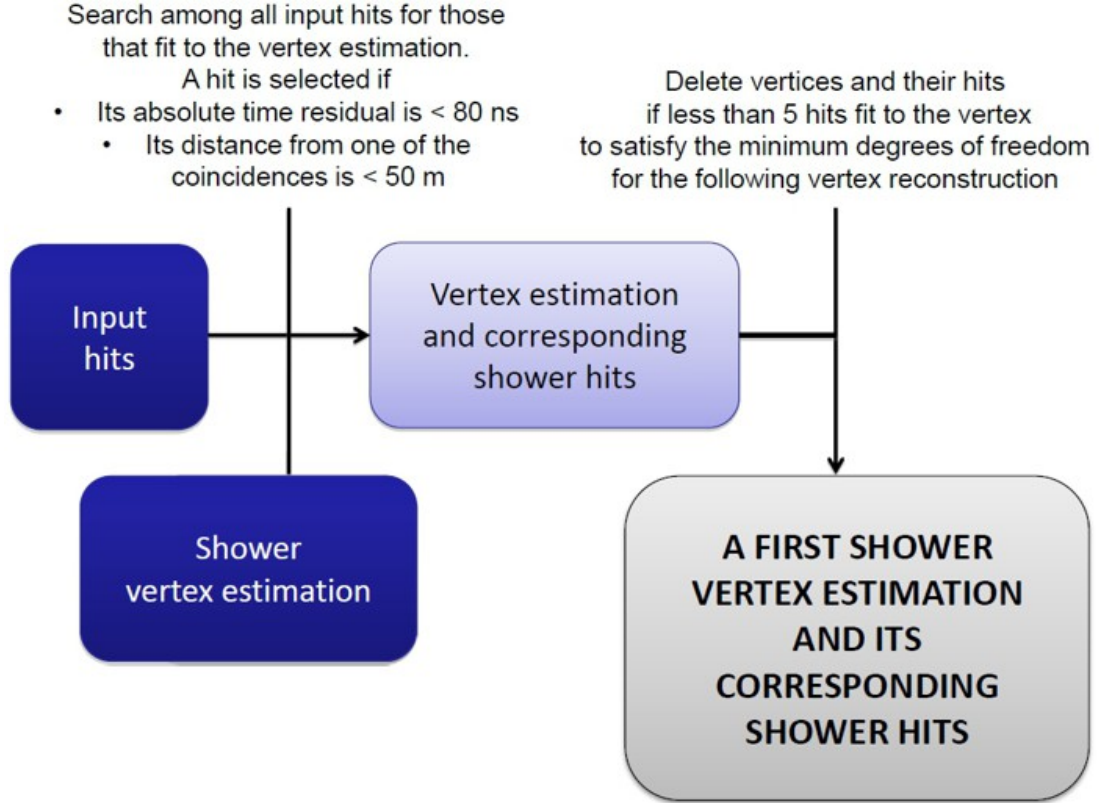
Figure 6.5: *Scheme of the shower hit identification in the I3DusjShowerIdentifier hit selection.* For the previously estimated vertex position the list of all input hits is searched for fitting hits. The selection criteria are the absolute time residual (following equation (6.1)) of the hit respective to this vertex that has to be below 80 ns and the position of the optical module that has to be closer than 50 m to one of the coincidences from which the vertex has been estimated or to this vertex itself. If less than 5 hits have been selected, the event will be discarded and no further shower reconstruction will be performed. All numbers in this plot are configurable parameters. The given values are those that have been used for this analysis.

Although more than one vertex can be found by this procedure, in the following all vertices except for the one that has been found from the most coincidences are discarded. By doing so the module is capable of finding a rough vertex estimation and shower hits in 80% (for showers with an energy of 100 GeV) up to 100 % (at 10 TeV) of all RBR Monte-Carlo shower events. Figure 6.6 shows the efficiency of the complete Dusj shower hit selection (i.e. the ARS hit filter and this module) to identify shower events correctly.
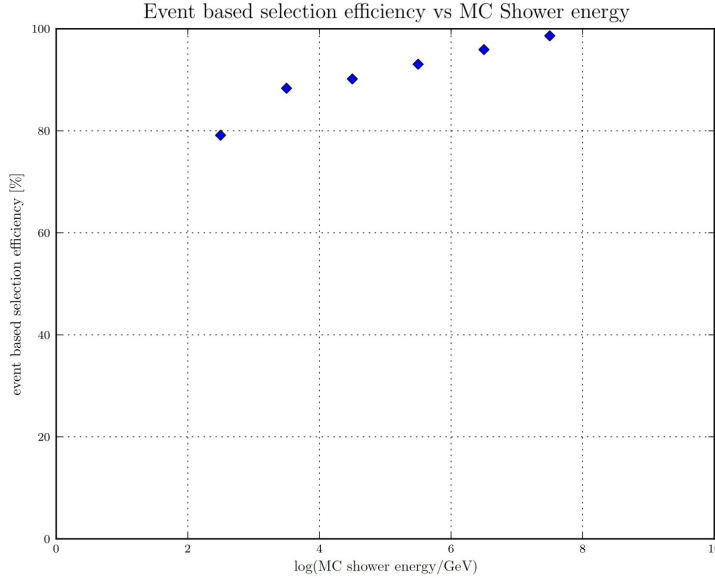
Figure 6.6: *Shower event selection efficiency of the Dusj hit selection.* The figure shows the fraction of shower events with respect to all shower events in the RBR that have been successfully identified as shower events by the **I3DusjShowerIdentifier** and the **I3RemovePulsesAfterARSDeadTime** for each decade in the logarithmic shower energy. An event is determined as a shower event whenever the vertex estimation pre-fit succeeded and at least five hits fit to the point-like light emission assumption.

To evaluate the efficiency of selecting shower signal hits among background hits and the purity of the selected hit sample, at first one has to define the term *signal hit* in the RBR Monte-Carlo. During the detector simulation with *TriggerEfficiency* (see chapter 5.1.3) the information whether a particular hit has been created from signal or background photons or both is discarded. Thus, to define the sample of *true signal hits* within all snapshot hits a cut on the time residual with respect to the *true* Monte-Carlo vertex position is performed. Figure 6.7 shows how this cut is done. For the identification of the signal hits in the hit selection also a cut on the time residual is done but in this case, of course, time residuals are evaluated respective to the internal pre-fit vertex estimation, not the Monte-Carlo truth.

Figure 6.8 then shows the efficiency of the complete Dusj shower hit selection (i.e. the ARS hit filter and this module) to identify a signal hit originating from the shower among the sample of background hits in events that have already been identified as
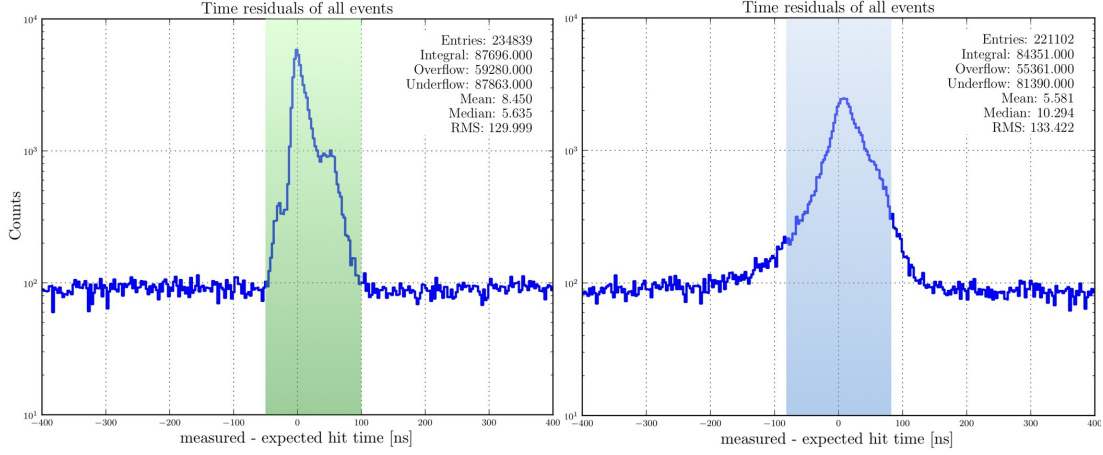
Figure 6.7: *The definition of true signal hits in the RBR Monte-Carlo.* The figure illustrates how *true signal hits* and *selected signal hits* are defined. The left plot shows the distribution of all snapshot hits' time residuals (following equation (6.1)) with respect to the *true Monte-Carlo vertex*. To define the true signal hits all hits are chosen for which the time residual is inside a window of $[-50\,\mathrm{ns}, 100\,\mathrm{ns}]$ (marked in green). The right plot shows the distribution of all snapshot hits' time residuals with respect to the *pre-fit vertex* of the **I3DusjShowerIdentifier**. Here, the signal hits are selected within a time residual window of $\pm 80\,\mathrm{ns}$ (marked in blue), as described in chapter 6.1.2. The plot was created from all shower Monte-Carlo events in run 50990 of the RBR.

shower events. Finally, figure 6.9 shows the purity of the selected hit sample that is the fraction of signal hits with respect to all selected hits. One can derive from the plots that the efficiency of selecting shower hits works just at a mean of around 50%, which might seem a little bit low but is the cost one has to pay to reach the very high purity in the selected sample that is above 99% throughout all energies. Such a high purity is required for the reconstruction of the shower parameters using the Dusj project as the PDF tables have been generated without background hits.
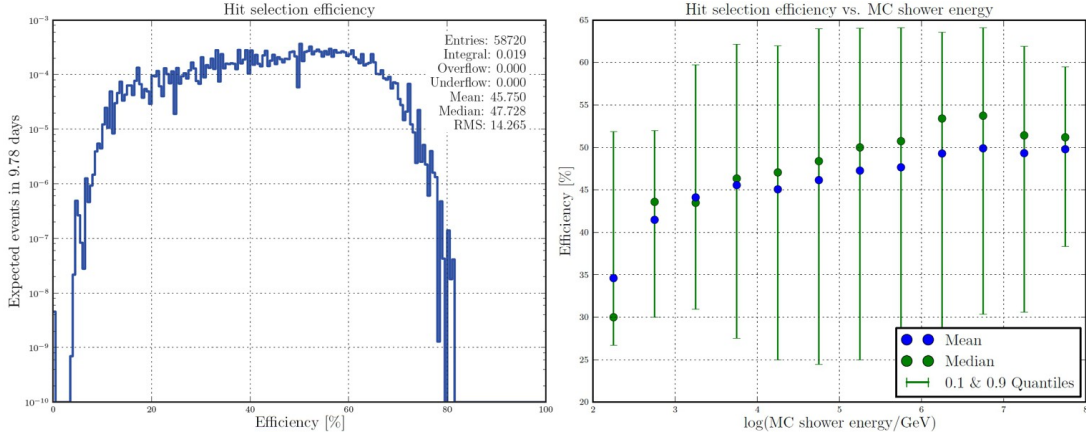
Figure 6.8: *Shower signal hit selection efficiency of the Dusj hit selection.* The figure shows the distribution of event-wise signal hit selection efficiency of the **I3DusjShowerIdentifier** and the **I3RemovePulsesAfterARSDeadTime**. For each event the fraction of all selected shower signal hits with respect to all shower signal hits in the event has been evaluated. The left plot shows the distribution of all events of the high energy simulations (see chapter 5.2) weighted with an atmospheric neutrino flux. The right plot illustrates the tendency of the efficiency with Monte-Carlo shower energy. Therefore, for each semi-decade in shower energy a separate distribution has been drawn, from which the mean, median and the quantiles have been calculated. Note that the error bars in the plot show the 10 % and 90 % quantiles of the distribution, not the error of the mean/median. The plots have been created from 10% of all RBR runs up to 2011 with a run number ending with 0.
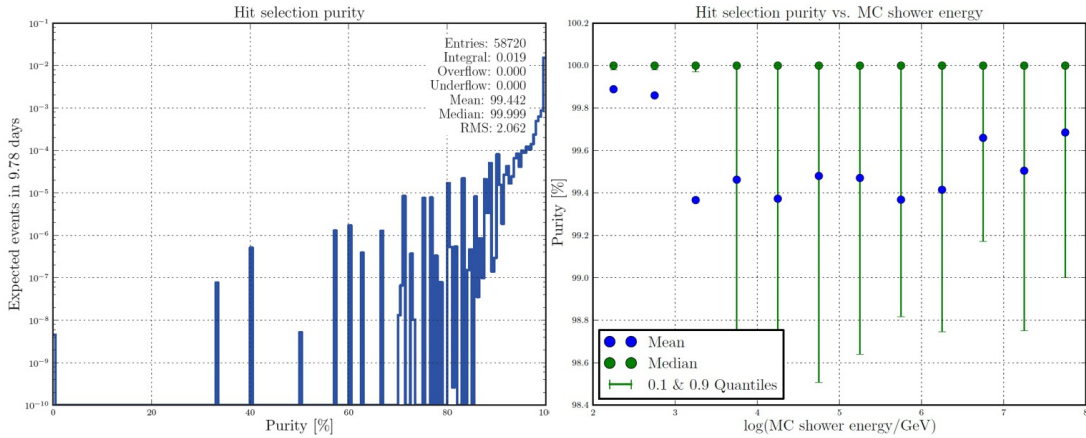
Figure 6.9: *Purity of a shower signal hit sample selected by the Dusj hit selection.* The figure shows the distribution of event-wise signal hit purity in hit samples that have been selected by the **I3DusjShowerIdentifier** and the **I3RemovePulsesAfterARSDeadTime**. For each event the fraction of all selected shower signal hits with respect to all selected hits (including falsely selected background hits) in the event has been evaluated. The left plot shows the distribution of all events of the high energy simulations (see chapter 5.2) weighted with an atmospheric neutrino flux. The right plot illustrates the tendency of the purity with Monte-Carlo shower energy. Therefore, for each semi-decade in shower energy a separate distribution has been drawn, from which the mean, median and the quantiles have been calculated. Note that the error bars in the plot show the 10 % and 90 % quantiles of the distribution, not the error of the mean/median. The plots have been created from 10% of all RBR runs up to 2011 with a run number ending with 0.

6.1.3 Further minimum constraints on the pre-selected shower events

The introduced hit selection lets pass all events where the pre-fit vertex estimation succeeded and at least 5 hits have been identified as shower hits. However, there might be event topologies, like all hits located on one string, that will not have a big chance of being reconstructed well. Thus, further minimum constraints are applied to the selected shower event before passing it to the shower parameter reconstruction. This task is performed by the **I3MinimumConstraintsFilter** that is part of the project *icepick*. Here events will be discarded, where one of the following conditions is not fulfilled:

- Number of selected shower hits > 4

- Number of strings that have detected the selected hits > 1

- Number of optical modules that have detected the selected hits > 2

- Number of storeys that have detected the selected hits > 1

Of course, this additional filter diminishes the event efficiency further, especially in the low energy region. However, the remaining events now hold enough information for a successful shower parameter reconstruction, this means almost all events that pass this filter will also pass the following maximum likelihood fits without failures.

6.2 Shower parameter reconstruction

The main part in the reconstruction of the shower is a two-part maximum likelihood fit to obtain the shower parameters, using the previously selected shower signal hits as input. The first fit determines the position of the interaction vertex and the interaction time of the shower with a much higher accuracy than the roughly estimated pre-fit during the hit selection step. With this vertex position as input a second fit evaluates the energy of the shower and the direction of the inducing neutrino. Both fits make use of the Gulliver framework (see appendix A.2). The development of these algorithms followed an idea first introduced in [112].

Both reconstruction steps follow the same principle. A SeaTray service calculates the probability (likelihood) that the measured sample of shower signal hits fits to a certain shower assumption and provides this information to the Gulliver shower fitter module (see appendix A.2). Therefore, for each single hit i the probability p is evaluated that this hit has been created by a shower hypothesis, denoted as S. This probability is called *PDF value* for hit i

$$pdf_i = p(i, S) \tag{6.3}$$

The probability that the whole sample of hits originates from the shower assumption is then the multiplication of all probabilities obtained from the single hits, or in case of logarithmic probabilities, the sum of the logarithmic probabilities for the single hits. This probability for the whole sample is called *likelihood (LLH) value*.

$$LLH \quad = \quad \prod_{i=1}^{N_{\text{hits}}} pdf_i \tag{6.4}$$

$$-\log LLH \quad = \quad \sum_{i=1}^{N_{\text{hits}}} -\log pdf_i \tag{6.5}$$

In both following fits the shower assumption is varied until the likelihood reaches its maximum. The shower assumption with the highest likelihood matches the measured hit pattern best and hence, is believed to be the true shower. Over the whole search space of possible shower hypotheses this likelihood value can differ by many orders of magnitude. Thus, the logarithmic likelihood is used for the fit and as the fit routines prefer looking for minima in a multidimensional search space the negative logarithmic likelihood is minimized.

A measure for the quality of the fit result is the reduced log-likelihood that is the value of the final log-likelihood divided by the degrees of freedom.

$$rLogL = \frac{LogL}{N_{\text{dof}}} \tag{6.6}$$

Degrees of freedom is defined as the number of free parameters in the minimization process. For example if a vertex reconstruction that fits four parameters (three spacial coordinates and one interaction time) is performed, a minimum hit sample of at least four hits is required. Each additional hit is a free parameter in the minimization. Thus degrees of freedom is evaluated as follows:

$$N_{\text{dof}} = N_{\text{hits}} - N_{\text{fitparameters}} \tag{6.7}$$

The probabilities (6.3) for the single hits are read out from PDF tables that have been generated in advance from an electron neutrino Monte-Carlo production, internally named *prod11*, that was released in July 2011. The simulation was performed by the ANTARES simulation working group and was the predecessor production of the RBR for shower events. Here no run-by-run based information was applied to the simulation. Instead a perfectly working detector was assumed, which is appropriate for the generation of the PDF tables, as no background hits are included in the tables. Further, as the PDF tables contain information *per hit*, not *per event*, there is no need to exclude not working OMs because all OMs have the same design. The software that was used for this production was GENHEN v6r7 [86] [87] [88] as event generator and

GEASIM v4r12 [105] as shower and photon simulation, hence, the same software as for the RBR, but in a slightly earlier version. The simulation was performed with the following settings:

- Neutrino energy range: $10^2 - 10^9$ GeV

- Neutral current ν_μ ν_e and charged current ν_e reactions

- Anti-neutrino and neutrino types

- 4π neutrino direction

- One particle approximation [106] activated for neutrino energies $> 10^5$ GeV

The simulation of the PMT response and the DAQ system (see chapter 3.3) is performed in a SeaTray chain. The charge saturation that varies from OM to OM is taken into account by applying a randomized saturation level to each hit, following the distribution that was obtained from real ANTARES calibrations. A distribution of the saturation levels is given in figure 3.9. See also appendix B.5.1.2 for more information on this.

As this simulation does not include photon scattering, only direct photons are taken into account in the creation of the PDF tables. Hence, also for the maximum likelihood fit, hits that passed the ARS hit selection, as described in section 6.1.1, are used to ensure that the reconstruction is performed on hits from direct photons only.

The Dusj package also provides tools to create new PDF tables from future Monte-Carlo simulations. These tools are described in appendix B.5.

6.2.1 Vertex position and interaction time

The reconstruction of the shower vertex position is done by a Gulliver maximum likelihood fit using the Dusj service **I3DusjShowerVertexPDF** for the likelihood calculation. The service accesses the PDF table that stores probabilities that a single hit has been created from a certain shower vertex and interaction time assumption. As table format the ROOT [113] class **TH2D** was chosen. Figure 6.10 shows the content of this PDF table that is the probability that a single hit, measured at an OM with a certain distance from the shower vertex at a certain time since the interaction time, has been created by the shower vertex and interaction time assumption. One can basically see the linear light spread indicated by a very sharp straight line in the PDF table.

The likelihood for the whole event to be induced by the shower assumption is then calculated according to equation (6.4). An illustration of the four dimensional likelihood landscape is given in figure 6.11 showing an event with a clear extremum at the true
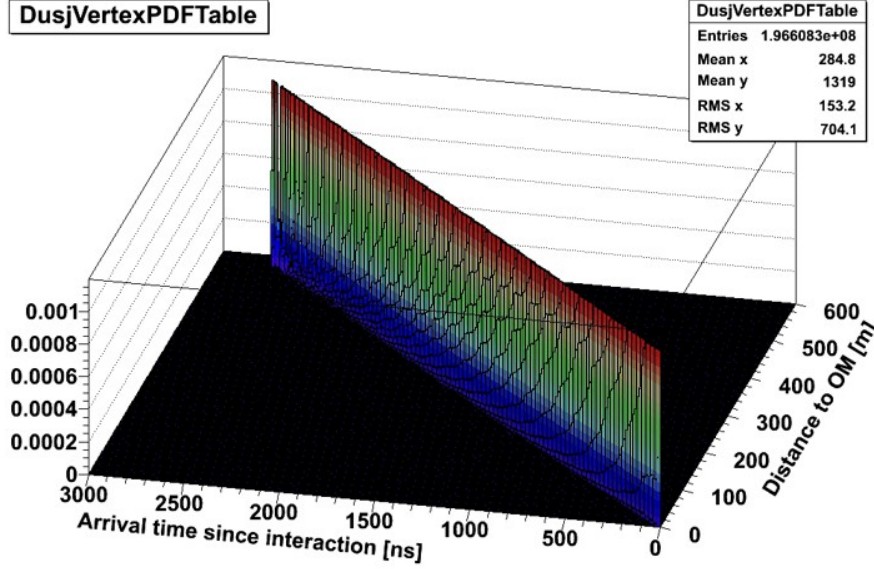
Figure 6.10: *PDF table for the vertex position and interaction time reconstruction.* The table stores the probability that from a shower vertex assumption a hit is recorded at a certain distance from this vertex (x-axis) and at a certain time since the interaction time (y-axis). In the table all OM-Distance-rows are normalized to the same value, to give each distance the same weight.

vertex position. However, in some other events the extremum might be less distinctive or even several local minima might occur. Thus, for this analysis the minimization is repeated five times using slightly varying seeds as input. The result with the lowest negative log-likelihood value will be selected and passed to the energy and direction reconstruction. During the first iteration the time of the first selected shower hit that is part of the *triggered hits* (see chapter 3.3.1) is taken for the time seed and the center of gravity of the selected hits' charges as seed for the position. For the four subsequent fits the first seed is varied randomly to ±50 ns for the time and 10 m in different directions for the position.

Table C.13 in appendix C.2 lists all configuration parameters of this service. Appendix B.6 holds the configuration that was used for this analysis, also regarding the Gulliver services that have to be configured in a way that the shower energy and neutrino direction will not be varied during the fit. To vary energy and direction makes no sense as those parameters have no impact on the evaluation of the vertex likelihood. It will increase the computing time as the fit routine runs through a lot of steps that all yield the same result. See appendix A.2.3 for more information.

This fit procedure yields a resolution for the vertex position of about 3 m median error in shower events with 100 GeV shower energy, slightly increasing with energy up to about 8 m median error at 10 PeV in all RBR shower events that already passed an upper cut on the reduced vertex log-likelihood (VLLH) as defined in equation (6.6) at a value of 7.9. The choice of this cut is explained further in chapter 7 and will be used
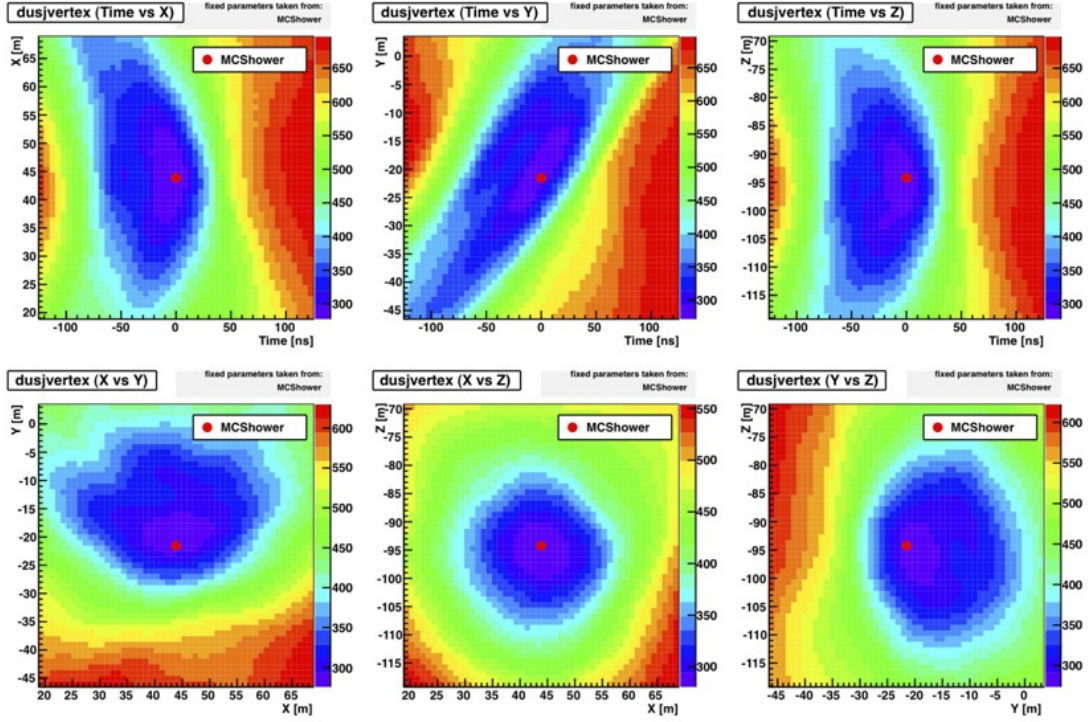
Figure 6.11: *Log-Likelihood landscape of an event as created by the I3DusjShowerVertexPDF service. The vertex likelihood is a four dimensional landscape, thus six plots are necessary to plot each of the four parameters (x, y and z of the vertex position and interaction time t) against each other. The coloured axis codes the value of the negative log-likelihood landscape as defined in equation (6.5). The red points mark the simulated shower parameters. The plots have been created from a shower event with 38 signal hits on 9 strings (shower energy about 3 TeV) using the service with default settings. Plots like these can be created using the script* **PlotDusjShowerVertexPDFLikelihood.py**

in the following diffuse flux analysis. Note that the given errors refer to the shower interaction vertex, not to the position of the maximum light deposition in the shower. The corresponding resolution for the interaction time is about 4 ns median error at 100 GeV and about 22 ns median error at 10 PeV.

The figures 6.12 and 6.13 show more detailed information about the reconstruction errors as function of the shower energy and the data taking period, also for events without the reduced vertex log-likelihood cut applied. From the period plots one can derive a stable reconstruction quality throughout all periods, except for slightly greater reconstruction errors in early periods when the detector was not yet fully established.
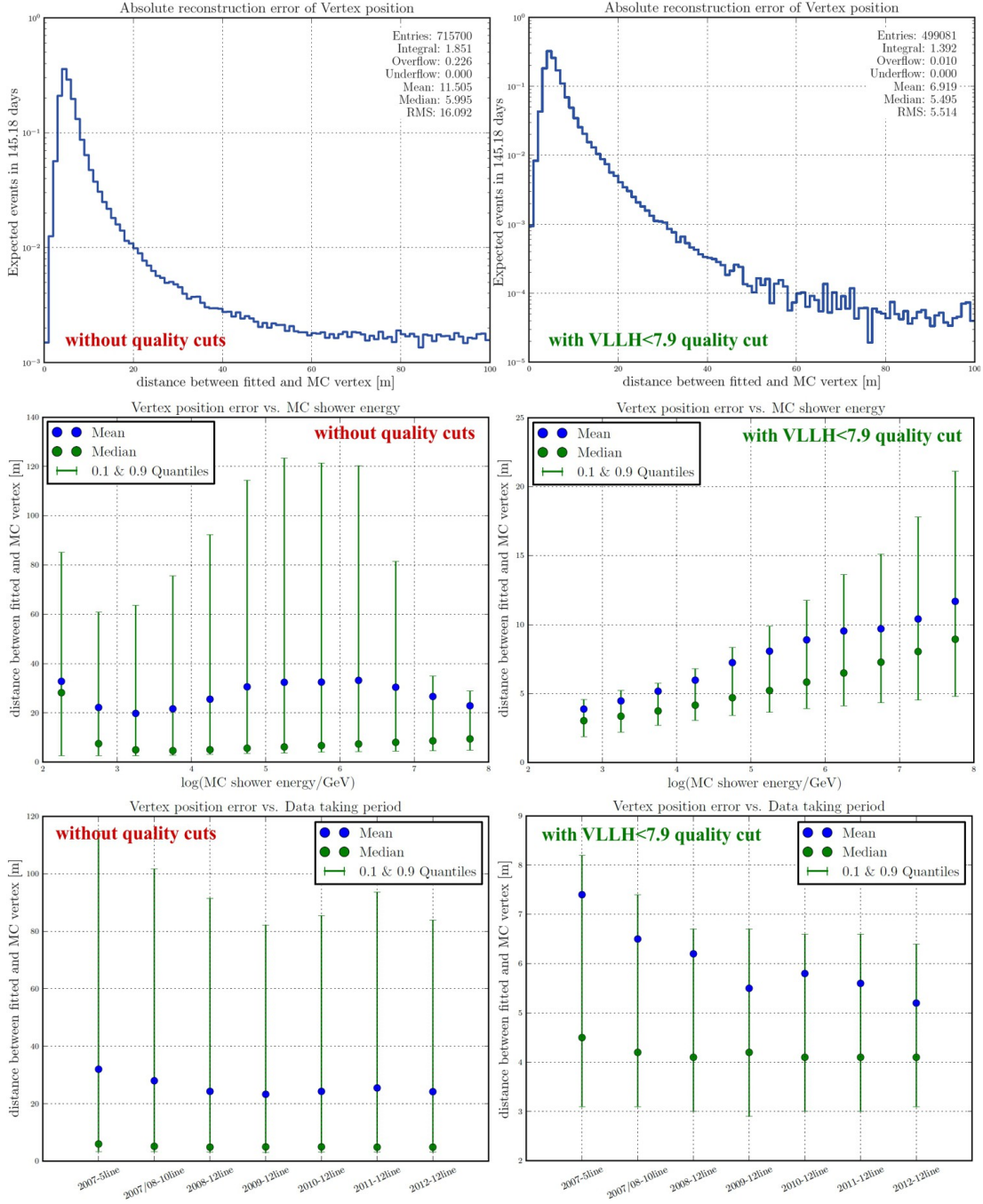
Figure 6.12: *Absolute reconstruction error of the vertex position.* The plots show the distributions of the event-wise absolute distance between the fitted and Monte-Carlo vertex position. The upper plots show the distribution of all shower events of the high energy RBR simulations (see chapter 5.2), weighted with a cosmic E^{-2} neutrino flux and a normalization of $4.5 \cdot 10^{-8}\,\mathrm{GeV/cm^2 \cdot sr \cdot s}$ per neutrino flavour. The middle plots illustrate the corresponding tendency of the vertex reconstruction error with Monte-Carlo shower energy. Therefore, for each semi-decade in shower energy a separate distribution has been drawn, from which the mean, median and the quantiles have been calculated. Note that the error bars in the plots show the 10 % and 90 % quantiles of the distribution, not the error of the mean/median. The tendency with the data taking period is shown in the lower plots for showers with an energy of 10 TeV. The presented quality is once for a data sample without any further quality cuts than the minimum constraints filter (see chapter 6.1.3) applied (left column) and once with an additional upper cut on the reduced vertex log-likelihood at 7.9 (see chapter 7) to remove badly reconstructed events (right column). The plots have been generated from all NC/CC shower events in the RBR runs with a run number ending with 0.

Figure 6.13: *Absolute reconstruction error of the interaction time.* The plots show the distributions of the event-wise absolute difference between the fitted and Monte-Carlo interaction time. The upper plots show the distribution of all shower events of the high energy RBR simulations (see chapter 5.2), weighted with a cosmic E^{-2} neutrino flux and a normalization of $4.5 \cdot 10^{-8}\,\mathrm{GeV/cm^2 \cdot sr \cdot s}$ per neutrino flavour. The middle plots illustrate the corresponding tendency of the time reconstruction error with Monte-Carlo shower energy. Therefore, for each semi-decade in shower energy a separate distribution has been drawn, from which the mean, median and the quantiles have been calculated. Note that the error bars in the plots show the 10 % and 90 % quantiles of the distribution, not the error of the mean/median. The tendency with the data taking period is shown in the lower plots for showers with an energy of 10 TeV. The presented quality is once for a data sample without any further quality cuts than the minimum constraints filter (see chapter 6.1.3) applied (left column) and once with an additional upper cut on the reduced vertex log-likelihood at 7.9 (see chapter 7) to remove badly reconstructed events (right column). The plots have been generated from all NC/CC shower events in the RBR runs with a run number ending with 0.

6.2.1.1   Additional features

This section gives a short description of features that are also implemented in the vertex likelihood service but have not been used for this analysis.

By default the evaluation of the likelihood is performed without any light attenuation. All hits contribute their PDF value with the same weight to the overall likelihood. This means that a hit measured far away from the vertex has the same impact than a very close hit. To give close hits a higher weight one might weight the PDF values with an exponential light attenuation. Then hits that are far away from the vertex assumption contribute less to the likelihood than close ones. To do this, set the parameter *ApplyWaterAbsorption* to true. The water absorption length, as configured in the parameter *WaterAbsorptionLength*, will be used for the evaluation of the weights. However, studies have shown that this feature has a very small impact on the likelihood and yield no significant improvement in the RBR. Thus, for this analysis this feature was not used.

Figure 6.14 gives an illustration of how the likelihood is evaluated when water absorption is applied and how the likelihood landscape (here shown just for x vs. y of the vertex position) changes marginally.
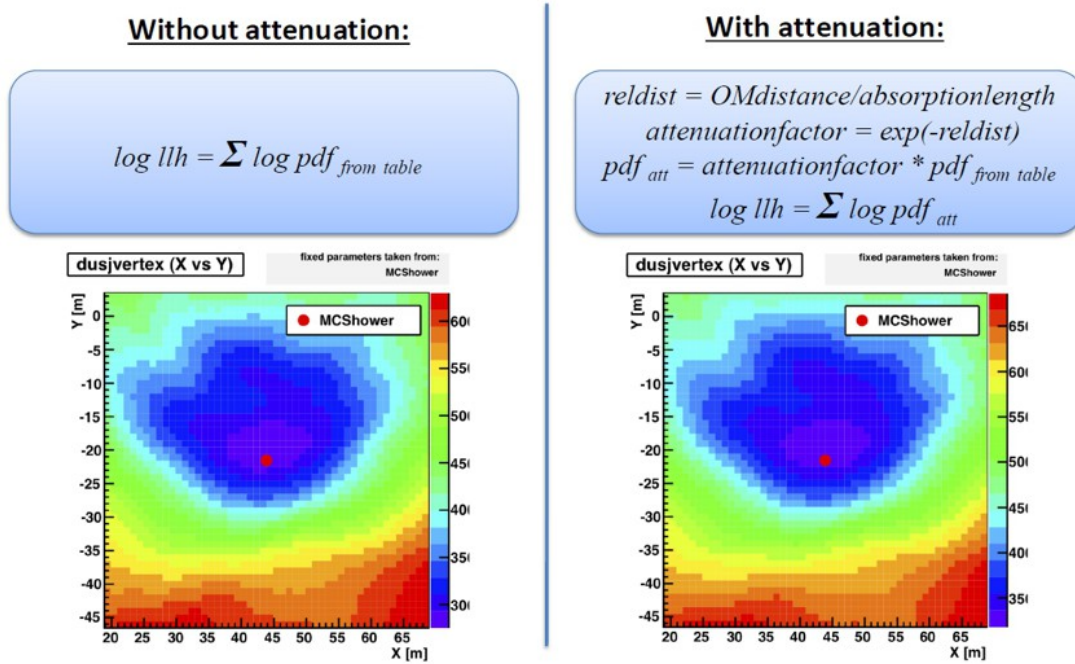
Figure 6.14: *Vertex likelihood calculation including light attenuation in water.* The scheme illustrates the differences in the calculation of the event likelihood once without water attenuation, where all hits have the same weight (left), and once with water attenuation included, where far hits contribute less to the likelihood value than close-by hits (right). One can clearly see in the example plot of the x vs y landscape of a shower event likelihood that this feature has just a marginal effect.

Further, in the default configuration the evaluation of the log-likelihood is done by summing up the logarithmic PDF values of the signal hits. On the other hand, an OM that has not detected a hit also contains information - namely the lack of hits - that can be included in the likelihood calculation as well. To do this, set the parameter *IncludeNotFiredOMs* to true. Each signal hit has a probability *pdf* (which is the PDF value from the table, corrected with the light attenuation as described above) to occur at a certain distance and at a certain time. Thus, the probability that an OM at a certain distance detects no hit is $1 - P$, where P is the integration of the *pdf* values over all times, which is in the PDF table the whole bin row for this distance (denoted as *binintegral* in the following). To ensure that only working OMs are considered in the likelihood calculation, the service uses the information about the condition of each individual OM to exclude all faulty or missing OMs from the calculation. However, again studies have shown that including the not fired OMs will increase the computing time by far as in each call of the likelihood function the service has to loop not just over the signal OMs but over all OMs! On the other hand including not fired OMs has a very small impact on the likelihood, which cannot justify the enormous increase in computing time. Thus, for this analysis the information from not fired OMs was not used. Figure 6.15 gives an illustration of how the likelihood is evaluated when considering not fired OMs and how the likelihood landscape (here shown just for x vs. y of the vertex position) again changes marginally. The weight w in the scheme corresponds to the steering parameter *NotFiredOMsWeight* and has been set to 1. in the plot.
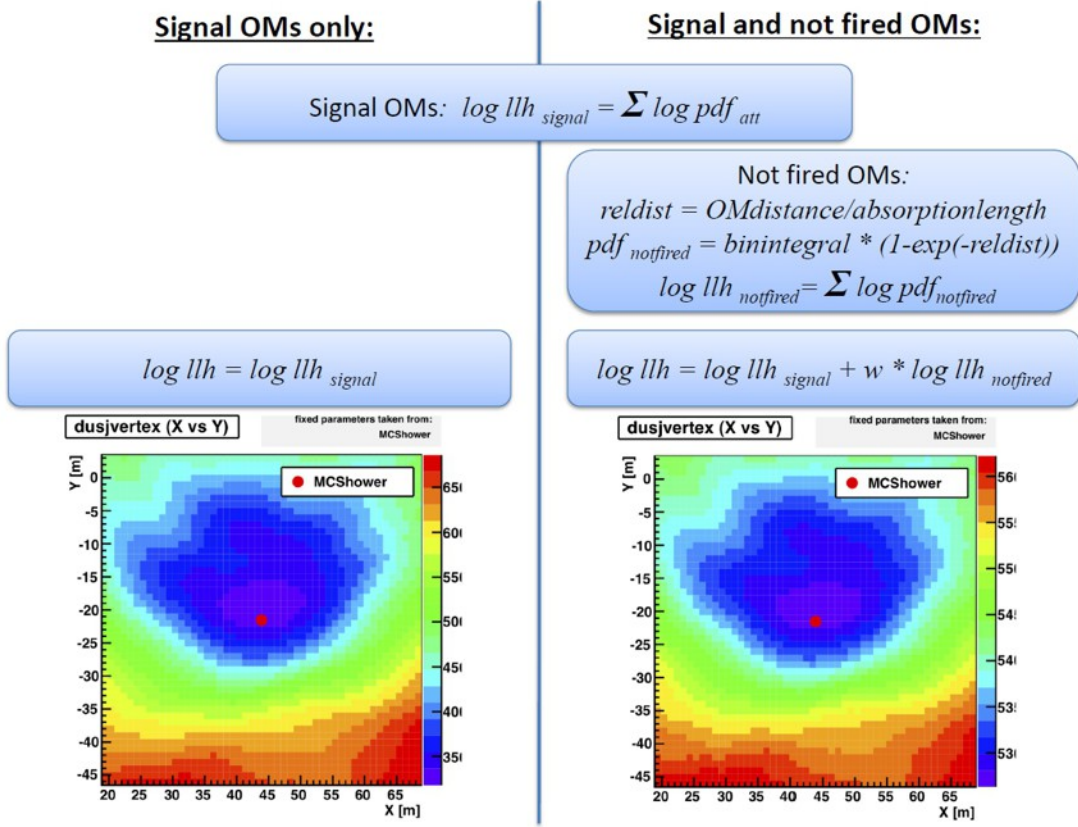
Figure 6.15: *Vertex likelihood calculation including not fired OMs.* The scheme illustrates the differences in the calculation of the event likelihood once from signal hits only (left), and once also taking OMs that have not been fired into account (right). The value *binintegral* is the summation of all entries along the time axis for one certain distance bin row in the PDF table. The value w is the weight that can be applied to not fired OMs via the parameter *NotFiredOMsWeight* and that has been set to 1. here. One can clearly see in the example plot of the x vs y landscape of a shower event that this feature has just a marginal effect.

6.2.2 Shower energy and neutrino direction

The reconstruction of the shower energy and neutrino direction is again done by a Gulliver maximum likelihood fit using another Dusj likelihood service, called **I3Dusj-ShowerEnergyDirectionPDF** for the likelihood calculation. The use of this service, however, requires a previously defined vertex position as input. Here, of course, the fit result of the precedent vertex reconstruction is used. The vertex is kept fixed during the fit of the shower energy and neutrino direction.

The service then evaluates the probability (likelihood) that a given sample of hits has been created from a hypothetical shower that has been induced by a neutrino from a certain direction and has a certain shower energy. Again, the goal of the fit is to modify this energy and direction assumption until the maximum probability has been found. The evaluation of the likelihood is done using again a Monte-Carlo based PDF table. Compared to the vertex reconstruction where the corresponding PDF table was a two dimensional histogram with one axis for the hit arrival time and one for the distance to the OM, here, a three dimensional table is needed, wherefore the ROOT [113] class **TH3D** was chosen. The table stores the probability that one single hit has been created from a certain shower hypothesis. The three observables that relate the hit attributes, such as charge and OM position, to this probability are:

- **Total charge at vertex**, which is the total charge c_{vertex} that is expected to be created at the vertex to cause this particular hit

- **Emission angle** of the hits' photons with respect to the neutrino direction

- **Shower energy** in logarithmic scale

The evaluation of the *total vertex charge* c_{vertex} can be done in two different ways:

- **assuming isotropic light emission** (which is the default and is used in this analysis). Here, the charge of a hit drops with its distance d from the vertex following d^{-2}, which is in case of showers a more realistic assumption than a d^{-1} drop that would be expected from pure light emission into the Cherenkov angle. The vertex charge calculation in this mode takes into account the water absorption length λ_w that is taken from the additional information stored in the ROOT file that contains the PDF table (to ensure that the same absorption length is used that has been used for the generation of the PDF table) where 60 m has been used. Further, the geometrical cross section of the OM A_{OM} is taken into account. The calculation is done as follows:

$$c_{\text{vertex}} = c_{\text{hit}} \cdot e^{\frac{d}{\lambda_w}} \cdot \frac{1}{\alpha} \cdot \frac{4\pi d^2}{A_{\text{OM}}^2} \qquad (6.8)$$

where the first factor is the measured charge of the hit, the second compensates the exponential light attenuation, α is the angular acceptance of the OM at the photon angle of incidence and the last factor relates the cross-section of the OM to the total surface of a sphere with the distance as radius. This is where the isotropic light assumption comes into play as of all isotropically emitted photons only the fraction will be detected that is emitted in the solid angle of the OM.

- **assuming pure Cherenkov light emission**. Here, the charge of a hit drops with d^{-1}, which is valid only for a very sharp light emission into the Cherenkov angle. But as in shower events the light emission peak is blurred out, the drop turns out to be more like d^{-2}. Thus, using the isotropic mode to evaluate the vertex charge yields better results but for the sake of completeness also this option has been kept for further studies. In this mode the vertex charge is calculated as follows

$$c_{\text{vertex}} = c_{\text{hit}} \cdot e^{\frac{d}{\lambda w}} \cdot \frac{1}{\alpha} \cdot \cos\theta_{\text{Cerenkov}} \cdot d \qquad (6.9)$$

where θ_{Cerenkov} is the Cherenkov angle in water.

Depending on how the PDF table was created, the likelihood service will automatically choose the correct way to evaluate the total vertex charge during the reconstruction step.

Further, two different ways are implemented to weight the single entries in the PDF table. Once a way is chosen, it will be used for the table generation and for the reconstruction step:

- **hit-based** (which is the default and is used in the following). In this case the PDF table stores the probability that the evaluated total vertex charge, evaluated from a single *hit* that has been emitted at a certain angle with respect to the neutrino direction, has been created by a shower event assumption with a certain shower energy. During the generation step of the pdf tables each triple of values, evaluated from one hit, will be filled into the histogram with a weight of 1. In the reconstruction step the overall likelihood is evaluated according to equation 6.4.

- **photon-based**. Here, the PDF table stores the probability that a single *photon* that has been emitted at a certain angle with respect to the neutrino direction has been created by a shower event assumption with a certain shower energy and a total vertex charge. The total vertex charge again is evaluated from the measured hit that has been caused by this and other parallel photons. To fill and readout the photon based table, each entry gets a weight that corresponds to the charge c_{initial} (number of photons) that this hit was expected to have when it was emitted from the given vertex position. This number of photons is not taken

from the Monte-Carlo truth but calculated from the measured charge c_{hit} of the detected hit to ensure that for example saturation effects are taken into account. This value is called in the following *initial hit charge*

$$c_{\text{initial}} = c_{\text{hit}} \cdot e^{\frac{d}{\lambda_w}} \tag{6.10}$$

The reason, why compared to the total vertex charge c_{vertex} only the hit charge and the light attenuation, but not the angular acceptance, is taken into account here, is because c_{initial} is used as weight for the table entries during the table generation. A very low angular acceptance in rare cases would create very high weights that result in high peaks in the PDF table that are almost impossible to be smoothed out later on. A smooth PDF table, however, is essential to provide also smooth likelihood landscapes that do not puzzle the minimizer algorithms with many local minima. When using photon-based PDF tables in the reconstruction step, a slightly modified likelihood calculation has to be applied to take into account that one hit originates from lots of photons. Thus equation (6.4) has to be modified so that each pdf_i value makes a contribution for every single photon.

$$LLH \quad = \quad \prod_{i=1}^{N_{\text{hits}}} pdf_i^{c_{\text{initial}}} \tag{6.11}$$

$$-\log LLH \quad = \quad \sum_{i=1}^{N_{\text{hits}}} -c_{\text{initial}} \cdot \log pdf_i \tag{6.12}$$

Depending on how the PDF table was created, the likelihood service will automatically choose the correct way to evaluate the likelihood. To avoid any bias from the generated flux spectrum of the Monte-Carlo production *prod11* that was used to create the PDF table, all shower-energy-bin-planes are normalized to the same value to give each energy the same probability to occur. Figure 6.16 shows an illustration of the content of this PDF table. As a full plot of this table would require a 4D-plot with axes for shower energy, vertex charge, emission angle & PDF value, only projections and bin-wise excerpts are plotted.

What might attract the readers attention in this plot is the flattening of the Cherenkov peak towards high energies (upper left plot). During the reconstruction the fit in principle looks for an excess of signal in the Cherenkov direction with respect to the neutrino direction. However, as the table has been filled with one entry per *hit* and not per *photon* the flattening is a limitation effect of the detector instrumentation. High energy showers with an energy above $10\,\text{PeV}$ fire each OM in the detector, also in backward direction, so that no excess in the Cherenkov angle is visible any more. If the table was created in *photon-based* mode, the Cherenkov peak would reach up to higher energies as of course an excess of *photons* in the Cherenkov angle is present throughout all energies.
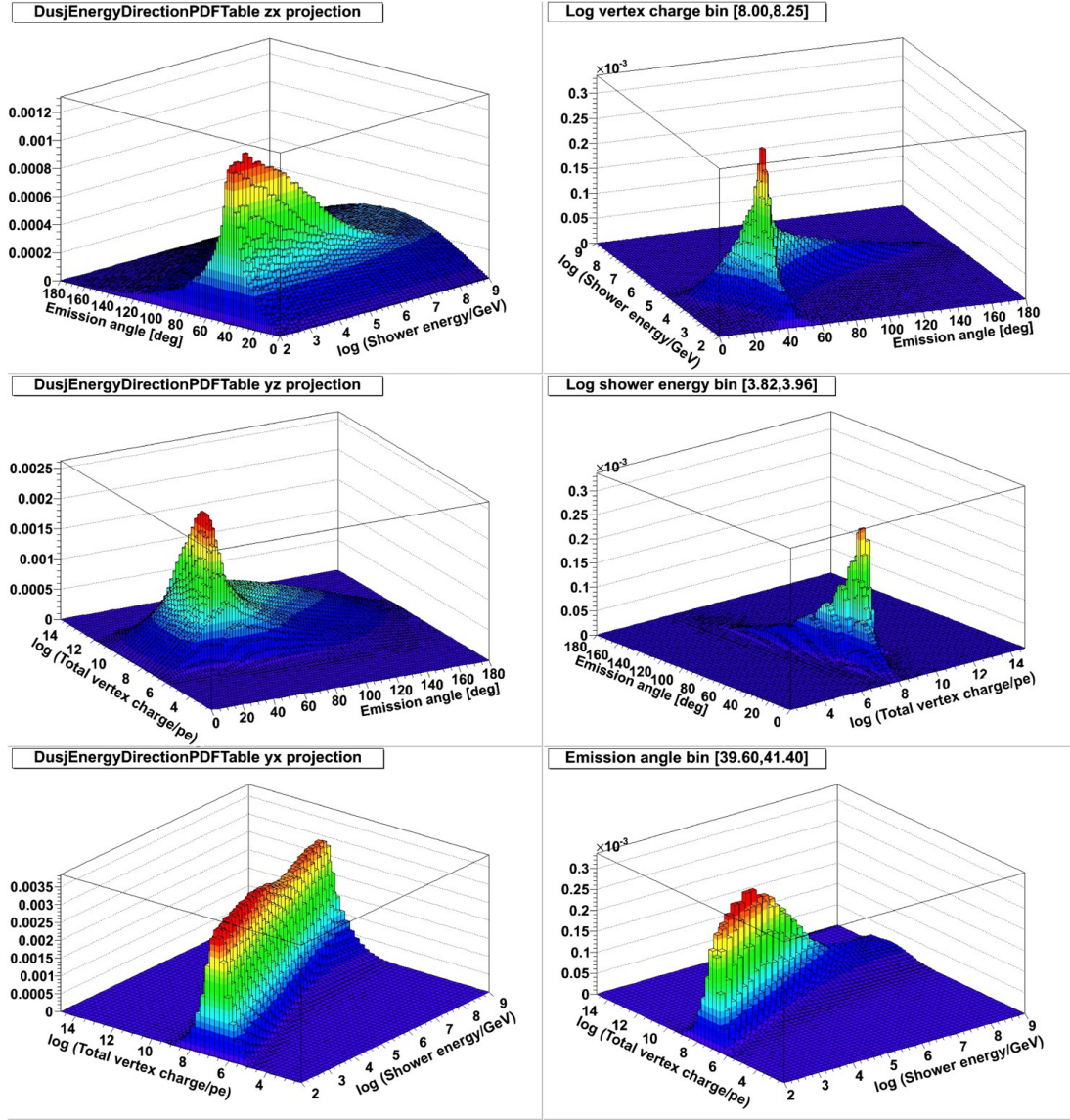
Figure 6.16: *PDF table for the shower energy and neutrino direction reconstruction.* The table stores the probability that from a shower with a certain energy a hit with a certain charge (folded into the observable *total vertex charge*) is emitted in a certain direction with respect to the neutrino direction. As the table has three dimensions only projections or excerpts can be illustrated. The left column of plots shows one axis against another integrated over all bins of the third axis, where the right column of plots shows one axis against another for just one specific bin of the third axis. In the table all shower-energy-bin-planes are normalized to the same value to give each energy the same probability to occur.

Nevertheless for this work, it was chosen to use a *hit-based* PDF table, as this mode offers one big advantage. When giving each hit the same weight, the reconstruction is very robust against single hits that have a corrupt calibration. For instance: The ANTARES OM is typically in saturation at $20-25$ pe (see also chapter 3.3), however, it happens that wrong calibration sets give single hits a charge up to a few hundred photo

electrons. If the PDF table, and hence also the likelihood calculation, is performed *hit-based*, the wrong hit contributes to the likelihood with the same weight as all the other correct ones and hence does, assuming enough hits in the sample, not change the likelihood too much. If, however, the fit is *photon-based*, this particular wrong hit will contribute to the likelihood with a huge weight and hence might force the minimization into a completely wrong direction. Thus, the decision was made in favour of robustness and therefore loose reconstruction quality for the highest energy events. But due to the relatively small size of the detector and the small flux of high energy events, a detection of such a high energy event is quite unlikely anyhow. And if it did happen, the reconstruction would probably tend to fit a somewhat lower energy, where the Cherenkov peak is still visible in the PDF table.

Also compared to the approach that is followed in the Q-Strategy [8], the robustness of this algorithm must be stressed. The energy reconstruction in the Q-Strategy is performed by relating the total cumulative charge of all hits - corrected for attenuation - to the shower energy. That procedure, again, makes the reconstruction liable to wrong hit charges, which is not the case in the *hit-based* PDF likelihood calculation used here.

An example of a likelihood landscape is shown in figure 6.17. Here, the zenith is defined as the angle from a vertically down-going neutrino (i.e. 180° is vertically up-going), whereas the azimuth defines the orientation on the surface. The shown event shows a clear extremum, but again, there are other events, for which the extremum might be less distinctive or even several local minima occur. Thus, for this analysis the minimization is repeated ten times using slightly varying seeds as input. The result with the lowest negative log-likelihood value will be selected and provides, together with the result from the vertex fit, the final reconstruction result. During the first iteration the seed for the direction is set to a horizontal incoming neutrino with an azimuth of 180°, the first energy seed is set to 100 TeV. For the nine subsequent fits the first seed is varied randomly to ±2 orders of magnitude for the energy and 90° in various directions for the neutrino direction.

Table C.14 in appendix C.2 lists all configuration parameters of this service. Appendix B.6 holds the configuration that was used for this analysis, also regarding the Gulliver services. As the energy and direction reconstruction requires an already fitted vertex position as input, the result of the previous vertex fit has to be passed to the fit routine. Further, it has to be ensured that this vertex and the interaction time will not be varied during the fit. See appendix A.2 for more technical information.

The whole fit procedure, where the energy and direction reconstruction relies on the quality of the vertex fit, yields a stable resolution for the neutrino direction of about 6° to 7° median error in shower events below 100 TeV shower energy, but looses quality with increasing energy up to about 41° median error at 10 PeV in all RBR shower events that already passed an upper cut on the reduced vertex log-likelihood
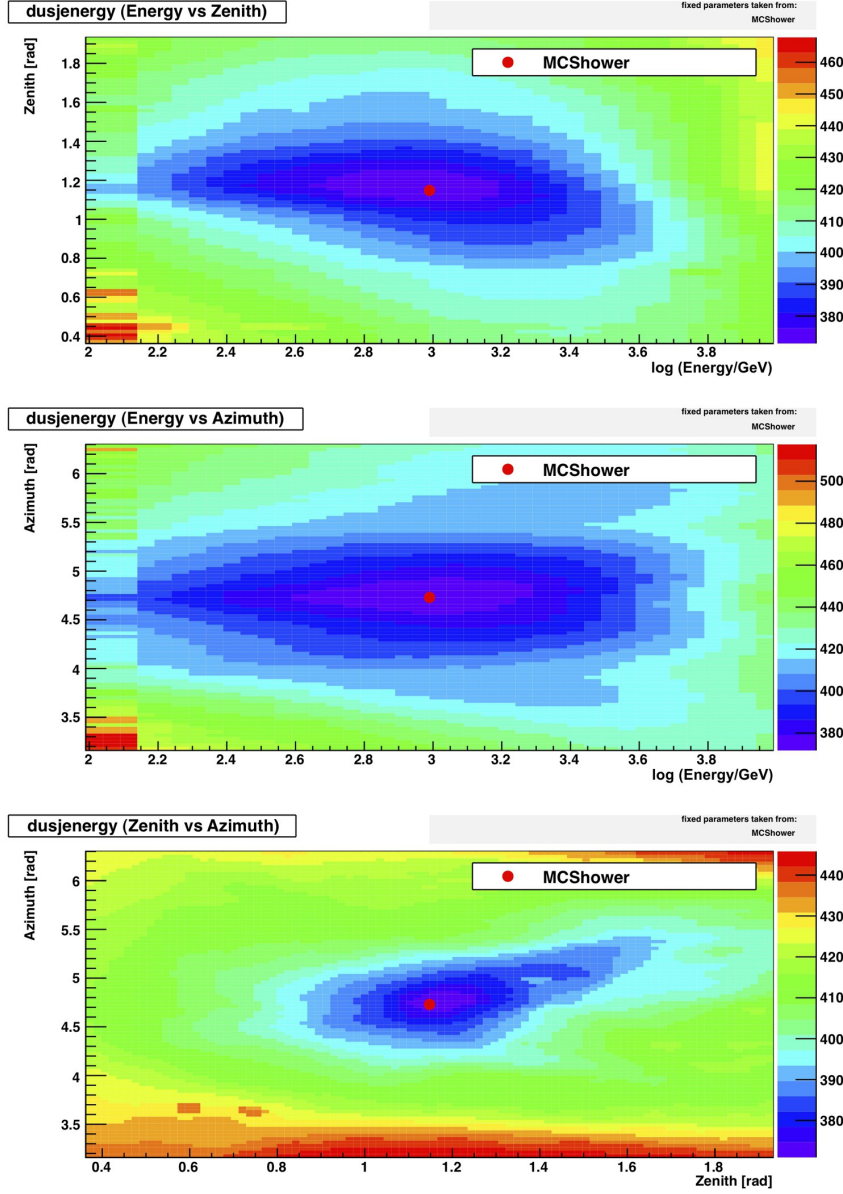
Figure 6.17: *Log-Likelihood landscape of an event as created by the I3DusjShowerEnergyDirectionPDF service.* The energy-direction likelihood is a three dimensional landscape, thus three plots are necessary to plot each of the parameters (shower energy, neutrino direction zenith and direction azimuth) against each other. The coloured axis codes the value of the negative log-likelihood landscape as defined in equation (6.5). The red points mark the simulated shower parameters. The plots have been created from a shower event with 38 signal hits on 9 strings (shower energy about 3 TeV) using the service with default settings. Plots like these can be created using the script **PlotDusjShowerEnergyDi-rectionPDFLikelihood.py**

(VLLH) as defined in equation (6.6) at a value of 7.9. The choice of this cut is explained further in chapter 7 and will be used in the following diffuse flux analysis. The drop in the direction reconstruction quality at high energies is expected as the PDF table has

been created in hit-based mode, where the Cherenkov peak flattens out at the highest energies.

The corresponding resolution for the shower energy is about -0.3 orders of magnitude mean error at $100\,\mathrm{GeV}$ slightly increasing up to -0.6 orders of magnitude mean error at $100\,\mathrm{PeV}$. An explanation for the fact that on average the shower energy is underestimated could also be the flattening of the Cherenkov peak in the table. The minimizer might tend to converge at a lower energy, where the Cherenkov peak is still more distinct and hence, the probability can reach higher values (see also upper left plot in figure 6.16).

The figures 6.18 and 6.19 show more detailed information about the reconstruction errors as function of the shower energy and of the data taking period. The accumulation of events with a wrong reconstructed direction that is about $80°$ from the simulated direction in the upper plots of figure 6.18 is caused by typically two-line events for which always a mirror solution in the neutrino direction emerges. A cut on events with detected pulses on at least three lines, as introduced later in chapter 7.2.1, reduces the number of events with such a mirror solution. However, there are also event topologies on three lines that allow the occurrence of the mirror solution.

It can be concluded that the Dusj reconstruction provides a stable reconstruction quality throughout all periods, except for slightly greater reconstruction errors in early periods when the detector was not yet fully established. Figure 6.20 shows the reconstruction error for zenith and azimuth separately.
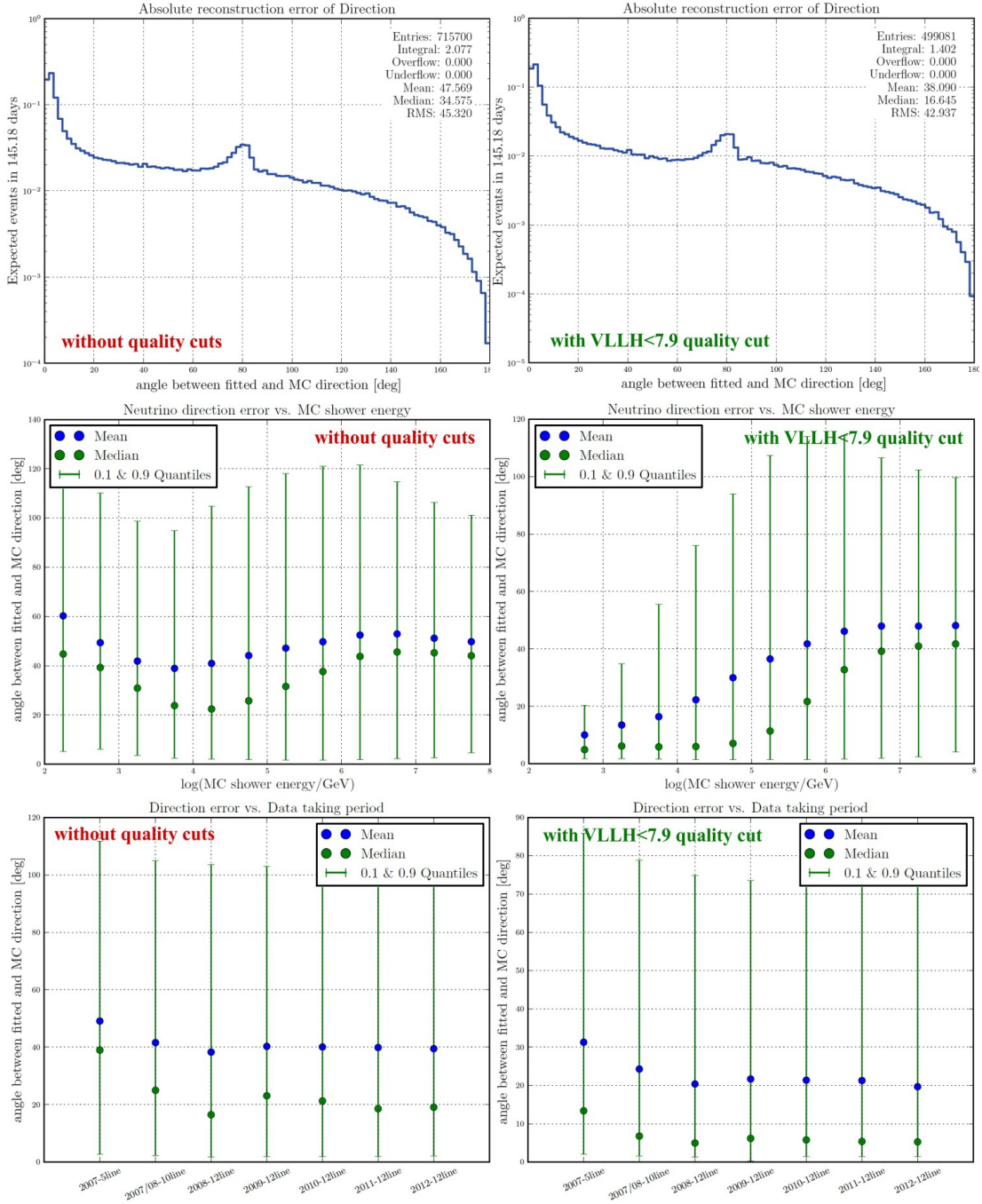
Figure 6.18: *Absolute reconstruction error of the neutrino direction.* The plots show the distributions of the event-wise absolute angle between the fitted and Monte-Carlo neutrino direction. The upper plots show the distribution of all shower events of the high energy RBR simulations (see chapter 5.2), weighted with a cosmic E^{-2} neutrino flux and a normalization of $4.5 \cdot 10^{-8} \, \text{GeV/cm}^2 \cdot \text{sr} \cdot \text{s}$ per neutrino flavour. The middle plots illustrate the corresponding tendency of the direction reconstruction error with Monte-Carlo shower energy. Therefore, for each semi-decade in shower energy a separate distribution has been drawn, from which the mean, median and the quantiles have been calculated. Note that the error bars in the plots show the 10 % and 90 % quantiles of the distribution, not the error of the mean/median. The tendency with the data taking period is shown in the lower plots for showers with an energy of 10 TeV. The presented quality is once for a data sample without any further quality cuts than the minimum constraints filter (see chapter 6.1.3) applied (left column) and once with an additional upper cut on the reduced vertex log-likelihood at 7.9 (see chapter 7) to remove badly reconstructed events (right column). The plots have been generated from all NC/CC shower events in the RBR runs with a run number ending with 0.

Figure 6.19: *Logarithmic reconstruction error of the shower energy.* The plots show the distributions of the event-wise difference of the logarithmic fitted and the logarithmic Monte-Carlo shower energy. The upper plots show the distribution of all shower events of the high energy RBR simulations (see chapter 5.2), weighted with a cosmic E^{-2} neutrino flux and a normalization of $4.5 \cdot 10^{-8} \, \mathrm{GeV/cm^2 \cdot sr \cdot s}$ per neutrino flavour. The middle plots illustrate the corresponding tendency of the energy reconstruction error with Monte-Carlo shower energy. Therefore, for each semi-decade in shower energy a separate distribution has been drawn, from which the mean, median and the quantiles have been calculated. Note that the error bars in the plots show the 10 % and 90 % quantiles of the distribution, not the error of the mean/median. The tendency with the data taking period is shown in the lower plots for showers with an energy of 10 TeV. The presented quality is once for a data sample without any further quality cuts than the minimum constraints filter (see chapter 6.1.3) applied (left column) and once with an additional upper cut on the reduced vertex log-likelihood at 7.9 (see chapter 7) to remove badly reconstructed events (right column). The plots have been generated from all NC/CC shower events in the RBR runs with a run number ending with 0.

Figure 6.20: *Reconstruction error of the zenith and azimuth of the neutrino direction.* The plots show the distributions of the event-wise difference between the fitted and Monte-Carlo value for zenith (upper row) and azimuth (lower row) of the neutrino direction. All shower events of the high energy RBR simulations (see chapter 5.2) have been used and weighted with a cosmic E^{-2} neutrino flux and a normalization of $4.5 \cdot 10^{-8}\,\mathrm{GeV/cm^2 \cdot sr \cdot s}$ per neutrino flavour. The presented quality is once for a data sample without any further quality cuts than the minimum constraints filter (see chapter 6.1.3) applied (left column) and once with an additional upper cut on the reduced vertex log-likelihood at 7.9 (see chapter 7) to remove badly reconstructed events (right column). The plots have been generated from all NC/CC shower events in the RBR runs with a run number ending with 0.

6.2.3 Simultaneous reconstruction of all 7 shower parameters

This section describes an alternative way to fit the seven shower parameters that is, however, not used in this analysis.

Instead of reconstructing the vertex first, and determine energy and direction afterwards, the Gulliver framework also offers the possibility to combine the two likelihood services to one for a simultaneous fit of all seven shower parameters. However, first attempts to try it this way did not yield the same reconstruction quality as the two-part fit strategy and has not been investigated further. In the two-part (default) strategy one can see that the vertex reconstruction yields a better accuracy than the reconstruction of the energy and direction. Thus, it seemed consequently to have an independent reliable vertex reconstruction and do the more difficult and less accurate direction and shower reconstruction later on without influencing the vertex fit result any more. When fitting everything in one step one could expect that the uncertainty in the direction and shower likelihood will level down the quality of the vertex reconstruction. But in principle the simultaneous fit can be performed by combining the two Dusj likelihood services as it is explained in appendix B.2.

However, it should be remarked that in a global fit of all seven parameters using charge and time information simultaneously, it often is a welcome solution for the minimizer to choose a high shower energy and therefore place the vertex position incorrectly far outside of the detector. Then, this requires the introduction of a kind of containment cut to remove events that have a fitted vertex outside the instrumented volume. When reconstructing the vertex independently and from the time information only, as it is done in this analysis, such a containment cut is no longer necessary as for a fixed vertex the energy can not be increased arbitrarily, but is constrained by the distance of the vertex to the single hits.

6.3 Cut parameters for quality and purity cuts

The previously introduced reconstruction steps (the hit selection and the two Gulliver maximum likelihood fits) already provide a lot of potential cut parameters that are ready to be used as quality parameters to remove badly reconstructed events or to suppress track-like events. Some more parameters are evaluated by the module **I3DusjShowerCutValuesCollector** and stored, together with the existing ones, in one common set of cut values. This provides clarity of the reconstruction result as all relevant information has been standardized and offers the possibility to easily perform cuts on these parameters using tools that are part of the Dusj project. For more technical information about how to perform the cuts see appendix B.3. Additional parameters that are evaluated by this module are explained in the following.

For the vertex fit (and an optional pre-fit) a chi-square of time residuals (following equation (6.1)) is evaluated as a measure for the quality of the fitted vertex and interaction time. By summing up the squares of time residuals from all N selected shower hits the time residual chi-square is evaluated as follows:

$$\chi^2 = \frac{1}{N_{\text{hits}}} \sum_{i=1}^{N_{\text{hits}}} t_{\text{res},i}^2 \tag{6.13}$$

For each complete fit (where both, vertex and energy-direction fits are available) the quadrupole moment of the shower hits is evaluated that is a measure for the spacial distribution of the hits in relation to a track (which is the fitted neutrino direction in this case). The range of the evaluated quadrupole moment is between -2.0 and 1.0. Table 6.1 gives an overview of how the possible values of the quadrupole moment are related to a certain event shape. Of course, these examples are just special cases, the quadrupole moment can yield any floating value in the given range.

Table 6.1: Possible values of the quadrupole momentum

Value	Event layout
1.0	The hits are distributed on an (infinitesimally) thin disk that is perpendicular to the neutrino direction.
0.0	The hits are completely spherically arranged with the neutrino track going through the center of the sphere.
-1.0	The hits are arranged in an elliptical shape with the neutrino track going through the center of the ellipse and following the more elongated axis.
-2.0	Like -1.0, but the long axis of the ellipse is infinitely extended.

6.4 Random decision forest muon/shower classification

One major task that has to be done before any kind of neutrino physics analysis with ANTARES can be performed is to reduce the huge amount of atmospheric muon events that contaminate the sample of cosmic and atmospheric neutrinos and that are 5-6 orders of magnitude higher in number with respect to the shower signal events. In the following a random decision forest (RDF) method is introduced that is able to suppress the atmospheric muon background by 5-6 orders of magnitude. However, in the course of this work the RBR simulation for showers that has been performed without photon scattering turned out to be not completely reliable regarding some of the Dusj quality parameters and the RDF classification. Hence, what is presented in the following has not been used for this analysis, but in principle provides a powerful tool for atmospheric muon suppression that can be used for future Monte-Carlo simulations. More details on the encountered problems in the current RBR (v2) are presented in chapter 7.1.

The Dusj reconstruction chain provides a set of quality parameters that have been

evaluated during the hit selection and the two maximum likelihood fits (see chapter 6.3). Some of these parameters are a measure for the goodness of the fit and how well the fit result matches to the assumption of a point-like shower event. Thus, they can be used to discriminate muon track events from shower events as muons will have a worse agreement to the point-like event assumption than a shower does.

Whereas a sequence of hard cuts on various parameters tends to remove too many signal events (showers) in order to reach an adequate level of background (muon) suppression, the use of a tool for multivariate data analysis could help to improve the classification efficiency. Within the SeaTray framework an implementation of a random decision forest algorithm is implemented in the project *antares-rdfclassify*. By default this project has been developed and trained to classify muon track events only and separate up-going from down-going muons [114].

But for this purpose five of the Dusj quality parameters have been used as input features for the training of a new forest. The criteria to select parameters among all available Dusj quality parameters were a sufficiently good agreement between Monte-Carlo and ANTARES data in this parameter and the potential to separate muon track from shower events, i.e. a significant difference in the distribution of this parameter between muon and shower events. Distributions of these parameters are shown in figure 6.21. The chosen parameters are:

- **DusjShowerIdentifierReducedChiSquare.** A reduced chi-square of time residuals of the selected shower signal hits with respect to the prefit vertex estimation of the hit selection as given in equation (6.2).

- **DusjShowerRecoVertexFitReducedLogLikelihood.** The reduced negative final log-likelihood value of the vertex reconstruction as given in equation (6.6).

- **DusjShowerRecoFinalFitReducedLogLikelihood.** The reduced negative final log-likelihood value of the energy-direction reconstruction as given in equation (6.6).

- **FitTimeResidualChiSquare.** A chi-square of time residuals of the selected shower signal hits with respect to the final vertex reconstruction result as given in equation (6.13).

- **FitQuadrupoleMoment.** A value that is a measure for the spacial distribution of the hits in relation to the fitted direction (see chapter 6.3).
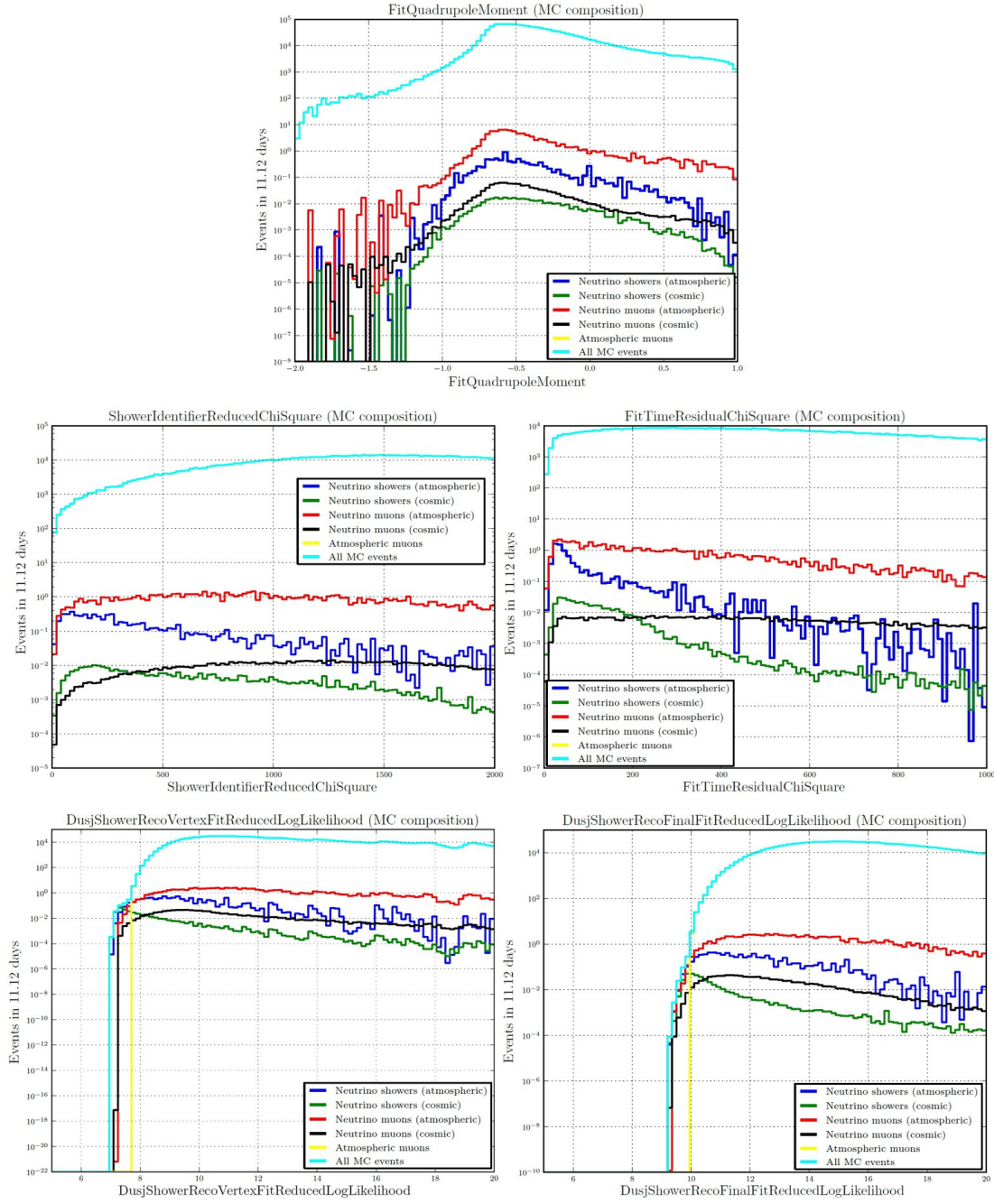
Figure 6.21: *Distributions of the five Dusj quality parameters used in the RDF for different event types.* For each of the five quality parameters that are used in the random decision forest muon/shower classification the distribution is drawn for shower events weighted with an atmospheric neutrino flux (dark blue) and a cosmic neutrino flux (green), for muon track events weighted with an atmospheric neutrino flux (red) and a cosmic neutrino flux (black), atmospheric muons (yellow) and the sum of all (light blue). As atmospheric muons are the dominant contribution, their distribution (yellow) mostly equals that of the sum (light blue), hence, the yellow line mostly is hidden behind the light blue one. For the cosmic neutrino flux an E^{-2} spectrum was assumed with a normalization of $4.5 \cdot 10^{-8}\,\mathrm{GeV/cm^2 \cdot sr \cdot s}$ per neutrino flavour. The atmospheric flux contains conventional (Bartol [9]) and prompt (Enberg [10]) neutrinos. The plots have been generated from 50% of all RBR runs for 2010 with a run number ending with 0. The limitation was due to computing memory reasons. All other periods show a similar behaviour.

The random decision forest looks for dependencies between the single parameters and joins them to two new cut parameters: an integer called *RDFClass* that stores the ID of the evaluated class and a floating value called *RDFSafety* that is a measure for how sure the classification is about the evaluated event class. The benefit of cutting just on the classification result often is a gain in efficiency as less signal events have to be discarded compared to hard cuts and still the same background rejection level is reached.

Figure 6.22 shows an illustration of how a classification with the random decision forest is done. For this forest 100 trees have been trained, each with a different randomly chosen set of Monte-Carlo events, where the RBR MUPAGE (see chapter 5) simulation represents the class *muon* and all NC and CC shower simulations of the RBR are included in the class *shower*. For each tree three randomly chosen of the five quality parameters have been used, means each tree will perform its classification based on a varying subset of the five quality parameters. As the detector configurations of the 5-line, 10-line and 12-line data taking periods obviously differ, three completely independent forests have been created, one for each detector configuration, to ensure the optimum classification rate for the whole data taking period. The training has been made using 25 % of the RBR runs with a run number ending with 0. These events cannot simultaneously serve as test sample as the classification of the same events, with which the forest has been trained, would result in an unrealistic 100 % correct classification, because those events are already known by the forest. A random decision forest classification always has to be performed on unknown events. In the training only events are considered that fulfil the following conditions:

- The fit status of the final fit is *OK*.

- The fit for the vertex position and interaction time converged within the set fit limits, means the convergence positions (as described in appendix A.2.1.2) are in the interval $[-1.0, 1.0]$.

A crucial parameter in the training of these random decision forests is the number of simulated events from each class that is used. One could imagine that an equal number of shower events and muon events would be the fairest way, but on the other hand in reality atmospheric muons are by 5-6 orders of magnitude more frequent than shower events. Further, the main goal for this classification is not a "fair" discrimination between showers and muons in a sense that each event has the same chance of being classified correctly. The primary aim was to suppress the huge amount of atmospheric muons at any cost, and cost here certainly means the efficiency of classifying a shower as shower. Therefore, it is more important to identify a muon correctly than to identify a shower correctly, as misclassified muons will contaminate the final analysis sample, whereas misclassified showers will be simply removed. A further influencing parameter is the fraction of events from the input dataset that will be used for the training of
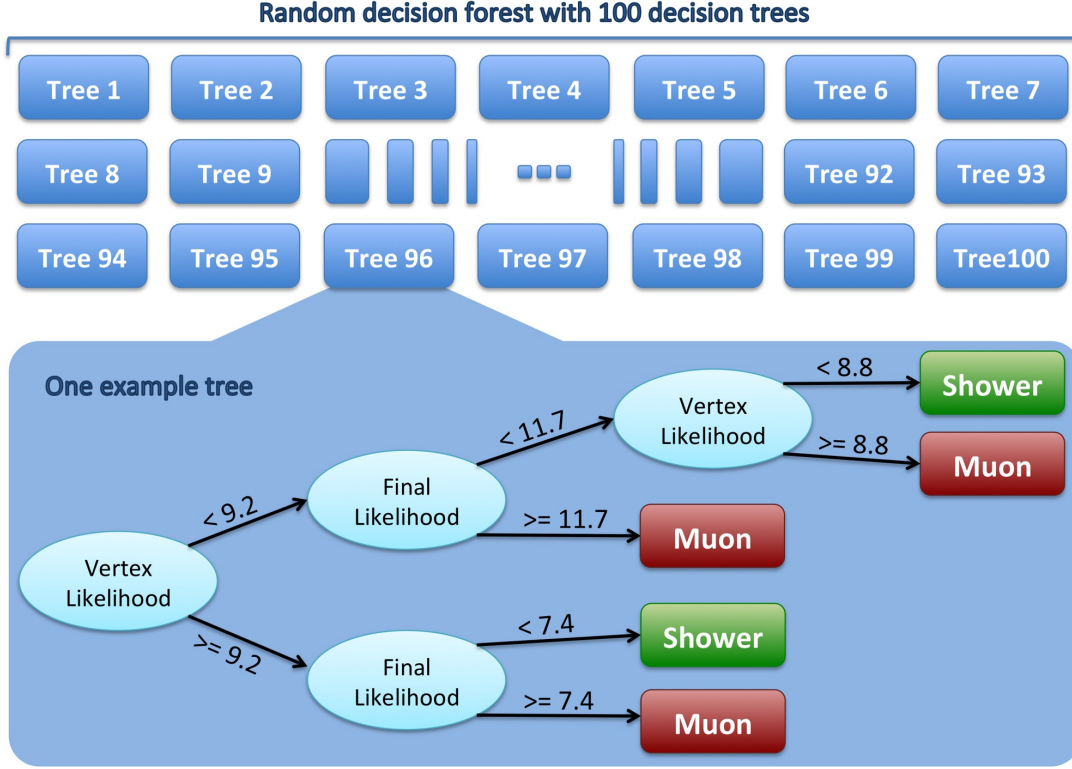
Figure 6.22: *Scheme of a muon/shower classification with a random decision forest.* From the evaluated five quality parameters in one event 100 trees decide individually whether the event is a shower or a muon event. The decision inside one tree is made by following a subsequent set of questions of either-or. The trees have been trained previously using the RBR simulations. Finally the number of trees that classified the event as a shower event can be used as single discriminating parameter to separate muon from shower events.

one individual tree. To create a variety between the single trees not only the quality parameters are varied but also the simulated events that are used for training. An extensive optimization process finally yielded the best values for those parameters to provide the optimum muon suppression rate. Table 6.2 lists the number of events that have been used for the different detector configurations.

Table 6.2: Event numbers that have been used for the random decision forest training

Data period	Muons	Showers	Ratio	Fraction used per tree
5-line	35229	5185	6.8 : 1	2 %
10-line	55442	5337	10.4 : 1	2 %
12-line	139663	13455	10.4 : 1	0.5 %

To simplify the classification result the two output parameters *RDFSafety* and *RDF-Class* are merged to one quality parameter q. This parameter then holds the fraction of the 100 trees that classified the event as shower, which in this case can be regarded

as the probability that the classified event is a shower event.

$$q = RDFSafety \quad \text{(for } RDFClass == 1, \text{ shower)} \tag{6.14}$$

$$q = 1 - RDFSafety \quad \text{(for } RDFClass == 0, \text{ muon)} \tag{6.15}$$

Figure 6.23 shows the distribution of the modified *RDFSafety* for different simulated event types and for different fluxes. One can clearly derive from the plots the great potential of separating atmospheric muon track events from all kinds of shower events.
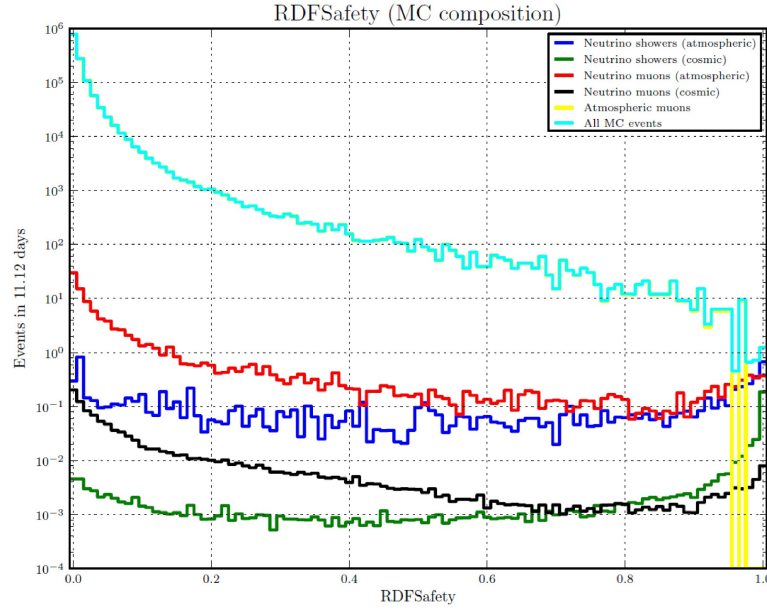
Figure 6.23: *Distributions of the modified RDFSafety for different event types.* The plot shows the modified result of the random decision forest classification according to equation (6.14) and (6.15). The distributions are drawn for shower events weighted with an atmospheric neutrino flux (dark blue) and a cosmic neutrino flux (green), for muon track events weighted with an atmospheric neutrino flux (red) and a cosmic neutrino flux (black), atmospheric muons (yellow) and all together (light blue). As atmospheric muons are the dominant contribution, their distribution (yellow) mostly equals that of the sum (light blue), hence, the yellow line mostly is hidden behind the light blue one. For the cosmic neutrino flux an E^{-2} spectrum was assumed with a normalization of $4.5 \cdot 10^{-8} \, \text{GeV/cm}^2 \cdot \text{sr} \cdot \text{s}$ per neutrino flavour. The atmospheric flux contains conventional (Bartol [9]) and prompt (Enberg [10]) neutrinos. The plot has been generated from 50% of all RBR runs for 2010 with a run number ending with 0. The limitation was due to computing memory reasons. All other periods show a similar behaviour.

When using just the classified event type *RDFClass* as discriminator between showers and muons one gains a reduction of atmospheric muons by $2.5 - 3.0$ orders of magnitude, at the cost of loosing about 15% of shower events from the high energy simulations and about 50% in the low energy simulations (see chapter 5.2). When also taking the *RDFSafety* value into account this classification is able to reduce the atmospheric muon background by 6 orders of magnitude, which let survive just one atmospheric muon event in the remaining 75% of the 0-ending runs of the RBR simulation. However, it should be stressed again, that the RDF classification is not used in

this analysis to avoid problems that are further described in chapter 7.1.

Some technical information about how to build a new random decision forest for muon/shower separation and how to apply it to the analysis chain is given in appendix B.4.

6.5   Reconstruction efficiency and effective area

This section gives and overview of the efficiency of the complete Dusj reconstruction strategy. All presented plots have been created using the Dusj reconstruction in the same configuration that was used for this analysis and that is printed in detail in appendix B.6.

Figure 6.24 shows the shower event reconstruction efficiency of the Dusj chain as function of the Monte-Carlo shower energy directly after the reconstruction and with an upper quality cut on the reduced vertex log-likelihood at a value of 7.9 applied. The choice of the cut is further explained in chapter 7.1.
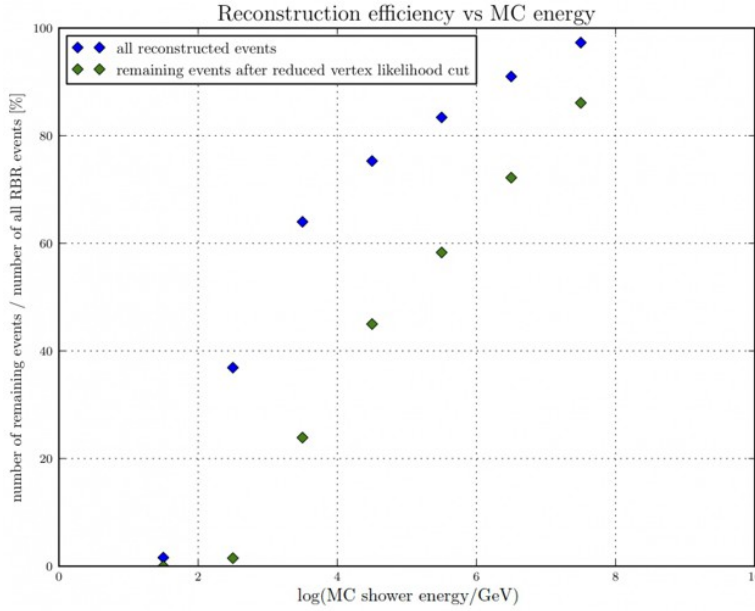
Figure 6.24: *Shower event reconstruction efficiency of full Dusj chain.* For each decade in the logarithmic shower energy the figure shows the fraction of successfully reconstructed shower events (i.e. that have a good fit status) with respect to all shower events in RBR, once right after the Dusj reconstruction (blue) and once after an upper cut on the reduced vertex log-likelihood at 7.9 to suppress atmospheric muons (see chapter 7.1) (green). The most restrictive event filter in the reconstruction is the minimum constraints filter that discards single line events and those where less than 5 hits have been identified by the hit selection. An event that passes this filter will be reconstructed with a good fit status with a very high probability. However, note that later in the course of the analysis also 2-line events will be removed. The plot has been generated from all RBR runs with a run number ending with 0.

Another measure for the efficiency of a reconstruction in combination with the detector response (which is not included in the efficiency plot above as the reference sample in that case was all detected RBR shower events) is the **effective area**. A neutrino with an energy E that moves towards the detector sees the geometrical profile of the instrumented volume that changes with the neutrino zenith angle Θ. However, due to the small cross-section the neutrino most likely will traverse through the detector without any interaction. Hence, by correcting the geometrical profile (or the instrumented volume) by the cross-section $\sigma(E)$, the earth transmission probability $P_E(E, \Theta)$, the target nucleon density ρN_A and the effective volume V_{eff} one obtains the effective profile that the neutrino is exposed to. This effective area can be calculated as follows:

$$A_{\text{eff}}(E, \Theta) = V_{\text{eff}}(E, \Theta) \cdot \rho N_A \cdot \sigma(E) \cdot P_E(E, \Theta) \tag{6.16}$$

The effective volume V_{eff} is defined as the fraction of simulated events within a generation volume V_{gen} that survive a certain reconstruction or cut level. This is where the efficiency of the reconstruction comes into play. V_{eff} can be calculated as follows:

$$V_{\text{eff}} = \frac{N_{\text{reco,cut}}}{N_{\text{gen}}} \cdot V_{\text{gen}} \tag{6.17}$$

To obtain the number of expected events from a neutrino flux $\Phi(E, \Theta)$ within an energy interval $[E_1, E_2]$, a zenith interval $[\Theta_1, \Theta_2]$ and for a given time t the product of the effective area and the flux has to be integrated over Θ and E

$$N_{\text{events}} = 2\pi \cdot t \int_{E_1}^{E_2} \int_{\Theta_1}^{\Theta_2} \Phi(E, \Theta) \cdot A_{\text{eff}}(E, \Theta) \mathrm{d}\Theta \mathrm{d}E \tag{6.18}$$

Here it was assumed that flux and effective area have no dependency on the azimuthal direction, hence, the factor 2π is simply multiplied to the integral. For a more detailed information on the effective area calculation see [36] [115].

Figure 6.25 shows the effective area of the detector with respect to showers when reconstructed with the Dusj strategy for NC and CC events, once directly after the reconstruction and once with the reduced vertex log-likelihood cut applied.
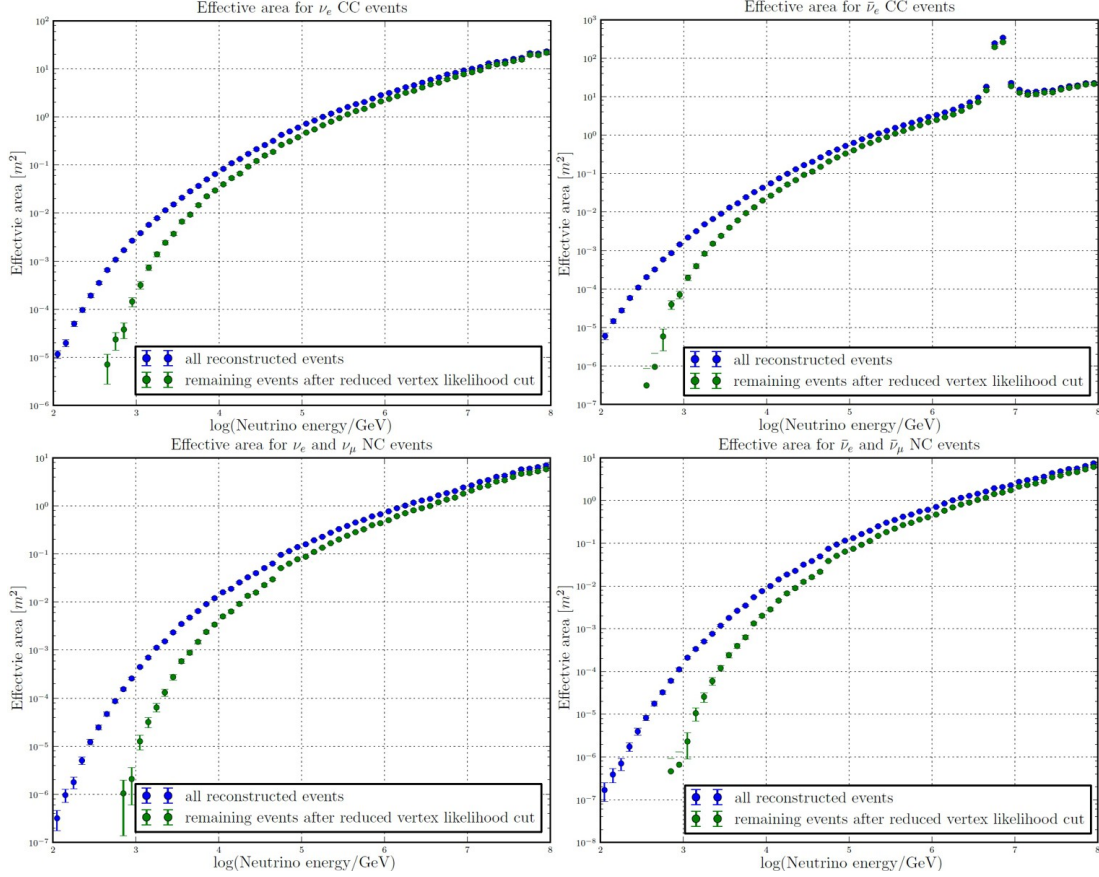
Figure 6.25: *Effective area of the Dusj shower reconstruction.* The plots show the effective area, as defined in equation (6.16), for shower events in ANTARES when reconstructed with the Dusj strategy. For CC ν_e (upper row) and NC ν_μ and ν_e (lower row) events the effective area has been evaluated as function of the neutrino energy, once for all successfully reconstructed shower events (i.e. that have a good fit status) right after the Dusj reconstruction (blue) and once after an upper cut on the reduced vertex log-likelihood at 7.9 to suppress atmospheric muons (see chapter 7.1) (green). The left column refers to events induced by neutrinos, the right column by anti-neutrinos. In the plots the integration over Θ has already been performed. The step at $\log E = 3.7$ occurs at a neutrino energy where in the Monte-Carlo the shower generation changes from a full simulation (at lower energies) to the One-Particle-Approximation (at higher energies). As in this approximation the shower is replaced by an equivalent electromagnetic shower, pure hadronic NC events are more affected by this change than CC events (see also chapter 5.1.2). The plot has been generated from all RBR runs with a run number ending with 0.

Chapter 7

Event selection

This chapter describes event filters that have been applied to the whole set of reconstructed RBR Monte-Carlo simulations and ANTARES data to filter out single events. Such event selections have been introduced to identify shower events and suppress atmospheric muons or to remove events that do not fulfil a certain quality standard.

The final choice of which filters are to be applied was made in an iterative process, where the whole analysis chain that is presented in the following chapters was repeated several times and each time was tested on 10 % of the ANTARES data (the runs with a run number ending with 0) or checked against further developments in the simulation software since RBR v2 has been released. Encountered problems in these tests made it necessary to introduce or modify the event selections and redo the analysis. Of course here, the final analysis chain is presented. Previous versions are documented for the ANTARES collaboration in internal notes [116] [117].

7.1   Atmospheric muon suppression

The first cut level that has to be applied before any kind of shower analysis can be performed is the suppression of muon track events, mainly atmospheric muons that are about 5-6 orders of magnitude more frequent than shower events induced by neutrinos. As first approach a random decision forest method was applied that is implemented as part of the Dusj reconstruction chain (see chapter 6.4). However, studies on the new Monte-Carlo simulations, where photon scattering is included for shower events (which is not the case in the currently used RBR v2), showed that this method is not stable enough against imminent changes in the simulation software that are planned for future Monte-Carlo productions. Hence, in the following a discussion of the observed problems is given, followed by an alternative approach to suppress muons that was finally used in this analysis.

7.1.1   The problem with the RDF classification

In chapter 6.4 a random decision forest muon/shower classification method was introduced as part of the Dusj reconstruction chain. This multivariate classifier has been trained from five quality parameters of the Dusj reconstruction and was intended to be used as atmospheric muon suppression within this analysis. The training as well as the determination of the final cut value has been performed using the RBR v2 simulation. After this cut about 50 % of all successfully reconstructed RBR shower events remain, averaged over all energies, when applying a cut on the modified *RDFSafety*, as defined in equation (6.14) and (6.15), at a value of 1.0, which equals to the statement that all 100 trees classified the event as shower.

In the meanwhile, however, thanks to further developments in the Monte-Carlo simulation software, a small test set of new, improved simulations of hadronic and electromagnetic showers is available. The major changes in these new simulations with respect to RBR v2 are:

- The photon propagation simulation software GEASIM has been replaced by KM3 which had been adapted to also generate light from showers (see chapter 5.1.2 for a description of the photon simulation software).

- The One-Particle-Approximation (OPA) has been improved and is now used throughout all energies.

- Photon scattering is included for the first time for showering events.

To study the impact of these changes on the efficiency and quality of the Dusj reconstruction a small test sample of run-by-run based simulations for 40 runs has been created by the ANTARES Monte-Carlo working group, using KM3 in version v4r5. It turned out that, when applying the same RDF cut to the new simulations, only about 4 % of all successfully reconstructed shower events remain, where it used to be 50 % in RBR v2. The number of successfully reconstructed events before the cut is consistent between the two simulation versions. Figure 7.1 shows the fraction of events that survive the cut as function of the true shower energy for the two different simulations.

To give a rough estimate of the impact of this issue on the following analysis the number of cut-surviving events in the high energy parts of the simulation (see chapter 5.2), starting at neutrino energies of 50 TeV has been evaluated. The low energy events have not been taken into account as, shown later in chapter 12, a lower cut on the fitted energy will be applied, so that almost the full low energy simulation parts are discarded. In the high energy simulations about 60 % of all reconstructed events survive the RDF cut in RBR v2 whereas only 5 % survive in KM3 v4r5. Thus, with the new simulation the number of expected events after the RDF cut is only 8.3 % of the expected number
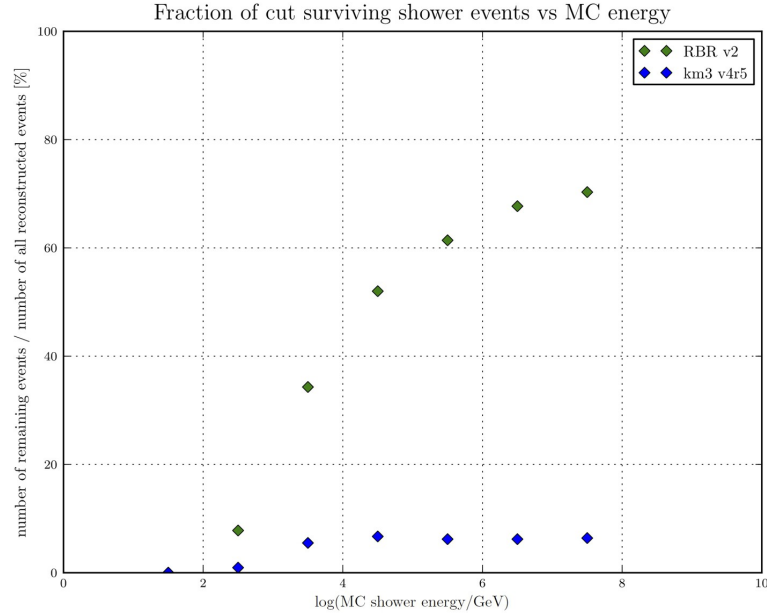
Figure 7.1: *Fraction of events that survive the deprecated RDF atmospheric muon suppression cut.* For each decade in the logarithmic shower energy the figure shows the fraction of shower events that survive the RDF atmospheric muon cut with respect to all successfully reconstructed shower events in RBR v2 (blue) and KM3 v4r5 (green). The latter one has been obtained from a run-by-run based test simulation for 40 runs.

in the RBR v2, which equals a systematic error due to uncertainties in the simulation of $-92\,\%$!

This implies the question, which one of the simulation types can be trusted? Is there a "more correct" one? And further: How do we know whether the real data behaves like one or the other simulation or even completely different?

The answer might be the following: A cut that shows such a big instability regarding small changes in the simulation should not be applied at all. The changes in the simulation, which are mainly the inclusion of photon scattering, are not extensive enough to give reason to expect such huge differences in the outcome of the analysis. Two reasons cause this difference:

First, for the training and classification with the random decision forest, five quality parameters are used, where two of them are chi-squares of time residuals, one with respect to the pre-fit and one to the final fitted vertex (see chapter 6.4). The time residual of a hit is the difference between the measured arrival time and the expected arrival time from a point-like light source without photon scattering. This value, of course, slightly changes with the inclusion of photon scattering in the Monte-Carlo as the hit arrival times are no longer matching as precisely to the point-like assumption as with unscattered photons. As a consequence the chi-square distributions change.

Although the ARS hit selection, as described in chapter 6.1.1, was introduced due to the same reason that is to remove hits from scattered late photons, also the first (direct) hits are already affected by the scattering, even if scattering shifts their arrival time just to a few nanoseconds later. In the quadratic sum of the time residuals this difference adds up and makes the chi-square value worse shifting the distribution of shower events towards the "muon region". This makes it much harder for the RDF to classify shower events correctly, especially when it was trained on Monte-Carlo without photon scattering. Figure 7.2 illustrates the distributions of one of the critical chi-square parameters for the new and the old simulation.
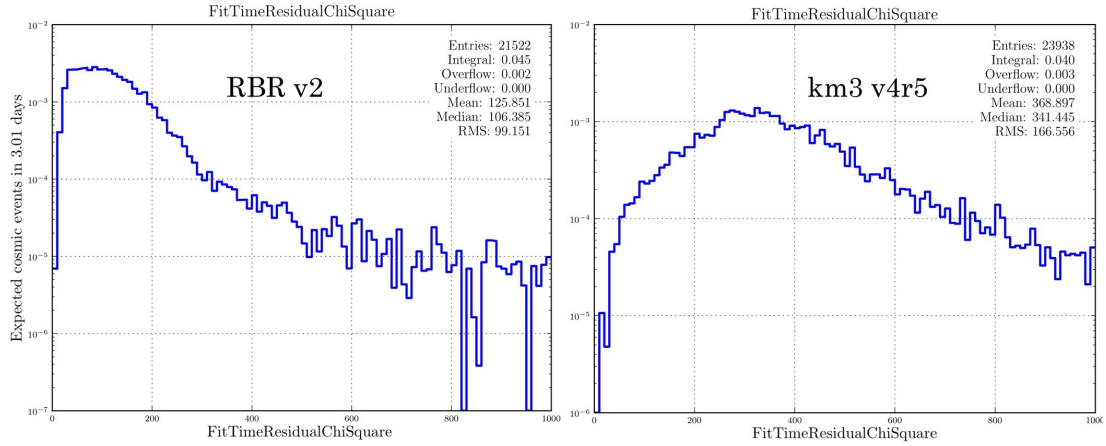
Figure 7.2: *Time residual chi-square distribution for RBR v2 and KM3 v4r5.* The plots show the distribution of the time residual chi-square (equation (6.13)), one of the five quality parameters that have been used for the RDF training, for ν_μ and ν_e shower events following a cosmic E^{-2} spectrum, once for the RBR v2 Monte-Carlo (left) and once for the new KM3 v4r5 simulations (right). The plots have been generated from a small run-by-run based test simulation for 40 runs with KM3 v4r5 and the corresponding RBR v2, where in both cases the high energy parts (see chapter 5.2) have been used.

At this point it should be stressed that the ARS hit selection (the selection of the first, direct hits) was introduced to preserve the reconstruction quality that is obtained from un-scattered Monte-Carlo. Here, the removal of the scattered hits ensures that the reconstruction quality itself does not significantly get worse. What is affected here is only the quality parameters containing time residual chi-squares.

A second issue is the following: To suppress as much of the atmospheric muon background as possible the RDF cut was applied at a value of $RDFSafety = 1.0$, which is the ultimate possible cut when all 100 trees in the forest agree that the event is a shower. As shown in chapter 6.4, the classification was optimized by varying the number of events that were used for the training, the muon/shower ratio and the fraction of events per tree until the best suppression level was reached. However, a random decision forest that has been optimized to the extremes and that is used for a cut at the ultimate upper end will probably always have difficulties when suddenly being fed with events where small changes are included and where the hit patterns in the classified events do not match exactly those that have been used for the training.

Thus, it is questionable in principle, whether a multivariate analysis should be used in regions where the parameter distributions show steep slopes or where it is incalculable how small changes in the simulation effect the classification.

Hence, in order to prevent an over-optimization of the RDF towards features that do not have an origin in physics but in some artefacts that might occur due to different implementations in the simulation software, it was chosen not to use a multivariate tool any longer but to apply a hard cut on one of the Dusj quality parameters as discriminator between muon and shower like events, as will be explained in the following.

7.1.2 The cut on the reduced vertex log-likelihood

To replace the random decision forest cut by an alternative muon suppression cut, the Dusj quality parameters, as introduced in chapter 6.3, have been studied. The choice of the appropriate cut parameter and the value where the cut is applied was aimed at finding the optimum balance between the two following requirements:

- Do not loose too many shower events and simultaneously don't let pass too many atmospheric muons, i.e. keep the signal to background ratio high.

- Keep the differences between the new and the old Monte-Carlo as small as possible, that means make the strategy more stable against changes in the simulations.

The parameter that fulfils both conditions is the *final reduced log-likelihood value of the vertex fit* (VLLH) that has already been used as one of the five quality parameters for the RDF classification before (see chapter 6.4). As shown in figure 7.3 the agreement between RBR v2 and KM3 v4r5 is much higher in this parameter than for the chi-square (figure 7.2) as here no time residuals are involved. The value of the reduced vertex log-likelihood is a measure how well the fit result matches the assumption of a point-like light source without photon scattering.

Further, the parameter has the potential to separate shower from muon events (as shown in figure 6.21) and yields a good agreement also with experimental data (figure 9.4). For the discrimination between shower and muon events this parameter is more suitable than, for example, the reduced log-likelihood value of the energy and direction fit as the arrival time of hits from a muon track shows a greater discrepancy from a point-like light source assumption (used for the vertex fit) as the discrepancy of the angular light distribution or the charge deposition (used in the energy and direction fit) is between muon and shower events.

One could also think about training a new RDF without the two quality parameters that are based on time residuals. However, among the three remaining parameters
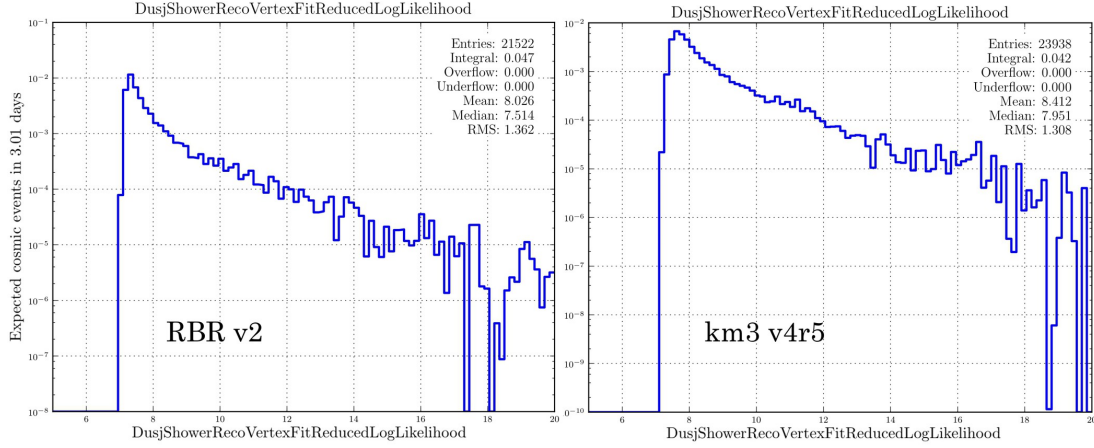
Figure 7.3: *Reduced log-likelihood distribution of the vertex fit for RBR v2 and KM3 v4r5.* The plots show the distribution of the final reduced log-likelihood value of the vertex fit, for ν_μ and ν_e shower events following a cosmic E^{-2} spectrum, once for the RBR v2 Monte-Carlo (left) and once for the new KM3 v4r5 simulations (right). The plots have been generated from a small run-by-run based test simulation for 40 runs with KM3 v4r5 and the corresponding RBR v2, where in both cases the high energy parts (see chapter 5.2) have been used.

that are quite stable against changes in the simulation, it is the reduced vertex log-likelihood that has the biggest potential to separate showers from muons, whereas the other two (the reduced energy-direction log-likelihood and the quadrupole moment) have less capability of separating the events. Thus, one cannot expect much gain from such a new forest compared to a single cut on the most capable parameter that is the reduced vertex log-likelihood.

To determine the final cut value that yields the optimum balance between a good shower event selection efficiency and stability against changes in the simulation, for four different upper cut values of the reduced vertex log-likelihood from 7.7 to 8.0, with a step width of 0.1, the fraction of cut-surviving shower events has been evaluated for both simulations from the high-energy samples (see chapter 5.2). Here, the shower event selection efficiency is defined as the number of shower events that survive the cut divided by the number of all successfully reconstructed shower events. In addition the number of remaining atmospheric muons has been evaluated, where the muon selection efficiency is evaluated in the same manner as the efficiency for showers.

Table 7.1 lists the results of this study. The last column in the table holds the scaling factor s that is the ratio of the efficiencies for KM3 v4r5 over RBR v2. From N expected shower events in RBR v2 after the cut only $s \cdot N$ events could be expected from KM3 v4r5. This scaling factor has been determined from the high energy simulations of the small 40-runs test sample as the low energy simulations will be discarded later during the analysis (see chapter 12). For comparison also the deprecated RDF cut has been listed once more.

Table 7.1: Differences in the shower and muon event selection efficiency between RBR v2 and KM3 simulations for various upper cuts on the reduced vertex log-likelihood

Applied cut	Remaining atmospheric muons per day	Atmospheric muon selection efficiency in RBR v2 [%]	Shower selection efficiency in RBR v2 [%]	Shower selection efficiency in KM3 v4r5 [%]	Shower scaling factor KM3/ RBRv2
RDFSafety = 1.0	0.17	$1.6 \cdot 10^{-4}$	60	5	0.083
VLLH < 7.7	0.08	$7.7 \cdot 10^{-5}$	62	29	0.47
VLLH < 7.8	0.33	$3.2 \cdot 10^{-4}$	66	38	0.57
VLLH < 7.9	1.23	$1.2 \cdot 10^{-3}$	70	48	0.69
VLLH < 8.0	3.68	$3.6 \cdot 10^{-3}$	72	56	0.78

What can be derived from the table is that with a looser cut on the reduced vertex log-likelihood (towards higher values) the agreement between RBR v2 and KM3 v4r5 improves, resulting in a better scaling factor towards 1.0. This behaviour is expected as for a looser cut more events are allowed to pass that do not completely match the assumption of a point-like light source without photon scattering. The tightest cut at 7.7 only lets pass events with a very good agreement to the point-like assumption, of which in case of KM3, where photon scattering is included, less events exist. Thus, the difference between the simulations gets larger with a more tight cut on the reduced vertex log-likelihood.

On the other hand a more tight cut on the reduced vertex log-likelihood provides a data set with a better signal to background ratio as in this case more atmospheric muons are suppressed. For a looser cut on the reduced vertex log-likelihood more atmospheric muons still contaminate the sample that have to be filtered out later by other procedures.

As a compromise between the two competing aims a final cut at a value of 7.9 was chosen for the reduced vertex log-likelihood. The scaling factor of 0.69 will be taken into account as systematic error of $^{+0}_{-31}$ % that will be applied to the number of shower events (see chapter 11). With this systematic error included, it is possible to use the number of atmospheric and cosmic shower events that still have been obtained from the RBR v2 simulation.

A welcome side-effect of this cut is that it simultaneously acts as an atmospheric *neutrino* suppression. From figure 7.4 can be derived that the distribution of the reduced vertex log-likelihood changes with the shower energy, where low energy events typically have a higher value. The atmospheric neutrino flux in general is located at lower energies compared to the cosmic E^{-2} flux. Hence, as the majority of atmospheric neutrino events after the reconstruction has an energy between $100 \, \text{GeV}$ and $1 \, \text{TeV}$

they will be stronger suppressed compared to the cosmic neutrino events for which the majority of events is located between $1\,\mathrm{TeV}$ and $1\,\mathrm{PeV}$.
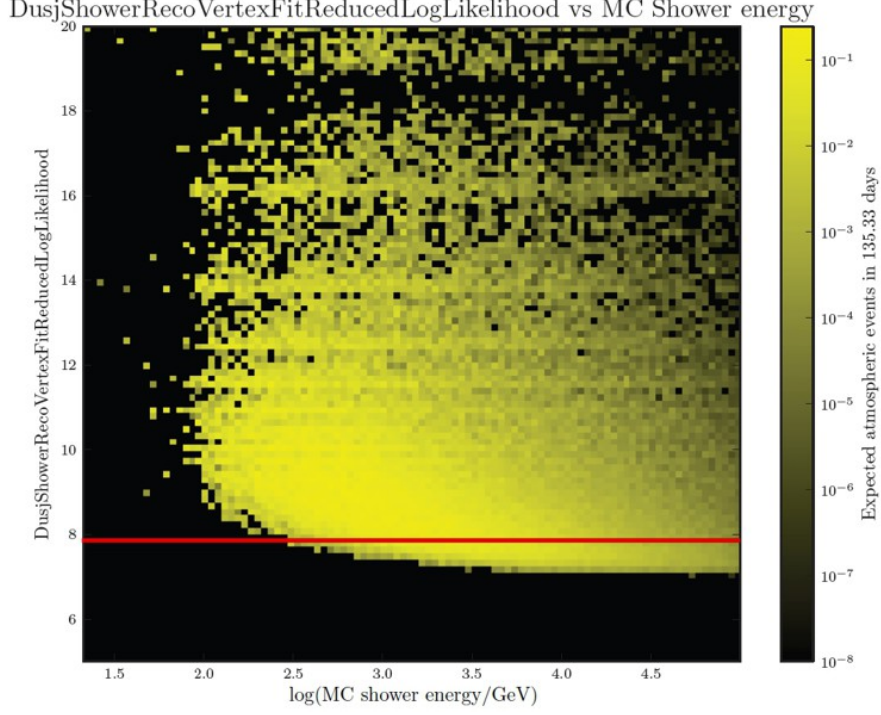
Figure 7.4: *Reduced log-likelihood distribution of the vertex fit as function of the shower energy.* The plot shows the distribution of the final reduced log-likelihood value of the vertex fit as function of the Monte-Carlo shower energy, for ν_μ and ν_e shower events following an atmospheric neutrino spectrum. The red line marks the cut at 7.9 that is applied as muon suppression in this analysis. The plots have been generated from all NC/CC shower events of the RBR runs with a run number ending with 0.

It should be further mentioned that a cut on the reduced vertex log-likelihood must not only be regarded as a muon suppression cut, but simultaneously serves as quality cut that removes badly reconstructed shower events. As it is a measure for how good the fit result matches the assumption of a point-like light source, also shower events that do not fully match this assumption, typically due to bad calibrations or contamination of optical background hits, will be removed by this cut to a certain extent. The reconstruction quality of the Dusj reconstruction after the reduced vertex log-likelihood cut is given in figure 6.12 for the vertex position, in figure 6.13 for the interaction time, in figure 6.18 for the neutrino direction and in figure 6.19 for the shower energy.

7.2   Further quality cuts

Once the majority of atmospheric muons has been suppressed, one could in principle start with an analysis of neutrino events. However, in the course of this work, it turned out that further data quality cuts are to be applied. Whereas later in chapter 8.4

complete ANTARES runs will be classified according to their data quality and some of them will be removed, here just single events are discarded. The selection criteria emerged from the study of 10 % of the ANTARES data (the runs with a run number ending with 0) and are described in the following.

7.2.1 Multi line filter

By default the Dusj reconstruction performs for each event a fit of the seven shower parameters where the precedent hit selection found at least 5 hits on at least two lines, which is an adequate choice for the determination of the shower vertex and energy. However, concerning the direction reconstruction, a two-line event causes an ambiguity in the likelihood function where a second minimum might occur, the so-called mirror solution. Figure 7.5 illustrates such an event.
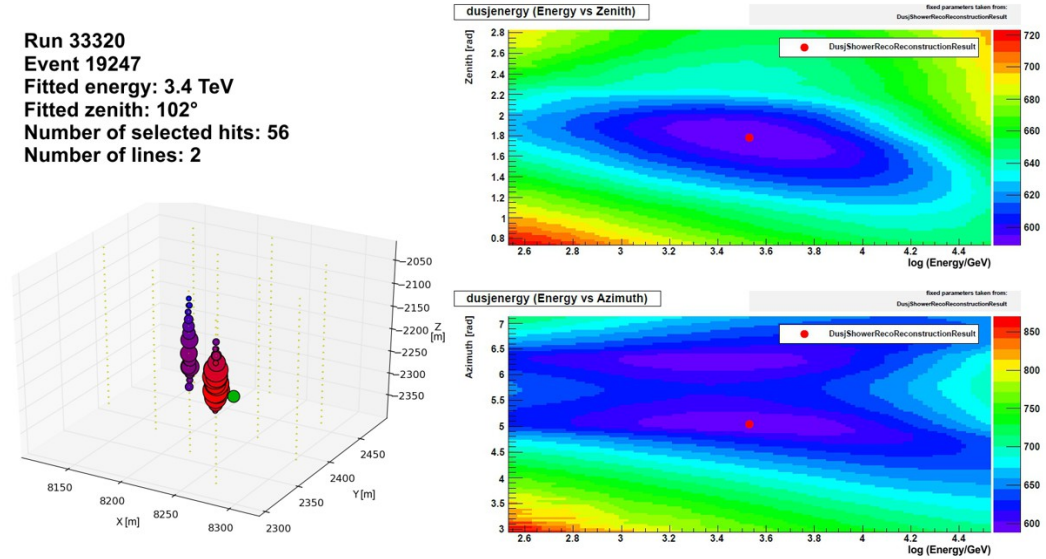
Figure 7.5: *Event topology of a reconstructed ANTARES two-line event.* The plots illustrate the topology of an ANTARES event that has been reconstructed as shower based on a hit sample that is distributed on just two lines. The left figure shows a sketch of the hit pattern in the detector. Each circle marks a selected hit where the size illustrates the charge and the color the arrival time from early (red) to late (blue). The green circle marks the reconstructed vertex position. The image has been created using a script from [118]. The plots on the right side illustrate the corresponding log-likelihood function as evaluated by the **I3DusjShowerEnergyDirectionPDF** service (see chapter 6.2.2). Here the red points mark the fit result for energy, zenith and direction. One can clearly see the two equiprobable solutions in the azimuthal direction.

As the ANTARES lines are arranged parallel and orientated vertically, a hit pattern that is located on just two lines has a shape that is almost a plane. In the given example the vertex is reconstructed approximately in the same plane as one string holds all the early hits. In this case for the reconstruction of the direction (where the vertex is kept fixed) two equiprobable solutions exist that are inclined by the Cherenkov angle (42°)

against the plane, on both sides respectively. For both possible directions the fit finds an excess of hits in the Cherenkov direction. Hence, it must be assumed that for such events the fit routine chooses the wrong minimum and thus the wrong direction in up to 50 % of all cases, depending how plane the hit distribution really is. This effect is expressed in a small fraction of events that have a reconstructed direction that is about 80° away from the truth, as can be clearly seen in figure 6.18.

Due to the vertical orientation of the ANTARES strings it is mostly the azimuthal direction that is affected by the mirror solution, however, an effect on the zenith angle cannot be completely excluded. As in this analysis the fitted zenith plays an important role as cut parameter in the following sensitivity optimization (see chapter 12), events, where the hit selection found hits on less than 3 lines, are removed. This filter diminishes the number of expected cosmic events by just about 5 %, as the majority of two-line events is already removed by the previous cut on the reduced vertex log-likelihood.

7.2.2 Sparking event filter

The study of the measured ANTARES events in runs with a run number ending with 0 that survive the muon suppression cut (the reduced vertex log-likelihood cut) revealed a not negligible amount of events for which the vertex position has been fitted close to the position of an OM (within the reconstruction errors). Such events are suspected to be *sparking events*.

The high voltage inside the PMTs sometimes create a spark-over that is expressed as a bright flash inside the OM. This means that the device that actually should detect photons from showers that are regarded as point-like light source suddenly itself turns into a point-like light source. Such sparking events have not been simulated in the RBR Monte-Carlo. Although this phenomenon is quite rare, it has to be taken into account in shower analyses as such sparks imitate real shower events and survive, due to its perfect point-like pattern, even the strongest muon suppression cut. A study on the mentioned 10 % of the ANTARES data, where 213 events survive the reduced vertex log-likelihood cut, showed that 6 of them are strong sparking candidates. These events are illustrated in figure 7.6.
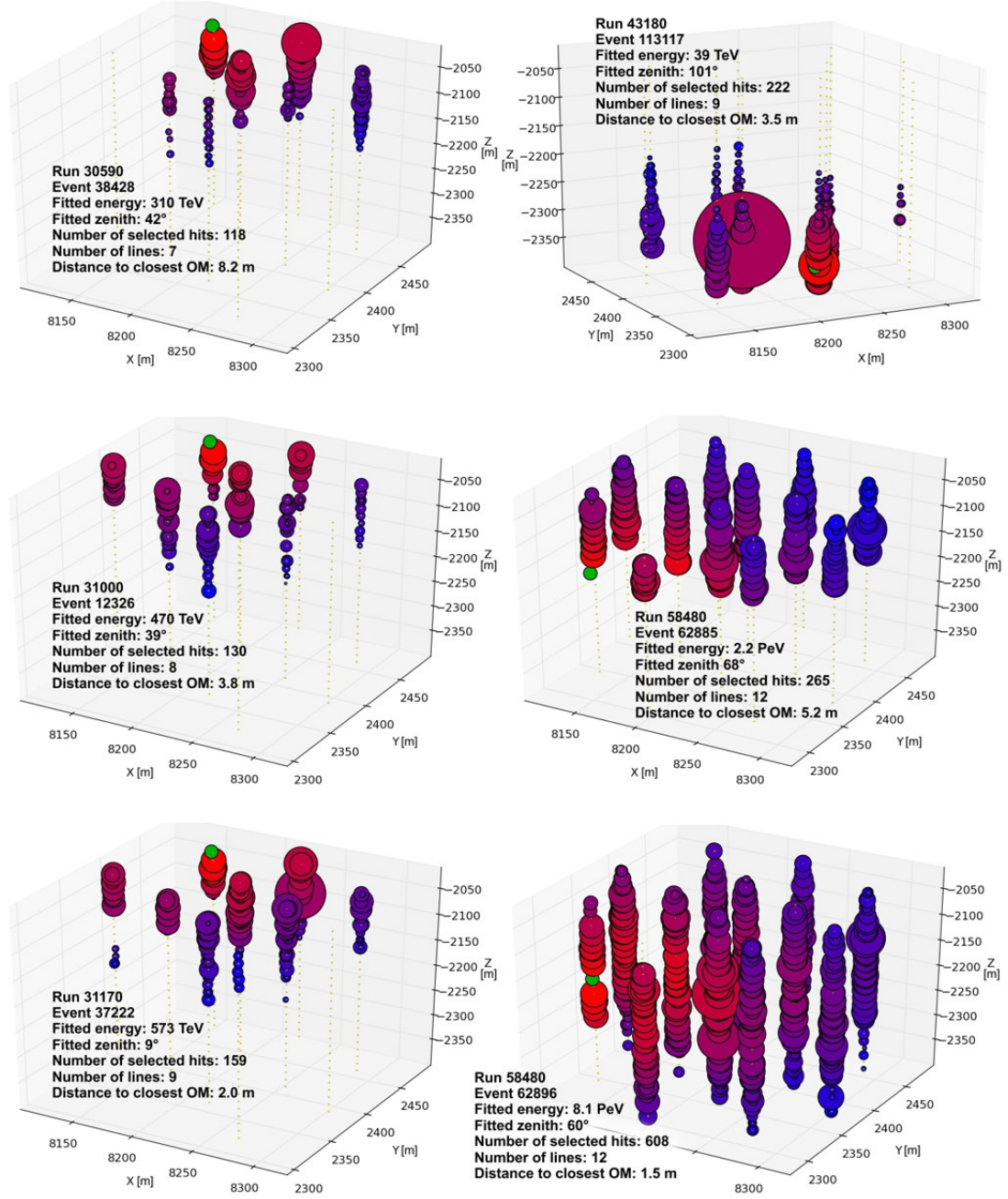
Figure 7.6: *Suspected sparking events after the reduced vertex log-likelihood cut.* The plots illustrate the topologies of 6 reconstructed ANTARES events that are suspected to be sparking events. From 213 events in 10 % of the data (runs with a run number ending with 0) that survive the reduced vertex log-likelihood cut these six have a vertex position that is close to an OM. For each of the events the hit pattern in the detector is given. Each circle marks a selected hit where the size illustrates the charge and the color the arrival time from early (red) to late (blue). The green circle marks the reconstructed vertex position. Images have been created using a script from [118]. The three events in the left column have been recorded in three different runs from December 2007 to January 2008 and seem to have the same sparking origin. The two lower right events are very high energy sparks that occurred within 1 second. The reason why in one only the upper part of the detector has indicated hits is an artefact of the hit selection. In this particular case hits from the lower half of the detector did not pass the time residual criterion to be selected (see chapter 6.1.2), but of course the lower half detected hits, too.

A shown later in chapter 8.2 there is a small number of ANTARES runs that have a high rate of sparking events, so that for these cases the complete run has to be excluded from the analysis as its contamination by false point-like shower imitating events is too high. The here presented filter has been introduced to be sure that also in seemingly "healthy" runs rare occurrences of sparks are removed. From the study of the confirmed sparking runs, however, one can learn how to do so, as will be explained in the following.

Figure 7.7 shows the distance of the fitted vertex to the closest OM, once for sparking runs and once for normal runs, from all events that have been reconstructed as up-going. One can see that the excess of very closely fitted vertices accumulates at distances up to $10 - 15$ m from the OM, which reflects the mean vertex reconstruction error of about 10 m at high energies (see figure 6.12). Note that the cited reconstruction quality is valid for a data set after the reduced vertex log-likelihood cut at a value of 7.9. However, in this figure a looser cut at 10.0 was applied to increase statistics.
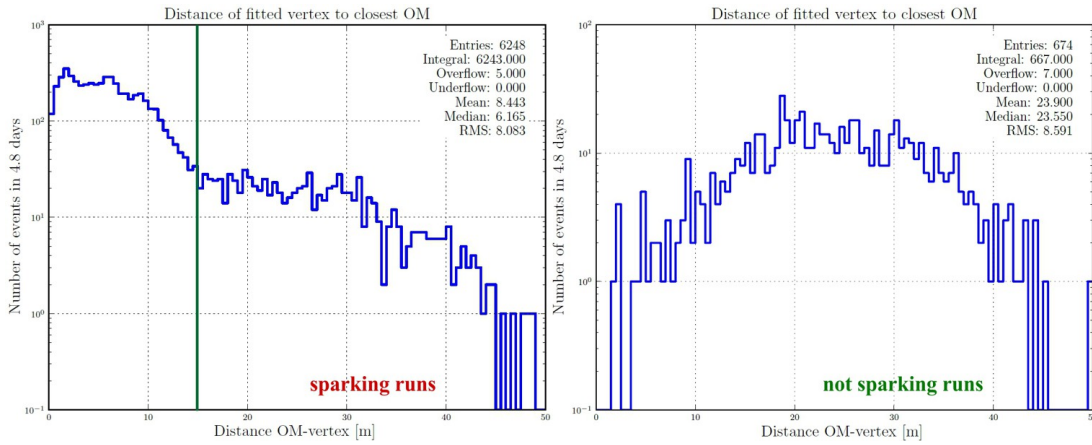
Figure 7.7: *Distance of the fitted vertex to the closest OM in sparking runs.* The plots show the distribution of the event-wise distance between the fitted vertex and the closest OM in 48 confirmed and suspected sparking ANTARES runs (left)(see chapter 8.2) and normal ANTARES runs with a corresponding life time (right). The plots have been created from all as up-going reconstructed events that survived an upper cut on the reduced vertex log-likelihood at a value of 10.0. Here, the cut is less restrictive compared to the usual cut at 7.9 to increase statistics. The green line marks the cut that will be applied as sparking event filter for this analysis.

What can be derived from this study is that removing all events where the vertex is fitted closer than 15 m to any of the OMs should safely remove all sparking events. This filter will diminish the number of expected cosmic signal events by another 8% with respect to events that survived the reduced vertex log-likelihood and the multi line filters, but is essential to ensure that the final sample of events, from which the upper limit is evaluated later on, is not contaminated by sparking events.

Chapter 8

Data quality and run selection

During the development phase of the Dusj reconstruction project all studies and optimizations have been performed on Monte-Carlo simulations with a constant white noise up to 150 kHz per OM as background. The main challenge to handle a hit sample with high background rates is a task for the hit selection as at this point a hit sample, as pure as possible, has to be selected and passed to the further shower parameter reconstruction. In intermediate quality tests this hit selection always has proven to provide a very pure hit sample within the whole tested background rate range up to 150 kHz.

With the introduction of a run-by-run based simulation, however, the question arises how stable the reconstruction is with different data taking conditions. In the RBR simulations the constant white noise has been replaced by the OM-wise background rates that have been prevailed during the data taking of the corresponding data run. A more detailed description of the RBR simulation is given in chapter 5.

This section introduces some checks that have been performed on the RBR simulations to figure out, whether there are runs that have to be excluded from the analysis. The selection criteria for the run selection were

- A good reconstruction quality in the RBR simulation.

- A good agreement of data and simulation in the reconstruction result.

- No technical problems must have occurred.

8.1 The data quality parameter

The data quality parameter *QualityBasic (QB)* was introduced by the ANTARES data quality working group to join the data taking condition parameters, such as background rate or number of working OMs, etc., into one parameter in order to classify the quality

of an ANTARES data run based on a single parameter. Its definition follows a ranking from 0 (worst condition) up to 4 (best condition). A detailed description is given in [119] and is summarized in table 8.1.

Table 8.1: Run classification using the data quality parameter QB

QB value	Data taking condition
4	Noise rate (base line) $\leq 120\,\mathrm{kHz}$, burst fraction $\leq 20\,\%$ and $80\,\%$ of all OMs are working
3	Noise rate (base line) $\leq 120\,\mathrm{kHz}$, burst fraction $> 20\,\%$ but $\leq 40\,\%$ and $80\,\%$ of all OMs are working
2	Noise rate (base line) $> 120\,\mathrm{kHz}$ or burst fraction $> 40\,\%$ but still $80\,\%$ of all OMs are working
1	Noise rate (base line) $> 120\,\mathrm{kHz}$ or burst fraction $> 40\,\%$ or less than $80\,\%$ of all OMs are working
0	Run duration is $\leq 1000\,\mathrm{s}$, muon rate $\geq 100\,\mathrm{Hz}$, absolute timing errors, or other problems. It is suggested to exclude these runs from an analysis.

The parameters *base line rate* and *burst fraction* are further explained in chapter 4.1.

To evaluate how a run selection based on the QB parameter affects the Dusj shower reconstruction, separate performance checks and comparisons of simulation and data have been done on all runs with a run number ending with 0 that share one value of the QB parameter. From these performance histograms again the mean, median, root-mean-square and the quantiles have been extracted. The figures 8.1 and 8.2 show the tendency of these variables with the quality basic parameter for the fitted energy and direction, as well as the tendency of their Monte-Carlo data ratio. Figure 8.3 illustrates the Monte-Carlo data ratio concerning the reduced vertex log-likelihood and figure 8.4 the ratio of reconstructed events in Monte-Carlo and data as function of the QB parameter.

What one can derive from the plots is that the Dusj reconstruction is able to handle all kinds of runs, no matter what their quality basic classification is. There is no significant drop in the performance when going to lower QB values. Also the ratio of Monte-Carlo and data shows a stable behaviour for any value of the quality basic parameter, in the fit results as well as in the number of reconstructed events.

Thus, the conclusion would be that it is not necessary to exclude runs on the basis of the QB value regarding the reconstruction quality. However, where QB values from 1 to 4 really classify the environmental and detector conditions during the data taking, $QB = 0$ is also used to indicate potential technical problems. Hence, for this analysis only runs with a $QB > 0$ have been used. Runs that have been removed by this criterion are listed in appendix D.2.
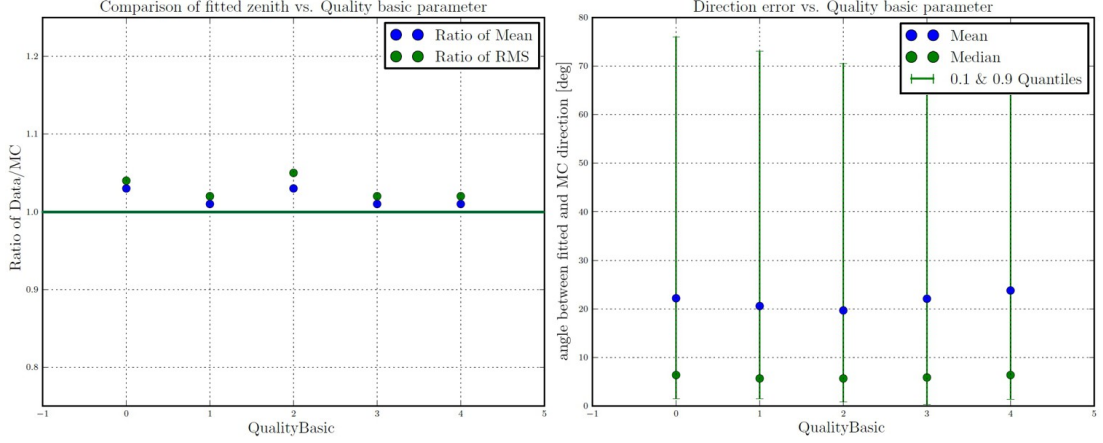
Figure 8.1: *Performance and Monte-Carlo data comparison of the direction reconstruction as function of the quality basic parameter.* The right plot shows the reconstruction quality of the direction fit. Therefore, for each value of the QB parameter a separate distribution of the event-wise angle between the fitted and the true neutrino direction has been drawn, where from the mean, median, root-mean-square and the quantiles have been calculated. The plot shows the quality for shower events with an energy of 10 TeV after an upper cut on the reduced vertex log-likelihood at 7.9. Note that the error bars in the plot show the 10 % and 90 % quantiles of the distribution, not the error of the mean/median. The left plot shows the Data-MC ratio of the mean and root-mean-square of the fitted zenith as function of the QB parameter for all events that passed the Dusj reconstruction. The simulated events at this stage, of course, are dominated by atmospheric muons. The plots have been generated from all RBR runs with a run number ending with 0.
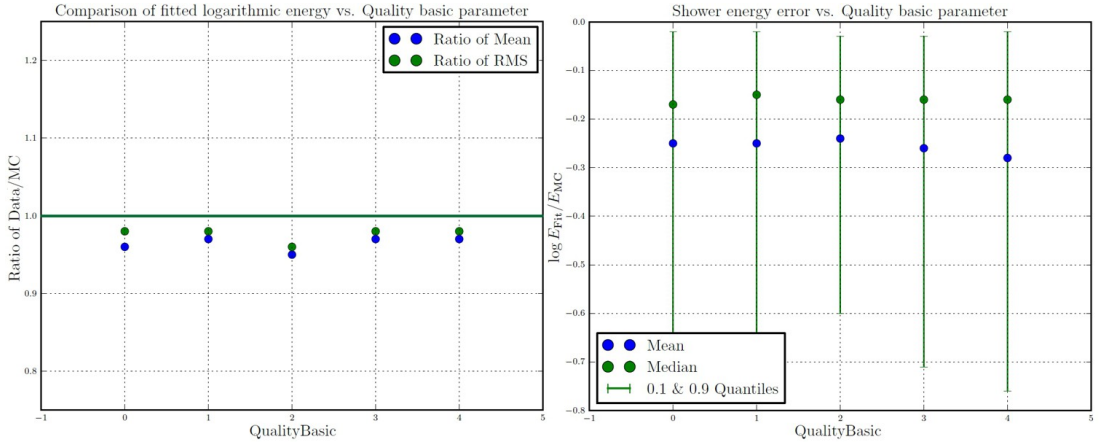
Figure 8.2: *Performance and Monte-Carlo data comparison of the energy reconstruction as function of the quality basic parameter.* The right plot shows the reconstruction quality of the energy fit. Therefore, for each value of the QB parameter a separate distribution of the event-wise logarithmic difference between the fitted and the true shower energy has been drawn, where from the mean, median, root-mean-square and the quantiles have been calculated. The plot shows the quality for shower events with an energy of 10 TeV after an upper cut on the reduced vertex log-likelihood at 7.9. Note that the error bars in the plot show the 10 % and 90 % quantiles of the distribution, not the error of the mean/median. The left plot shows the Data-MC ratio of the mean and root-mean-square of the logarithmic fitted shower energy as function of the QB parameter for all events that passed the Dusj reconstruction. The simulated events at this stage, of course, are dominated by atmospheric muons. The plots have been generated from all RBR runs with a run number ending with 0.
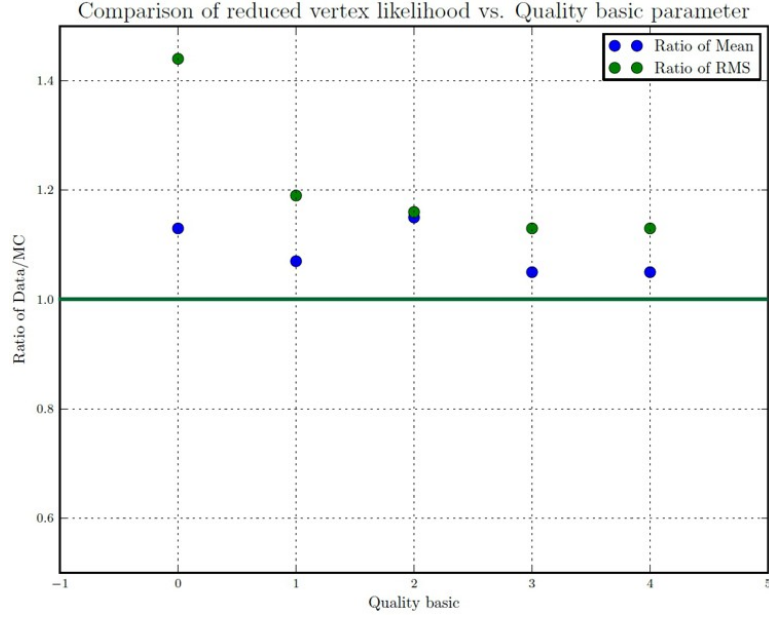
Figure 8.3: *Monte-Carlo data comparison of the reduced vertex likelihood as function of the quality basic parameter.* The plot shows the Data-MC ratio of the mean and root-mean-square of the reduced vertex log-likelihood as function of the QB parameter. Therefore, for each value of the quality basic parameter a separate distribution has been drawn from all events that pass the Dusj reconstruction. The simulated events at this stage, of course, are dominated by atmospheric muons. The plots have been generated from all RBR runs with a run number ending with 0.
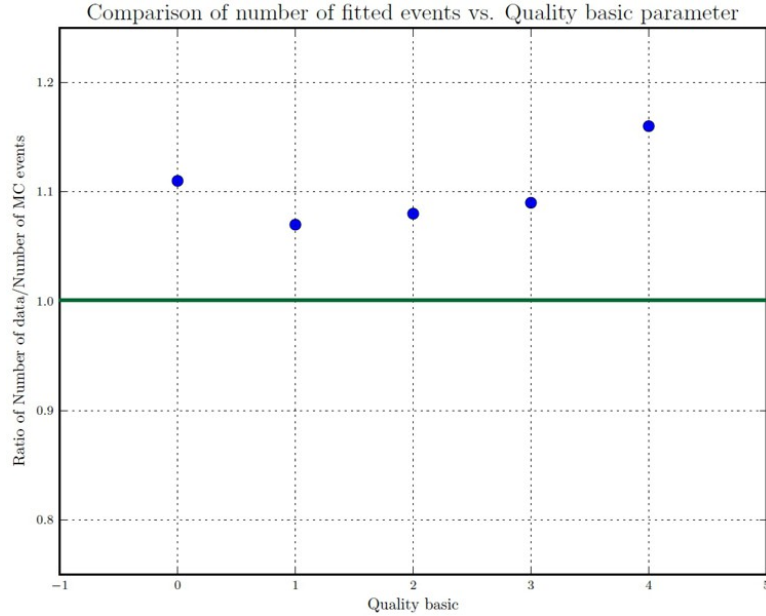
Figure 8.4: *Ratio of the number of reconstructed data and Monte-Carlo events as function of the quality basic parameter.* The plot shows the ratio of successfully reconstructed data and Monte-Carlo events as function of the QB parameter. The simulated events at this stage, of course, are dominated by atmospheric muons. The plots have been generated from all RBR runs with a run number ending with 0.

8.2   Sparking runs

Runs in which sparking events that have been introduced in chapter 7.2.2 are recorded with a constantly high rate are called sparking runs. Whereas the previously introduced sparking event filter is intended to remove single rare sparking events in runs that usually behave normally, in sparking runs an affected OM sparks permanently causing a high contamination of false point-like events. Up to June 2013 the ANTARES data quality working group declared 59 runs to be confirmed or suspected sparking runs that are not used for this analysis. The run numbers of these runs are printed in appendix D.2.

8.3   Excluded run setups

Also for quality reasons further runs have to be excluded that have been taken with a preliminary or test detector configuration. In regular intervals the operation settings, such as the high voltage of the OMs, calibration procedures, etc., have been updated and tested with preliminary run setups that may produce not completely reliable data as the setup might be not completely optimized yet. Hence, the following runs have not been used for this analysis:

- Runs that have been marked as *PRELIM*. They have been taken with preliminary settings after some setup parameters were changed.

- Runs that have been marked as *SCAN*. They have been taken with intermediate settings during the optimization processes and have been recorded for monitoring purposes.

A list of such runs is given in appendix D.2.

8.4   Final run selection

The development of the Dusj shower reconstruction and the following analysis has been performed without using the recorded ANTARES data in order to avoid a bias of the analysis towards an expectation from the data. Nevertheless, a consistency check between the simulation and real data was performed at various stages of the analysis, but this check was always based on just 10 % of the real data, leaving the rest untouched. The runs that have been used were those with a run number ending with 0. These runs have been *burned* and cannot be taken into account for the evaluation of the final upper limit. In the following this 10 % test sample is referred to as *burn sample*, where the remaining runs are denoted as *full sample*.

The selection of runs for the analysis of the burn sample and the full run sample was chosen according to the availability of RBR simulations. Therefore, a list of runs, for which a RBR v2 simulation was available on the Lyon mass storage system [84] on June, 19th 2013, was created. However, some missing input files of the RBR, incomplete data sets or corrupt files in the corresponding official data productions *prod_2012-04* (for 2007-2011) and *prod_2013-02* (for 2012) made it inevitable to exclude further runs as whenever a part of the simulation or data is missing for one run, an analysis cannot be performed on it. The data productions have been created, just like the RBR simulations, to be used by the whole collaboration to ensure that all analyses are based on the same correctly calibrated data. These productions have been created by the ANTARES analysis tools working group.

For some rare runs the sample of the MUPAGE atmospheric muon simulation does not contain any event after the reconstruction step, even before the atmospheric muon suppression is applied. As for these runs obviously a problem occurred, they are removed as well.

Table 8.2 lists the number of runs that have been selected or excluded for the burn sample and the full sample. The negative numbers in brackets indicate the subsequent reduction of runs compared to the set in the corresponding line above. That does not necessarily mean that for example the full sample contains just 347 QB=0 runs as there is of course an overlap of QB=0 and SCAN runs and some of them might be already removed by the SCAN run criterion. A detailed, full list of all selected and excluded runs can be found in the appendix D.

Table 8.2: Selection of runs for the analysis

Run sample	Full sample	Burn sample
All available RBR v2	12926	1392
Failures in RBR processing	12891 (-35)	1391 (-1)
Failures in data processing	12806 (-85)	1383 (-8)
MUPAGE simulation empty after reconstruction	12796 (-10)	1383 (-0)
Sparking runs	12754 (-42)	1377 (-6)
SCAN runs	12291 (-463)	1331 (-46)
PRELIM runs	12159 (-132)	1311 (-20)
Quality basic 0 runs	11812 (-347)	1266 (-45)
Final number of runs	**11812**	**1266**

The equivalent data taking life time of the full sample is **1247.0 days**, that of the burn sample **135.3 days**.

All reconstructed data and Monte-Carlo files are named *shower production 13-07-00* within this context and are currently stored at the Lyon computing centre [84] at */sps/km3net/users/folger/phd/shower/showerproduction/13-07-00/results/*

Chapter 9

Monte-Carlo and data comparison of the burn sample

This section provides a collection of plots to show the comparison of the simulated Monte-Carlo events to recorded detector data for the fit result and the reduced vertex log-likelihood. To follow the course of the analysis the comparison at this stage is given just for the burn sample as in a blind analysis the data of the full sample must not be evaluated before the complete analysis chain is fully developed. Some more plots, showing the comparison for the full sample, are given in chapter 14.

The comparison has been performed from data sets at two different stages, first from the complete sample of successfully reconstructed events and afterwards from the event sample that passed the event selection criteria as introduced in chapter 7.

The Monte-Carlo part of the plots is a composition of all kind of simulated atmospheric events in the RBR:

- **Atmospheric muons** as simulated by MUPAGE, weighted with a factor 3, as one third of the real data taking lifetime was simulated.

- **Atmospheric electron** & **muon neutrino shower and track events**, weighted with the Bartol [9] flux as conventional and the Enberg [10] flux as prompt contribution.

For more information about the weighting and the event simulation, see chapter 5.

In the ANTARES data taking process various different trigger algorithms are implemented to look for any kind of physics events in the time continuous data stream. The triggers that have been used for this analysis, and hence for the comparison, are listed in table 3.1 in chapter 3.3.1, where also a short description of the triggering in ANTARES is given.

The major point of interest in the shower reconstruction result is the shower energy and the neutrino direction (especially the zenith angle) as those parameters will be

used as cut parameters in the optimization of the sensitivity for the diffuse flux analysis (see chapter 12). Figure 9.1 and 9.2 show the Monte-Carlo data comparison for these parameters. Here and in the following, the zenith is defined as the angle from a vertically down-going neutrino (i.e. 180° is vertically up-going).
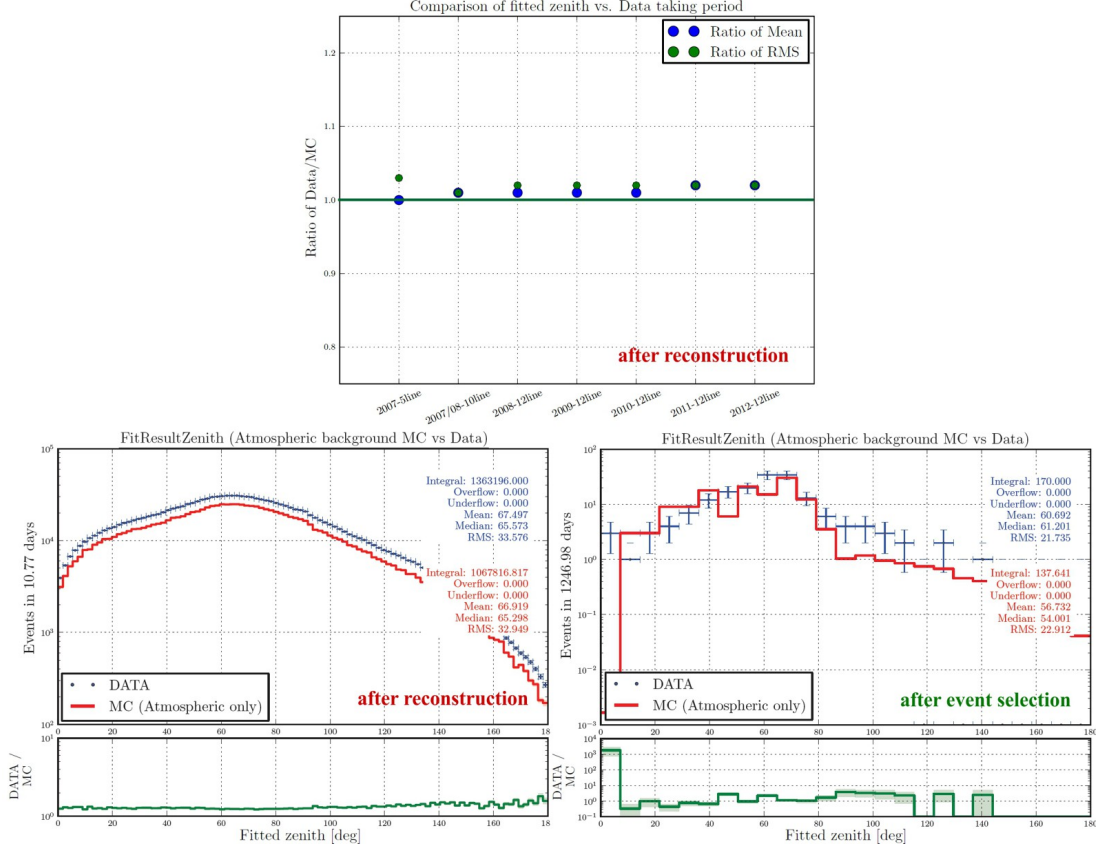
Figure 9.1: *Monte-Carlo data comparison of the fitted zenith in the burn sample.* The lower plots show the distributions of the fitted zenith for atmospheric Monte-Carlo (red) and data events (blue) from the sample of all events that have been successfully reconstructed, i.e. that are still dominated by atmospheric muons (left), and from those that remain after the event selection criteria from chapter 7 have been applied (right). The error bars on the data sample mark the Poisson statistical errors, but no systematic errors. The upper plot shows the tendency of the Data-MC ratio of mean and root-mean-square of the distributions from all reconstructed events with the data taking period. The simulated events contain atmospheric muons and electron and muon neutrinos. Note that the extrapolation of atmospheric muons (as introduced in chapter 10.3) is not yet included and slightly increases the Monte-Carlo distribution in the horizontal region after the event selection (lower right). The plots have been generated from all runs with a run number ending with 0. Due to computing memory limitations the lower left plot has been created from 50 % of those runs from 2009 only. All other periods show a similar behaviour.

From the comparison after the reconstruction, where no atmospheric muon suppression is applied yet and hence, the data is mainly compared to the MUPAGE simulation, a very good agreement in the distributions is found, apart from an excess of data events that changes with the data taking period and is highest for 2009 (see figure 9.3). But regarding the shape of the fit parameters a great stability is given during the whole
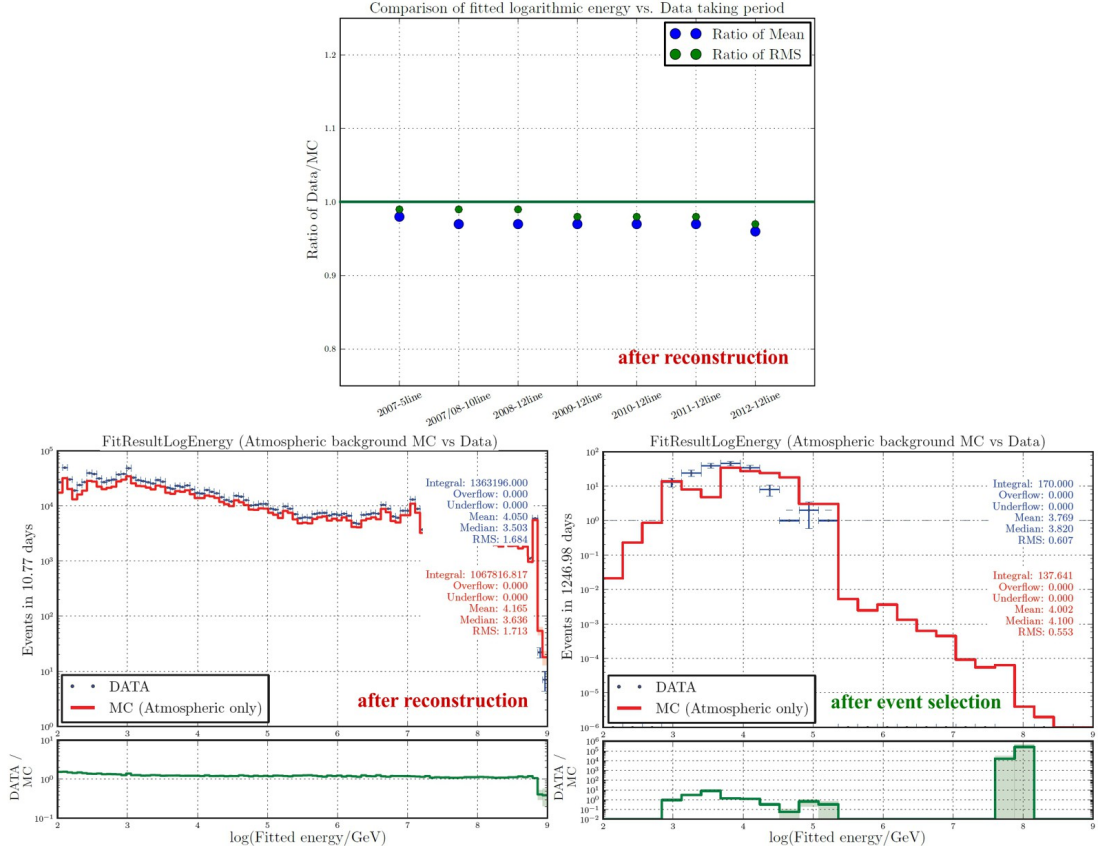
Figure 9.2: *Monte-Carlo data comparison of the fitted shower energy in the burn sample.* The lower plots show the distributions of the logarithmic fitted shower energy for atmospheric Monte-Carlo (red) and data events (blue) from the sample of all events that have been successfully reconstructed, i.e. that are still dominated by atmospheric muons (left), and from those that remain after the event selection criteria from chapter 7 have been applied (right). The error bars on the data sample mark the Poisson statistical errors, but no systematic errors. The upper plot shows the tendency of the Data-MC ratio of mean and root-mean-square of the logarithmic distributions from all reconstructed events with the data taking period. The simulated events contain atmospheric muons and electron and muon neutrinos. Note that the extrapolation of atmospheric muons (as introduced in chapter 10.3) is not yet included but is not expected to yield a big difference from the shown Monte-Carlo distribution. The plots have been generated from all runs with a run number ending with 0. Due to computing memory limitations the lower left plot has been created from 50 % of those runs from 2009 only. All other periods show a similar behaviour.

data taking period, as can be derived from the mean and root-mean-square tendency plots. The difference of the mean and root-mean-square values between Monte-Carlo and data never exceeds 5 %. The Dusj reconstruction itself seems to produce a very nice agreement between simulated and recorded events, at least right after the reconstruction.

After the event selection, where the number of atmospheric muons in the RBR of the burn sample has been reduced to 129, again an excess of data events can be observed, especially in the horizontal up-going region (zenith > 90°) which might be

an indication for a deficiency of atmospheric muon events in this region, probably due to low statistics. Hence, an extrapolation method for atmospheric muons up to higher zenith angles is introduced in chapter 10.3. The discrepancy in the low energy region is of minor concern as low energy events will be removed during the optimization process later anyway.
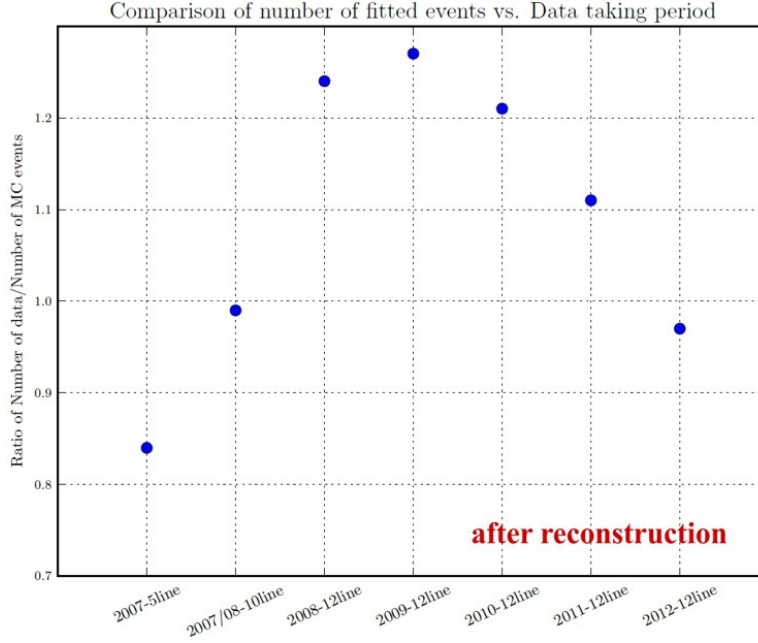
Figure 9.3: *Ratio of the number of reconstructed data and Monte-Carlo events in the burn sample.* The plots show the ratio of events (Data / Monte-Carlo) that successfully passed the shower reconstruction, hence, mainly atmospheric muons. The simulated events, nevertheless, contain also atmospheric electron and muon neutrinos. The plots have been generated from all RBR runs with a number ending with 0.

From figure 9.3 one can derive that for most of the data taking period an excess in the number of data events with respect to the number of Monte-Carlo events exists. The strength of this excess varies with the data taking period. While in earlier periods, when the detector was not fully established, less events are recorded than expected from Monte-Carlo, an excess it observed for the 12-line period. This excess, however, decreases with time, which could be an indication for an age-related decline of the PMT efficiency. Right after the reconstruction the average excess, integrated over the whole period, in the burn sample is $12.2\,\%$ in favour of data events. After the event selection criteria (see chapter 7) have been applied 170 data events remain while from the RBR simulation without any corrections 138 ± 20 are expected. In the burn sample 43 atmospheric muon events from MUPAGE survive the event selection cuts. These scale up to 129 expected atmospheric muon events with a statistical error of $3 \cdot \sqrt{43} \approx 19.7$. Assuming that the remaining part of the simulation that comes from neutrino events is precise due to the large statistics, and taking into account a Poisson error of $\sqrt{170} \approx 13.0$ on the number of recorded data events, the excess of ≈ 30 events

could be explained as a statistical over-fluctuation. However, note that systematic effects have not been taken into account here. They are discussed in chapter 11 and will further enlarge the error intervals.

On the other hand the plots show that the larger part of these 170 data events is settled in the low-energy region of the fitted shower energy. Thus, most of them will be removed by an energy cut during the MRF optimization (see chapter 12). Further, there are still additional contributions to be added to the simulation from corrections and estimations, e.g. high multiplicity muon bundles, that are described in chapter 10 and that are not taken into account in the simulations. These corrections are not yet included in the plots here.

Figure 9.4 shows the Monte-Carlo data comparison for the reduced vertex log-likelihood that is used to suppress atmospheric muons to a certain extent (see also chapter 7)
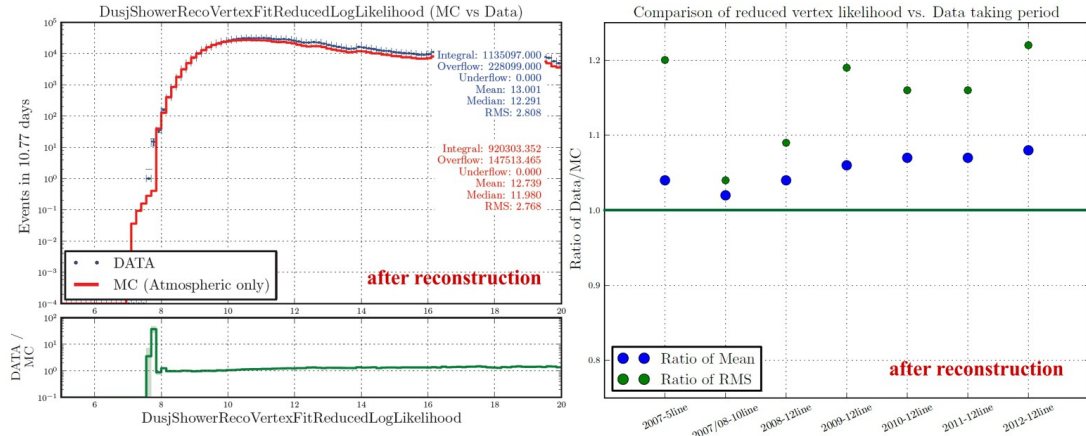
Figure 9.4: *Monte-Carlo data comparison of the reduced vertex log-likelihood in the burn sample.* The left plot shows the distributions of the reduced vertex log-likelihood for atmospheric Monte-Carlo (red) and data events (blue) from the sample of all events that have been successfully reconstructed, i.e. that are still dominated by atmospheric muons. The error bars on the data sample mark the Poisson statistical errors, but no systematic errors. The right plot shows the tendency of the Data-MC ratio of mean and root-mean-square of the logarithmic distributions from all reconstructed events with the data taking period. The simulated events contain atmospheric muons and electron and muon neutrinos. Note that the extrapolation of atmospheric muons (as introduced in chapter 10.3) is not yet included but is not expected to yield a big difference from the shown Monte-Carlo distribution. The plots have been generated from all runs with a run number ending with 0. Due to computing memory limitations the left plot has been created from 50 % of those runs from 2009 only. All other periods show a similar behaviour.

Here larger fluctuations up to 20 % can be observed, already at the stage right after the reconstruction. However, these fluctuations are caused by events with very high (bad) log-likelihood values above 20, reaching up to 100. But as the interesting region for the identification of shower events is the other end of the distribution at low (good) log-likelihood values, the observed differences are no serious issue. The cut on the reduced vertex log-likelihood is applied at a value of 7.9. When comparing

simulation and data in the reduced vertex log-likelihood interval from 0 to 20, again a good stability is reached with differences not exceeding 5 %.

To give a summary of the comparison: Concerning the parameters that are used as cut values within this analysis, Monte-Carlo and data show a quite good but not perfect agreement. However, the total integrated event numbers of simulation and data are compatible when taking errors, especially systematic uncertainties from the simulation or on the atmospheric flux, into account (see chapter 11). Small deviations in the shapes of the distribution, especially after the muon suppression, may also inherit from the simulation software of the RBR v2 that is not fully developed as for example photon scattering in shower events is still missing.

Chapter 10

Further corrections and estimations

Due to some simplified assumptions in the RBR (see also chapter 5), some corrections and estimations are necessary to compensate for missing parts in the simulation and to complete the number of expected events:

- As no simulation for tau neutrino events is included in the RBR, the contribution for **cosmic and prompt atmospheric tau neutrinos** is estimated in chapter 10.1. This estimation accounts for $\approx 30\,\%$ of the finally derived number of expected cosmic signal events (see also table 12.1).

- In the simulation of atmospheric muons no events with a higher bundle multiplicity (the number of simultaneously traversing muons) than 200 have been generated. In air shower events, however, not just one muon is produced, but a whole muon bundle is generated that can simultaneously traverse the detector. An estimation of the **contribution from muon bundles with more than 200 muons** is given in chapter 10.2. However, this correction is with $< 1\,\%$ after the final cuts rather small (see also table 12.1).

- In the following sensitivity optimization that is discussed in chapter 12 two additional cuts on the fitted energy and the fitted zenith will be applied, where afterwards no atmospheric muon from the MUPAGE simulation remains in the sample. Hence, an **extrapolation for the expectation of atmospheric muons** is presented in chapter 10.3 that in the end accounts for $\approx 40\,\%$ of the final number of expected atmospheric background events (see also table 12.1).

- Due to computing reasons **no vertex shower was simulated in the ν_μ CC simulations for neutrino energies above** $100\,\mathrm{TeV}$. Corrections for the number of cosmic and atmospheric muon neutrino events to compensate this deficiency are evaluated in chapter 10.4. For the cosmic signal this correction accounts for $\approx 9\,\%$, for the atmospheric background $\approx 3\,\%$ (see also table 12.1).

10.1   Estimation of the contribution from tau neutrinos

As tau neutrino events are not simulated in the RBR, in the following an estimation of the contribution of cosmic and prompt atmospheric tau neutrinos is presented. The conventional atmospheric high energy neutrino flux ($E_\nu > 100\,\text{GeV}$) does not contain a tau neutrino contribution. Thus, the increase of the background that originates from the prompt component only is expected to be small. The cosmic neutrino flux, however, is expected to consist to one third of tau neutrinos as due to neutrino oscillations over very long baselines a flavour ratio of $\nu_\mu : \nu_e : \nu_\tau = 1 : 1 : 1$ is expected upon arrival at Earth.

To estimate the contribution of cosmic tau neutrinos that cause a neutral current interaction is very simple as the NC cross-sections are identical for all three neutrino flavours. Let $N_{\nu_e \text{NC}}$ and $N_{\nu_\mu \text{NC}}$ be the number of expected NC events for ν_e and ν_μ and their anti-neutrinos after a certain cut stage, then the expected number of events from ν_τ NC interactions is

$$N_{\nu_\tau \text{NC}} = \frac{N_{\nu_e \text{NC}} + N_{\nu_\mu \text{NC}}}{2} \tag{10.1}$$

As the mass of the tau lepton of $1.78\,\text{GeV}$ [43] is relatively low compared to the high energy neutrinos that are detected with ANTARES, it is assumed that the cross-sections for deep inelastic scattering are compatible to those of the electron neutrino, also for CC interactions. However, the CC simulations contain a significant number of events from the Glashow resonance that occurs for $\bar{\nu}_e$ at neutrino energies at $6.3\,\text{PeV}$. Here the electron anti-neutrino scatters with an electron instead of the nucleon [67]. As only electron anti-neutrinos can cause this specific interaction, the number of Glashow resonant events has to be removed for the estimation of the tau anti-neutrino events. Figure 10.1 shows the spectra of the cosmic and atmospheric neutrino fluxes of $\bar{\nu}_e$ events that cause CC interactions from a simulated event sample after the Dusj reconstruction when no further event selection cuts are applied.

For each of these spectra the fraction of events that induce a Glashow resonance can be evaluated by integrating over the entries in the resonance peak and removing the interpolated baseline of deep inelastic scattering events below the peak. Let the ratio of Glashow events over all detected events from this flux be η_{Glashow}.

In deep inelastic scattering CC processes of tau neutrinos the resulting particle will be a tau lepton for which a couple of decay modes are allowed as with a mass of $1.78\,\text{GeV}$ it is heavy enough to also produce light mesons, like for example pions. With its very short lifetime of $2.9 \cdot 10^{-13}\,\text{s}$ [43] the tau lepton will quickly decay into one of its branches. Whenever here a hadron is produced, a hadronic shower is induced. Tau leptons that decay directly into electrons cause electromagnetic showers. The only
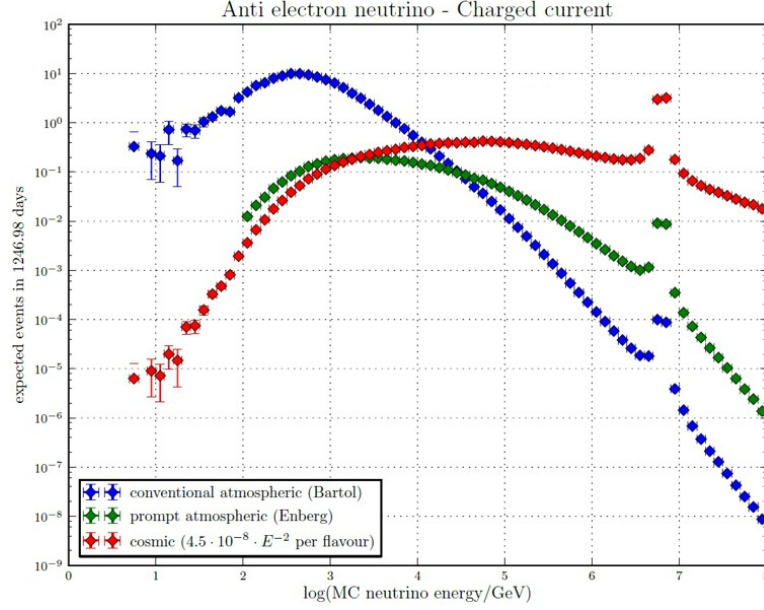
Figure 10.1: *Distributions of the Monte-Carlo neutrino energy for electron anti-neutrinos after the reconstruction.* The plot shows the spectra of the cosmic neutrino flux (red) and the conventional Bartol [9] (blue) and prompt Enberg [10] (green) atmospheric neutrino flux of $\bar{\nu}_e$ events that cause CC interactions and that have been successfully reconstructed. The plot has been generated from the electron anti-neutrino simulations of all runs in the RBR full sample, to illustrate the Glashow resonance peak at 6.3 PeV.

channel where tau events do not produce a shower is the direct decay into a muon

$$\tau^- \rightarrow \mu^- + \bar{\nu}_\mu + \nu_\tau \tag{10.2}$$

that occurs with a branching ratio of $(17.36 \pm 0.05)\,\%$ [43]. Thus, the fraction of ν_τ CC interactions that produce shower events is $\eta_{\tau,\text{shower}} = (82.64 \pm 0.05)\,\%$.

Taking these two facts into account the expected number of events from $\bar{\nu}_\tau$ CC interactions is:

$$N_{\bar{\nu}_\tau\text{CC}}^{\sim} = N_{\bar{\nu}_e\text{CC}} \cdot (1 - \eta_{\text{Glashow}}) \cdot \eta_{\tau,\text{shower}} \tag{10.3}$$

that for ν_τ CC:

$$N_{\nu_\tau\text{CC}}^{\sim} = N_{\nu_e\text{CC}} \cdot \eta_{\tau,\text{shower}} \tag{10.4}$$

The superscript $\sim$ indicates that these event numbers are not yet final as probably not all tau lepton events will be reconstructed as successfully as electron events would have been. An electron, once it is produced, will immediately induce an electromagnetic shower via Bremsstrahlung and pair production due to its short interaction length in water (35 cm [36]), whereas a tau lepton survives its mean life time. Taking into account Lorentz time dilatation the tau lepton will travel a certain distance before its decay.

This distance is a function of the energy E_τ.

$$d_\tau = \gamma c t_\tau \approx 50\,\mathrm{m} \cdot E_\tau/\mathrm{PeV} \tag{10.5}$$

A tau lepton with an energy of $1\,\mathrm{PeV}$ thus travels a distance of $50\,\mathrm{m}$ before it decays. Along this path it emits Cherenkov photons, just like a muon does. Due to the short lifetime the event now contains two induced showers, the vertex shower and the tau lepton decay shower.

It must be assumed that these double shower events will not be reconstructed with the same quality or pass the reduced vertex log-likelihood cut as easily as a pure electromagnetic shower event as with two contained showers and a track in between not all pulses match the fit assumption of **one** point-like light source. Thus, an additional correction has to be introduced. For neutrino energies below $100\,\mathrm{TeV}$ the tau lepton track length is below $5\,\mathrm{m}$ which is about the vertex resolution of the Dusj reconstruction at those energies. Hence, it is assumed that events below this energy can be treated as electron neutrino events.

However, above this energy, where the track gets significantly long enough to cause deviations from the point-like light source assumption, it is a priori not known how many of these events will pass the cuts as no tau neutrino simulation is available. Some of them definitely will as only a fraction of the neutrino energy will be passed to the tau lepton, which is a function of the Bjorken scaling variable y ($E_\tau = (1 - y)E_\nu$). Thus, also high energy tau neutrinos can produce tau leptons below the threshold. As a rough estimation the number of ν_τ CC events (and anti-neutrinos) above an energy of $100\,\mathrm{TeV}$ will be multiplied by a factor of 0.5 and the same value will be assumed as systematic error.

To capture the example of figure 10.1, after the reconstruction 18.0 cosmic electron anti-neutrino CC events are expected from the full sample (1247 days). By removing the Glashow resonance contribution (here $\eta_\mathrm{Glashow} = 34.2\,\%$) the estimation for the tau anti-neutrino CC channel yields 11.9 events, whereof in 9.80 events the tau lepton decays into a shower. However, 4.26 of these tau lepton showers are induced by tau neutrinos above $100\,\mathrm{TeV}$, thus they will be reduced to 2.13 ± 2.13. Hence, the total contribution from cosmic tau anti neutrino CC events in this case is 7.66 ± 2.13. Consider that the additional systematic errors from the simulations are not included in the given errors yet (see chapter 11).

The estimation of the prompt atmospheric ν_τ contribution follows the same principle as for the cosmic flux. Again it is evaluated from the ν_e channel, where in this case the prompt ν_e flux is used, of course. The only difference is that the expected prompt flavour ratio is not $\nu_e : \nu_\tau = 1 : 1$ (as it is for the cosmic flux), but $\nu_e : \nu_\tau \approx 17 : 1$ [10]. Hence, the evaluated number of ν_τ from the procedure described above is additionally divided by 17.

Of course, this estimation procedure has to be repeated after each individual cut stage that is applied to the event sample.

10.2   Extrapolation of high multiplicity atmospheric muon bundles

In the standard RBR atmospheric muon MUPAGE simulation muon bundle events (events in which several parallel muons traverse the detector) are taken into account only to a maximum number of 200 muons per bundle. Of course, nature is able to produce muon bundles with a higher multiplicity as well. To study the influence of events with a higher multiplicity than 200 on this analysis a separate run-by-run based simulation of atmospheric muons including bundle multiplicities up to 1000 has been reconstructed with the Dusj reconstruction and processed through the event selection criteria that have been introduced in chapter 7.

The simulation has been created by Laura Core [94] using randomly chosen run configurations from the 12-line data taking period 2008-2011 and an energy threshold of the primary cosmic particle of 3 TeV. Within this study 2168 different runs from this sample have been used, each representing a lifetime of 3800 s, which gives a total effective lifetime of about 95 days. Altogether 5510 muon bundle events with a multiplicity above 200 are contained in this sample.

After the multi line filter, the sparking event filter and the cut on the reduced vertex log-likelihood have been applied, none of the 5510 high multiplicity events is left in the sample. However, from figure 10.2, where the distribution of the reduced vertex log-likelihood is drawn for those events that survived the sparking event and multi line filters, one can derive that for some of the events the value of the reduced vertex log-likelihood gets quite close to 7.9, which raises concerns that some high multiplicity events do survive all event selections if statistics would have been increased. Hence, an extrapolation method is applied to give an estimation of how many events are expected to survive. This number is denoted as $N(<7.9)_{\text{extrapolated}}$.

Figure 10.2 also shows the extrapolation function that has been obtained by fitting a second order polynomial to the logarithmic number of events.

$$\log N(L) = A + B \cdot L + C \cdot L^2 \qquad (10.6)$$

The fit has been performed using the ROOT [113] framework and yielded $A = -44.3$, $B = 9.35$ and $C = -0.477$, where from an expectation of $N(<7.9)_{\text{extrapolated}} = 5.41$ high multiplicity muon bundles could be derived for a lifetime of 95.35 days, which is definitely a quite pessimistic estimation regarding the fact that the fitted extrapolation is above the simulated events in the region of the reduced vertex log-likelihood around

7.9. However, even with this conservative extrapolation it is shown in the following that the high multiplicity muon bundle contribution is very small.
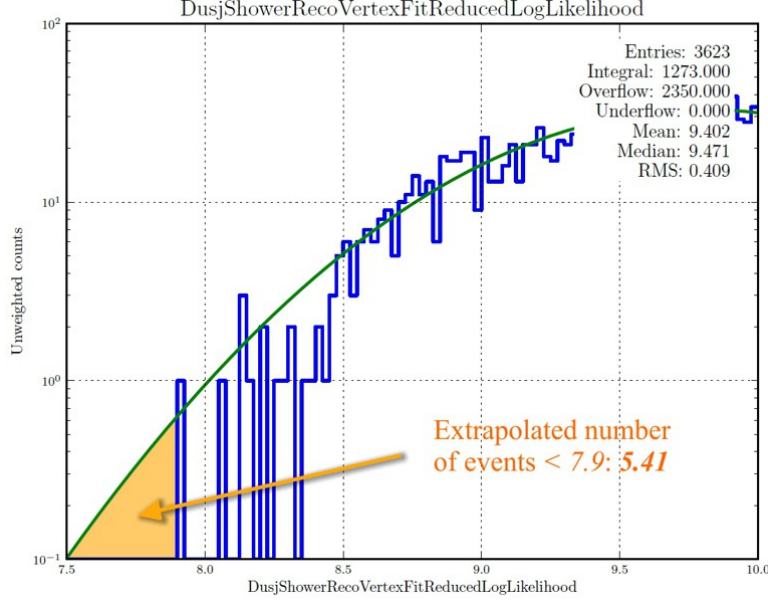
Figure 10.2: *Distribution of the reduced vertex log-likelihood for high multiplicity muon bundles.* The plot shows the distribution of the reduced vertex log-likelihood for atmospheric muon bundle events with a minimum multiplicity of 200 muons that survived the sparking event and multi line filters (see chapter 7) (blue). The plot has been generated from a separate run-by-run based MUPAGE simulation including multiplicities up to 1000 that represent a lifetime of 95 days. The line (green) is the fit that is used to extrapolate the number of events to lower values of the reduced vertex log-likelihood. The orange area indicates the extrapolated number of events that are expected to survive an additional upper cut on the reduced vertex log-likelihood at 7.9. See text for further information.

During the sensitivity optimization process that is shown later in chapter 12 two additional cuts will be introduced: A lower cut on the fitted zenith Θ and a lower cut on the fitted energy E. The question now is, what fraction of the 5.41 extrapolated events will also survive these two cuts? As the zenith and energy distribution of the extrapolated events is unknown, the fraction of surviving events, denoted as $R(<7.9, >\theta, >E)$, again has to be extrapolated from the whole simulated high multiplicity event sample.

Therefore, for different upper cuts on the reduced vertex log-likelihood L (from 8.0 up to 11.0 using a step width of 0.1) the ratio of remaining events after all three cuts over the number of events after the single L cut $R(<L, >\theta, >E) = N(<L, >\theta, >E)/N(<L)$ is evaluated. This ratio is then extrapolated to lower values of L. It is evident that this extrapolation step has to be repeated for each individual set of cuts on θ and E and is shown here for the cut pair $\Theta > 94°$ and $\log(E/\mathrm{GeV}) > 4.0$, which will turn out to be the optimized set of cuts to yield the best sensitivity later on.

Figure 10.3 shows the ratio $R(<L, >94°, >4.0)$ as function of the reduced vertex log-likelihood upper cut L, here for the chosen energy and zenith cuts. As fit func-

tion again equation (10.6) was used, which yields an extrapolated value for the ratio $R(<7.9, >94°, >4.0)_{\text{extrapolated}} = 2.15 \cdot 10^{-4}$.
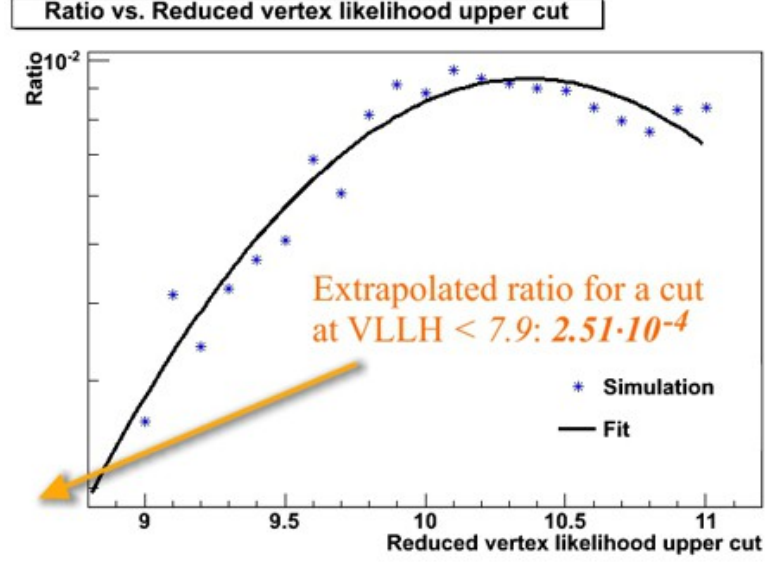
Figure 10.3: *Fraction of energy and zenith cut surviving high multiplicity muon bundles as function of a previous cut on the reduced vertex log-likelihood.* The plot shows the ratio of high multiplicity muon bundles (at least 200 muons per bundle) that survive an upper cut on the reduced vertex log-likelihood (x-axis) and an additional pair of lower cuts on the logarithmic fitted energy > 4.0 and the fitted zenith > 94°, over those that survived the single reduced vertex log-likelihood upper cut (blue points). The plot has been generated from a separate run-by-run based MUPAGE simulation including multiplicities up to 1000 that represent a lifetime of 95 days. The line (black) is the fit that is used to extrapolate the ratio to lower values of the reduced vertex log-likelihood. See text for further information.

The final extrapolated contribution of high multiplicity events (including more than 200 muons) is then, firstly, the extrapolated overall number at 7.9, scaled with, secondly, the extrapolated ratio:

$$
\begin{aligned}
N(<7.9, &>94°, >4.0) \\
&= N(<7.9)_{\text{extrapolated}} \cdot R(<7.9, >94°, >4.0)_{\text{extrapolated}} \\
&= 1.16 \cdot 10^{-3}
\end{aligned}
\tag{10.7}
$$

The number corresponds to a lifetime of 95.35 days. Hence, for the full analysis sample of 1247 days only a very small contribution of 0.015 events is expected, even from this quite pessimistic fit.

10.3 Extrapolation for atmospheric muons

During the optimization of this analysis that is shown in chapter 12 a pair of lower cuts on the fitted zenith and the fitted energy is applied to the simulated event sample and

varied until the best sensitivity is obtained. It turned out that this is the case at cut combinations where all atmospheric muons are removed from the sample. As only one third of the actual lifetime was simulated the statistical error on 0 MUPAGE events is 0^{+3}_{-0}. But instead of having 0 events with a large error included in the calculations, a further extrapolation method was used to give a better estimation of the remaining atmospheric muons that must be expected to survive the final cuts.

The chosen extrapolation strategy is the same that was used for high multiplicity muons in chapter 10.2, with the difference that the first extrapolation step can be skipped as after a cut on the reduced vertex log-likelihood at 7.9 the number of surviving atmospheric muon events is known and does not have to be extrapolated. In the burn sample (135 days lifetime) 129 atmospheric MUPAGE muons survive the reduced vertex log-likelihood cut and the sparking event and multi line filters, whereas in the full sample (1247 days) 1359 events remain in the event sample. Those numbers have already multiplied by 3 to get the contribution for the real lifetime.

However, the second step, i.e. the extrapolation of the ratio, has to be performed, as of course after the final cut on zenith and energy no MUPAGE event remains. Figure 10.4 shows the event ratio as function of the reduced vertex log-likelihood upper cut and the corresponding fit function, again for a fixed zenith cut at $\theta > 94°$ and energy cut $log(E/\text{GeV}) > 4.0$, which will be the final cuts for the optimized analysis. For this set of cuts, the extrapolation yields an atmospheric muon contribution of 0.18 for the burn sample and 1.85 for the full sample which is consistent with 0^{+3}_{-0} remaining MUPAGE events. Of course, the extrapolation of the ratio has to be repeated for each individual set of zenith and energy cuts.

To verify that this extrapolation procedure works correctly, the interpolation has also been performed for different zenith cuts without the cuts on the fitted energy. At this stage, an extrapolation is actually not necessary as still some atmospheric muon events survive the cut, but now they can be compared to the extrapolated number of events. Table 10.1 shows that the number of atmospheric muon events as obtained from this extrapolation method agrees with the actual remaining simulated events within Poisson statistical errors. Apart from the listed cuts in the table, the event sample has already passed the multi line and sparking event filters.

Table 10.1: Test of the atmospheric muon extrapolation for different zenith cuts

| Reduced vertex likelihood upper cut	Zenith lower cut [deg]	Extrapolated events in 1247 days	Actual remaining simulated events in 1247 days
7.9	74	157.6 ± 12.6	174 ± 13
7.9	78	98.9 ± 9.9	93 ± 10
7.9	88	37.9 ± 6.2	39 ± 6
7.9	94	18.9 ± 4.3	21 ± 5
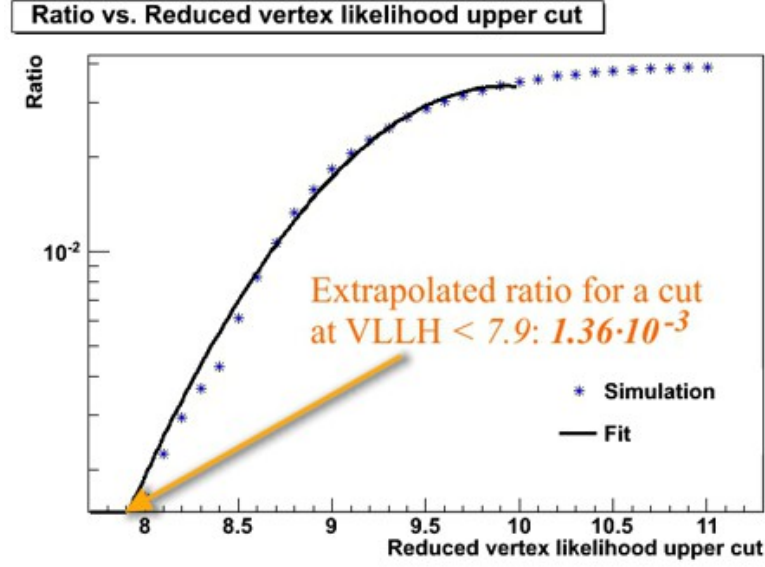
Figure 10.4: *Fraction of energy and zenith cut surviving atmospheric muons as function of a previous cut on the reduced vertex log-likelihood.* The plot shows the ratio of atmospheric muon events that survive an upper cut on the reduced vertex log-likelihood (x-axis) and an additional pair of cuts at the logarithmic fitted energy/GeV > 4.0 and the fitted zenith > 94°, over those that survived the single reduced vertex log-likelihood upper cut (blue points). The plot has been generated from the complete RBR MUPAGE simulation. The line (black) is the fit that is used to extrapolate the ratio to lower values of the reduced vertex log-likelihood. See text and also chapter 10.2 for further information.

10.4 Correction for missing vertex showers in muon neutrino events

The neutrino interactions in the RBR simulations include events with a neutrino energy up to 10^8 GeV. For computing reasons, however, in muon neutrino CC track events vertex showers that may be detected if the muon neutrino interaction takes place inside the instrumented volume are not simulated for neutrino energies above 10^5 GeV. For muon track analyses this might be of minor concern, but in a shower analysis, where usually a strong cut is performed to detect shower events, the absence of these vertex showers is recognizable as a drop in the number of selected events at this energy threshold. Figure 10.5 illustrates the distribution of the *Monte-Carlo neutrino energy* of all ν_μ CC events that survive the reduced vertex log-likelihood cut.

It is clearly noticeable that at the neutrino energy of 10^5 GeV the distributions suddenly fall off by one order of magnitude. Below this step almost all surviving events are starting muon track events, where a vertex shower is inside the detector. This vertex shower has been identified by the shower reconstruction and fitted well enough to make the event survive the reduced vertex log-likelihood cut. Above the step all remaining events survive this cut by chance. Events that should survive due to a vertex shower inside the detector are not simulated and therefore missing, which
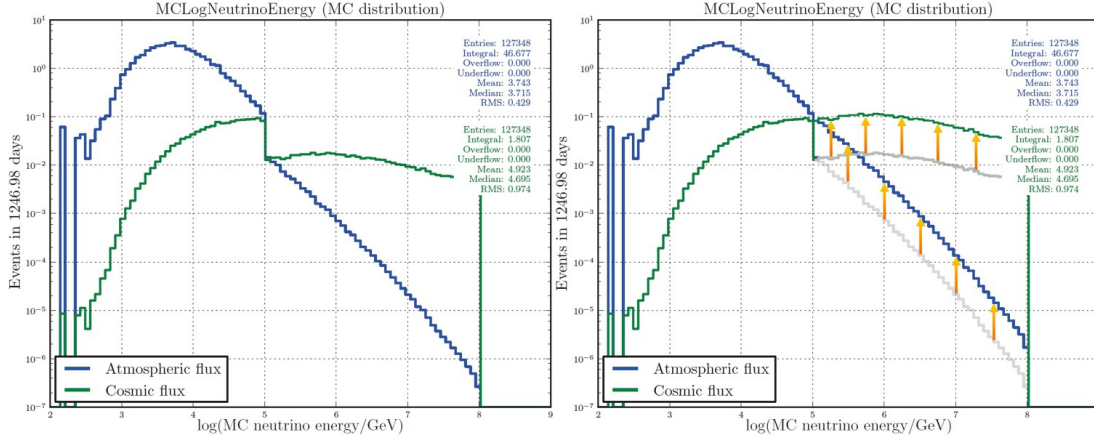
Figure 10.5: *Distributions of the Monte-Carlo neutrino energy for muon neutrino charged current events after the reduced vertex log-likelihood cut.* The left plot shows the distribution of the Monte-Carlo neutrino energy for $\nu_\mu + \bar{\nu}_\mu$ events in the remaining simulated sample after the upper cut on the reduced vertex log-likelihood at 7.9 for the atmospheric neutrino flux (blue) and cosmic neutrino flux (green). The plot has been generated from the muon neutrino ν_μ CC simulations. In those simulations no vertex shower is simulated any more if the neutrino energy is above 10^5 GeV. The absence of such events causes a step in the distribution. The right plot illustrates how this issue is corrected by lifting the distribution above the step to match the one below. See text for further information.

explains the step. To take the lack of information in this simplified simulation into account, a correction to the number of ν_μ CC track events was introduced by shifting the distributions above the step upwards to match the ones, where the vertex shower is still included (as visualized in the right plot in figure 10.5). Therefore, it is assumed that the distribution of events that are selected by chance follows the distribution of events that would have been selected due to a true vertex shower, which is admittedly a priori not known, but the best guess one can do at this point.

The magnitude of the shift was evaluated by adjusting the part above 10^5 GeV to match continuously and continuously differentiable to the part below 10^5 GeV. Therefore, the mean slope of the five last bins before the step and the five first bins after the step have been calculated. Then the high-energy distribution is shifted until the slope at the step position is identical to the evaluated mean value. This adjustment has to be performed separately for each flux, i.e. the cosmic and prompt/conventional atmospheric fluxes, and repeated after each cut stage in the analysis. To give an example, table 10.2 lists the additional contribution that has to be added due to this correction for the full sample after the reduced vertex log-likelihood cut. The *adjustment factor* is the value by which the number of events above 10^5 GeV is scaled.

In this table the atmospheric flux following Bartol [9] (conventional) and Enberg [10] (prompt) was used. The cosmic flux refers to an E^{-2} spectrum with a normalization of $4.5 \cdot 10^{-8}$ GeV/cm$^2 \cdot$ sr $\cdot$ s. The given errors are statistical errors and those that arise from the slope adjustment, where the error on the mean slope was propagated using

Table 10.2: Corrections for missing vertex showers in simulations of high energy muon neutrino track events after the reduced vertex log-likelihood cut

Flux	Events uncorrected	Adjustment factor	Events corrected	Difference
Cosmic ν_μ CC	1.06 ± 0.004	7.76 ± 0.19	2.81 ± 0.005	$+(165 \pm 5)\,\%$
Cosmic $\bar{\nu}_\mu$ CC	0.75 ± 0.003	6.97 ± 0.21	2.24 ± 0.005	$+(199 \pm 7)\,\%$
Conventional ν_μ CC	40.8 ± 0.2	5.8 ± 4.7	41.0 ± 0.3	$+(0.62 \pm 0.61)\,\%$
Conventional $\bar{\nu}_\mu$ CC	5.49 ± 0.02	5.57 ± 3.42	5.55 ± 0.05	$+(1.11 \pm 0.82)\,\%$
Prompt ν_μ CC	0.26 ± 0.001	8.22 ± 0.65	0.30 ± 0.004	$+(19.2 \pm 1.6)\,\%$
Prompt $\bar{\nu}_\mu$ CC	0.14 ± 0.001	7.48 ± 0.41	0.18 ± 0.003	$+(28.7 \pm 2.1)\,\%$

Gaussian error propagation

$$\Delta f(x,y) = \sqrt{\left(\frac{\partial f}{\partial x} \cdot \Delta x\right)^2 + \left(\frac{\partial f}{\partial y} \cdot \Delta y\right)^2} \qquad (10.8)$$

to the corrected number of expected events.

As expected, the relative correction is highest for the cosmic flux, as it dominates at higher energies. However, note that later an additional cut on the fitted energy will be applied and hence the correction gets even higher. But as it is only the ν_μ CC channel that is affected, the impact is limited. After the very final cuts (see chapter 12) the total number (from all flavours and interactions) of cosmic signal events has to be increased by $\approx 9\,\%$ due to this issue. The atmospheric background increases by $\approx 3\,\%$.

Chapter 11

Systematic uncertainties

This section introduces the systematic uncertainties that have been taken into account for this analysis. The derived systematic errors on the number of events are caused by

- the uncertainty on the atmospheric fluxes: σ_{flux}

- the uncertainty of simulation input parameters, such as absorption length, scattering length and PMT efficiency: $\sigma_{\text{simulation}}$

- the difference between the RBR and the future simulation software tools (see chapter 7.1): σ_{software}

Errors that inherit from the estimation of tau neutrino events (now denoted as $\sigma_{\tau\,\text{estimation}}$) or the correction for the missing vertex showers in ν_μ CC simulations (here $\sigma_{\text{missingvertex}}$) have already been introduced in chapter 10.

Finally, different errors σ on the same sample of event types, e.g. all errors that are applied to one specific neutrino flavour, type and interaction channel, are added up in quadrature:

$$\sigma_{\text{tot}} = \sqrt{\sigma_{\text{statistal}}^2 + \sigma_{\text{flux}}^2 + \sigma_{\text{simulation}}^2 + \sigma_{\text{software}}^2 + \sigma_{\tau\,\text{estimation}}^2 + \sigma_{\text{missingvertex}}^2} \quad (11.1)$$

Depending on the type of events not all single components have a contribution, for instance the error of the missing vertex shower correction is only taken into account for ν_μ CC events, the tau estimation error just for ν_τ events, etc... To obtain the final error on the total number of events from all channels, σ_{tot} from each flavour, type and interaction channel is added up linearly.

11.1 Uncertainties on the muon and neutrino fluxes

The total uncertainty on the conventional atmospheric neutrino flux was assumed to be $\pm 30\,\%$ as it is suggested in [77] [23]. The same was assumed as relative error on the

number of atmospheric muons.

The uncertainty on the prompt atmospheric flux follows the parametrization in [10], where in addition to the flux parametrization also energy-dependent upper and lower bounds of the error band are given. All three parametrizations (flux and errors) are implemented in the neutrinoflux package [80] [81]. The average error, integrated over all energies, is approximately $^{+25}_{-40}$ %. However, here the full parametrizations are used for the evaluation. The numbers are not simply multiplied with the integrated percentage, as done with the conventional flux.

The cosmic neutrino test flux is assumed to be precise.

11.2   Uncertainties from differences in the simulation software tools

As discussed in chapter 7.1 a study on the new simulation software *KM3 v4r5*, where compared to the RBR photon scattering is included for the first time in shower events, revealed differences in the shower reconstruction and selection efficiency. This made it necessary to introduce the single cut on the reduced vertex log-likelihood instead of the previously used random decision forest classifier to minimize the difference between the currently used RBR simulation and this future software and simultaneously not to loose too much sensitivity. The compromise that was chosen then was a cut on the reduced vertex log-likelihood at a value of 7.9. With such a cut the difference between the two shower simulations are 31 % in favour of the old RBR simulation. If the analysis would have been performed with the - up to now not yet created - new simulation, about 31 % less shower events would have survived the cuts. Hence a systematic error σ_{software} of $^{+0}_{-31}$ % is applied to the number of neutrino events from the shower channels, i.e. all except for ν_μ CC and atmospheric muon events.

11.3   Uncertainties in the Monte-Carlo simulation

From the statistical point of view the Monte-Carlo neutrino event simulations in the RBR can be regarded as very precise as for each run a large number of events is generated (see chapter 5). However, the outcome of such a simulation depends on the choice of the physical input parameters, such as light absorption length in water, scattering length or PMT efficiency. Those parameters are of course not known exactly. To estimate the systematic error that inherits from the uncertainty of those input parameters, a small subset of run-by-run based simulations has been created by the ANTARES Monte-Carlo working group, where the input parameters have been changed by ± 10 % respective to their nominal value that was used in the RBR simulations.

For the atmospheric muon MUPAGE simulation a sample of 10 different runs, representing a lifetime of about 18 hours, was produced, for the GENHEN neutrino simulations 40 different runs with a lifetime of 3 days were generated. All in all seven samples have been produced, one with the same values for the parameters as in the official RBR simulations, two by changing the absorption length to ±10 % of its nominal value, two by changing the scattering length to ±10 %, and two by changing the PMT efficiency to ±10 %.

Table 11.1 lists the deviations in the number of ν_μ CC track events in the modified simulations with respect to the simulation using standard values. The numbers have been obtained from the event sample after the reduced vertex log-likelihood cut, once for an atmospheric and once for a cosmic flux of muon neutrinos interacting in charged current reactions. The corresponding numbers for all types of shower events are given in table 11.2.

Table 11.3 lists the deviations for atmospheric muon events. For statistical reasons the event numbers for the MUPAGE simulation were obtained from all events that pass the reconstruction as after the reduced vertex log-likelihood cut no atmospheric muon is left in this small simulation.

Table 11.1: Systematic errors for the charged current muon neutrino event numbers after an upper cut on the reduced vertex log-likelihood at 7.9 from uncertainties in the simulation

| Parameter modification | Deviation in number of events | | | | | |
| | Absorption length | | Scattering length | | PMT efficiency | |
	Atm.	Cosm.	Atm.	Cosm.	Atm.	Cosm.
−10 %	−10 %	−6 %	+4 %	+1 %	+2 %	+4 %
+10 %	−19 %	+4 %	−1 %	+4 %	+5 %	+2 %

Table 11.2: Systematic errors for the shower event numbers after an upper cut on the reduced vertex log-likelihood at 7.9 from uncertainties in the simulation

| Parameter modification | Deviation in number of events | | | | | |
| | Absorption length | | Scattering length | | PMT efficiency | |
	Atm.	Cosm.	Atm.	Cosm.	Atm.	Cosm.
−10 %	−30 %	−10 %	−11 %	−3 %	−17 %	−3 %
+10 %	+33 %	+13 %	+33 %	+5 %	+28 %	+10 %

Table 11.3: Systematic errors for the atmospheric muon event numbers after the reconstruction from uncertainties in the simulation

| Parameter modification | Deviation in number of events | | |
	Absorption length	Scattering length	PMT efficiency
−10 %	−14 %	+2 %	−17 %
+10 %	+13 %	−2 %	+16 %

Although these systematic errors are subject to variations, depending on which cuts are applied, the here evaluated values are used throughout all cut stages of this analysis.

They have been obtained from a representative cut stage, for which the number of remaining events is still high enough to ensure that the systematic error is significantly higher than the statistical error. For atmospheric muons this cut stage is right after the reconstruction, for all other events after the reduced vertex log-likelihood cut. The evaluated errors from the changes of the single parameters are joined to one systematic simulation error by adding them up in quadrature:

$$\sigma_{\text{simulation}} = \sqrt{\sigma_{\text{absorption}}^2 + \sigma_{\text{scattering}}^2 + \sigma_{\text{PMTefficiency}}^2} \qquad (11.2)$$

Hence, to take into account the uncertainty of the simulation input parameters a systematic error of $^{+21\%}_{-22\%}$ will be applied to the number of atmospheric muon events. The systematic error for the atmospheric neutrino background is $^{+6\%}_{-19\%}$ (muon tracks) and $^{+54\%}_{-36\%}$ (showers), that for the cosmic neutrino signal is $^{+7\%}_{-6\%}$ (muon tracks) and $^{+17\%}_{-11\%}$ (showers).

Chapter 12

Sensitivity for a diffuse flux

Although quite a large amount of data has been taken during the six years of the experiment, it is still unlikely that a cosmic neutrino flux can be proven with it. For the IceCube telescope whose volume is about 100 times larger than that of ANTARES it took 662 days of data taking (which is approximately half of the time used in this analysis) to find a first evidence for a cosmic neutrino flux at a $4\,\sigma$ level with a normalization of $1.2 \cdot 10^{-8}\,\mathrm{GeV/cm^2 \cdot sr \cdot s}$ per neutrino flavour [4]. To give a rough estimation what can be expected from this work: The IceCube analysis that provides a fair comparison to this work is probably the diffuse shower analysis with the IceCube40 detector, where 371 days of data were analysed. In that analysis just one third of lifetime compared to this work was used, but instead about 3 times as many strings have been instrumented. The upper limit on the diffuse cosmic neutrino flux from that analysis was set to $2.5 \cdot 10^{-8}\,\mathrm{GeV/cm^2 \cdot sr \cdot s}$ per neutrino flavour [12] that is still a factor two above the later measured flux. The detection of the cosmic neutrino flux with this analysis is therefore unlikely.

Hence, in the following a strategy is presented to evaluate and optimize the sensitivity for an upper limit on the diffuse cosmic neutrino flux from shower events.

12.1   The model rejection potential technique

To optimize the sensitivity for an upper limit the model rejection potential technique, as introduced in [14], was chosen. It follows an approach by Feldman and Cousins [5]. In the following short outline of this technique the observables n_{obs} (total number of observed events), n_{b} (number of expected atmospheric background events) and n_{s} (number of cosmic signal events) are used.

Based on Poisson statistics a method, the so-called Neyman construction, is presented in [5] to evaluate confidence level intervals for an unknown n_{s}, when n_{obs} are measured and n_{b} background events are expected. The Neyman construction provides

an interval $[n_{\text{s,min}}, n_{\text{s,max}}]$ that covers all possible values of the number of contained signal events within the number of observed events in a way that in hypothetical frequent repetitions of the experiment the true number of signal events lies within this interval in a certain percentage of all cases. This percentage is called *confidence level* and was set to 90 % for this analysis. The interval then is called 90 % *confidence interval*

$$\mu_{90}(n_{\text{obs}}, n_{\text{b}}) = (\mu_{90,1}, \mu_{90,2}) \tag{12.1}$$

In this case n_{b} is obtained from the RBR Monte-Carlo simulations and contains

- Atmospheric muons

- Shower and muon track events induced by atmospheric (conventional and prompt) neutrinos

Then the *upper limit* on a diffuse cosmic neutrino flux can be calculated to

$$\Phi_{90\,\%} = \Phi_{\text{Test}} \frac{\mu_{90,2}(n_{\text{obs}}, n_{\text{b}})}{n_{\text{s}}} \tag{12.2}$$

where here, n_{s} is the number of expected cosmic signal events, derived from the simulation and assuming a cosmic test flux Φ_{Test}. This test flux is arbitrary, as it is contained twice in equation (12.2), once directly and once indirectly in the value of n_{s}, and hence, cancels out. In this work an E^{-2} test flux with a normalization of $4.5 \cdot 10^{-8}\,\text{GeV/cm}^2 \cdot \text{sr} \cdot \text{s}$ per neutrino flavour was chosen.

To obtain the best possible result for the upper limit, $\Phi_{90\,\%}$ has to be minimized by finding the optimum set of cuts on the simulation and data samples. However, this procedure is not conform with a blind analysis as here the data has to be known before the optimum cuts have been figured out. Thereby a bias in the minimization strategy or even in the event reconstruction might be included that depends on the data. For example, if from simulations no signal event is expected, one could possibly change the set of cuts until the number of observed data events equals the number of expected background events. In this case one would have tuned the analysis strategy to provide exactly the expected result. To avoid this bias a modified strategy, the *model rejection potential technique*, is presented in [14] that is based on simulations only and for which measured data is not required any more during the optimization process.

In the model rejection potential technique, the number of observed events n_{obs} is not known. Thus, the idea is to allow any possible value $n_{\text{obs}} \geq 0$ and calculate an *average upper limit* from all these values. Assuming that no cosmic signal event n_{s} is expected from simulations the Poisson probability to measure a hypothetical value for

n_{obs}, where n_{b} atmospheric events are expected is given as

$$p(n_{\mathrm{obs}}, n_{\mathrm{b}}) = \frac{n_{\mathrm{b}}^{n_{\mathrm{obs}}}}{n_{\mathrm{obs}}!} e^{-n_{\mathrm{b}}} \tag{12.3}$$

which now is the probability for the hypothetical upper limit, resulting from n_{obs} events, to occur. The average upper limit then is the mean value of all possible upper limits, weighted with the Poisson probability of occurrence:

$$\bar{\mu}_{90,2}(n_{\mathrm{b}}) = \sum_{n_{\mathrm{obs}}=0}^{\infty} \mu_{90,2}(n_{\mathrm{obs}}, n_{\mathrm{b}}) \cdot p(n_{\mathrm{obs}}, n_{\mathrm{b}}) \tag{12.4}$$

that is no longer a function of n_{obs}. Then, following the same principle as in equation (12.2), the term

$$\bar{\bar{\Phi}}_{90\,\%} = \Phi_{\mathrm{Test}} \frac{\bar{\mu}_{90,2}(n_{\mathrm{b}})}{n_{\mathrm{s}}} \tag{12.5}$$

is regarded as the potential of the experiment to set an upper limit, that means to exclude a flux above the derived value. This potential is called *sensitivity*. One can obtain the strongest constraint on the diffuse flux, i.e. the lowest upper limit, from the simulation by optimizing the set of cuts on the simulated events, such that the so-called *model rejection factor*

$$MRF = \frac{\bar{\mu}_{90,2}(n_{\mathrm{b}})}{n_{\mathrm{s}}} \tag{12.6}$$

is minimized. In the following this optimization is performed by using the complete RBR simulations of the full 1247 days sample. A check on $10\,\%$ of the data, which is the 135 days burn sample, is presented in chapter 13. With the optimized set of cuts, finally the full sample is analysed in chapter 14.

The calculations of the confidence intervals in this work are performed using the class **TFeldmanCousins** that is part of the ROOT [113] framework.

12.2 Sensitivity optimization

The event sample that was used for the sensitivity optimization includes all simulated events in the RBR of the full sample (1247 days) that pass the event selection criteria introduced in chapter 7. In this sample still 1359 simulated atmospheric muons are contained, compared to a cosmic signal expectation of ≈ 35 events from the test flux. This background is included in the MRF minimization and has to be suppressed by additional cuts. Therefore, a pair of lower cuts on the fitted energy E and the fitted zenith Θ has been introduced. This means in the end only events are taken into account where the fitted energy exceeds a certain value and where the direction is "more up-going" than a certain value.

Figure 12.1 shows the number of expected signal and background events from the RBR, where the signal part includes cosmic muon and electron neutrino events in any interaction channel with a flux normalization of $4.5 \cdot 10^{-8}\,\mathrm{GeV/cm^2 \cdot sr \cdot s}$ per flavour, and the background part contains conventional and prompt atmospheric muon and electron neutrino events and atmospheric muons. One can derive from the plots that a sufficiently high background rejection can be obtained from either cutting high in energy or cutting high in zenith.
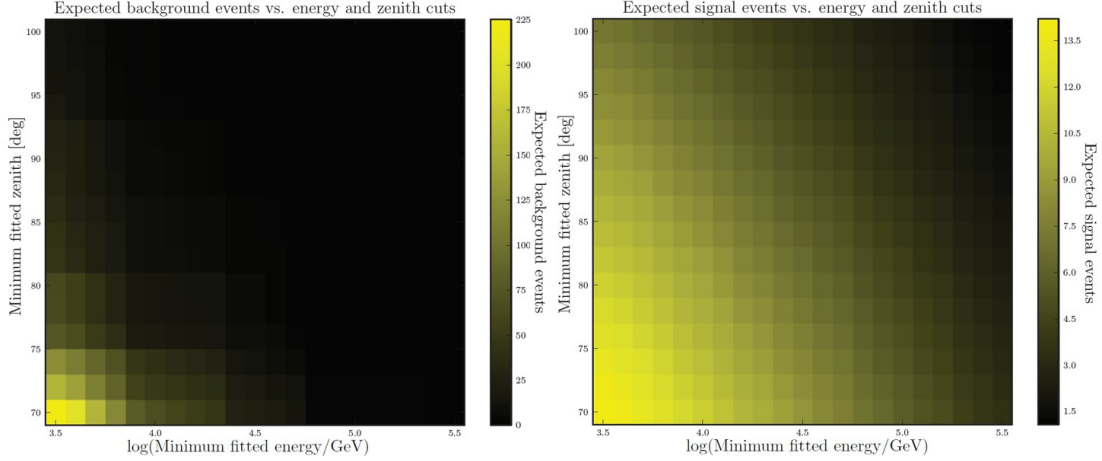
Figure 12.1: *Expected number of cosmic and atmospheric RBR events in the full sample as function of the energy and zenith cuts.* The plots show the number of expected atmospheric background neutrino and atmospheric muon events (left) and cosmic signal neutrino events (right) as function of the applied lower cuts on the fitted energy and the fitted zenith. For the cosmic neutrino flux an E^{-2} spectrum was assumed with a normalization of $4.5 \cdot 10^{-8}\,\mathrm{GeV/cm^2 \cdot sr \cdot s}$ per neutrino flavour. Note that only RBR simulations have been taken into account here. The corrections introduced in chapter 10, e.g. the tau neutrino estimation, is not included in the plot.

The criterion to define the *optimum set of cuts* between removing as much background as possible and loosing as little signal as necessary is the MRF (equation (12.6)). For that cut combination where the MRF is minimal the best sensitivity is obtained according to equation (12.5).

Figure 12.2 illustrates the MRF landscape as a function of the lower cuts on the fitted zenith and the fitted energy. One can recognize a valley of minima that is located in a region where all atmospheric muons are cut away. The valley ranges, as expected, from a region of high zenith but low energy cuts to a region of high energy but low zenith cuts. The fact that high energy cuts can remove atmospheric muons can be well understood as atmospheric muons are lower energetic than cosmic neutrino events. This of course requires a sufficiently good reconstruction of the muon energy, which could be approved by the left plot in figure 12.3. For the remaining atmospheric muon events after the event selections the muon energy is reconstructed with a mean error of about -0.25 orders of magnitude, which is just a slightly worse resolution than for low energy shower events.

On the other side, a stronger cut on the fitted zenith also improves the signal-to-background ratio as atmospheric muons are by nature down-going events and applying a stronger up-going cut decreases the chance of keeping muons that are mis-reconstructed as up-going in the sample. Again, a good direction reconstruction for the remaining atmospheric muons is implied, which is confirmed by the right plot in figure 12.3. For those muons a mean error of $\approx 7°$ is obtained, which is also comparable to that of the shower events.
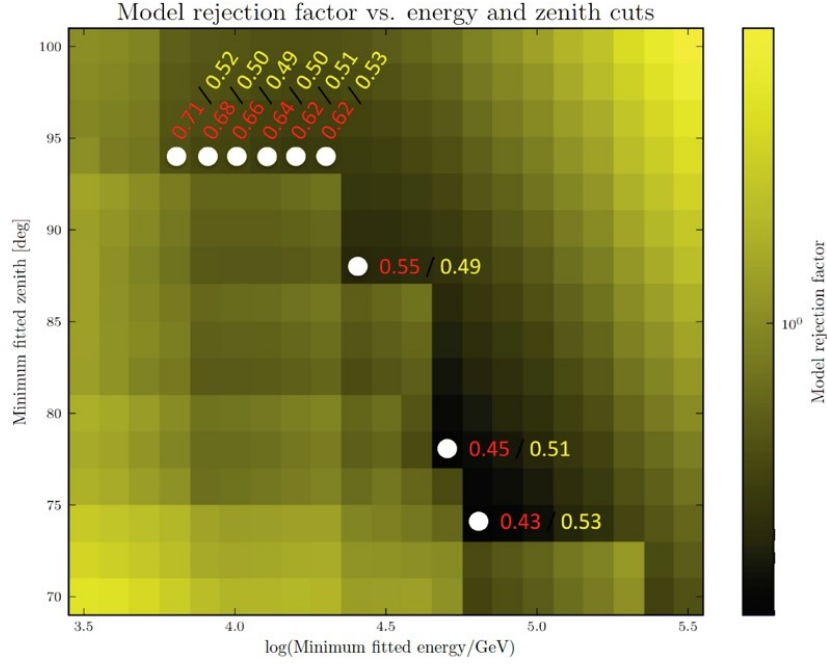
Figure 12.2: *MRF landscape in the full 1247 days sample as function of the energy and zenith cuts.* The plot shows the evaluated model rejection factor as function of the applied lower cuts on the fitted energy and the fitted zenith. The evaluation has been performed using the complete RBR simulation, i.e. in the black-to-yellow color coding of the MRF the corrections introduced in chapter 10 are not yet included (e.g. tau neutrino estimations). The white points mark cut combinations in the valley of minima that yield the lowest MRF values. The red numbers refer to the MRF as evaluated from RBR only and give the value of the color coding in the plot. The yellow numbers represent the corresponding MRF values when all corrections are included.

For selected cut combinations in the valley of MRF minima (figure 12.2) the value of the MRF has been evaluated in two different ways:

- The *red* values refer to a value that has been obtained by taking into account the RBR simulation only without all the corrections introduced in chapter 10. The aim was to perform the first MRF scanning based on simulated events only and avoid any bias from uncertainties of the additional estimations, such as the tau neutrino correction or atmospheric muon extrapolation.

- The *yellow* values then represent the re-evaluated MRF value, now including all the corrections.
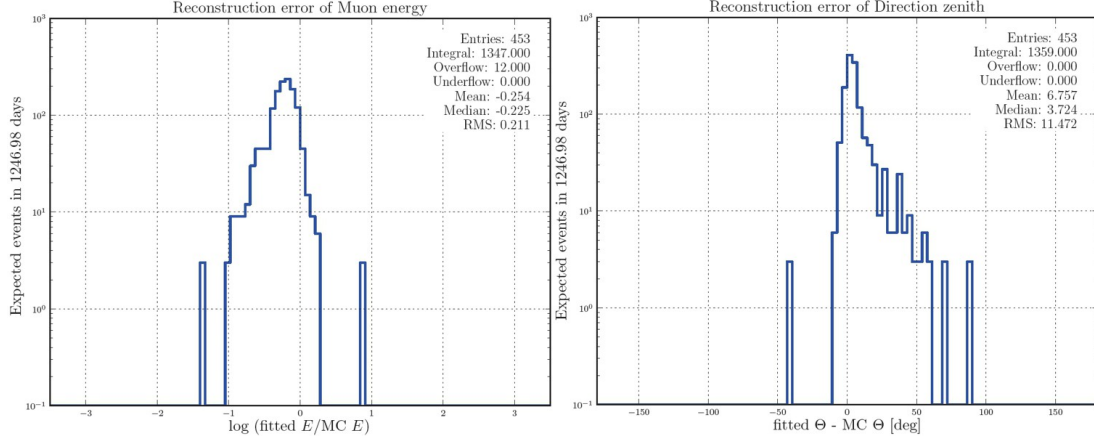
Figure 12.3: *Reconstruction quality for the remaining atmospheric muons in the full 1247 days sample after the event selection.* The plot shows the distributions of the event-wise logarithmic difference between the (Dusj-) fitted and Monte-Carlo muon energy (left) and the difference between the (Dusj-) fitted and the Monte-Carlo zenith of the muon direction (right) for all MUPAGE atmospheric muon events in the full 1247 days RBR Monte-Carlo that survive the event selection criteria introduced in chapter 7.

From the RBR-only evaluation the preferred cut combination would be at $\Theta > 74°$ and $\log E > 4.8$. For this case no tau neutrino events have been added to the signal and 0 remaining MUPAGE events are really taken as 0 atmospheric muon events. However, when applying the atmospheric muon extrapolation, the tau neutrino estimation and the correction for the missing vertex showers, the MRF tends to yield approximately the same value throughout the whole valley.

A stronger cut on the energy improves the MRF as the cosmic neutrino flux is higher energetic than the atmospheric neutrino flux. The fact that also a stronger cut on the zenith is able to yield comparable good MRF values is reasoned by a feature of the Dusj reconstruction. It turned out that the reconstruction for low energy events is more efficient for up-going than for down-going events whereas for high energy events the efficiency is almost isotropic. Hence, cutting stronger in the fitted zenith reduces the atmospheric neutrino background stronger than the cosmic neutrino signal.

From the constancy of the re-evaluated MRF values throughout the whole valley of minima one can conclude that the analysis strategy is able to provide a quite stable result, independent from where the final cuts are set within the valley of minima. As the final obtained upper limit, however, will have a validity range for the energy of the events, a cut on lower energies (and therefore higher zenith angles) is preferred. Hence, the final optimized cut pair was chosen at a zenith angle $\Theta > 94°$ and an energy $\log(E/\text{GeV}) > 4.0$.

Table 12.1 lists the number of expected events after these final cuts sorted by its origin and the different kinds of corrections and estimations that have been applied.

The errors in that table are statistical errors and those that inherit from the single corrections. Systematic errors, as introduced in chapter 11, are only included in the final row holding the sum of all. Statistical errors from weighted event numbers are evaluated from the Poisson error of the simulated event numbers. If N simulated Monte-Carlo events scale to α events, expected from a certain flux assumption, the relative error on the simulated events is $\sqrt{N}/N$ and hence, the error on the scaled events is

$$\Delta\alpha = \alpha \cdot \frac{\sqrt{N}}{N} \tag{12.7}$$

For the MUPAGE simulation, where each event has to be scaled with a factor of 3, the error thus is $3 \cdot \sqrt{N}$.

Table 12.1: Expected number of signal and background events sorted by their origin or correction for the full 1247 days sample after the final cuts

Sample/Correction	Signal events	Background events
RBR cosmic test flux	6.58 ± 0.01	-
RBR atmospheric Bartol [9]	-	2.32 ± 0.01
RBR prompt Enberg [10]	-	0.56 ± 0.002
Cosmic ν_τ estimation	2.91 ± 1.02	-
Prompt ν_τ estimation	-	0.02 ± 0.002
Atmospheric muon extrapolation	-	1.85 ± 1.36
High multiplicity muon bundles	-	0.015 ± 0.006
Missing vertex shower correction	0.96 ± 0.08	0.16 ± 0.06
+ Systematic uncertainties	see chapter 11	
Total	$10.45^{+2.37}_{-3.61}$	$4.92^{+2.85}_{-2.96}$

Table 12.2 lists all event numbers sorted by their neutrino flavour, type and interaction channel. Here, all corrections and systematic errors are included for each value. The Glashow resonance events for $\bar{\nu}_e$ have been counted in the CC channel. Small discrepancies in the total sum are due to rounding effects.

Taking into account $4.92^{+2.85}_{-2.96}$ background events, the Feldman-Cousins average 90% confidence interval upper limit is evaluated to $5.14^{+0.97}_{-1.24}$, where the errors have been obtained from evaluating the confidence interval upper limit including the upper and lower error on the background. From $10.45^{+2.37}_{-3.61}$ signal events, the MRF then is evaluated to $0.49^{+0.19}_{-0.16}$, where in this case the errors have been calculated by Gaussian error propagation (equation (10.8)) combining the upper error of the confidence interval with the lower error of the signal for the upper error of the MRF and vice versa, as the MRF will increase if the confidence interval increases or the number of signal events drops. From this the sensitivity per neutrino flavour from the full 1247 days sample is calculated to:

$$E^2 \cdot \bar{\Phi}_{90\%} = 2.21^{+0.87}_{-0.73} \cdot 10^{-8} \, \text{GeV/cm}^2 \cdot \text{sr} \cdot \text{s} \tag{12.8}$$

Table 12.2: Expected number of signal and background events sorted by neutrino flavour, type and interaction channel for the full 1247 days sample after the final cuts

Event type	Conventional atmospheric events	Prompt atmospheric events	Cosmic events
ν_e NC	$0.02^{+0.01}_{-0.01}$	$0.02^{+0.007}_{-0.01}$	$0.32^{+0.05}_{-0.10}$
$\bar{\nu}_e$ NC	$0.007^{+0.004}_{-0.004}$	$0.02^{+0.006}_{-0.009}$	$0.28^{+0.05}_{-0.09}$
ν_e CC	$0.42^{+0.26}_{-0.23}$	$0.23^{+0.07}_{-0.12}$	$2.08^{+0.35}_{-0.69}$
$\bar{\nu}_e$ CC	$0.15^{+0.10}_{-0.09}$	$0.20^{+0.06}_{-0.11}$	$2.89^{+0.49}_{-0.95}$
ν_μ NC	$0.51^{+0.32}_{-0.29}$	$0.02^{+0.007}_{-0.01}$	$0.32^{+0.05}_{-0.10}$
$\bar{\nu}_\mu$ NC	$0.10^{+0.06}_{-0.06}$	$0.02^{+0.006}_{-0.009}$	$0.28^{+0.05}_{-0.09}$
ν_μ CC	$1.05^{+0.33}_{-0.38}$	$0.04^{+0.008}_{-0.008}$	$0.78^{+0.07}_{-0.06}$
$\bar{\nu}_\mu$ CC	$0.19^{+0.06}_{-0.07}$	$0.03^{+0.006}_{-0.006}$	$0.60^{+0.06}_{-0.05}$
ν_τ NC	0	$0.001^{+0.000}_{-0.001}$	$0.32^{+0.05}_{-0.10}$
$\bar{\nu}_\tau$ NC	0	$0.001^{+0.000}_{-0.000}$	$0.28^{+0.05}_{-0.09}$
ν_τ CC	0	$0.01^{+0.005}_{-0.007}$	$1.22^{+0.55}_{-0.65}$
$\bar{\nu}_\tau$ CC	0	$0.008^{+0.003}_{-0.005}$	$1.10^{+0.55}_{-0.63}$
Atm. muons	$1.87^{*+1.53}_{-1.54}$	0	0
Total	$4.31^{+2.66}_{-2.66}$	$0.61^{+0.19}_{-0.30}$	$10.45^{+2.37}_{-3.61}$

* After 0 remaining MUPAGE events the atmospheric muon extrapolation and the high multiplicity extrapolation were used.

Chapter 13

Test on the 135 days burn sample

Before unblinding the complete available ANTARES data a test of the presented analysis is performed using the 135 days burn sample (all runs with a run number ending with 0). A comparison of Monte-Carlo and data regarding the distribution of the cut parameters has already been presented in chapter 9. Here, apart from a small excess of data events compared to simulations that is - especially after the event selection cuts - noticeable for horizontal events, no severe problems have been observed.

Table 13.1 lists the number of events after the final optimized cuts (as introduced in chapter 12), sorted by their origin or the different corrections and estimations that have been applied. Compared to table 12.1, where the same numbers are listed for the full simulated lifetime of 1247 days, one can see that for the burn sample the numbers scale down by approximately a factor of 9 as it is expected from the ratio of the lifetimes. Again, only statistical errors (following equation 12.7) and those that inherit from the specific correction are considered, except for the last row holding the total sum, where also systematic errors are included.

Table 13.1: Expected number of signal and background events sorted by their origin or correction for the 135 days burn sample after the final cuts

Sample/Correction	Signal events	Background events
RBR cosmic test flux	0.72 ± 0.004	-
RBR atmospheric Bartol [9]	-	0.26 ± 0.003
RBR prompt Enberg [10]	-	0.06 ± 0.001
Cosmic ν_τ estimation	0.32 ± 0.11	-
Prompt ν_τ estimation	-	0.002 ± 0.002
Atmospheric muon extrapolation	-	$0.18^{+2.82*}_{-0.18*}$
High multiplicity muon bundles	-	0.002 ± 0.001
Missing vertex shower correction	0.12 ± 0.02	0.02 ± 0.01
+ Systematic uncertainties	see chapter 11	
Total	$1.16^{+0.27}_{-0.40}$	$0.52^{+2.97}_{-0.33}$

* Errors have been adjusted to reach the statistical errors on 0 MUPAGE events that is $^{+3}_{-0}$.

For all cosmic event numbers an E^{-2} test flux with a normalization of $4.5 \cdot 10^{-8}$ GeV/cm$^2 \cdot$ sr $\cdot$ s per neutrino flavour was used. Table 13.2 lists all event numbers sorted by their neutrino flavour, type and interaction channel. Here, all corrections and systematic errors are included for each value. The Glashow resonance events for $\bar{\nu}_e$ have been counted in the CC channel. Small discrepancies in the total sum inherit from rounding effects.

Table 13.2: Expected number of signal and background events sorted by neutrino flavour, type and interaction channel for the 135 days burn sample after the final cuts

Event type	Conventional atmospheric events	Prompt atmospheric events	Cosmic events
ν_e NC	$0.002^{+0.001}_{-0.001}$	$0.002^{+0.001}_{-0.001}$	$0.03^{+0.01}_{-0.01}$
$\bar{\nu}_e$ NC	$0.001^{+0.000}_{-0.000}$	$0.002^{+0.001}_{-0.001}$	$0.03^{+0.01}_{-0.01}$
ν_e CC	$0.05^{+0.03}_{-0.03}$	$0.03^{+0.01}_{-0.01}$	$0.23^{+0.04}_{-0.07}$
$\bar{\nu}_e$ CC	$0.02^{+0.01}_{-0.01}$	$0.02^{+0.01}_{-0.01}$	$0.32^{+0.06}_{-0.11}$
ν_μ NC	$0.05^{+0.03}_{-0.03}$	$0.002^{+0.001}_{-0.001}$	$0.03^{+0.01}_{-0.01}$
$\bar{\nu}_\mu$ NC	$0.01^{+0.007}_{-0.006}$	$0.002^{+0.001}_{-0.001}$	$0.03^{+0.01}_{-0.01}$
ν_μ CC	$0.12^{+0.04}_{-0.04}$	$0.004^{+0.001}_{-0.001}$	$0.07^{+0.01}_{-0.01}$
$\bar{\nu}_\mu$ CC	$0.02^{+0.01}_{-0.01}$	$0.005^{+0.001}_{-0.001}$	$0.10^{+0.01}_{-0.01}$
ν_τ NC	0	$0.000^{+0.000}_{-0.000}$	$0.03^{+0.01}_{-0.01}$
$\bar{\nu}_\tau$ NC	0	$0.000^{+0.000}_{-0.000}$	$0.03^{+0.01}_{-0.01}$
ν_τ CC	0	$0.001^{+0.000}_{-0.001}$	$0.13^{+0.06}_{-0.07}$
$\bar{\nu}_\tau$ CC	0	$0.001^{+0.000}_{-0.001}$	$0.12^{+0.06}_{-0.07}$
Atm. muons	$0.18^{*+2.82^{**}}_{-0.18^{**}}$	0	0
Total	$0.45^{+2.95}_{-0.30}$	$0.07^{+0.02}_{-0.03}$	$1.16^{+0.27}_{-0.40}$

* After 0 remaining MUPAGE events the atmospheric muon extrapolation and the high multiplicity extrapolation were used.

** Errors have been adjusted to reach the statistical errors on 0 MUPAGE events that is $^{+3}_{-0}$.

To finally compare simulations to data, table 13.3 lists the number of simulated and measured events at each cut level including all corrections, estimations and systematic errors. The error on the detected data events is the statistical Poisson error $\sqrt{N}$. The ratio has been evaluated by dividing the number of data events by the sum of all simulated atmospheric events. The errors on the ratio has been calculated via Gaussian error propagation (equation (10.8)) using the lower error on the background for the upper error on the ratio and vice versa, as a lower background increases the ratio.

At each cut stage an excess of measured data events above a background only assumption can be observed. But taking into account all systematic errors the excess is always below the given upper error, for each cut stage respectively. After the zenith cut 12 data events remain in the sample, where the atmospheric background expectation is 8.1 ± 4.5. This excess was already observed in the data and Monte-Carlo comparison in figure 9.1 in chapter 9, where the differences between simulation and data was highest for horizontal events. However, note that in this plot the corrections from chapter 10,

Table 13.3: Expected number of simulated and measured events including all corrections and systematic errors for the 135 days burn sample after different cut stages

Event class	Reco output	+ VLLH < 7.9	+ Multi line filter	+ Spark-ing filter	+ zenith > 94°	+ logE > 4.0
Cosmic $\nu_\mu\nu_e\nu_\tau$ shower events	$7.2^{+1.5}_{-2.7}$	$3.8^{+0.9}_{-1.4}$	$3.7^{+0.8}_{-1.4}$	$3.4^{+0.8}_{-1.3}$	$1.5^{+0.3}_{-0.6}$	$0.99^{+0.25}_{-0.38}$
Cosmic ν_μ track events	$12.9^{+0.9}_{-0.8}$	$0.6^{+0.1}_{-0.1}$	$0.6^{+0.1}_{-0.1}$	$0.5^{+0.1}_{-0.04}$	$0.3^{+0.02}_{-0.02}$	$0.17^{+0.02}_{-0.02}$
Atmospheric $\nu_\mu\nu_e\nu_\tau$ shower events	103^{+63}_{-58}	$6.4^{+3.9}_{-3.6}$	$6.0^{+3.6}_{-3.3}$	$5.0^{+3.0}_{-2.8}$	$3.6^{+2.2}_{-2.0}$	$0.19^{+0.10}_{-0.10}$
Atmospheric ν_μ track events	1077^{+329}_{-382}	$4.9^{+1.5}_{-1.7}$	$4.4^{+1.4}_{-1.6}$	$3.7^{+1.1}_{-1.3}$	$2.7^{+0.8}_{-1.0}$	$0.15^{+0.05}_{-0.05}$
Atmospheric muons	$(1.4\pm0.5)\cdot 10^7$	171^{*+68}_{-69}	152^{*+61}_{-62}	137^{*+55}_{-56}	$1.8^{**+1.5}_{-1.5}$	$0.18^{**+2.82***}_{-0.18***}$
Data events	$1.6 \cdot 10^7$	202 ± 14.2	193 ± 13.9	170 ± 13.0	12 ± 3.5	1 ± 1
Ratio Data / Backg. only	$1.12^{+0.41}_{-0.41}$	$1.11^{+0.46}_{-0.45}$	$1.19^{+0.50}_{-0.49}$	$1.17^{+0.49}_{-0.48}$	$1.48^{+0.92}_{-0.92}$	$1.92^{+2.27}_{-1.92}$

* Including high multiplicity extrapolation
** After 0 remaining MUPAGE events the atmospheric muon extrapolation and the high multiplicity extrapolation were used.
*** Errors have been adjusted to reach the statistical errors on 0 MUPAGE events that is $^{+3}_{-0}$.

such as the extrapolation of atmospheric muons, is not included. After the final cut then 1 data event remains, where an atmospheric background contribution of $0.52^{+2.97}_{-0.33}$ events is expected. Here, the statistical error on the extrapolated number of 0.18 atmospheric muons has been set to $^{+2.82}_{-0.18}$ to ensure that the statistical error on originally 0 remaining MUPAGE events is covered. As in the RBR MUPAGE simulations for atmospheric muons only one third of the lifetime is simulated the Poisson error on 0 events is $^{+3\cdot\sqrt{1}}_{0}$. For both discussed cut stages the excess of data events, hence, is within the statistical and systematic errors of a background only hypothesis.

From $0.52^{+2.97}_{-0.33}$ background events the average 90 % confidence interval upper limit, following equation (12.4), is evaluated to $2.88^{+1.74}_{-0.27}$. Hence, taking into account $1.16^{+0.27}_{-0.40}$ signal events, the MRF, after equation (12.6), is $2.48^{+1.73}_{-0.62}$. Following equation (12.5) the sensitivity per neutrino flavour from the 135 days burn sample is calculated to:

$$E^2 \cdot \bar{\Phi}_{90\%} = 1.12^{+0.78}_{-0.28} \cdot 10^{-7} \, \text{GeV/cm}^2 \cdot \text{sr} \cdot \text{s} \tag{13.1}$$

13.1   Upper limit

From 1 remaining data event and 0.52 expected background events the Feldman-Cousins 90 % confidence interval upper limit, as introduced in 12.1, yields a value of $\mu_{90,2} = 3.84$. As upper limit one would obtain a value of $E^2 \cdot \Phi_{90\%} = 1.49 \cdot 10^{-7}\,\mathrm{GeV/cm^2 \cdot sr \cdot s}$ per neutrino flavour, following equation (12.2). However, this method is based on Poisson statistics only and does not take into account systematic errors. Hence, a modified approach is presented in [15] to include systematic errors in the signal and background efficiencies. Therefore, the program **Pole 1.0** [16] was used that performs the Neyman-Construction assuming Gaussian PDF functions for the errors of the signal and background efficiencies.

As relative errors on the efficiencies that are required as input parameters for Pole 1.0 the respective mean of the upper and the lower systematic error over the number of events have been used. The errors on the signal events, as given in table 13.3, are primarily systematic errors, thus they can be used directly for the evaluation of the relative signal efficiency error, for which a value of $(0.27 + 0.40)/(2 \cdot 1.16) = 0.29$ is obtained.

For the background the Poisson error on the atmospheric muon extrapolation has to be removed from the total given error to get the pure systematic error. The error assumption of $0.18^{+2.82}_{-0.18}$ in table 13.3 was an ad hoc assumption to include the statistical error on 0 remaining MUPAGE events, that is $3 \cdot \sqrt{1} = 3$ and must not be taken into account for Pole 1.0. The remaining systematic error on the atmospheric muon extrapolation is ± 0.07. Hence, the relative background efficiency error from the complete remaining systematic errors (for atmospheric ν events see table 13.3) is $(0.22 + 0.22)/(2 \cdot 0.52) = 0.42$.

Using these values in Pole 1.0 the confidence interval upper limit raises to 4.25. Hence, from the 135 days burn sample the flux upper limit per neutrino flavour, following equation (12.2), is evaluated to:

$$E^2 \cdot \Phi_{90\%} = 1.65 \cdot 10^{-7}\,\mathrm{GeV/cm^2 \cdot sr \cdot s} \tag{13.2}$$

A data card that was used to run the Pole 1.0 program is printed in appendix E.1.

13.2   The remaining up-going data events

To get an impression of what kind of events survive the event selection criteria introduced in chapter 7 and the zenith lower cut at 94° the data events that remain in the burn sample after these cuts have been investigated in further detail before analysing the full data sample. It was during these studies, when it, for example, became obvious

that a sparking event filter has to be added to the analysis chain as in the data sample after the reduced vertex log-likelihood cut some suspicious events appeared (see also chapter 7.2.2). With the new filter included the MRF optimization was repeated and after some iterations the analysis chain converged to its final state that was presented here, where now 12 data events survive the "stronger up-going" cut at 94°, slightly below the horizon.

Table 13.4 lists the properties of these events, where the event that also survives the logarithmic fitted energy lower cut at 4.0 is printed in bold font. The number of hits/strings and the total charge always refer to the selected shower hits. The *vertex position* of an event is named *detector* if the vertex is fitted inside the instrumented volume, *center* if the vertex is closer than half of the radius in horizontal direction and a quarter of the height in vertical direction to the detector center. If the position is fitted outside the instrumented volume the distance to the detector edge is given, marked with *v* if the distance is in vertical direction (i.e. below the detector) or *h* for horizontal direction. *Burst fraction* and *mean rate* are explained in chapter 4.1, *quality basic* in chapter 8.1.

What can be derived from the table is:

- For all remaining events the vertex is contained in the detector or very close to it with a maximum of $\approx 60\,\mathrm{m}$ distance from the edge of the instrumented volume.

- Two of them have been detected in conditions with a mean background rate above $200\,\mathrm{kHz}$.

- All events have been detected in the 12-line configuration of the detector.

- The integrated charge of all selected shower hits is not directly connected to the fitted energy, which is expected due to the fit procedure of the Dusj reconstruction, where the energy is not related to the total charge but evaluated from each single hit.

- The high energy event that survives the final cut has been detected in a good run with a quality basic value of 4.

To validate the result of the fit procedure, for each of these events the likelihood landscapes of the two maximum likelihood fits have been plotted, all showing that the fit converged well in the minimum. To give an example, figure 13.1 shows the four dimensional log-likelihood landscape of the vertex fit for the finally remaining data event, for which a clear minimum can be seen that has been found well by the minimizer. Figure 13.2 shows the landscape of the energy direction fit. Here, one can see a broader minimum which reflects well the angular and energy resolution of the Dusj reconstruction. The event would have also survived the cuts if the minimizer

Table 13.4: Remaining data events in the burn sample after event selection cuts and a lower cut on the fitted zenith

Run ID	Event ID	Trigger counter	Detector configuration	Date [UTC]	Fitted energy [TeV]	Fitted zenith [°]	# hits / strings	Total charge [pe]	Vertex position	Run burst fraction	Run mean rate [kHz]	Quality basic
41400	47104	752409	12Line	2009-06-19 20:39	2.8	98	39/3	194	Detector	0.19	202	2
43450	32585	282256	12Line	2009-09-27 14:34	2.5	104	74/5	477	Center	0.42	270	1
46150	17735	1640015	12Line	2010-01-28 07:46	0.8	139	49/4	211	Detector	0.34	175	1
51140	49565	156280	12Line	2010-08-14 22:55	7.0	115	136/6	835	Detector	0.05	80	4
53300	40913	2613984	12Line	2010-11-22 01:33	1.6	99	51/3	145	Detector	0.06	63	4
54260	**1639**	**2925759**	**12Line**	**2011-01-01 06:51**	**98.0**	**114**	**146/7**	**1158**	**57 h***	**0.16**	**92**	**4**
57700	34266	763380	12Line	2011-05-28 19:59	1.1	105	52/3	237	Detector	0.13	65	1
58650	35514	1436605	12Line	2011-07-14 17:04	2.2	127	42/5	344	13 h*	0.13	94	4
59930	2497	138881	12Line	2011-09-26 09:29	0.8	129	59/3	278	Detector	0.22	111	3
60290	47011	115612	12Line	2011-10-14 23:04	0.8	104	50/3	371	Detector	0.28	120	1
61850	12391	872460	12Line	2011-12-29 02:09	0.8	98	45/4	157	Detector	0.12	72	4
62170	101244	134734	12Line	2012-01-15 00:56	9.2	100	78/4	458	28 h*	0.19	88	4

* Distance in meters to detector edge, (h) horizontally, (v) vertically

had converged on a slightly different location inside the broader area of the minimum, represented by purple colour. In the azimuth a second local minimum is observed that is a mirror solution at a direction that is tilted by twice the Cherenkov angle. However, as no cut on the azimuth is performed, it would not have made a difference if the minimizer converged in the other minimum. Finally, figure 13.3 shows the distribution of the selected shower hits in the detector scheme.
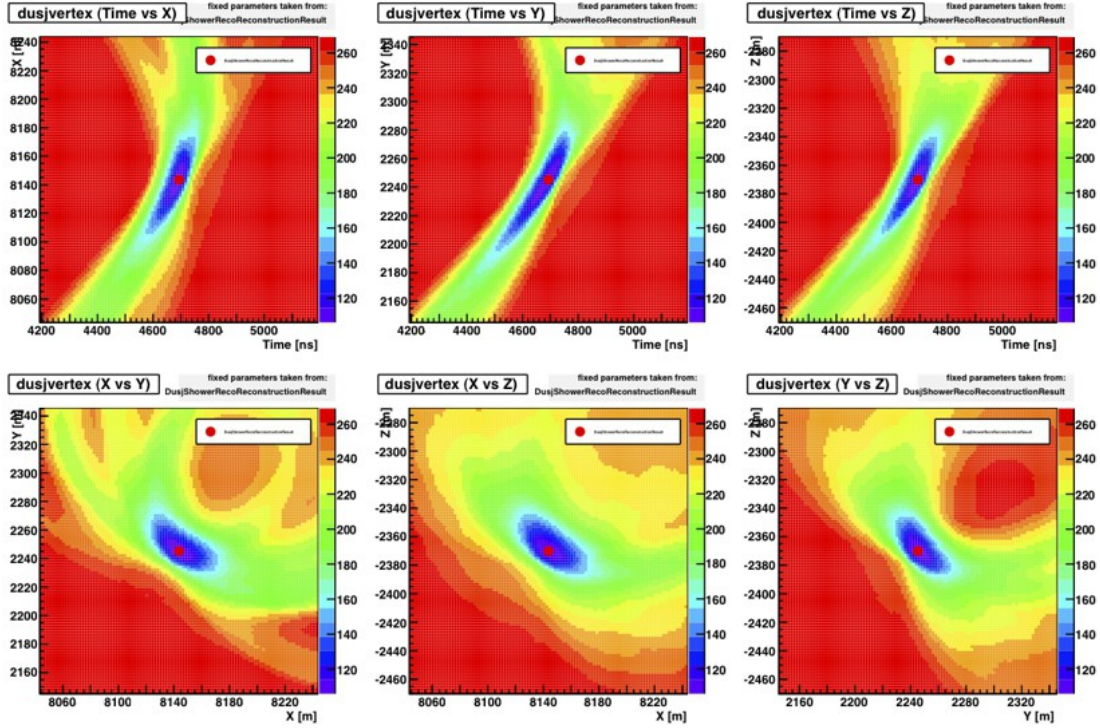
Figure 13.1: *Vertex log-likelihood landscape of an event in run 54260.* The plots show the four dimensional vertex log-likelihood landscape of the ANTARES data event (ID 1639 / Trigger-Counter 2925759) in run 54260. Each plot shows the landscape as function of two of the fit parameters x, y, z and *time*, where the two not displayed ones are kept fixed from the fit result. The red points mark the position where the minimizer converged.
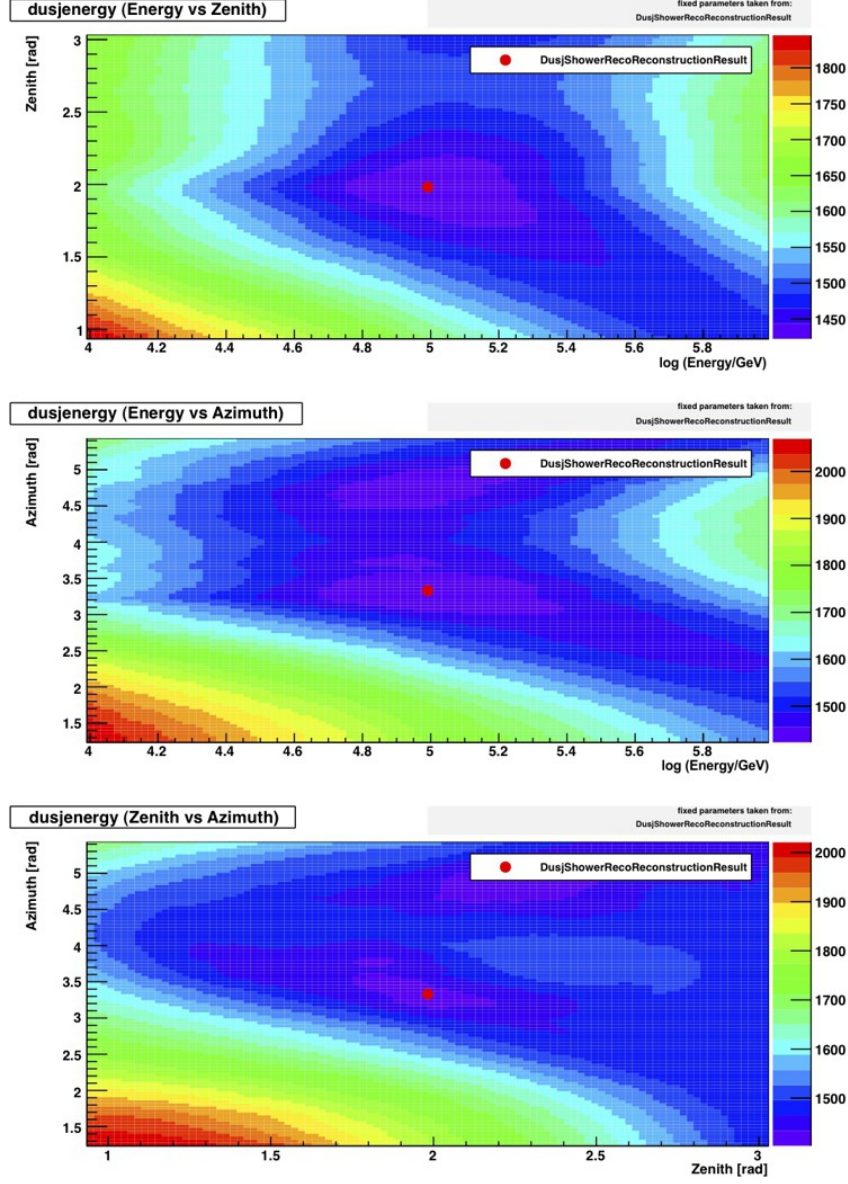
Figure 13.2: *Energy direction log-likelihood landscape of an event in run 54260.* The plots show the three dimensional energy direction log-likelihood landscape of the ANTARES data event (ID 1639 / Trigger-Counter 2925759) in run 54260. Each plot shows the landscape as function of two of the fit parameters *energy*, *zenith* and *azimuth*, where the third one is kept fixed from the fit result. The red points mark the position where the minimizer converged.
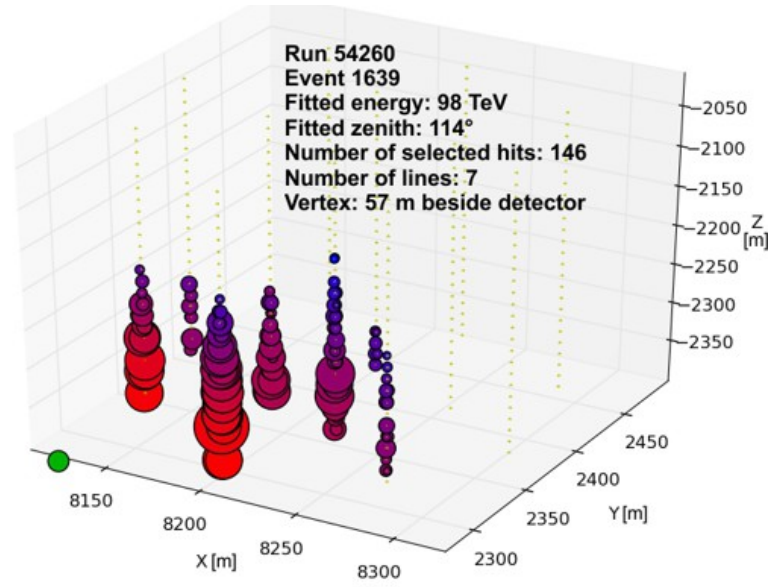
Figure 13.3: *Distribution of the selected shower hits in the detector for an event in run 54260.* The figure illustrates the distribution of the selected shower hits in the detector for the data event (ID 1639 / Trigger-Counter 2925759) in run 54260. Each circle marks a detected hit, where the size is related to the hit charge and the color indicates the arrival time from early (red) to late (blue). The green point marks the reconstructed vertex position at (8143, 2245, -2370). The image has been created using a script from [118].

Chapter 14

Analysis of the full 1247 days sample

In an extensive refereeing process the work up to this point, including the test on the burn sample, has been evaluated by four representative members of the ANTARES collaboration from different institutes. During this process that lasted half a year the analysis got its final fine-tuning, such as for example the introduction of the sparking event filter. What is presented in the previous chapters, of course, is already the updated version. Finally the analysis chain was accepted in March 2014 and the decision was made to unblind the remaining 90 % of the data that was not looked at until now.

The unblinding of the full 1247 days sample revealed 8 remaining events after the final cuts (as introduced in chapter 12.2) where $4.92^{+2.85}_{-2.96}$ are expected from atmospheric background. Table 14.1 lists the number of simulated and measured events at each cut level including all corrections, estimations and systematic errors. The error on the detected data events is the statistical Poisson error $\sqrt{N}$. The ratio has been evaluated by dividing the number of data events by the sum of all atmospheric events. The errors on the ratio has been calculated via Gaussian error propagation (equation (10.8)) using the lower error on the background for the upper error on the ratio and vice versa, as a lower background increases the ratio.

Again for the cosmic test flux an E^{-2} spectrum with a normalization of $4.5 \cdot 10^{-8}\,\mathrm{GeV/cm^2 \cdot sr \cdot s}$ per neutrino flavour was used. Whereas in the corresponding table for the burn sample (table 13.3 in chapter 13) an excess of data compared to an atmospheric background only hypothesis was observed throughout all cut stages, here the excess is in favour of Monte-Carlo and is less distinctive. Thus, compared to the burn sample the measurement is more compatible with the atmospheric neutrino and muon flux. However, after the final cut the excess again is in the measurement and accounts for $+63\,\%$. This suggests the assumption of having found an indication for a cosmic signal, which is encouraged by the fact that for earlier cut stages less data events are measured than expected from atmospheric background and thus, the analysis of the full sample does not have an intrinsic over-fluctuation of measured data events, as it looked like in the burn sample. The excess over background does not emerge before the cut on the fitted energy is applied.

Table 14.1: Expected number of simulated and measured events including all corrections and systematic errors for the full 1247 days sample after different cut stages

Event class	Reco output	+ VLLH < 7.9	+ Multi line filter	+ Spark-ing filter	+ zenith > 94°	+ logE > 4.0
Cosmic $\nu_\mu\nu_e\nu_\tau$ shower events	$65.7^{+13.3}_{-24.1}$	$35.1^{+7.9}_{-12.9}$	$33.7^{+7.6}_{-12.7}$	$31.0^{+7.1}_{-11.5}$	$14.05^{+3.01}_{-5.03}$	$9.07^{+2.24}_{-3.50}$
Cosmic ν_μ track events	$119.7^{+8.6}_{-7.4}$	$5.05^{+0.37}_{-0.32}$	$4.77^{+0.35}_{-0.31}$	$4.37^{+0.35}_{-0.31}$	$2.03^{+0.15}_{-0.13}$	$1.38^{+0.13}_{-0.12}$
Atmospheric $\nu_\mu\nu_e\nu_\tau$ shower events	949^{+582}_{-531}	$60.0^{+35.9}_{-33.6}$	$55.6^{+33.3}_{-31.2}$	$47.3^{+28.3}_{-26.5}$	$33.9^{+20.3}_{-19.0}$	$1.74^{+0.92}_{-0.96}$
Atmospheric ν_μ track events	10073^{+3081}_{-3575}	$47.1^{+14.4}_{-16.7}$	$43.0^{+13.1}_{-15.2}$	$36.7^{+11.2}_{-13.0}$	$26.8^{+8.2}_{-9.5}$	$1.31^{+0.40}_{-0.46}$
Atmospheric muons	$(1.31 \pm 0.5) \cdot 10^8$	1744^{*+693}_{-702}	1511^{*+558}_{-568}	1430^{*+529}_{-537}	$21.1^{**+11.1}_{-11.1}$	$1.87^{**+1.52}_{-1.53}$
Data events	$1.46\cdot10^8 \pm 1.2 \cdot 10^4$	1727 ± 41.6	1592 ± 39.9	1394 ± 37.3	60 ± 7.8	8 ± 2.8
Ratio Data / Backg. only	$1.11^{+0.42}_{-0.41}$	$0.93^{+0.38}_{-0.37}$	$0.99^{+0.38}_{-0.37}$	$0.92^{+0.35}_{-0.35}$	$0.73^{+0.37}_{-0.37}$	$1.63^{+1.13}_{-1.10}$

* Including high multiplicity extrapolation
** After 0 remaining MUPAGE events the atmospheric muon extrapolation and the high multiplicity extrapolation are used.

The tables that list the event numbers, sorted by the different neutrino types, flavours and interaction channels as well as by contributions from different corrections and estimations have already been shown in chapter 12.2 (see tables 12.1 and 12.2).

Another indication that the measured excess is due to a cosmic neutrino flux can be found in Monte-Carlo and data comparison plots that now can be drawn with a greater statistical significance than from the burn sample. In chapter 9 it was shown that right after the reconstruction, i.e. when no shower event selection is applied yet, the distributions of the fitted shower energy and the zenith angle agree well between simulation and data, apart from a constant offset throughout the whole energy and zenith angle range that accounts for 12 % in favour of data. After the shower event selection criteria from chapter 7 have been applied, the sample is still dominated by atmospheric muons at a ratio of $17 \pm 10 : 1$ with respect to atmospheric neutrino events. Concerning the fitted zenith these events still show a good agreement between simulation and data, as it is shown in figure 14.1. Concerning the fitted energy (figure 14.2, left plot), however, the reconstruction of data events tends to yield a slightly lower energy than predicted from atmospheric muon simulations. But with the up-going cut (zenith $> 94°$) applied those muons are removed and the agreement improves for the remaining neutrino events (figure 14.2, right plot). For the high energy region above 10 TeV, where the final cut is applied, an excess of data over background emerges that finally yields 8 over

4.92 events. Hence, the excess is observed not until all atmospheric muons have been removed and the atmospheric neutrino background has been reduced by the energy cut. Note that in the comparison plots the extrapolation for atmospheric muons (as introduced in chapter 10.3) is not included. From that an additional contribution of $1.87^{+1.52}_{-1.53}$ events is added to the sample after the final cuts.
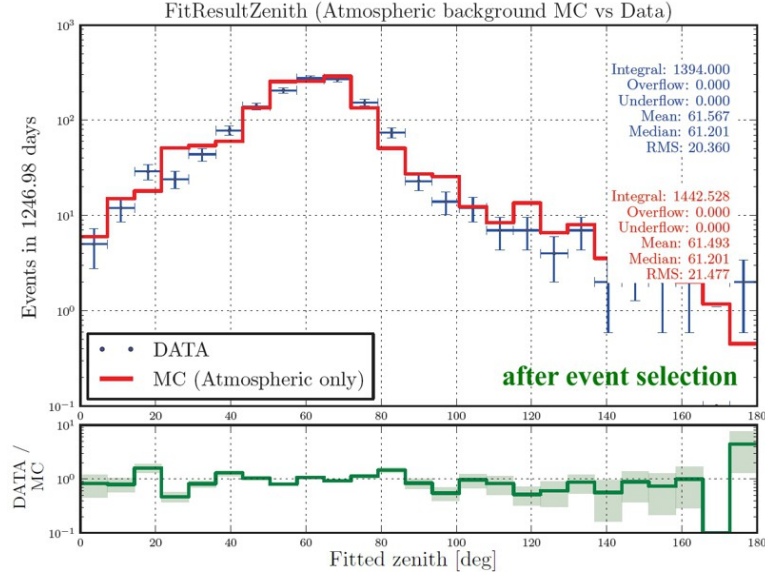
Figure 14.1: *Monte-Carlo data comparison of the fitted zenith in the full sample.* The plot shows the distributions of the fitted zenith for atmospheric Monte-Carlo (red) and data events (blue) from the sample of events that remain after the event selection criteria from chapter 7 have been applied. The error bars on the data sample mark the Poisson statistical errors, but no systematic errors. The simulated events contain atmospheric muons and electron and muon neutrinos. Note that the extrapolation of atmospheric muons (as introduced in chapter 10.3) is not yet included and slightly increases the Monte-Carlo distribution in the horizontal region. The plots have been generated from all runs of the full 1247 days sample.

From Poisson statistics the probability to measure an excess of 8 or more events, where 4.92 are expected is calculated to 12.52%. Hence, by looking at a one-sided Gaussian distribution this refers to a significance of $1.53\,\sigma$. If the excess really originates from a cosmic signal, the statistical power, however, is rather small. It should be further mentioned that the 8 events are still compatible with a background only hypothesis, when taking the systematic and statistical error on the simulation that is $4.92^{+2.85}_{-2.96}$ and the Poisson error on the measurement 8 ± 2.8 into account.

14.1 Upper limit

In the same manner as for the burn sample (see chapter 13.1) an upper limit on the diffuse cosmic neutrino flux can be evaluated, now from the full 1247 days. Following the Feldman-Cousins approach as introduced in chapter 12.1 a 90% confidence interval
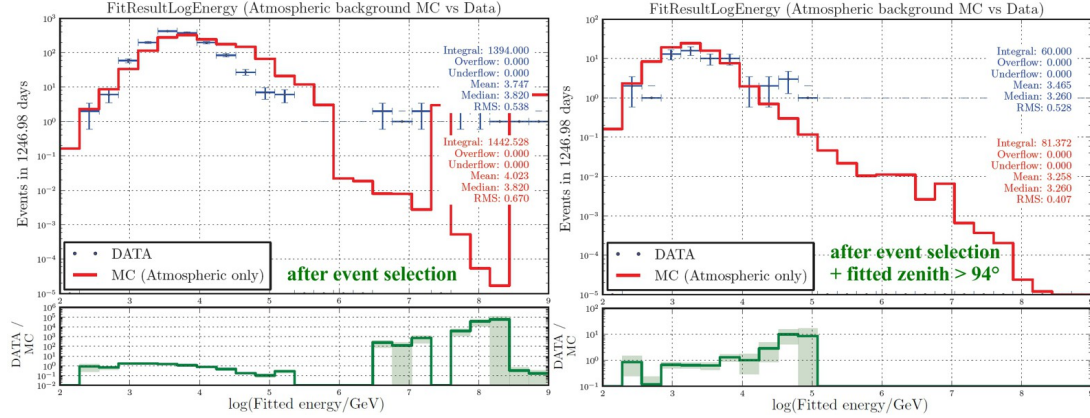
Figure 14.2: *Monte-Carlo data comparison of the fitted shower energy in the full sample.* The plots show the distributions of the logarithmic fitted shower energy for atmospheric Monte-Carlo (red) and data events (blue) from the sample of events that remain after the event selection criteria from chapter 7 have been applied (left) and that survive an additional lower cut on the fitted zenith at 94° (right). The error bars on the data sample mark the Poisson statistical errors, but no systematic errors. The simulated events contain atmospheric muons and electron and muon neutrinos. Note that the extrapolation of atmospheric muons (as introduced in chapter 10.3) is not yet included and increases the Monte-Carlo distribution above 10 TeV by ≈ 1.9 events. The plots have been generated from all runs of the full 1247 days sample.

upper limit of $\mu_{90,2} = 9.08$ is evaluated from 8 measured and 4.92 expected background events. From equation (12.2) this transfers to an upper limit on the neutrino flux of $E^2 \cdot \Phi_{90\%} = 3.91 \cdot 10^{-8} \, \text{GeV/cm}^2 \cdot \text{sr} \cdot \text{s}$ per neutrino flavour, however, without having taken systematic errors into account.

To include systematic errors in the Neyman-Construction the Program **Pole 1.0** [15][16] was used that assumes Gaussian PDF functions for the errors of the signal and background efficiency. The relative errors on the efficiencies again have been taken from the mean of the upper and the lower systematic error over the event number. The errors on the signal events, as given in table 14.1, are primarily systematic errors. Thus, they can be used directly for the evaluation of the relative signal efficiency error, wherefore a value of $(2.37 + 3.62)/(2 \cdot 10.45) = 0.29$ is obtained.

For the background, the Poisson error on the atmospheric muon extrapolation has to be removed from the total given error to get the pure systematic error. The error of $1.87^{+1.52}_{-1.53}$ is dominated by the Poisson error that is ± 1.37. The remaining systematic error on the atmospheric muon extrapolation is $^{+0.68}_{-0.69}$. Hence, the relative background efficiency error from the complete remaining systematic errors (for atmospheric ν events see table 14.1) is $(2.00 + 2.11)/(2 \cdot 4.92) = 0.42$. As expected, both relative systematic errors yield the same values as for the burn sample.

Using these values in Pole 1.0 the confidence interval upper limit raises to 11.40. Hence, for the full 1247 days sample the upper limit on the diffuse cosmic neutrino flux

per neutrino flavour, following equation (12.2), is evaluated to:

$$E^2 \cdot \Phi_{90\%} = 4.91 \cdot 10^{-8} \, \mathrm{GeV/cm^2 \cdot sr \cdot s} \tag{14.1}$$

A data card that was used to run the Pole 1.0 program is printed in appendix E.2.

To obtain the validity range for the evaluated limit the distribution of the Monte-Carlo shower energy from all simulated events that survive the final cuts was used. Figure 14.3 shows the combined distribution for CC ν_e and NC ν_μ and ν_e events (and their anti-neutrinos), i.e. all event channels and flavours that are covered by the RBR simulation without any corrections from chapter 10.
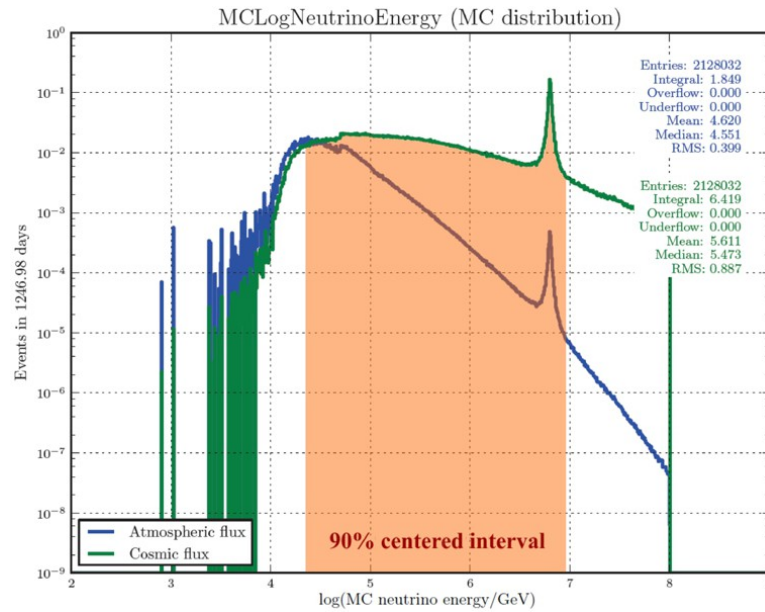
Figure 14.3: *Monte-Carlo shower energy spectra of remaining simulated events after the final cuts.* The plot shows the Monte-Carlo shower energy spectra of the remaining atmospheric (blue) and cosmic (green) simulated neutrino events after the final cuts. All simulated events in the RBR, i.e. CC ν_e and NC ν_μ and ν_e events (and their anti-neutrinos) are included in the plot. The corrections that have been introduced in chapter 10, such as for example the estimation of ν_τ, have not been taken into account here. The orange interval was placed in a way that 90 % of all cosmic events are covered, where above and below 5 % are excluded, respectively. The plot has been generated from all runs of the full 1247 days sample.

An interval (indicated by the orange area) that covers 90 % of the events was placed centred, with 5 % of the events being excluded above and below, respectively. Hence, the validity range of the limit is defined as the energy interval that holds 90 % of the detectable events after the final cuts. This interval was evaluated to

$$E_{90\%} = [22.7 \, \mathrm{TeV}, 7.8 \, \mathrm{PeV}] \tag{14.2}$$

14.2   The remaining up-going data events

Compared to the burn sample, where 12 data events remained after the lower cut on the fitted zenith at 94°, in the full sample 60 events are left, which is significantly less than would have been expected from the scaling of the lifetimes (111 events). It seems as if the burn sample is not really a good representative sub sample for the whole data, as it holds a substantial larger number of finally selected, shower-like events, which also is reflected in the fact that in the burn sample the excess was observed in data over background throughout all cut stages, whereas in the full sample it is mostly vice versa. The reason for this, however, is not yet understood as the selection of the burn sample runs was quite randomly (by using all runs with a run number ending with the digit 0) and also covers the whole data taking period.

The tables 14.2 - 14.4 list the properties of the 60 up-going (zenith > 94°) events, where the 8 events that also survive the logarithmic fitted energy lower cut at 4.0 are printed in bold font. The number of hits/strings and the total charge always refer to the selected shower hits. The *vertex position* of an event is named *detector* if the vertex is fitted inside the instrumented volume, *center* if the vertex is closer than half of the radius in horizontal direction and a quarter of the height in vertical direction to the detector center. If the position is fitted outside the instrumented volume the distance to the detector edge is given, marked with v if the distance is in vertical direction (i.e. below the detector) or h for horizontal direction. *Burst fraction* and *mean rate* are explained in chapter 4.1, *quality basic* in chapter 8.1.

What catches one's eye in these tables is that - compared to the burn sample - now also a fraction of events from the 5-line and 10-line detector configuration periods survive all the cuts, which was of course expected, as for instance the 5-line period holds about 17 % of the total lifetime. Further, the average number of lines that finally have been used for the fit in these 60 events is 4.3, which means that also in the fully operational detector the selected hits are arranged in a configuration that would have also been feasible with the 5-line detector. Note that the hit selection, as introduced in chapter 6.1, was tuned to provide a very high purity and therefore looses approximately half of the signal hits.

However, what is remarkable is the fact that 3 of the 8 finally selected high energy events (printed in bold) have been detected during the 5-line period, where from simulation a background contribution of just 0.57 events is expected. The probability of having an over-fluctuation of 3 or more events is 2 %, which yields a statistical significance of $2.3\,\sigma$. In return, other data taking periods, such as the complete years of 2008 and 2011, do not contribute any event.

Among the 60 events for 35 the vertex position has been reconstructed inside the instrumented volume. For the remaining, not contained events the maximum distance

of the fitted shower vertex to the detector edge is 84 m, which is slightly farther than observed in the burn sample but still within expectations as for cosmic neutrino simulations the fitted vertex can reach positions of up to 150 m from the detector edge. Of course, high energy events cover a larger volume in possible vertex position results than low energy events as a low energy event that is located far off the detector has a smaller change of causing signals in the OMs. Note that the vertex fit is performed on the timing information of the hits only. The energy is reconstructed in a second step with the vertex position kept fixed to avoid that the fit chooses a vertex position far outside and falsely increases the energy instead (see chapter 6.2).

After the final cut on the fitted energy only events with a vertex outside the detector remain. Figure 14.4 shows an artist's view of these 8 events and their selected shower hits in the detector. 6 of them appear as nice shower events, for which another shower vertex reconstruction algorithm, called BBFit [7], yields a vertex position not farther away than 15 m. BBFit is a very fast and robust fit that reconstructs an event twice, as a shower and as a muon track event, and decides based on some quality parameters, which of them yields the best agreement to the data. For these 6 events the routine denoted the hit pattern clearly as shower. For the first 5-line event (RunID 26397) the vertex position result of BBFit differs by 116 m from the Dusj result, however, the event was also selected as shower by BBFit. Unfortunately, one event (RunID 43639) survived the final cuts by a very unlucky chance. It is basically a single line event that only could pass the multi line filter (see chapter 7.2.1) as two single hits on two different neighbouring lines have been selected by the hit selection. To avoid that background hits are accidentally selected as showers hits, if they pass the time residual condition by chance, an additional safety criterion was applied that requires from each hit to be closer than 50 m to a coincidence of big hits or the preliminary vertex estimation (see chapter 6.1.2 for a detailed description of this routine). Both conditions have been unluckily fulfilled for both single hits. BBFit classifies the event as clear muon track.

Table 14.2: Remaining data events in the full sample after event selection cuts and a lower cut on the fitted zenith (Part 1 of 3)

Run ID	Event ID	Trigger counter	Detector configuration	Detector Date [UTC]	Fitted energy [TeV]	Fitted zenith [°]	# hits / strings	Total charge [pe]	Vertex position	Run burst fraction	Run mean rate [kHz]	Quality basic
26397	129099	4046	5Line	2007-03-02 06:37	42.1	126	42/3	168	29 h, 45 v*	0.41	91	1
27893	74913	21742	5Line	2007-05-26 19:43	16.3	98	75/3	321	61 h*	0.05	63	4
28446	20087	96972	5Line	2007-06-22 11:45	2.6	177	64/4	383	Detector	0.06	65	4
28722	45202	426	5Line	2007-07-13 03:29	39.1	106	186/5	1373	22 h*	0.04	63	4
29551	113754	1678	5Line	2007-09-19 19:35	2.1	99	47/4	194	25 h*	0.57	125	1
30162	59159	703	5Line	2007-11-02 07:27	1.6	115	51/3	197	20 h*	0.11	60	1
30336	124385	1501	5Line	2007-11-17 14:47	1.1	111	42/3	193	Center	0.07	55	4
30592	10231	13420	10Line	2007-12-10 13:39	1.9	109	64/5	264	Detector	0.16	60	4
31275	90189	1336	10Line	2008-01-12 18:18	1.6	108	56/5	319	Detector	0.07	52	4
32283	70238	18906	10Line	2008-02-24 13:33	3.0	134	85/4	568	Detector	0.02	54	4
33713	100118	9127	10Line	2008-04-23 03:48	1.5	159	47/4	210	Detector	0.14	63	4
34796	33243	6663	12Line	2008-06-12 18:08	1.8	108	55/3	217	Detector	0.04	63	4
35336	42797	10550	12Line	2008-09-13 11:48	1.0	101	44/4	146	Center	0.22	148	3
35933	30513	74729	12Line	2008-10-02 21:20	1.1	143	70/6	282	Detector	0.28	194	3
36475	31623	9522	12Line	2008-10-18 02:45	4.7	122	67/4	648	14 v*	0.22	145	3
36552	7188	4464	12Line	2008-10-21 23:33	1.6	150	56/4	280	Center	0.48	344	2
37783	25390	13777	12Line	2008-12-12 08:40	4.7	112	70/5	280	Detector	0.15	92	4
39104	57792	37941	12Line	2009-02-14 17:29	2.8	117	50/5	168	7 v*	0.33	191	3
39122	63278	81877	12Line	2009-02-15 18:21	8.4	117	48/4	167	47 h*	0.10	73	4
39331	63304	50873	12Line	2009-02-25 13:39	7.4	105	51/5	151	19 h, 44 v*	0.14	96	4
40119	6	46	12Line	2009-04-13 08:02	2.2	104	52/3	452	Detector	0.31	243	3
42119	148518	280014	12Line	2009-07-25 19:47	6.0	101	73/4	429	Detector	0.09	118	4
43639	66178	479501	12Line	2009-10-05 06:08	87.5	130	36/3	74	84 h, 1 v*	0.09	90	4
45946	71285	2061417	12Line	2010-01-20 08:21	1.1	134	50/4	197	Detector	0.11	73	4

* Distance in meters to detector edge, (h) horizontally, (v) vertically

Table 14.3: Remaining data events in the full sample after event selection cuts and a lower cut on the fitted zenith (Part 2 of 3)

Run ID	Event ID	Trigger counter	Detector config-uration	Date [UTC]	Fitted energy [TeV]	Fitted zenith [°]	# hits / strings	Total charge [pe]	Vertex position	Run burst frac-tion	Run mean rate [kHz]	Quality basic
46009	9533	400972	12Line	2010-01-23 01:54	0.9	129	47/3	283	Detector	0.09	64	4
46852	**51708**	**917709**	**12Line**	**2010-02-25 19:44**	**39.3**	**143**	**91/6**	**603**	**84 v***	**0.13**	**87**	**1**
47679	12186	77946	12Line	2010-03-30 16:42	9.1	148	69/3	557	5 h, 20 v*	0.23	138	1
47838	65111	673623	12Line	2010-04-06 03:50	0.8	124	44/3	310	8 h*	0.08	67	4
49425	**32175**	**104853**	**12Line**	**2010-06-19 10:41**	**21.4**	**101**	**88/6**	**562**	**22 v***	**0.36**	**235**	**1**
49518	64893	1587	12Line	2010-06-22 11:44	1.0	105	50/5	143	Center	0.60	438	1
50675	10418	889360	12Line	2010-07-29 03:20	6.7	136	60/5	269	5 h*	0.53	396	1
51411	20931	590464	12Line	2010-08-23 00:46	2.5	114	65/5	420	Detector	0.26	163	3
51879	**9640**	**274664**	**12Line**	**2010-09-10 11:27**	**15.0**	**120**	**50/3**	**318**	**40 h***	**0.16**	**100**	**4**
51991	6122	153796	12Line	2010-09-15 06:43	5.4	94	71/4	380	Detector	0.18	103	4
52087	97516	465265	12Line	2010-09-20 06:03	0.3	160	37/3	169	Detector	0.25	145	3
53119	29228	609027	12Line	2010-11-14 20:33	1.2	145	55/3	265	Detector	0.06	56	4
54326	36824	4031901	12Line	2011-01-04 10:05	1.2	110	63/4	371	10 h*	0.16	85	4
55894	106093	204907	12Line	2011-03-11 01:47	2.9	114	82/6	387	Detector	0.27	136	1
58045	78338	186199	12Line	2011-06-14 04:55	1.1	157	53/3	273	Detector	0.11	111	4
58498	29935	388601	12Line	2011-07-07 06:08	1.4	106	45/4	250	27 h*	0.42	204	1
58686	30898	1716155	12Line	2011-07-16 15:35	0.8	107	49/4	332	Detector	0.11	83	4
58812	25119	67234	12Line	2011-07-24 03:54	1.1	101	46/4	126	Detector	0.41	232	1
58892	39915	17513	12Line	2011-08-04 15:44	0.5	154	47/4	181	Center	0.10	90	4
59425	99043	90861	12Line	2011-09-01 07:23	0.7	100	48/5	200	Detector	0.15	101	4
59692	54812	680785	12Line	2011-09-15 08:33	5.9	99	61/4	331	51 h*	0.16	95	4
59712	19763	1057429	12Line	2011-09-16 06:00	1.4	100	39/4	230	4 h*	0.19	104	4
59797	6532	2136	12Line	2011-09-19 01:20	4.8	94	77/7	452	Detector	0.19	109	4
60226	91161	1165187	12Line	2011-10-12 02:13	1.5	135	46/4	166	Detector	0.31	132	1

* Distance in meters to detector edge, (h) horizontally, (v) vertically

Table 14.4: Remaining data events in the full sample after event selection cuts and a lower cut on the fitted zenith (Part 3 of 3)

Run ID	Event ID	Trigger counter	Detector config-uration	Date [UTC]	Fitted energy [TeV]	Fitted zenith [°]	# hits / strings	Total charge [pe]	Vertex position	Run burst frac-tion	Run mean rate [kHz]	Quality basic
60704	47177	5632054	12Line	2011-11-02 10:54	1.7	133	50/5	205	Detector	0.09	65	4
60861	33966	41994	12Line	2011-11-09 14:24	2.8	120	66/3	465	Detector	0.17	84	4
61975	85577	2908926	12Line	2012-01-04 17:15	1.5	97	59/4	153	Center	0.10	62	4
62139	7176	2287775	12Line	2012-01-13 04:49	2.7	102	55/3	427	15 $h*$	0.37	220	3
62228	38130	279600	12Line	2012-01-16 16:19	7.1	96	97/7	519	Detector	0.20	94	4
62834	**30474**	**384475**	**12Line**	**2012-02-19 17:11**	**28.1**	**118**	**99/7**	**456**	**69 $v*$**	**0.16**	**66**	**4**
63013	66930	11840	12Line	2012-02-29 01:07	7.8	137	65/4	263	36 $h*$	0.38	214	3
64914	34922	24770	12Line	2012-06-19 05:00	4.5	99	62/5	517	Detector	0.39	307	2
65259	40468	89673	12Line	2012-07-04 21:42	1.6	96	59/4	227	Detector	0.13	106	4
65434	19098	251505	12Line	2012-07-12 16:09	0.3	115	40/3	133	Center	0.37	198	3
66772	36322	3313506	12Line	2012-09-19 02:56	1.8	126	48/4	313	Detector	0.12	67	1
67723	71283	449623	12Line	2012-11-06 07:31	2.3	175	55/7	220	34 $v*$	0.23	103	1

* Distance in meters to detector edge, (h) horizontally, (v) vertically
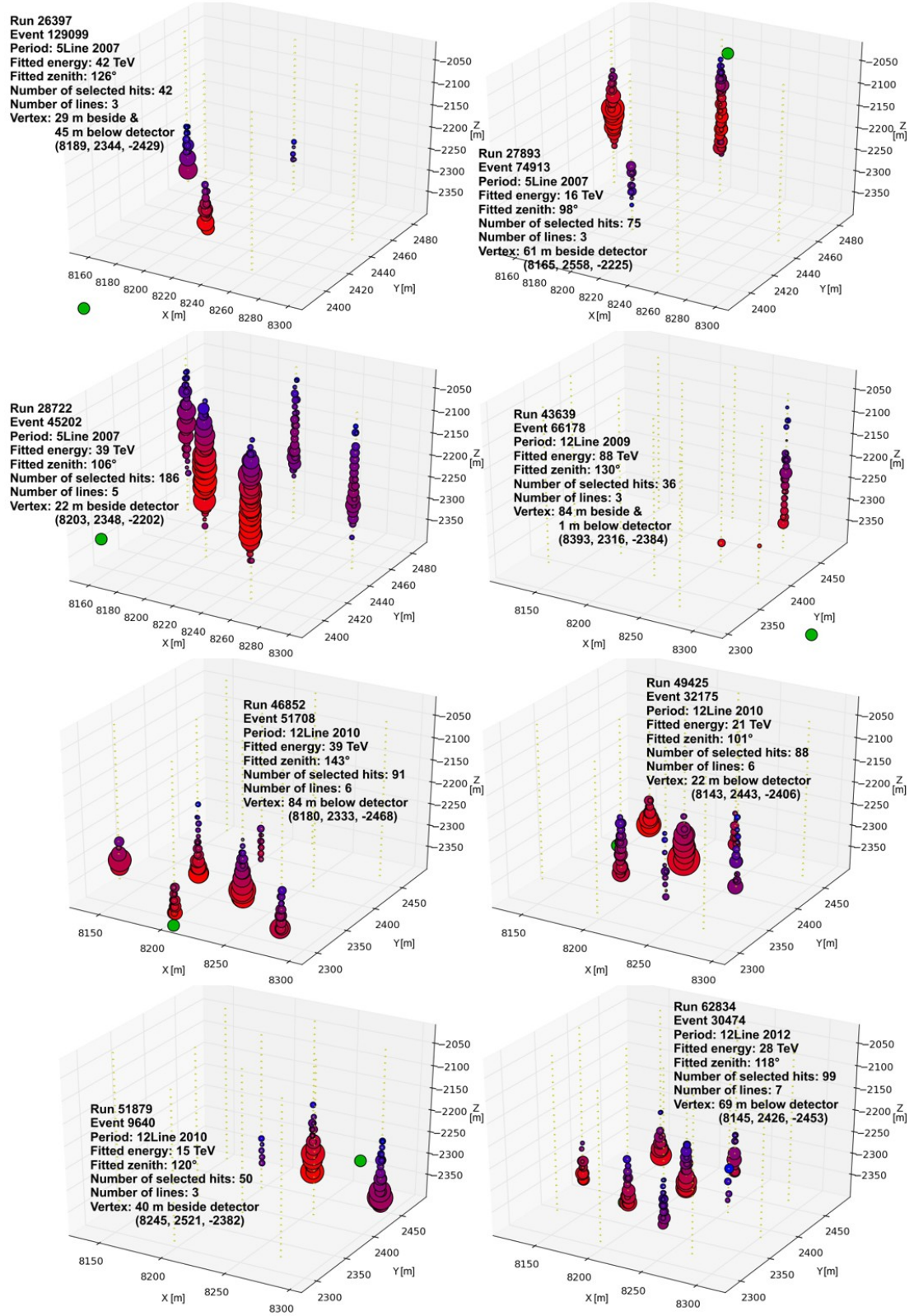
Figure 14.4: *Distribution of the selected shower hits in the 8 final selected data events of the full sample.* The figure illustrates the distributions of the selected shower hits in the detector for the 8 data events that survived all cuts and are used for the upper limit calculation from the full sample. Each circle marks a detected hit, where the size is related to the hit charge and the color indicates the arrival time from early (red) to late (blue). The green points mark the corresponding reconstructed vertex positions. Images have been created using a script from [118].

14.3   Contained shower candidates

The sparking event filter that removes all events, where the vertex is fitted closer than 15 m to any of the OMs, reduces the instrumented volume by about one quarter, which of course lowers the probability of detecting fully contained shower events, for which vertex and hit pattern are completely inside the detector. As shown in chapter 7.2.2 the choice of 15 m was made to be on the safe side and for sure remove any event that could be of sparking origin. However, this cut also might have deselected contained shower events that are caused by a true neutrino interaction.

Unfortunately among the selected 60 "up-going" data events there is no contained shower event with an energy above 10 TeV. However, there are some that have been removed by the sparking event filter but do not necessarily have to be sparking events. Figure 14.5 shows the four contained events with the highest fitted energy that have a distance between the vertex and the closest OM of at least 10 m but not more than 15 m, i.e. those that have been removed by the sparking filter but are nevertheless not too close to an OM.

Between 10 and 100 TeV the reconstruction yields a mean error of $6 - 8$ m and a median error $4 - 5$ m on the vertex position (see figure 6.12 in chapter 6.2.1). Hence, those four events have a good chance to originate from a neutrino and not from a sparking OM. However, once they are deselected, they are, of course, not used for the upper limit calculation, but just shown here for demonstration.

14.4   Limits from different flux models

The presented upper limit on the diffuse cosmic neutrino flux was evaluated by optimizing a pair of zenith and energy cuts assuming an unbroken E^{-2} cosmic neutrino spectrum with a flavour ratio of $1 : 1 : 1$. For the atmospheric neutrino flux the Bartol [9] parametrization was used for the conventional component and the Enberg [10] for the prompt component.

However, recent measurements with the IceCube detector, where for the first time an evidence for a cosmic neutrino flux was found, yielded indications that the cosmic neutrino spectrum may have a cut-off at ≈ 2 PeV [4]. If this is true, less cosmic signal events could be expected and contribute to the calculation of the upper limit, especially the Glashow resonance at 6.3 PeV [67] that represent $\approx 30\,\%$ of the CC $\bar{\nu}_e$ contribution and $\approx 9\,\%$ of the overall signal of 10.45 after the final cuts (see also table 12.2) would no longer occur. The best fit to the normalization of an E^{-2} spectrum that matches the IceCube data was found to be $1.2 \cdot 10^{-8}\,\mathrm{GeV/cm^2 \cdot sr \cdot s}$ per neutrino flavour [4]. Assuming this as test-flux the 10.45 events would scale down to 2.79 from an unbroken
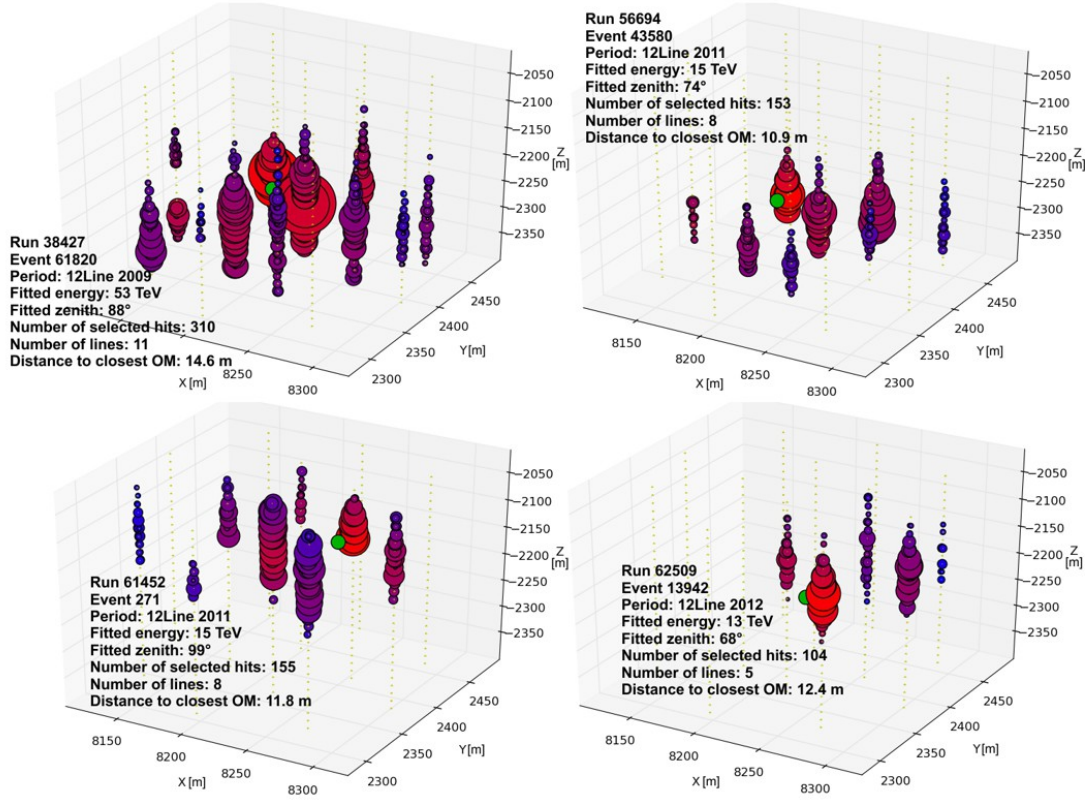
Figure 14.5: *Candidates for contained shower events in the full sample that have been removed by the sparking event filter.* The figure illustrates the four contained shower events with the highest energy that survived the multi line filter and the cut on the reduced vertex log-likelihood, but have been deselected by the sparking event filter and nevertheless have a minimum distance of 10 m to the closest OM. Each circle marks a detected hit, where the size is related to the hit charge and the color indicates the arrival time from early (red) to late (blue). The green points mark the corresponding reconstructed vertex positions. The lower left event would have survived all further cuts, the other three failed because of the zenith cut. Images have been created using a script from [118].

spectrum and 2.14 including the cut-off.

Further, the sensitivity for the diffuse neutrino searches with IceCube reached a level that allows the study of the prompt atmospheric neutrino flux, too. A recent analysis set a 90 % confidence upper limit on the prompt flux that is a factor of 3.8 above the predictions from Enberg [82]. Hence, using this upper limit to evaluate the prompt contribution instead of the Enberg parametrization increases the number of expected background events from 4.92 to 6.63 (see also table 12.2).

Table 14.5 lists the re-evaluated sensitivities and upper limits from the modified flux assumptions. However, note that changing the cosmic and/or the atmospheric fluxes actually requires a re-optimization of the zenith and energy cuts as for different event expectations the MRF minimization could yield a lower value at a different set of cuts. However, this has not been done here. The modified limits have been calculated from

the same cuts for which the data unblinding was granted. But regarding the facts that the MRF landscape still will have its minima at cut combinations where the last atmospheric muon is removed and that within this valley of minima no big difference between the single cut combinations is observed (see figure 12.2) the here presented values are expected to be close to presumably re-optimized ones.

Table 14.5: Sensitivities and upper limits from different atmospheric and cosmic flux assumptions

	Unbroken cosmic E^{-2} flux	**Cosmic flux with a cut-off at 2 PeV**
Bartol [9] + Enberg [10] atmospheric flux	Signal events: $2.79^{+0.63}_{-0.96}$* Background events: $4.92^{+2.85}_{-2.96}$ Sensitivity**: $2.21^{+0.87}_{-0.73} \cdot 10^{-8}$ Pole upper limit**: $4.92 \cdot 10^{-8}$	Signal events: $2.14^{+0.48}_{-0.73}$* Background events: $4.92^{+2.85}_{-2.96}$ Sensitivity**: $2.89^{+1.13}_{-0.95} \cdot 10^{-8}$ Pole upper limit**: $6.40 \cdot 10^{-8}$
Bartol [9] + 3.8·Enberg [10] atmospheric flux	Signal events: $2.79^{+0.63}_{-0.96}$* Background events: $6.63^{+3.36}_{-3.79}$ Sensitivity**: $2.48^{+0.95}_{-0.81} \cdot 10^{-8}$ Pole upper limit**: $4.05 \cdot 10^{-8}$	Signal events: $2.14^{+0.48}_{-0.73}$* Background events: $6.63^{+3.36}_{-3.79}$ Sensitivity**: $3.22^{+1.24}_{-1.07} \cdot 10^{-8}$ Pole upper limit**: $5.28 \cdot 10^{-8}$

* From test flux normalization of $1.2 \cdot 10^{-8} \, \text{GeV/cm}^2 \cdot \text{sr} \cdot \text{s}$
** Per neutrino flavour in units $\text{GeV/cm}^2 \cdot \text{sr} \cdot \text{s}$

To increase the background by raising the prompt contribution, of course, worsens the sensitivity, but here yields a better upper limit as the higher background expectation of 6.63 is closer to the measurement of 8 events. Following the Poisson statistics the best agreement between 8 measured events and expectations is yielded by the combination unbroken cosmic spectrum & normal prompt flux: $P(8, 7.71) = 13.9\,\%$. To match the measurement of 8 data events, together with the atmospheric background of $4.92^{+2.85}_{-2.96}$ events, $3.08^{+2.96}_{-2.85}$ cosmic events would have been required. The Monte-Carlo prediction for a cosmic flux normalization of $1.2 \cdot 10^{-8} \, \text{GeV/cm}^2 \cdot \text{sr} \cdot \text{s}$ is $2.79^{+0.63}_{-0.96}$ events. From the ratio of the two event numbers the normalization of a corresponding unbroken flux that fits the measured ANTARES data best is calculated to $1.32^{+1.35}_{-1.26} \cdot 10^{-8} \, \text{GeV/cm}^2 \cdot \text{sr} \cdot \text{s}$ per neutrino flavour. The errors have been calculated using Gaussian error propagation (equation (10.8)).

Chapter 15

Summary and outlook

In this work a search for the diffuse cosmic neutrino flux with shower events was performed using the ANTARES [1] data from 2007 - 2012. The ANTARES neutrino telescope is a three-dimensional array of 885 photo multipliers on 12 vertical lines that has been set up in the deep sea to detect the Cherenkov radiation [2] from particles that emerge from interactions of high energy neutrinos with nucleons in water. These neutrino events, however, are superimposed by a background of atmospheric muons that are about 6 orders of magnitude more frequent. Hence, one challenge was to suppress this background and to find event signatures that are caused by neutrino events. Among the latter ones shower-like events from hadronic and electromagnetic cascades that appear as point-like light source have to be separated from track-like events that are for example induced by a deep inelastic charged current muon neutrino interaction.

For this purpose a software package, called the *Dusj* shower reconstruction, was developed that is capable of identifying shower signatures in the data and reconstruct their event properties, such as the shower vertex position, interaction time, shower energy and neutrino direction. The tool was implemented in the official analysis framework *SeaTray* [6] that is used within the ANTARES collaboration for data processing. Already existing shower reconstruction codes, such as for example *BBFit* [7], had been designed to reconstruct the vertex position and interaction time only. But as for the analysis of the diffuse flux also the energy of the events must be known, it became essential to introduce a tool for a complete shower parameter reconstruction. With that aim two different approaches have been followed in parallel as independent PhD theses within the collaboration: the *Q-Strategy* [8] and this work.

The Q-Strategy evaluates the shower energy from the *entirety of the selected shower signal hits* by relating the energy to the sum of all signals' charges. By doing so it only can produce reliable results for events that are contained in the instrumented volume as for partially contained events a fraction of the total charge is missing and hence, the energy is under-estimated. The reconstruction method that is used in the Dusj algorithm is a two-step maximum likelihood fit that makes use of Monte-Carlo based

PDF tables. In these tables the shower parameters, such as the shower energy, are related to the properties of *each single signal hit*, which offers the great advantage - compared to the Q-Strategy - to also be able to reconstruct events that are located at the detector edge or that even took place outside the instrumented volume. Thus, in this work the search for shower events was no longer restricted to contained events only.

In the region of interest between 1 TeV and 1 PeV shower energy the Dusj algorithm achieves a reconstruction accuracy of $4 - 6$ m (median) and $5 - 9$ m (mean) for the vertex position. The shower energy is reconstructed with a slight underestimation of $0.2 - 0.3$ orders of magnitude (median) and $0.3 - 0.5$ orders of magnitude (mean). The reconstruction of the neutrino direction yields a stable median error of $6°$ for showers below 100 TeV, but looses quality for higher energies. At 1 PeV the median error is approximately $25°$. The corresponding mean error yields values of $15° - 40°$. Concerning all shower parameters the better accuracy values always refer to lower energies. The given values refer to events that have passed a certain quality criterion that is an upper cut on the final reduced log-likelihood value of the vertex fit. With this cut applied about 10% (at 1 TeV) to 60% (at 1 PeV) of all detected shower events remain, where the atmospheric muon background is reduced by 5-6 orders of magnitude. Without this quality cut the fit routine is able to reconstruct successfully 50% (at 1 TeV) to 90% (at 1 PeV) of all detected showers.

As the data taking conditions at the ANTARES site are subject to environmental variations that are reflected in variable optical background rates and occasional light bursts from bioluminescent lifeforms, varying with a time scale of days, some periods had to be excluded from the analysis. Finally, an effective data taking lifetime of 1247 days was used. In this data only events were taken into account that fulfilled all of the following requirements:

- Event passed the reconstruction successfully.

- Event passed the reduced vertex log-likelihood quality cut.

- Shower signal hits have to be selected on at least 3 different lines.

- The vertex position was fitted not closer than 15 m to any of the OMs.

The latter criterion is aimed to remove occasional events, where the high voltage inside the PMTs create a spark-over that is expressed as a bright, point-like flash and could pretend a neutrino induced particle shower.

The development of the reconstruction algorithm as well as the tuning of the final analysis have been performed using the official collaboration-wide Monte-Carlo simulation of neutrino and atmospheric muon events. Here, for each data taking run (that

lasts for a few hours) an individual simulation had been created taking into account the data taking conditions that had prevailed during the run. As no simulation of tau neutrino events was available the contribution from cosmic tau neutrinos was estimated from the electron neutrino simulation. Further, due to low statistics in the atmospheric muon simulation, especially after the very final cuts, an extrapolation method was introduced to estimate the muon contamination after all simulated events have been removed. The contamination was estimated to $\approx 38\,\%$ in case if no cosmic signal is assumed and all other events originate from atmospheric neutrinos, and $\approx 26\,\%$ when taking an additional cosmic E^{-2} neutrino flux with a normalization of $1.2 \cdot 10^{-8}\,\mathrm{GeV/cm^2 \cdot sr \cdot s}$ and a cut-off at $2\,\mathrm{PeV}$ (i.e. a flux as recently measured by IceCube [4]) into account. An additional correction to the charged current muon neutrino simulations has been applied to compensate for missing hadronic vertex showers that have not been simulated for high energy events due to computing reasons.

As in the currently used version of the official Monte-Carlo no photon scattering is simulated for shower events, a small test sample of an updated simulation with photon scattering included was generated to study the effect of this deficiency on the analysis. As a consequence the cuts that have originally been designed to separate track-like events from shower-like events and that made use of an optimized multivariate algorithm had to be replaced by another less restrictive cut (on the reduced vertex log-likelihood) in order to stay compatible between the currently used and future simulations.

Systematic errors that have been taken into account in the analysis arise on the one hand from the uncertainty of the atmospheric flux models, where $\pm 30\,\%$ was assumed for the atmospheric muon and the conventional atmospheric neutrino flux (Bartol [9]), and approximately $^{+25}_{-40}\,\%$ on the prompt component as predicted by Enberg [10]. Systematic effects from uncertainties in the simulation input parameters on the other hand, such as light absorption length, scattering length and PMT efficiency, add up to $^{+54}_{-47}\,\%$ for showers from atmospheric neutrinos and $^{+17}_{-32}\,\%$ from cosmic neutrinos. This error also contains a contribution from the lack of simulated photon scattering for shower events in the current Monte-Carlo simulations. For track-like events the corresponding error from the simulation input parameters is $10 - 20\,\%$.

The analysis was performed as blind search that has been optimized using simulated events only and without looking into the data to avoid any bias from expectations that emerge from previous measurements, such as for example done by IceCube [11] [12] [13]. As the first IceCube shower analyses that have been performed using the data from a not completely established IceCube detector were not able to measure any signal from a diffuse cosmic neutrino flux, even though the instrumented volume of IceCube exceeds that of ANTARES by far, this analysis has been optimized for the evaluation of an upper limit on the diffuse cosmic neutrino flux. For this the model rejection potential technique [14] was used. A pair of lower cuts on the fitted shower energy and

the zenith angle of the neutrino direction - that affects the number of remaining events from a cosmic neutrino flux and from the atmospheric muon and neutrino background - was varied until the best sensitivity was obtained. The sensitivity is a measure for the strength of a flux that can be on average excluded by this analysis with a 90 % confidence level. Here, this value has been evaluated to:

$$E^2 \cdot \bar{\Phi}_{90\,\%} = 2.21^{+0.87}_{-0.73} \cdot 10^{-8}\,\mathrm{GeV/cm^2 \cdot sr \cdot s} \tag{15.1}$$

The final analysis strategy was tested on 10 % of the ANTARES data, where no severe problems have been encountered. An observed excess of data events over the expectation from atmospheric background simulations was within the evaluated systematic and statistical errors. After an extensive refereeing process by several members of the ANTARES collaboration from different institutes the remaining 90 % of the data have been analysed and revealed 8 remaining events in 1247 days after the final cuts, where $4.92^{+2.85}_{-2.96}$ are expected from the atmospheric background (muons, conventional neutrinos as predicted by Bartol [9] and prompt neutrinos as predicted by Enberg [10]). The excess over background has a significance of $1.5\,\sigma$ and could be an indication for a contribution from a cosmic neutrino flux. The measured flux by IceCube including the cut-off [4] would contribute another $2.14^{+0.48}_{-0.73}$ cosmic events to the atmospheric expectations. However, the measured 8 events are also compatible with a background only assumption when taking the systematic and statistical errors on the simulation and the Poisson error of $\sqrt{8} = 2.8$ into account.

Assuming an unbroken cosmic E^{-2} neutrino flux with a flavour ratio of $\nu_\mu : \nu_e : \nu_\tau = 1 : 1 : 1$ a 90 % confidence upper limit on the diffuse cosmic neutrino flux per flavour was evaluated to:

$$E^2 \cdot \Phi_{90\,\%} = 4.91 \cdot 10^{-8}\,\mathrm{GeV/cm^2 \cdot sr \cdot s} \tag{15.2}$$

The limit is valid in the energy range from 22.7 TeV to 7.8 PeV and has been calculated using the Feldman-Cousins approach [5]. Systematic errors have been taken into account with the **Pole 1.0** program [15][16] that assumes Gaussian error distributions for the signal and background.

Figure 15.1 shows the evaluated upper limit (printed as green line) in the context of the results of other experiments and analyses.
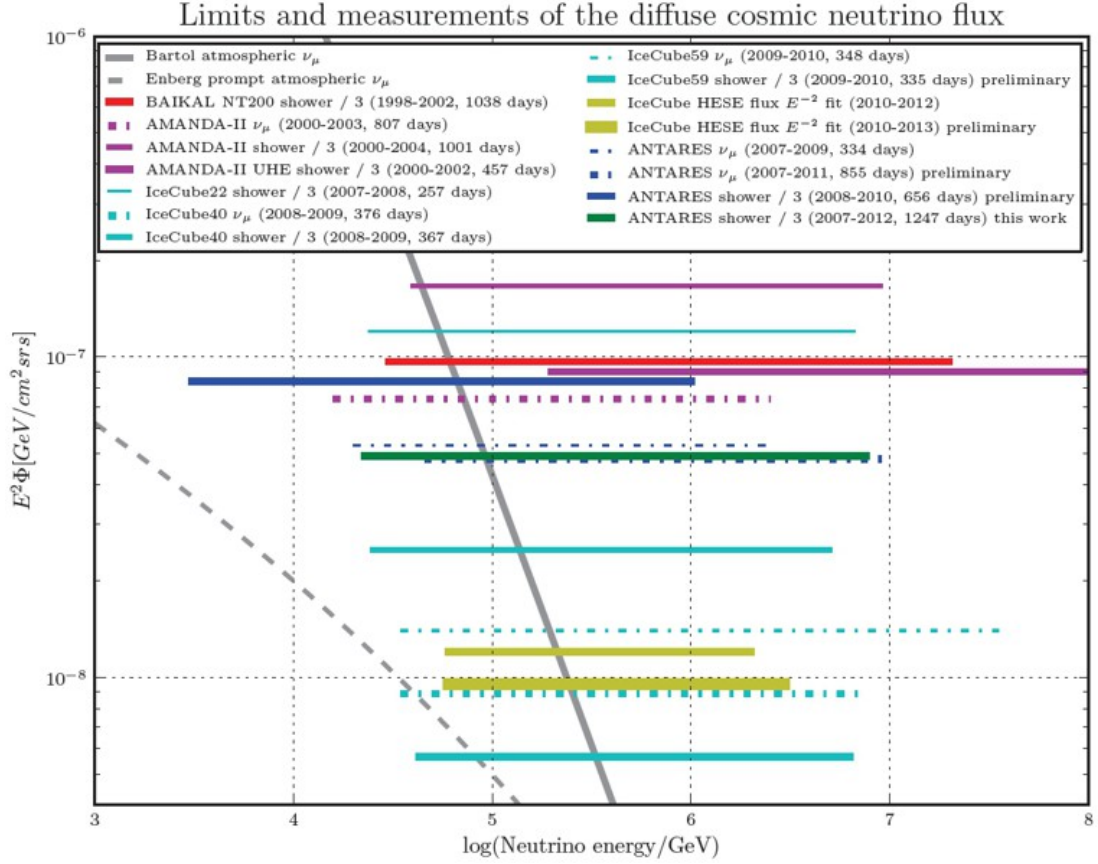
Figure 15.1: *The result of this work in the context of previous analyses.* The plot shows the upper limit that was evaluated as the result of this work (green) compared to other analyses of the diffuse cosmic neutrino flux. Limits from all flavour shower analyses are divided by 3 (i.e. they are given per flavour) to be able to compare them to limits from ν_μ analyses. Only the analysis of the IceCube data since 2010 could prove the existence of a flux from cosmic high energy neutrinos and fit a flux expectation (yellow) [4] [17]. All other lines mark upper limits from ν_μ analyses (dashed-dotted lines) and all flavour shower analyses (solid lines), sorted by experiment: BAIKAL [18], AMANDA [19] [20] [21], IceCube [11] [22] [12] [23] [13] and ANTARES [24] [25] [8]. For comparison, the atmospheric ν_μ fluxes (grey lines) as calculated by Bartol [9] and Enberg [10] have been added. All fluxes represent the sum of neutrino and anti-neutrino.

15.1 Discussion of the result

Looking figure 15.1, the resulting upper limit from the shower analysis in this work agrees well with the results of previous ANTARES diffuse flux analyses that had been performed in the muon neutrino channel.

Compared to the results obtained with AMANDA-II, which was instrumented slightly more sparsely (677 OMs on 19 strings) than ANTARES, the limit from this work is a factor of 3.4 better than the limit of a 1001 days AMANDA-II shower analysis, where $1.67 \cdot 10^{-7}\,\mathrm{GeV/cm^2 \cdot sr \cdot s}$ per neutrino flavour had been obtained [20]. Considering

this, the ANTARES result is quite encouraging as even if the event numbers of that AMANDA-II analysis are scaled by ≈ 1.6 to compensate for the differences in lifetime and number of OMs, the AMANDA limit would not reach the 10^{-8} level.

However, the aimed goal to reach the limit of the IceCube40 shower analysis ($2.5 \cdot 10^{-8} \, \mathrm{GeV/cm^2 \cdot sr \cdot s}$ [12]) was not achieved. With an effective lifetime of 367 days, i.e. approximately one third of the lifetime in this work, but three times as many strings instead, the two analyses could be regarded as competitive. And although the sensitivity of $2.21^{+0.87}_{-0.73} \cdot 10^{-8} \, \mathrm{GeV/cm^2 \cdot sr \cdot s}$ that was obtained with this analysis reaches the IceCube40 limit, finally, the result for ANTARES is a factor of 2 higher compared to IceCube40, which is of course due to the measured excess of data over background.

The other ANTARES shower analysis that was part of the parallel PhD thesis [8] evaluated an upper limit of $8.4 \cdot 10^{-8} \, \mathrm{GeV/cm^2 \cdot sr \cdot s}$ per neutrino flavour from 656 days of lifetime (2008 - 2011 data). However, this limit is without having taken into account systematic errors (as done in this work using Pole 1.0) and is printed here for comparison only. Further, it has not been checked how the results, especially the applied cuts, change when using an updated simulation with photon scattering included. Concerning the analysis using the Dusj reconstruction this issue had a major impact on the choice of the cut parameters as in a simulation without photon-scattering the separation of track-like and shower-like events can reach an unnatural high level that would pretend to obtain a better sensitivity and a better upper limit than the analysis intrinsically can achieve. Hence, the solution that was chosen for this analysis was to loosen the shower selection cut, which led to a slightly less effective track/shower separation, but a better agreement between the currently used and the updated future Monte-Carlo simulation was achieved instead. The larger contamination of atmospheric muons that one has to deal with when loosening the shower cut is removed later by the lower cuts on the fitted zenith and shower energy.

For future analyses, however, it is recommended to re-optimize the procedure, once the new official Monte-Carlo production is available that is expected to be approximately by the end of 2014. With the new production one could train a new random decision forest, again using five (or even more) of the Dusj quality parameters as it was intended in the first place instead of just using a single cut on the reduced vertex log-likelihood. This is expected to yield an improved atmospheric muon suppression which will in the end allow to loosen the final energy and zenith cuts and hence, improve the sensitivity.

It could be further worth building new PDF tables for the Dusj reconstruction using this new set of simulated events as of course the current tables do not include photon scattering either. To compensate the lack of photon scattering for this analysis the ARS hit filter was introduced that only selects hits that are caused by direct photons

(i.e. on each OM the first detected hit was selected only). However, once the correct amount of scattered, late hits is included in the PDF tables this filter might be no longer required, which will probably increase the hit selection efficiency, especially for high energy events.

To avoid the selection of events that are basically single line events and survive the final cuts due to some single matching hits on other lines (as happened for one of the final 8 remaining data events) it is suggested to enhance the multi-line filter in a way that not just three lines have to be selected but each of the lines also must have a certain amount of hits.

15.2 An extrapolation into the future

To conclude this work, in the following an extrapolation is presented that estimates the sensitivity and the expected measurement result of this analysis up to 2020. For this estimation it was assumed that the reconstruction and analysis strategy is the same, i.e. is not updated with a new Monte-Carlo version including photon scattering.

From this analysis the number of expected simulated and measured events per year can be extrapolated from the average of the years 2009 - 2012, i.e. those years where the full 12-line configuration was operational throughout the whole year. The average effective data taking lifetime per year in that period was 214.8 days. After the final cuts the average number of events per year is:

- 0.57 events from atmospheric neutrinos (Bartol [9] and Enberg [10] flux models)

- 0.32 atmospheric muons (from the extrapolation of the MUPAGE simulations [95] [96])

- 0.52 from a cosmic E^{-2} neutrino flux with a normalization of $1.2 \cdot 10^{-8} \, \mathrm{GeV/cm^2} \cdot \mathrm{sr} \cdot \mathrm{s}$ per neutrino flavour

- 1.25 recorded data events

From the earlier periods 2007 - 2008, when the detector was incrementally increased, and that contribute to the total sample with an effective lifetime of 387.7 days, an additional contribution of 0.78 atmospheric neutrino, 0.58 atmospheric muon, 0.74 cosmic and 3 measured events is taken into account.

Figure 15.2 illustrates the result of the extrapolation. Currently it is foreseen to run the ANTARES detector until 2016. By then the sensitivity of this analysis reaches a level of $1.58 \cdot 10^{-8} \, \mathrm{GeV/cm^2} \cdot \mathrm{sr} \cdot \mathrm{s}$ per neutrino flavour, i.e. a factor of 1.4 better compared to the current value but not low enough to approach the IceCube flux [4].

The excess of measured data over background would have increased to $1.7\,\sigma$, compared to $1.5\,\sigma$ that was observed in this work. Assuming a hypothetical extension of the data taking with ANTARES up to 2020 the sensitivity would reach $1.26 \cdot 10^{-8}\,\mathrm{GeV/cm^2 \cdot sr \cdot s}$ per neutrino flavour, the excess significance $1.85\,\sigma$, i.e. still slightly above the IceCube flux.
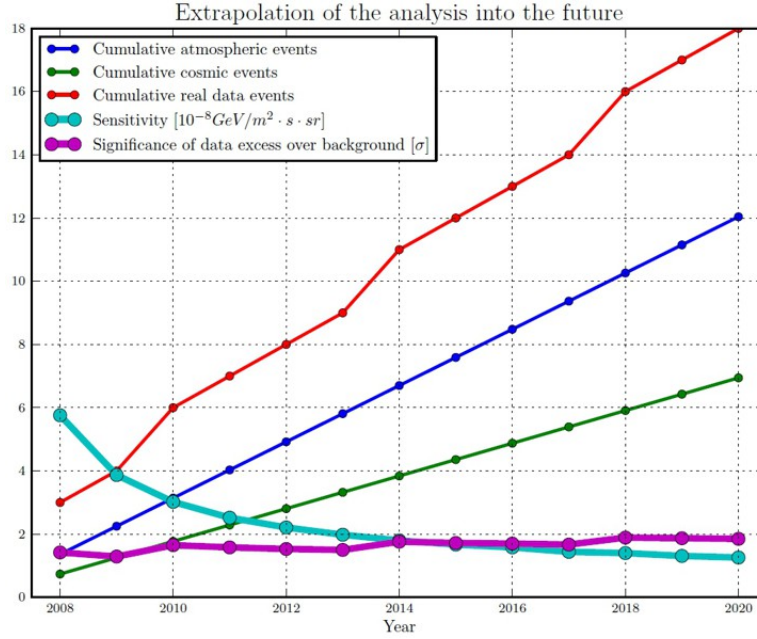

Figure 15.2: *Extrapolation of the analysis into the future.* The plot shows expectations for this analysis for the following years, assuming a continuation of the simulation and data taking without any changes. The extrapolation has been performed by averaging over the years 2009 - 2012, when the detector was operational in its 12-line configuration throughout the whole year. Presented is the cumulative number atmospheric events (dark blue), cosmic events (green) and recorded data events (red) that are expected after the final cuts by the end of a year and the resulting sensitivity (light blue) and the significance of the data excess over background (violet). The atmospheric background contains conventional (Bartol [9]) and prompt (Enberg [10]) atmospheric neutrinos, as well as atmospheric muons. The cosmic events refer to an E^{-2} neutrino flux with a normalization of $1.2 \cdot 10^{-8}\,\mathrm{GeV/cm^2 \cdot sr \cdot s}$ per neutrino flavour.

However, it should be stressed again that the applied track/shower separation cut (the reduced vertex log-likelihood cut) in this analysis is definitely not the optimum that can be achieved in atmospheric muon suppression. It was a compromise between a good sensitivity and a stability towards uncertainties in the Monte-Carlo. It was chosen in a way that the discrepancies between this and future simulation codes are kept as small as possible and simultaneously not too much sensitivity is lost. The missing photon scattering did not allow to use an optimized random decision forest for the separation as the parameters that have been used for this multivariate analysis change with the inclusion of photon scattering. Thus, once a full production of new Monte-Carlo is available, a more sophisticated track/shower separation can be applied again and hence, a better sensitivity as given from the extrapolation can be expected.

With this work it was shown that it is feasible to perform an analysis of the diffuse cosmic neutrino flux with ANTARES, also using shower events. The obtained results agree well with results of previous analyses. The introduction of the Dusj shower reconstruction algorithm paved the way to include shower events also in future analyses and neutrino searches, with ANTARES and also with future neutrino telescopes like KM3NeT [58], for which first studies have recently begun to use the reconstruction tool as standard shower reconstruction algorithm.

Appendix A

Analysis software framework

This chapter gives a brief introduction of the software that has been used for this analysis. A framework called *SeaTray* [6] was used to handle the huge amount of simulated and measured data events. The framework takes care of the data access and storage by offering a dedicated data file format and applying any required tasks and processes to this data. It is further described in appendix A.1. The reconstruction of the events (see also chapter 6) makes use of a tool called *Gulliver* [110] that is a sub-framework within SeaTray, dedicated to maximum likelihood reconstructions, which is discussed in appendix A.2.

A.1 The SeaTray framework

SeaTray [6] is a software framework that is used within the ANTARES collaboration for mass data event reconstruction. The framework is an adaption of the *IceTray* framework [120] that has been developed by the IceCube collaboration. Both collaborations now share the basic data structure and core data classes. It is written in C++ [108] and Python [109].

Within SeaTray all relevant event reconstruction algorithms that are currently used in ANTARES are implemented. Further, all necessary tools to read in the physics data, to access additional information, such as for example triangulated OM positions or OM calibration data, to apply the calibration to the raw detector hits, to reconstruct events and to write the result to dedicated output files are included in the framework.

Figure A.1 illustrates the work flow of the data processing with the framework. All data, once read in from simulated or recorded data input files, is stored in so-called *frames*. Each frame is a container that gathers all relevant data belonging to one physics event, such as recorded hits, data quality information or results of the single reconstruction algorithms. This data can be accessed and modified by *modules*. Each module represents one particular step in the whole process chain, for instance

a module that calibrates the hits, another one that tries to fit a muon trajectory to these hits, etc... The data frame will be successively passed through all the modules in the chain. Also one single reconstruction tool (such as the shower reconstruction that has been developed as part of this work and is described in chapter 6) can be divided into modules, as one can perform a hit selection, one can do the fit, another one evaluates quality parameters, etc... This modularity offers a great flexibility to exchange single parts of the reconstruction chain without having to modify the others. Further, some helper classes called *services* exist that can not directly access the data in the frame, but provide help to the modules. Such a service is for example one that generates random numbers, which may be required by some modules but, of course, no direct access to the frame is needed to create them. To sort the data by its content, different types of frames are available, such as for example a *Geometry* frame to store the triangulated OM positions, a *Calibration* frame to store the currently valid OM calibration data or *Physics* frames that contain the data for one event.
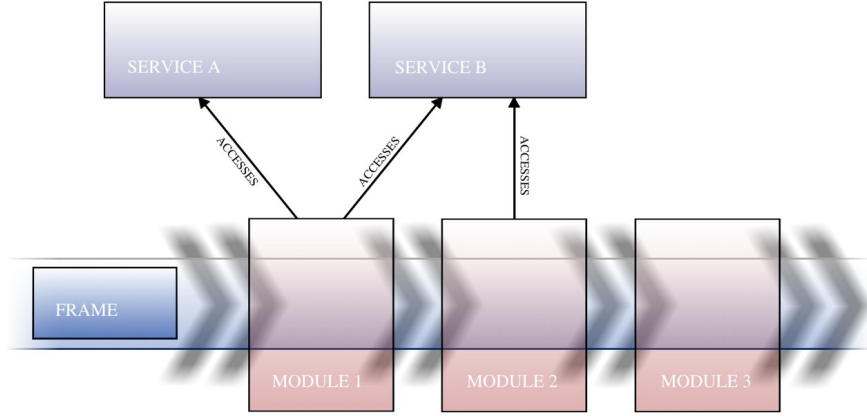

Figure A.1: *Work flow of the data processing with SeaTray.* The figure illustrates the way how data is processed with SeaTray. Data that is stored in *frames* will be passed through a consecutive chain of *modules* that can use or modify the data. *Services* are helper classes that may be used by the modules. See text for further explanations. Image from [63].

In ANTARES the preprocessing of the data that is reading in raw data, calibrating hits and applying standard reconstruction tools is handled in official data productions to ensure that each following physics analysis is based on the same, correctly calibrated data. The whole recorded detector data as well as the complete simulated RBR simulation (as discussed in chapter 5) undergoes this process.

To trace changes in the code development the version control tool *Subversion* (SVN) [111] is used that flags each committed change with an unique revision number. In regular intervals official software releases are created from the content of a well-tested revision.

The data production and RBR v2 simulation that were used for this analysis have been created with the software release *12-04-prod* in SVN revision 9079. The recon-

struction of the events with the *Dusj* algorithm that has been developed as part of this work (see chapter 6) has been performed using the software trunk in SVN revision 10926. The official data productions are internally named *prod_2012-04* (for the 2007-2011 data) and *prod_2013-02* (for the 2012 data). The reconstruction of these data productions as well as the complete RBR v2 with the Dusj code have been named *showerproduction_12-07-00*.

A.2 Maximum likelihood event reconstruction with Gulliver

The *Gulliver* framework [110] is a sub-framework in SeaTray that has been written by David Boersma for the IceCube Collaboration and that can be used for any kind of maximum likelihood reconstructions, where each event assumption is associated with a probability of occurrence. The final fit result then is the event with the highest probability.

For this Gulliver provides a very generic interface to link together the four parts that are required for a maximum likelihood fit: A *seed service* to provide an initial event hypothesis, a *minimizer service* that contains the mathematical implementation of the minimization strategy[1], a *parametrization service* that parametrizes the physics event properties (in case of showers the vertex position, interaction time, shower energy and neutrino direction) and their corresponding limits in the fit search space, and finally a *likelihood service* that contains the physics to provide the probability for an event hypothesis to match to the measured hit sample (the likelihood landscape).

The advantage of this separation into four independent parts is a great flexibility in exchanging one of the parts without changing the others. For example: to change the physics likelihood, simply the likelihood service has to be replaced. All other parts can be used in the same way as before. Although Gulliver was introduced for muon track reconstruction, it can be used for shower reconstruction as well. Within this work a SeaTray module called **I3ShowerFitter** has been developed for this purpose to adapt the framework for the requirements of fitting shower events. In the following analysis this module makes use of Gulliver in order to link the Dusj likelihood services that are the implementation of the Dusj shower reconstruction (see chapter 6) to existing minimizer services. Further a new seed service **I3ShowerSeedService** and a new parametrization **I3ShowerParametrizationService** have been developed. The following description has been previously distributed as internal note [121] within the collaboration.

---

[1]A minimizer is used to find the minimum in the landscape of the negative logarithmic likelihood, which is equivalent to the maximum of the unmodified likelihood landscape.

A.2.1 The main module I3ShowerFitter

The **I3ShowerFitter** is a Gulliver-based reconstruction module that has been developed as a generic basis for any kind of maximum likelihood based shower reconstruction. It basically is an adoption (with small extensions) of the existing module **I3SimpleFitter** [110] that is the generic tool for a Gulliver-based muon track reconstruction. The **I3ShowerFitter** uses an instance of the Gulliver base class **I3Gulliver** to connect the likelihood, parametrization and minimizer services to a full maximum likelihood tool. Figure A.2 gives an illustration how the services are connected to the main module. In principle all four services are fully exchangeable, however, within this work, of course, the dedicated shower services have been used.
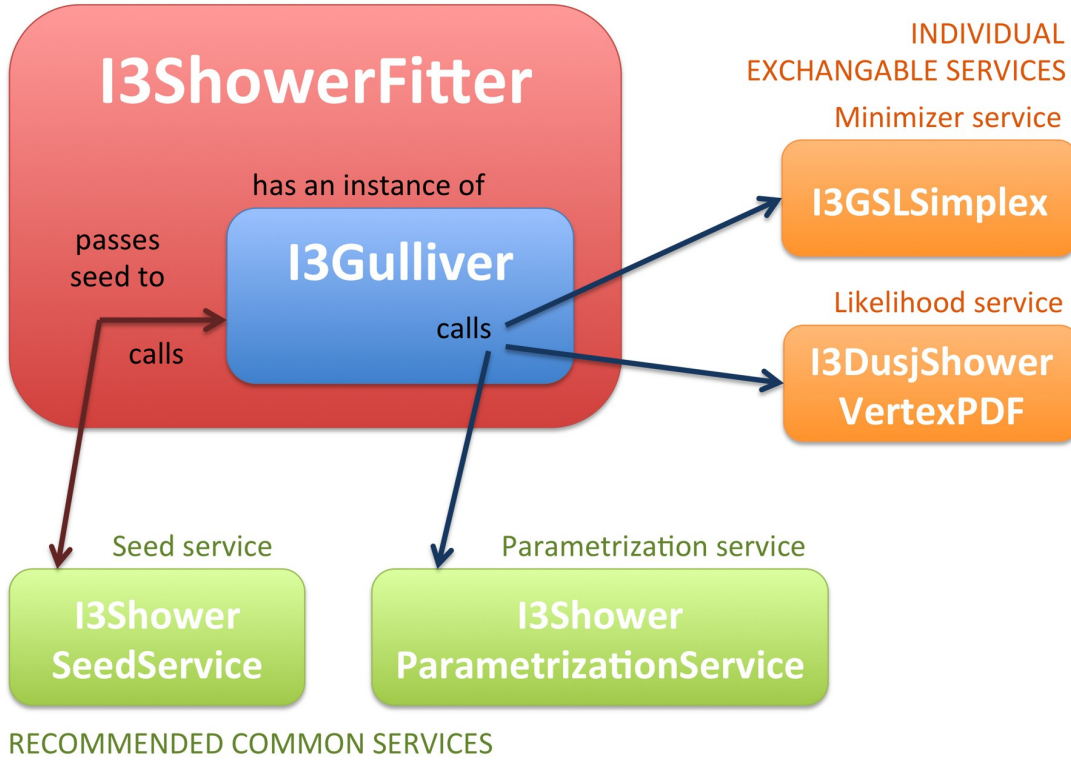

Figure A.2: *Scheme of the work flow of a shower reconstruction using the Gulliver **I3ShowerFitter**.* Using the example of the Dusj vertex reconstruction (see chapter 6.2.1) the figure illustrates the functionality of the Gulliver **I3ShowerFitter**. This module uses an instance of **I3Gulliver** for a maximum likelihood reconstruction. The seed service **I3ShowerSeedService** and the parametrization service **I3ShowerParametrizationService** are generic tools that can be used for any kind of shower reconstruction with Gulliver. In this work the minimizer **I3GSLSimplex** [122] [123] is used to minimize the likelihood landscape that is provided by the likelihood service **I3DusjShowerVertexPDF**. The reconstruction of the shower energy and neutrino direction works in the same manner, where the vertex likelihood service is replaced by the **I3DusjShowerEnergyDirectionPDF** service. Both likelihood services are explained in further detail in chapter 6.2.

The **I3ShowerFitter** basically does three things:

- It calls a seed service that provides start values for the fit routine. The **I3Shower-SeedService** takes shower-specific features into account to provide seeds that are convenient for any kind of further shower reconstruction. For each event also more than one seed can be created by smearing the shower parameters of the first seed randomly in different directions. For example in this analysis, 5 seeds are created for the vertex reconstruction. The best of the five results serves as input for the following energy-direction reconstruction where 10 seeds will be created. (See appendix A.2.2 for more information about this service)

- The instance of **I3Gulliver** takes the seed(s) and does the actual minimizing fit for each seed.

- Finally the module checks whether for one of the parameters the fit ran against one of the fit boundaries and writes this information into a class called **I3Shower-FitterCutParams**. (See appendix A.2.1.2). The module can write out the results of the fits from all seeds or just the one that yielded the best likelihood value. Further a container called **I3LogLikelihoodFitParams** (see appendix A.2.1.1) that stores the final likelihood value (the probability that is related to the fit result), number of evaluations and degrees of freedom is written to the frame.

To do the actual fit **I3Gulliver** needs three SeaTray services that are independent from each other and can separately be exchanged:

- A *likelihood service* that provides the likelihood landscape from a given event hypothesis. Here, of course, the Dusj likelihood services as described in chapters 6.2.1 and 6.2.2 are used.

- A *parametrization service* that extracts the physics parameters from the event hypothesis (vertex, interaction time, shower energy, direction) and passes them as vector of numbers to the minimizer and back. Further, this service sets the fit boundaries and step lengths for the fit. To take shower-features into account the **I3ShowerParametrizationService** (see also appendix A.2.3) has been developed for this work.

- A *minimizer service* that scans and minimizes the likelihood landscape by varying the abstract numbers that it got from the parametrization service. A minimizer service is just a mathematical algorithm that does not care about the physical meaning of the value that it gets from the parametrization. Examples for such minimizers are **I3GulliverAnnealing** [124], **I3GulliverMinuit** [113] or **I3GSLSimplex** [122] [123]. The choice of an appropriate minimizer is

always a question of balance between computing time and accuracy. For this work **I3GSLSimplex** has proven as a robust tool and a good compromise between reliably finding the global minimum in the shower likelihood landscapes and computing time. Hence, it was used for the reconstruction.

The whole Gulliver package is divided into three SeaTray projects (sub-parts of the whole SeaTray framework) that have to be installed in the SeaTray installation.

- *gulliver.* The main project that contains the **I3Gulliver** core and several internal helper classes and output containers. Further, virtual base classes for the different kind of services are implemented here. All services that can be used in Gulliver have to inherit (depending on its type) from **I3ParametrizationBase**, **I3EventLogLikelihoodBase**, **I3MinimizerBase** or **I3SeedServiceBase**.

- *lilliput.* This project contains all different kinds of implementations for the Gulliver services that are derived from the base classes in the project *gulliver*. The services **I3ShowerSeedService** and **I3ShowerParametrizationService** have been added to this project.

- *gulliver-modules.* This project contains modules that use Gulliver for reconstruction. The **I3ShowerFitter** is now part of this project.

After the minimizing fit routine has been performed for each of the seeds, the configuring parameter *StoragePolicy* defines which results will be written to the frame. Possible settings are:

- *OnlyBestFit*: Only the result with the best likelihood value and its corresponding seed, cut parameters and fit parameters is written to frame.

- *AllFitsInVectors*: All fit results are stored in a vector. The same is true for the seeds, fit and cut parameters.

- *AllFits*: All fit results are stored as separate particles. The same is true for the seeds, fit and cut parameters.

The module writes out the results as **I3Particle** (or **I3ParticleVect**). The Gulliver fit parameters are stored under the same name with the suffix *_FitParams*, the cut parameters with the suffix *_CutParams*, seeds are called *_Seeds*. If *StoragePolicy* is *AllFits* the single results/fit parameters/cut parameters/seeds are enumerated, starting with 0. Table C.1, printed in appendix C.1, lists all configuration parameters of this module. The given default values are those that are implemented in the module, not the ones that are used in this work! The configuration that was used for the reconstruction within this analysis is given in appendix B.6.

A.2.1.1 Fit quality parameters I3LogLikelihoodFitParams

The class **I3LogLikelihoodFitParams** is an additional output that is written to the frame in any Gulliver-based reconstruction. It is part of the project *gulliver* and contains four parameters that are a measure for the goodness of the fit result.

- *LogL*: Final minimum negative log likelihood value that is related to the fit result.

- *rLogL*: Reduced final negative log likelihood value as evaluated from equation (6.6) in chapter 6.2.

- *Ndof*: Degrees of freedom of the fit as evaluated from equation (6.7) in chapter 6.2.

- *Nmini*: Number of minimizer calls during the fit routine.

A.2.1.2 Fit convergence parameters I3ShowerFitterCutParams

The class **I3ShowerFitterCutParams** has been introduced to collect additional cut parameters to trap badly reconstructed events. The class contains one value for each fitted parameter that holds the information where the fit has converged with respect to the fit boundaries and the start value that were set for this parameter. This can be useful to identify bad fits where the minimizer converged at one of the boundaries. The parameters are named *TimeConvergencePosition*, *XConvergencePosition*, etc... To summarize the meaning of these values: ± 1 indicates a problem (means the fit ran towards one boundary), values in-between are good, 0 means the fit converged at the start value. Some minimizer implementations, however, ignore the specified fit boundaries and may converge beyond the limits. In this case the convergence position is set to ± 2. The detailed calculation of these parameters is listed in table A.1.

A.2.2 Generating start values using the I3ShowerSeedService

The **I3ShowerSeedService** is a SeaTray service that provides event seeds for any kind of shower reconstructions. The service has been implemented with a focus on shower reconstruction and therefore offers some features to create seeds that take shower specific attributes into account, such as for example the vertex position that is approximately expected at a position where most of the light is deposited in the detector. When reconstructing muon tracks the vertex position has less importance as it is located somewhere on the track. The service can create one or more seeds per event which can be requested by any SeaTray module via the method *GetSeed(i)*. The service is part of the project *lilliput* that provides all kind of services to reconstruction modules that use the Gulliver framework.

Table A.1: Description of the attainable values for the convergence positions in the class I3ShowerFitterCutParams

	SPECIFIED FIT BOUNDARIES			
	Both limits are set	Only lower limit is set	Only upper limit is set	No limits are set
2	fit result above upper limit	-	fit result above upper limit	-
1	fit result at upper limit	fit result is ∞	fit result at upper limit	fit result is ∞
$[0, 1]$	linear interpolation between start value and upper limit	0.5 for all fit results above start value	linear interpolation between start value and upper limit	0.5 for all fit results above start value
0	fit result at start value position			
$[-1, 0]$	linear interpolation between lower limit and start value		-0.5 for all fit results below start value	
-1	fit result is at lower limit		fit result is $-\infty$	
-2	fit result is below lower limit		-	

The shower seed service creates one basic seed. For each parameter (time, vertex, direction, energy) the user can choose individually how the seed value is to be created. It is also possible to take some of the shower parameter seeds from an existing input particle and only fill up the missing ones. From this basic first seed several alternatives can be created by shifting one or more of the basic seed values randomly. The level of this shift can be configured for each parameter independently. For example: Set *VertexShift* to 30 m and for each alternative seed the vertex will be shifted by 30 m from the basic seed in random directions. If *VertexShift* is set to 0 the vertex will be kept fixed for all alternative seeds.

Table C.2 in appendix C.1 lists all configuring parameters of the service. Again note that the given default values are those that are implemented in the service, not the ones that are used in this work! The configuration that was used for the reconstruction within this analysis is given in appendix B.6. The possible options that can be set for the seed creation of the different shower parameters are listed in the tables C.3 - C.6 in appendix C.1.

For the option *Fit* as *EnergySeedType* a rough correlation between the shower energy and the total charge of the event has been evaluated by doing a simple polynomial fit to a small Monte-Carlo shower simulation that has been performed with the standard ANTARES simulation software tools GENHEN and GEASIM (see chapter 5.1) . The fit correlates the total charge A (the cumulative charge of all shower signal hits) to the true shower energy E. The distribution and the corresponding fit graph is shown in figure A.3. The fitted graph is a 3rd order polynomial for which a ROOT [113]

chi-square fit yielded

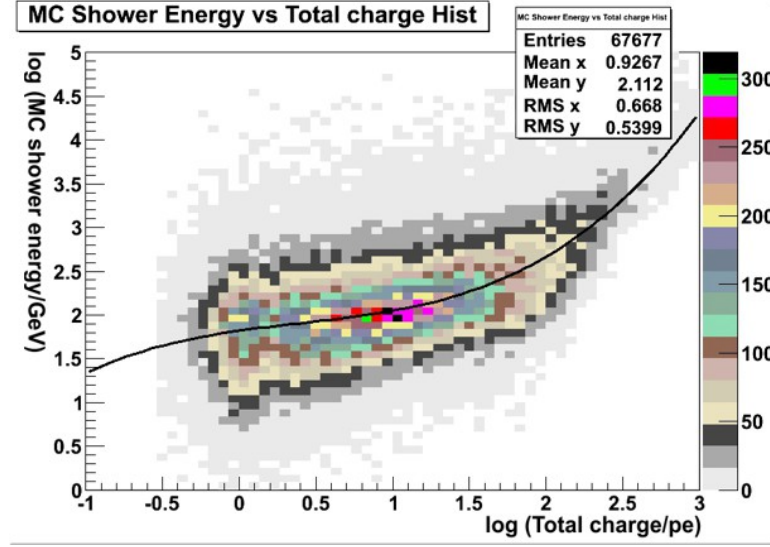$$\log E = 1.82 + 0.25a - 0.13a^2 + 0.11a^3 \tag{A.1}$$

where a is $\log A$.

Figure A.3: *Correlation fit between total charge and energy as rough estimation for an energy seed.* To create a seed for the energy in a shower reconstruction the service **I3ShowerSeedService** offers the possibility to use a rough estimation of the energy as function of the total charge of all signal hits. For this a 3rd order polynomial fit has been performed on a small shower simulation without background noise. The black line marks the result of a chi square fit using ROOT [113].

A.2.3 Setting fit limits and step sizes using the I3ShowerParametrizationService

The **I3ShowerParametrizationService** is a SeaTray service that provides a parametrization of shower events for maximum likelihood reconstructions that use the Gulliver framework. The parametrization is the interface between the likelihood service and the minimizer service, thus it contains methods that convert the physics shower parameters stored in an **I3Particle**, such as time, x, y, z, energy, zenith and azimuth, to abstract values that are seen by the minimizer and vice versa. Further, it can set suitable fit boundaries, start values and step sizes for the minimization for each of the seven shower parameters. If one parameter should be kept fixed during the fit, set its corresponding entry in the *StepsizeVector* to 0. Table C.7 in appendix C.1 lists all configuring parameters of the service. The configuration that was used for the reconstruction within this analysis is given in appendix B.6.

The *StepsizeVector* defines which parameters will be varied during the fit and which ones should be kept fixed. So set entries to 0 for parameters where the initial value

should be kept fixed. For all other parameters the entry defines the step size by which one minimizer step varies its value. Note: Depending on what minimizer service is chosen, the step size can have a different meaning, as for example most minimizers will diminish the step size automatically during the minimization procedure to gain accuracy.

When performing a Gulliver fit this parametrization service will try to set a start value for the fit for each of the seven shower parameters according to the following policy hierarchy:

1. If the user has set an entry in the *StartVector* (that is non NAN) this value will be taken as start value, no matter what has been provided by the seed service (see appendix A.2.2)

2. If not, the start value will be obtained from the seed that has been created by the seed service.

3. If the seed service value and the *StartVector* entry are both NAN, the start value will be set to the middle of the fit range [*UltimateLowerBound*, *UltimateUpperBound*].

4. If the value from the seed service and the *StartVector* entry are NAN and the fit has an unlimited range, print a warning and set the start value to 0.

After the start values for the seven shower parameters have been obtained, the service tries to set the fit boundaries according to the following rules:

- The ultimate limits are set in *UltimateUpperBoundVector* and *UltimateLowerBoundVector*. The fit will never exceed these absolute limits, unless some special minimizers ignore the fit limits... But to catch this case the *convergence positions* have been introduced as fit quality parameters, as described in appendix A.2.1.2.

- In addition one can set an *AdjustUpperIntervalVector* and an *AdjustLowerIntervalVector*. The actual search space is now adjusted around the start value (that can vary from event to event) in a way that *AdjustUpperIntervalVector*[i] is added to the start value and *AdjustLowerIntervalVector*[i] is subtracted from the start value for parameter i. If the adjusted range exceeds the ultimate limits, it, however, will be restricted to the setting of *UltimateUpperBoundVector* and *UltimateLowerBoundVector*. (See figure A.4)

- If one entry in *AdjustUpperIntervalVector* or *AdjustLowerIntervalVector* is NAN, no adjustment will be done for this parameter and the limits will always be taken from *UltimateUpperBoundVector* and *UltimateLowerBoundVector*.

- If for one parameter all limit settings are NAN, the fit will be unlimited for this parameter.

Figure A.4 gives an illustration of the fit boundary determination for one parameter.
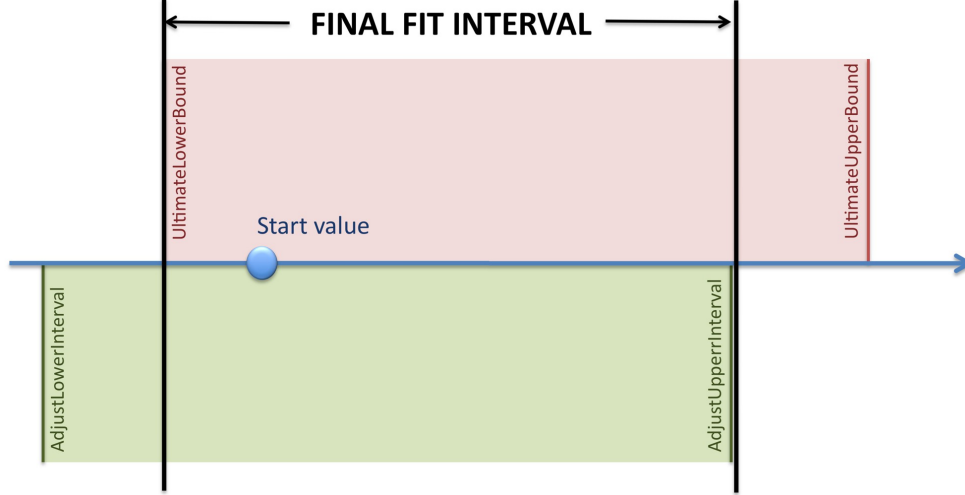

Figure A.4: *Illustration of how the fit limits are determined in the I3ShowerParametrizationService. For each of the seven shower parameters a search interval is defined, where the minimizer is allowed to look for the minimum in the likelihood landscape. The determination of this interval is configured in the shower parametrization service by two absolute ultimate boundaries that are kept fixed for each event and two adjusted boundaries that are arranged around the start value, which can vary from event to event.*

Appendix B

Technical description of the Dusj reconstruction project

This section illustrates the Dusj shower reconstruction project from a technical point of view, which is to be understood as supplement to chapter 6, where especially the physics behind the tools is explained in detail. In the following a more practical manual is given. To keep things clear the extended configuration tables of the single modules are printed separately in appendix C.2, but a unique reference is given whenever the corresponding module is mentioned. The reader is invited to also go through appendix A, where a technical description of the SeaTray and Gulliver software frameworks is given. A knowledge of these frameworks is required in the following.

B.1 How to reconstruct showers with the Dusj project

To apply the Dusj shower reconstruction to a physics event that is stored in a SeaTray frame the Python function **addDusjShowerReconstruction** can be used. The function gathers all SeaTray modules and services that are necessary for a complete reconstruction and event classification with the Dusj project. Further, the configuration of the single modules is also implemented in this function. As input the function requires the set of hits where from the event is to be reconstructed and that is expected to be a C++ class of type **I3RecoPulseSeriesMap** stored in the frame. Table C.8 in appendix C.2 lists all further arguments and default values of this function.

The main output of a Dusj shower reconstruction using this function is another **I3RecoPulseSeriesMap** holding the shower hits that were selected and used for the reconstruction, a C++ container of type **I3MapStringDouble** with a set of potential cut parameters for further quality and purity cuts, the output of the RDF classification represented by an integer of type **I3Int** that defines the classified event type and a floating value of type **I3Double** that stores the safety value of the classification, and an **AntaresRecoParticle** holding the final fit results and copies of some selected

quality parameters that are:

- **NumberOfHits:** The number of hits that have been selected as shower hits by the internal hit selection.

- **NumberOfUsedLines:** The number of lines with hits that have been selected as shower hits.

- **TotalAmplitude:** The integrated charge of all selected shower hits.

- **Lik:** The reduced log-likelihood value of the final fit result. (see chapter 6.2.2)

- **Chi2:** A chi-square of time residuals of the selected shower hits respective to the vertex fit result (following equation (6.13))

- **QualityParam:** The output of the random decision forest muon/shower classification. (see chapter 6.4)

B.2 How to combine the Dusj likelihood services for a global fit

This section describes an alternative way to fit the seven shower parameters that is, however, not used in this analysis. The default way is described in chapter 6.2.

Instead of reconstructing the vertex first, and determine energy and direction afterwards, as it is done by default, the Gulliver framework also offers the possibility to combine the two likelihood services to one for a simultaneous fit of all seven shower parameters. See also chapter 6.2.3.

To link the two likelihood services **I3DusjShowerVertexPDF** and **I3DusjShowerEnergyDirectionPDF** to one, Gulliver's **I3EventLogLikelihoodCombiner** can be used together with an adjustment of the parametrization service to vary all seven parameters simultaneously during the minimization process.

```
1   #Vertex likelihood service
2   tray.AddService("I3DusjShowerVertexPDFFactory", "Dusjvertex")(
3       ..... parameters
4     )
5   #Energy direction likelihood service
6   tray.AddService("I3DusjShowerEnergyDirectionPDFFactory", "
        Dusjenergydirection")(
7       ..... parameters
8     )
9   #Combine the likelihoods
10  tray.AddService("I3EventLogLikelihoodCombiner", "combinelikelihood")(
11    ("InputLogLikelihoods", ["Dusjvertex", "Dusjenergydirection"]),
```

```
12      ("RelativeWeights", [1.0, 1.0])
13      )
14    #Tell the parametrization to fit everything
15    tray.AddService("I3ShowerParametrizationFactory", "
        energyparametrization")(
16      ("StepsizeVector", [5.,1.,1.,1.,0.01,0.01,0.01]), # 5., 1. and 0.01
            is just an example. The important thing is that no entry is 0.
17      .....some more parameters
18      )
```

The parameter *RelativeWeights* of the combiner service allows to give the two likelihoods different weights, in a sense that the combined log-likelihood is calculated as follows:

$$- \log LLH_{\text{combined}} = \sum_{i=1}^{2} -w_i \cdot \log LLH_i \tag{B.1}$$

B.3 Collecting cut parameters with the I3DusjShower-CutValuesCollector

The module **I3DusjShowerCutValuesCollector** is aimed to collect all potential cut parameters that have been written to the frame as intermediate result by the single parts of the precedent shower parameter reconstruction and gather them in one common container. Further, some additional cut parameters are evaluated, such as chi-squares, the quadrupole momentum, etc... The output frame object that holds all the cut parameters is of type **I3MapStringDouble**. In this map the key is the name of the cut parameter and the value is the evaluated or copied value of the parameter for this event. See also chapter 6.3 for information about the additionally evaluated parameters.

As SeaTray, and especially the Gulliver framework, offers a great flexibility in exchanging single reconstruction steps or adding single modules to the reconstruction chain, the **DusjShowerCutValuesCollector** is able to store more parameters than are currently used in the default chain. Especially parameters that can be filled from an optional pre-fit or a separate energy reconstruction are not filled here as no separate pre-fit is performed and the energy is fitted together with the neutrino direction in one common fit. Thus, in this work the cut parameters container will be filled with 24 values per event. The tables C.16 - C.18 in appendix C.2.1 give a list of all cut parameters that can be written to the Dusj cut values container and that have a fixed name. In addition, for each reconstruction step that is a Gulliver maximum likelihood fit (no matter how many of them are included in the chain) the four quality parameters that are written out in the Gulliver internal class **I3LogLikelihoodFitParams** (see appendix A.2.1.1 for more information) can be added to the container. Those parameters are listed in table C.19, also in appendix C.2.1.

Table C.15 in appendix C.2 lists all global configuration parameters of the collector module. Note that depending on the specific configuration of the reconstruction chain not all parameters have to be filled. If one of the parameters, except *OutputMap*, is not set, the corresponding cut parameters will not be evaluated or collected and there will be no entry for them in the output map. The configuration that was used for this analysis is given in appendix B.6. To make plots of the values contained in the Dusj cut values map, use the Python script **PlotDusjShowerCutValues.py**.

B.3.1 How to cut on these parameters

Once the Dusj cut values container has been filled, the project provides some tools that allow to easily perform cuts on one or more of the parameters. Those cuts can be done from any Python script by using the Python class **DusjShowerCuts** or in an usual SeaTray chain by adding the module **I3ApplyDusjShowerCuts** that is a wrapper to create a SeaTray module from the Python class. In both cases the allowed ranges for each of the cut parameters can be set in a configuration text file that is passed to the cutter class. In this text file for each parameter the maximum and minimum value to be selected is specified. Any configuration file has to obey the following structure:

```
1    ############################################################
2    ############################################################
3    ####        DUSJ SHOWER CUT VALUES CONFIGFILE        ####
4    ############################################################
5    ############################################################
6    # Some commentary lines ...
7    # Another one ...
8    ——————————————— # This line is mandatory for the reader!
9    DusjShowerRecoPrefitLogLikelihood                    0    1000
10   DusjShowerRecoPrefitReducedLogLikelihood             0    8
11   DusjShowerRecoPrefitMinimizerCalls                   0    50000
12   DusjShowerRecoPrefitDegreesOfFreedom                 10   INF
13   PrefitTimeResidualChiSquare                          0    250
14   ...
```

Table C.20 in appendix C.2.2 gives an overview of the methods than can be used to handle the cutter class **DusjShowerCuts**, table C.22 lists the configuration parameters of the SeaTray module. Both make use of a helper class that reads in the configuration text file. The methods of this reader class are given in table C.21.

B.4 How to use the RDF as muon/shower discriminator

By default the Dusj project provides already built random decision forest tables that can be used for the discrimination between track-like and shower-like events. These

tables are based on five of the Dusj quality parameters (see also chapter 6.4).

The classification can be included in a SeaTray chain by adding the Python function **addDusjCutValuesRDFClassification**. Table C.23 in appendix C.2.3 lists all configuration parameters of this Python function.

If however, new RDF tables have to be created from future Monte-Carlo productions, the Dusj project provides some Python tools to keep the process simple. The training of a new random decision forest is done in two steps. At first feature tables that are text files storing the used parameters for a specific class have to be generated. For this, for each class (e.g. one class 'shower' and one class 'muon') a separate file has to be created. This can be done by using the Python function **CreateFeatureDataTable** that is defined in **DusjCutValuesRDFFeatureExtractTools.py**. The arguments of this function are listed in table C.26 in appendix C.2.3. From these table a random decision forest can be trained following the example script **ExampleTraining.py** from the SeaTray project *antares-rdfclassify*.

During the classification step the extraction of the features (parameters) has to be exactly the same as it was during the training step. To ensure this both, training and classification, make use of the same Python class **DusjCutValuesRDFFeatureExtract**. During the training process this class will be accessed directly when creating the feature tables, whereas during the classification step a wrapper called **I3DusjCutValuesRDFFeatureExtract** makes the class usable as a SeaTray module. Table C.25 lists the configuration parameters of the SeaTray module, table C.24 the methods of the feature extractor class, both in appendix C.2.3. More information about random decision forests and a more detailed manual how to use the project *antares-rdfclassify* can be found in [114].

B.5 How to create new Dusj PDF tables

The two PDF tables used for reconstruction of the shower parameters have to be filled from Monte-Carlo simulations. The parameters of the simulation (energy range, up-going/down-going, generation volume, etc...) define the allowed parameter ranges for the reconstruction. By default the project *antares-shower-reco-dusj* comes with already built PDF tables that have been created from the electron neutrino Monte-Carlo production *prod11* and that are ready to be used (see chapter 6.2).

At some point one might intend to create new PDF tables from an updated Monte-Carlo simulation. This section gives a manual how this can be done by using the Python scripts and functions that also have been used to create the *prod11* tables. Currently this procedure starts with one or more .evt files that are the output of the ANTARES simulation tool GEASIM (see chapter 5). As the Dusj PDF tables will

be created from signal hits only there is no need to apply a run-by-run based optical background. The detector simulation in this case is performed by a SeaTray chain that replaces the *TriggerEfficiency* program that is usually used in the RBR simulations. If, however, PDF tables should be created from a run-by-run simulation, also .i3 or .root files might be used as input. In this case the script **InstallDataFromEvtFile.py** has to be modified to read in those files and skip its own detector simulation. But please note that in any case, a hit sample without background is required for the creation of the tables.

Starting from a set of Monte-Carlo simulation .evt files, the creation of the PDF tables is done in two steps:

- **Converting the .evt files into .dusj files.** This step performs the detector simulation and extracts the relevant data from the Monte-Carlo simulations that will be used for the PDF table generation later on. This step is the most CPU time consuming part of the table generation and thus the possibility is provided to perform the conversion using the Lyon CPU cluster [84]. The resulting files serve as input for the generation of the vertex PDF table as well as for the energy-direction PDF table.

- **Creating the PDF tables from the .dusj files.** At this point the fine tuning on the true Monte-Carlo values (from the .dusj files) can be applied, such as smearing, setting range limits, axis binning, etc... The output will be two PDF tables stored in .root files (file format of the ROOT framework [113]).

B.5.1   Converting the Monte-Carlo files into the internal .dusj format

The conversion of a Monte-Carlo simulation into the .dusj format is done by the script **InstallDataFromEvtFile.py**. Currently only the .evt file format is supported as Monte-Carlo file input. From each .evt file a new .dusj file will be created. Table C.27 in appendix C.2.4 lists the configuration parameters of this Python script. The conversion has to be done just once. At this point the detector simulation is applied and all relevant Monte-Carlo data is extracted from the simulations without applying specific changes like smearing, binning, etc... These files contain the true Monte-Carlo information and serve as input for the final generation of the PDF tables.

The script will loop over all hits in all events and write one entry per hit into the .dusj file. This entry contains:

- The distance of the OM from the vertex

- The arrival time since the interaction time

- The emission angle from the vertex with respect to the neutrino direction

- The detected charge

- The angular acceptance of the OM at the hit's angle of incidence

- The shower energy that created this hit

Some of these parameters are derived parameters using the vertex position as input. Here the script offers two possibilities to define the vertex via the configuration parameter *vertextype*. The default configuration that turned out to yield better results is *vertex*, where the true Monte-Carlo interaction vertex position is used for further evaluation. If this parameter is set to *cog*, the center of gravity of the hits' amplitudes in the event is evaluated from all given shower hits and taken as vertex position. In the latter case events where the true Monte-Carlo vertex is outside the instrumented volume will not be taken into account as for not contained events the cog evaluation will produce a wrong estimation of the vertex position due to the fact the only a fraction of light is detected at the edge of the detector.

To take PMT saturation effects into account a saturation table has been generated in advance from various real ANTARES data runs from all over the data taking period. This ensures that the PMT saturation that may differ from OM to OM is applied appropriately, following on average the distribution from real ANTARES detector conditions. See also chapter 3.3 and appendix B.5.1.2.

A successfully created .dusj file will look as follows:

```
1   ############################################################
2   ###############   Dusj PDF DATA TABLE   #############
3   ############################################################
4   # HEADER
5   # table created on: Thu, 28 Feb 2013 14:40:33
6   # from script: InstallDataFromEvtFile.py
7   # version: 2.1
8   # inputfile: /sps/km3net/users/folger//phd/shower//mcfiles/prod11/evt
        //gea-OPA_gen_nuE_up_cc_1e5-1e6_run01.evt.bz2
9   # processed events: all
10  # ARS integrationtime: 40.00
11  # ARS deadtime: 250.00
12  # OM angular parametrization: Spring09
13  # Detector file: /sps/km3net/users/folger/SeaTray/trunk/src/antares-
        shower-reco-Dusj/resources/files/r12_c00_s01.det
14  # OM saturation table: ../resources/root/OMCal_run_30000_to_55000.
        root
15  # Vertex type: vertex
16  ############################################################
17  # ADDITIONALINFO
18  # Generated spectrum: -1.10
19  # Generated events: 10000
20  # OM diameter: 0.236220
```

```
21   #########################################################
22
23   Counter  | OMDistance       ArrivalTime      EmissionAngle   PulseCharge
            AngularAccept   ShowerEnergy
24   _____
25   00000001 | 2.27640550e+02 1.04795146e+03 5.19172113e+01 3.69843846e
            -01 1.14438910e-01 1.08570000e+05
26   00000002 | 2.65155285e+02 1.22494363e+03 5.54484182e+01 1.35339342e
            +00 7.65378172e-01 1.08570000e+05
27   00000003 | 1.83725784e+02 8.38168615e+02 3.49187601e+01 4.73881831e
            +00 8.36675376e-01 1.08570000e+05
28   00000004 | 1.83996678e+02 8.47128074e+02 3.46363015e+01 2.01371437e
            +00 6.08954777e-01 1.08570000e+05
29   00000005 | 1.84586804e+02 8.45253104e+02 3.47919949e+01 6.14037556e
            -01 1.68431257e-01 1.08570000e+05
30   00000006 | 1.90941285e+02 8.76574577e+02 3.68023587e+01 2.49816471e
            +00 9.77815330e-01 1.08570000e+05
31   00000007 | 1.91653875e+02 8.79796070e+02 3.65931019e+01 2.19905113e
            +00 3.88162183e-01 1.08570000e+05
32   00000008 | 1.91695292e+02 8.82967921e+02 3.68393816e+01 2.95046304e
            +00 3.57311842e-01 1.08570000e+05
33   00000009 | 1.99699607e+02 9.16088470e+02 3.88771402e+01 6.98517583e
            -01 4.63243774e-01 1.08570000e+05
34   00000010 | 1.99087492e+02 9.12540012e+02 3.88014470e+01 3.24876955e
            +00 9.79033706e-01 1.08570000e+05
35   ...
```

Once the Monte-Carlo simulations have been converted to .dusj files, they can be checked for errors by using the script **CheckDusjFile.py**. As input parameter −−*inputfile* this scripts expects the path and name of the .dusj file. The output of this check will look as follows:

```
1    ######################################################################
2    Filename  ................... OK
3    Number of photons  .......... OK
4    Generated events  ........... OK
5    Generated spectrum  ......... OK
6    OM diameter  ................ OK
7    ARS integrationtime  ........ OK
8    ARS deadtime  ............... OK
9    Detector file  .............. OK
10   OM angular parametrization .. OK
11   OM saturation table  ........ OK
12   Vertex type  ................ OK
13   Script  ..................... OK
14   Inputfile  .................. OK
15   Processed events  ........... OK
16   Date  ....................... OK
17   Version  .................... OK
18   Angular efficiency range .... OK
19   Arrival time range  ......... OK
20   Emission angle range  ....... OK
21   OM distance range  .......... OK
22   Pulse charge range  ......... OK
```

```
23    Shower energy range ........ OK
24 —————————————————————————————————————————————————————
```

To see the content of the .dusj file in plots, use the script **PlotDusjFile.py**. The script will create a .pdf file containing

- 1D histograms of the six values listed in the Dusj file

- 2D contour plots showing each value against the others

The parameter $--inputfile$ specifies the .dusj file that is to be plotted, $--log$ will create a logarithmic y-axis in 1D and a logarithmic z-axis in 2D plots.

B.5.1.1 The Dusj file reader

All scripts that read in .dusj files, such as those that finally create the PDF tables, use the Python class **DusjFileReader** to read out the data from the text file. When building the PDF tables from the .dusj files, it is probable that a table is created from more than one .dusj file. Hence, when using the **DusjFileReader** automatic checks will be performed to guarantee that the .dusj files match together and have been created with the same input parameters. Therefore the **DusjFileReader** compares the headers of the .dusj files and prints out warnings when inconsistencies have been detected. Table C.28 in appendix C.2.4 lists the methods of this class.

B.5.1.2 Randomized OM charge saturations

In Monte-Carlo simulations in principle it is allowed to have several thousand photons detected at one OM. There is no saturation limit as the physics simulation does not know about the dynamic range of each specific OM. On the contrary in measured ANTARES data, each OM has a different dynamic range and thus a different charge saturation. Most OMs reach their saturation at about $20 - 25$ pe. As the charge of the hits is an essential information for the reconstruction of the shower energy and as - especially for high energy showers - it is expected to have always hits from OMs that are in saturation it is important to include a realistic distribution of the OM charge saturation into the PDF tables. For this the real dynamic ranges of all OMs over the whole data taking period have been read out from the calibration database and stored in a ROOT table. From this table for each processed hit that will contribute with one entry to the PDF table a random OM saturation value was chosen following the distribution in the table. If the hit charge exceeds this randomly taken saturation level, the hit charge is clipped to the saturation level, as it would happen during real ANTARES data taking.

To create such a charge saturation distribution table use the Python script **GetOM-SaturationsFromDatabase.py** and specify the run from which the calibration is to be used via the parameter $--runnumber$. To include more than one run separate the single run IDs by commas. The saturation distribution that was used to generate the default Dusj PDF tables has been created from 250 runs in steps of 100 within the run number range from 30000 to 55000. This table is stored in the file **OMCal_run_30000_to_55000.root**. The content of the created .root file will be:

- A **TH1** histogram **cal_OM_saturations_all_ARS** containing the saturation distribution from all ARS in the given runs.

- A **TH1** histogram **cal_OM_saturations_good_ARS** containing the saturation for ARS for which *IsItOK()* is True.

- A **TH1** histogram **cal_OM_saturations_bad_ARS** containing the saturations for ARS for which *IsItOK()* is False.

- A vector of run numbers from which the tables have been created.

Here, of course the one containing the good ARS only was used for the randomization later on. Figure 3.9 in chapter 3.3 illustrates the content of these three tables for the specified default file.

The readout of the saturation table in the .root file can be done with a Python class called **RandomizeOMSaturations**. This class takes the .root file, gets out the table and provides random numbers that follow the distribution in the table. Table C.29 in appendix C.2.4 lists the methods of this Python class. An additional Python wrapper class called **I3RandomizeOMSaturations** makes this class accessible as a SeaTray module for any SeaTray Python script. In this case the module will take an input **I3RecoPulseSeriesMap**, get a randomized saturation value for each hit and writes out a new hit map where each hit for which the charge exceeded the randomized saturation has been clipped. Table C.30 in appendix C.2.4 lists the configuration parameters of this module.

B.5.2 Generating PDF tables from a set of .dusj files

Once all Monte-Carlo simulation files have been converted into .dusj format, it is quite simple to finally create the PDF tables. As this step is much less CPU time consuming compared to the conversion step, one could easily try out varying the configuration parameters of the generation scripts until the PDF table satisfies the main requirement for a successful reconstruction that is basically a smooth shape. Single peaks in the tables are to be avoided as they cause unwanted steps in the final evaluation of the

likelihood that probably will confuse the minimizing algorithms. Thus, using the following scripts in default mode will not necessarily produce nice PDF tables. For each specific set of simulation files one has to figure out the optimum settings for binning and axis range to avoid edges, steps, single peaks or large areas in the parameter space with no entry.

The final likelihood landscape will be evaluated by combining the PDF values from each single hit according to equation (6.4) in chapter 6.2. The primary focus should be to create a smooth likelihood landscape that will be passed to the minimizer. In principle this can be achieved in two different ways:

- *By smoothing the input values before filling them into the PDF table.* In this case the parameters *binning* and *smearing* of the two Python scripts described in the following sections are used to smooth out peaks and edges already in the PDF tables. For the generation of the default tables from *prod11*, however, no smearing was applied in the PDF tables. In this case the idea was to keep the PDF tables as close as possible to the Monte-Carlo truth and if necessary apply the smoothing later in the likelihood services (the second method).

- *By smoothing the already built PDF table.* This way allows to keep the information that is stored in the PDF table as accurate as possible as no smoothing is included in the table. If necessary, a smoothing can be applied to the whole table later on during the reconstruction step. For this the ROOT method *Smooth* is used in the Dusj likelihood services (see also chapter 6.2) that are configured following the tables C.13 and C.14 in appendix C.2.

By default the axis ranges in the following PDF tables are defined by the content of the .dusj file sample that is used as input for the table generation. The scripts will process a certain number of entries until a *bufferlength* is reached. The maximum and minimum of the - so far - processed entries define the axis ranges of the histogram. If during the further processing values are outside these ranges, they will be stored in the over- and underflow. Thus, to ensure that the data from the .dusj files is completely inside the axis ranges, *bufferlength* should be set as high as possible (limitation is memory). If the expected axis ranges can be estimated in advance, the limits can be set manually in both following scripts using the parameter *forcelimits*, where in this case *bufferlength* has no effect.

B.5.2.1 PDF table for the vertex reconstruction

The PDF table for the vertex reconstruction as described in chapter 6.2.1 is created by the Python script **BuildDusjVertexPDFTable.py** that reads in a sample of .dusj files where each line contains data from one hit of the Monte-Carlo simulation. A data

line holds the full information to fill the PDF table that is a ROOT **TH2D** histogram. In this case the values *OMDistance* and *ArrivalTime* are taken directly from the file and passed to the histogram without any further calculations. Table C.31 in appendix C.2.4 lists all configuration parameters. The script will write out a .root file that contains the following entries:

- **DusjVertexPDFTable**: The PDF table

- **TableInfo**: A map containing all steering parameters that have been set when the table was created.

- **DusjFilesInfoVec**: A vector containing information maps that hold the header infos of each .dusj file that was used to create the table.

The new PDF table can now be used in the likelihood service **I3DusjShower-VertexPDF** by setting the parameter *PDFTableFile* to the new .root file.

B.5.2.2   PDF table for the shower energy and neutrino direction reconstruction

The PDF table for the shower energy and neutrino direction reconstruction (as described in chapter 6.2.2) is created by the Python script **BuildDusjEnergyDirectionPDFTable.py** that reads in a sample of .dusj files where each line contains data from one hit of the Monte-Carlo simulation. A data line holds the full information to fill the PDF table that is in this case a ROOT **TH3D** histogram. Here, the values *OMDistance*, *PulseCharge* and *AngularEfficiency* are used to evaluate the *total vertex charge* that represents one axis in the histogram and the *initial hit charge* that is used as weight, if the table is created in *photon-based* mode. (See chapter 6.2.2 for more information.) The values *EmissionAngle* and *ShowerEnergy* are taken directly from the file and filled into the histogram. Table C.32 in appendix C.2.4 lists all configuration parameters. The script will write out a .root file that contains the following entries:

- **DusjEnergyDirectionPDFTable**: The PDF table

- **TableInfo**: A map containing all steering parameters that have been set when the table was created.

- **DusjFilesInfoVec**: A vector containing information maps that hold the header infos of each .dusj file that was used to create the table.

As the energy-direction PDF table has three axes, it might require more efforts to obtain a sufficient high quality of the PDF table. Note that in the table the shower-energy-bin-planes are normalized to the same value to give each energy the same probability to occur. The configuration parameter *minenergybincoverage* sets a minimum

requirement to the fraction of bins in the angle-vertexcharge plain for one energy bin that has to have entries to be taken into account in the normalization. If, for example, from all *chargebinning × anglebinning* available bins for one specific log-energy bin only 3 bins have entries, this bin should not be normalized as it would create unnatural high peaks. To trace the fine-tuning process on the PDF table the Python function **Plot-DusjEnergyDirectionPDFTable.py** can be used to create projection and excerpt plots of the 3D table.

The new PDF table can now be used in the likelihood service **I3DusjShower-EnergyDirectionPDF** by setting the parameter *PDFTableFile* to the new .root file.

B.6   SeaTray script for the Dusj shower reconstruction

This Python SeaTray script holds the configuration of the Dusj chain that was used for the reconstruction of the complete RBR simulation and ANTARES data for this analysis, which has internally been named *shower production 13-07-00*. To reconstruct events using this configuration use the Python function **addDusjShowerReconstruction.py** as introduced in appendix B.1.

```python
#!/usr/bin/env python
import sys, os, numpy


# IceTray inits
#------------------------------------------------------------
from icecube import icetray, dataclasses, antares_common
from icecube.icetray import I3Units
from icecube.antares_shower_reco_dusj import *
from I3Tray import *
load("libicetray")
load("libdataclasses")
load("libantares-shower-reco-dusj")
load("liblilliput")
load("libgulliver")
load("libgulliver-modules")
load("librdfclassify")
tray = I3Tray()

# Read input file
#------------------------------------------------------------
tray.AddModule("I3Reader","filereader")(
    ("FilenameList","whateverinputfiles")
    )

# Random service for various seeds
#------------------------------------------------------------
tray.AddService("I3SPRNGRandomServiceFactory","dusjrandom")(
    ("Seed",        1234),
    ("NStreams",   1235),
```

```
31        ("StreamNum", 1)
32      )
33
34
35  ###########################################
36  ## STEP 1: EVENT– AND HITSELECTION ##
37  ###########################################
38
39  # Remove hits that occur after an ARS dead time
40  # Required as lots of scattered hits in high energy
41  # showers puzzle the reconstruction otherwise
42  #————————————————————————————————————————
43  tray.AddModule("I3HitSelectorModule<I3RemovePulsesAfterARSDeadTime>", "
        cleandeadtimepulses")(
44          ("INmap", "CalibratedPulses"),
45          ("OUTmap", "DusjShowerRecoARSDeadTimeCleanedPulses"),
46          ("ARSDeadTime", 250.*I3Units.ns),
47          ("RemoveAlsoPulseFromSecondARS", True),
48          ("NoFrameNamingPostfix", True),
49          ("WriteSelectedHits", True),
50          ("WriteDeselectedHits", False)
51          )
52
53  # Hit selection
54  #————————————————————————————————————————
55  tray.AddModule("I3DusjShowerIdentifier", "dusjshoweridentifier")(
56          ("PrintLevel", 0),
57          ("InputPulses", "DusjShowerRecoARSDeadTimeCleanedPulses"),
58          ("SeedParticle", ""),
59          ("OutputPulses", "DusjShowerRecoShowerPulses"),
60          ("OutputVertex", "DusjShowerRecoShowerIdentifierVertex"),
61          ("OutputChiSquare", "
                DusjShowerRecoShowerIdentifierReducedChiSquare"),
62          ("WriteOutVertex", True),
63          ("WriteOutReducedChiSquare", True),
64          ("ShowerThreshold", 1.2),
65          ("MinimumNumberOfHits", 5),
66          ("MinimumNumberOfCoincidences", 1),
67          ("TimeTolerance", 80.*I3Units.ns),
68          ("ShowerResolution", 70.*I3Units.m),
69          ("PositionSteplength", 5.*I3Units.m),
70          ("TimeSteplength", 1.*I3Units.ns),
71          ("DistanceToCoincidence", 50.*I3Units.m),
72          ("CoincidenceWindow", 20.*I3Units.ns),
73          ("CoincidenceLevel", 2),
74          ("ScanIterations", 7),
75          ("FindBiggestShowerOnly", True),
76          ("EventContainsShowerOnly", True),
77          ("ChiSquareCut", 1000.)
78          )
79
80
81  ####################################
82  ## STEP 2: MINIMUM CONSTRAINTS ##
83  ####################################
84
```

```
85  # Minimum constraints filter
86  #————————————————————————————————————
87  tray.AddModule("I3IcePickModule<I3MinimumConstraintsFilter>", "
        dusjminconstraints")(
88          ("DecisionName", "DusjShowerRecoMinimumConstraintsFulfilled"),
89          ("DiscardEvents", False),
90          ("Map", "DusjShowerRecoShowerPulses"),
91          ("MinHits", 5),
92          ("MinOMs", 3),
93          ("MinStrings", 2),
94          ("MinLCMs", 2),
95          ("MinMLCMs", 0)
96          )
97
98
99  ########################################
100 ## STEP 3: VERTEX RECONSTRUCTION ##
101 ########################################
102
103 # Simplex minimizer
104 #————————————————————————————————————
105 tray.AddService("I3GSLSimplexFactory", "dusjsimplex_vertex")(
106          ("MaxIterations", 2000),
107          ("Tolerance", 1.E-6),
108          ("SimplexTolerance", 1.E-6),
109          ("FlatPatience", 0)
110          )
111
112 # The dusj shower vertex pdf service
113 #————————————————————————————————————
114 tray.AddService("I3DusjShowerVertexPDFFactory", "dusjvertex")(
115          ("InputPulses", "DusjShowerRecoShowerPulses"),
116          ("PDFTableFile", os.path.expandvars("$I3_SRC/antares-shower-
                reco-dusj/resources/root/DusjVertexPDFTable_directlight.root
                ")),
117          ("UseInterpolation", True),
118          ("PDFThreshold", 1.e-8),
119          ("Smoothness", 0),
120          ("ClipThreshold", 1.),
121          ("IncludeNotFiredOMs", False),
122          ("NotFiredOMsWeight", 1.),
123          ("InputOMConditionMap", ""),
124          ("WriteOutUsedTable", "")
125          )
126
127 # The seed
128 #————————————————————————————————————
129 tray.AddService("I3ShowerSeedServiceFactory", "dusjvertexseed")(
130          ("TimeSeedType", "FirstTriggered"),
131          ("VertexSeedType", "CenterOfAmplitude"),
132          ("EnergySeedType", "NAN"),
133          ("DirectionSeedType", "NAN"),
134          ("InputPulses", "DusjShowerRecoShowerPulses"),
135          ("NumberOfSeeds", 5),
136          ("TimeShift", 50.*I3Units.ns),
137          ("VertexShift", 10.*I3Units.m),
```

```
138            ("InputParticle", ""),
139            ("AvoidNAN", False)
140            )
141
142  # Parametrization
143  #——————————————
144  tray.AddService("I3ShowerParametrizationFactory", "
         dusjvertexparametrization")(
145            ("StartVector", [numpy.nan for i in range(7)]),
146            ("AdjustUpperIntervalVector", [1000.*I3Units.ns, 130.*I3Units.m
                 , 130.*I3Units.m, 180.*I3Units.m, numpy.nan, numpy.nan,
                 numpy.nan]),
147            ("AdjustLowerIntervalVector", [100.*I3Units.ns, 130.*I3Units.m,
                 130.*I3Units.m, 180.*I3Units.m, numpy.nan, numpy.nan, numpy
                 .nan]),
148            ("UltimateUpperBoundVector", [numpy.nan for i in range(7)]),
149            ("UltimateLowerBoundVector", [numpy.nan for i in range(7)]),
150            ("StepsizeVector", [50.*I3Units.ns, 10.*I3Units.m, 10.*I3Units.
                 m, 10.*I3Units.m, 0, 0, 0]), #keep energy and angle fixed
151            ("Can", [165.*I3Units.m, 165.*I3Units.m, 165.*I3Units.m]),
152            ("LimitToCanVolume", True)
153            )
154
155  # Fit
156  #——————————————————————
157  tray.AddModule("I3ShowerFitter", "dusjvertexfit")(
158            ("SeedService", "dusjvertexseed"),
159            ("LikelihoodService", "dusjvertex"),
160            ("ParametrizationService", "dusjvertexparametrization"),
161            ("MinimizerService", "dusjsimplex_vertex"),
162            ("StoragePolicy", "OnlyBestFit"),
163            ("FitOutput", "DusjShowerRecoVertexFit"),
164            ("WriteOutSeeds", True),
165            ("ConvertFitResultFromThetaPhi", False),
166            ("DoNotWriteFitParams", False),
167            ("DoNotWriteCutParams", False),
168            ("EventSelection", "DusjShowerRecoMinimumConstraintsFulfilled")
169            )
170
171
172  ########################################
173  ## STEP 4: ENERGY DIRECTION RECO ##
174  ########################################
175
176  # Simplex minimizer
177  #————————————————————————————————————————
178  tray.AddService("I3GSLSimplexFactory", "dusjsimplex_energydirection")(
179            ("MaxIterations", 2000),
180            ("Tolerance", 1.E−2),
181            ("SimplexTolerance", 1.E−2),
182            ("FlatPatience", 0)
183            )
184
185  # The dusj shower energy direction pdf service
186  #————————————————————————————————————————————————
```

```
187 tray.AddService("I3DusjShowerEnergyDirectionPDFFactory", "
       dusjenergydirection")(
188         ("InputPulses", "DusjShowerRecoShowerPulses"),
189         ("PDFTableFile", os.path.expandvars("$I3_SRC/antares-shower-
                reco-dusj/resources/root/
                DusjEnergyDirectionPDFTable_directlight.root")),
190         ("UseInterpolation", True),
191         ("PDFThreshold", 1.e-10),
192         ("Smoothness", 0),
193         ("ClipThreshold", 1.),
194         ("LogEnergyMin", 2),
195         ("LogEnergyMax", 9),
196         ("WriteOutUsedTable", ""),
197         ("WeightingMode", 0)
198         )
199
200 # The second seed
201 #————————————————————————————————————
202 tray.AddService("I3ShowerSeedServiceFactory", "dusjenergydirectionseed"
       )(
203         ("VertexSeedType", "InputParticle"),
204         ("TimeSeedType", "InputParticle"),
205         ("DirectionSeedType", "Horizontal"),
206         ("EnergySeedType", "Middle"),
207         ("InputPulses", "DusjShowerRecoShowerPulses"),
208         ("NumberOfSeeds", 10),
209         ("DirectionShift", 90.*I3Units.deg),
210         ("LogEnergyShift", 2.),
211         ("InputParticle", "DusjShowerRecoVertexFit_FitResult"),
212         ("AvoidNAN", False)
213         )
214
215 # Parametrization
216 #————————————————————————
217 tray.AddService("I3ShowerParametrizationFactory", "
       dusjenergydirectionparametrization")(
218         ("StartVector", [numpy.nan for i in range(7)]),
219         ("AdjustUpperIntervalVector", [numpy.nan for i in range(7)]),
220         ("AdjustLowerIntervalVector", [numpy.nan for i in range(7)]),
221         ("UltimateUpperBoundVector", [numpy.nan, numpy.nan, numpy.nan,
                numpy.nan, 1.e2, numpy.nan, numpy.nan]),
222         ("UltimateLowerBoundVector", [numpy.nan, numpy.nan, numpy.nan,
                numpy.nan, 1.e9, numpy.nan, numpy.nan]),
223         ("StepsizeVector", [0, 0, 0, 0, 1.e7, 45.*I3Units.deg, 90.*
                I3Units.deg]), #keep vertex and time fixed
224         )
225
226 # Fit
227 #————————————————————————
228 tray.AddModule("I3ShowerFitter", "dusjenergydirectionfit")(
229         ("SeedService", "dusjenergydirectionseed"),
230         ("LikelihoodService", "dusjenergydirection"),
231         ("ParametrizationService", "dusjenergydirectionparametrization"
                ),
232         ("MinimizerService", "dusjsimplex_energydirection"),
233         ("StoragePolicy", "OnlyBestFit"),
```

```
234              ("FitOutput", "DusjShowerRecoFinalFit"),
235              ("WriteOutSeeds", True),
236              ("ConvertFitResultFromThetaPhi", False),
237              ("DoNotWriteFitParams", False),
238              ("DoNotWriteCutParams", False),
239              ("EventSelection", "DusjShowerRecoMinimumConstraintsFulfilled")
240              )
241
242
243 ###################################
244 ## STEP 5: COLLECT CUT VALUES ##
245 ###################################
246
247 # Create the cut value container
248 #──────────────────────────────────────────────
249 tray.AddModule("I3DusjShowerCutValuesCollector", "dusjcutvalues")(
250              ("FitPulses", "DusjShowerRecoShowerPulses"),
251              ("FitResult", "DusjShowerRecoFinalFit_FitResult"),
252              ("PrefitPulses", ""),
253              ("PrefitResult", ""),
254              ("GulliverFitParams", ["DusjShowerRecoFinalFit_FitParams", "
                  DusjShowerRecoVertexFit_FitParams"]),
255              ("ShowerIdentifierReducedChiSquare", "
                  DusjShowerRecoShowerIdentifierReducedChiSquare"),
256              ("ShowerIdentifierVertex", "
                  DusjShowerRecoShowerIdentifierVertex"),
257              ("FitVertexConvergencePosition", "
                  DusjShowerRecoVertexFit_CutParams"),
258              ("FitTimeConvergencePosition", "
                  DusjShowerRecoVertexFit_CutParams"),
259              ("FitEnergyConvergencePosition", "
                  DusjShowerRecoFinalFit_CutParams"),
260              ("FitDirectionConvergencePosition", "
                  DusjShowerRecoFinalFit_CutParams"),
261              ("PrefitVertexConvergencePosition", ""),
262              ("PrefitTimeConvergencePosition", ""),
263              ("OutputMap", "DusjShowerRecoCutValues")
264              )
265
266
267 ##########################################
268 ## STEP 6: RDF EVENT CLASSIFICATION ##
269 ##########################################
270
271 # Extract features
272 #──────────────────────────────────────────────
273 tray.AddModule(I3DusjCutValuesRDFFeatureExtract, "dusjfeatureextract")(
274              ("InputCutValues", "DusjShowerRecoCutValues"),
275              ("UseParameters", ["ShowerIdentifierReducedChiSquare", "
                  DusjShowerRecoVertexFitReducedLogLikelihood", "
                  DusjShowerRecoFinalFitReducedLogLikelihood", "
                  FitTimeResidualChiSquare", "FitQuadrupoleMoment"]),
276              ("FeatureVectorName", "DusjShowerRecoRDFFeatures")
277              )
278
279 # Classify
```

```
280  #——————————————————————————————————
281  tray.AddModule("I3RDFClassify","rdfclassify")(
282          ("DataName", "DusjShowerRecoRDFFeatures"),
283          ("OutputName", "DusjShowerRecoRDF"),
284          ("RDFToLoad", os.path.expandvars("$I3_SRC/antares-shower-reco-
                  dusj/resources/rdf/RDF_RBRv2_LineX.rdf")) #X has to be
                  replaced for 5Line, 10Line or 12Line periods
285          )
286
287
288  ####################################################
289  ## STEP 7: CONVERT INTO ANTARES–RECO–PARTICLE ##
290  ####################################################
291
292  def ConvertToAntaresRecoParticle(frame):
293          antaresrecoparticle = antares_common.AntaresRecoParticle()
294          if not frame.Has("DusjShowerRecoFinalFit_FitResult"):
295                  frame.Put("DusjShowerRecoReconstructionResult",
                          antaresrecoparticle)
296                  return True
297          #Set general things
298          antaresrecoparticle.SetShape(dataclasses.I3Particle.Cascade)
299          antaresrecoparticle.SetStrategyId(antares_common.
                  AntaresRecoParticle.DUSJ_STRATEGY)
300          #Set things from fit result
301          fitresult = frame.Get("DusjShowerRecoFinalFit_FitResult")
302          antaresrecoparticle.SetPos(fitresult.GetPos())
303          antaresrecoparticle.SetTime(fitresult.GetTime())
304          antaresrecoparticle.SetDir(fitresult.GetZenith(), fitresult.
                  GetAzimuth())
305          antaresrecoparticle.SetEnergy(fitresult.GetEnergy())
306          antaresrecoparticle.SetFitStatus(fitresult.GetFitStatus())
307          #Set things from cut values
308          if frame.Has("DusjShowerRecoCutValues"):
309                  cutvalues = frame.Get("DusjShowerRecoCutValues")
310                  if cutvalues.keys().count("FitNumberOfStrings"):
311                          antaresrecoparticle.SetNumberOfUsedLines(int(
                                  cutvalues["FitNumberOfStrings"]))
312                  if cutvalues.keys().count("
                      DusjShowerRecoFinalFitDegreesOfFreedom"):
313                          antaresrecoparticle.SetNumberOfHits(int(
                                  cutvalues["
                                  DusjShowerRecoFinalFitDegreesOfFreedom"])+3)
                                  # +3 due to three fit parameters in final
                                  fit
314                  if cutvalues.keys().count("FitTotalCharge"):
315                          antaresrecoparticle.SetTotalAmplitude(cutvalues
                                  ["FitTotalCharge"])
316                  if cutvalues.keys().count("
                      DusjShowerRecoFinalFitReducedLogLikelihood"):
317                          antaresrecoparticle.SetLik(cutvalues["
                                  DusjShowerRecoFinalFitReducedLogLikelihood"
                                  ])
318                  if cutvalues.keys().count("FitTimeResidualChiSquare"):
319                          antaresrecoparticle.SetChi2(cutvalues["
                                  FitTimeResidualChiSquare"])
```

```python
320            #Set quality param from RDFSafety and RDFClass
321            if frame.Has("DusjShowerRecoRDFSafety") and frame.Has("
               DusjShowerRecoRDFClass"):
322                    rdfclass = frame.Get("DusjShowerRecoRDFClass")
323                    rdfsafety = frame.Get("DusjShowerRecoRDFSafety")
324                    if rdfclass.value == 1: # A shower
325                            antaresrecoparticle.SetQualityParam(rdfsafety.
                               value)
326                    elif rdfclass.value == 0: # A muon
327                            antaresrecoparticle.SetQualityParam(1. -
                               rdfsafety.value)
328                    else:
329                            print "ERROR␣(addDusjShowerReconstruction):␣
                               Invalid␣RDF␣class␣%i" % rdfclass.value
330            frame.Put("DusjShowerRecoReconstructionResult",
               antaresrecoparticle)
331            return True
332 tray.AddModule(ConvertToAntaresRecoParticle, "dusjparticleconverter")
333
334
335 # Writeout
336 #————————————————————————————————————
337 tray.AddModule("I3Writer","writer")(
338         ("filename","whateveroutputfile")
339         )
340
341
342 # Finalize
343 #————————————————————————————————————
344 tray.AddModule("TrashCan", "the␣can")
345 tray.Execute()
346 tray.Finish()
347    ...
```

Appendix C

Software configuration parameters

This section lists all configuration parameters, their default values and a brief description for all SeaTray modules and services that have been developed for this analysis. Note that the default values are those of the modules and not necessarily those that have been used in the Dusj reconstruction. The configuration as it was used for the Dusj reconstruction within this work is given in B.6.

C.1   Parameters of the shower tools in the Gulliver framework

Table C.1 lists the configuration parameters of the Gulliver main module **I3ShowerFitter** that is described in appendix A.2.1. Table C.2 shows the parameters for the seed service **I3ShowerSeedService** as explained in appendix A.2.2. The possible values that can be used for the different seed types of the interaction time, vertex, direction and energy are given in the tables C.3 - C.6, respectively. Finally, table C.7 lists the parameters for the **I3ShowerParametrizationService** as introduced in appendix A.2.3. In this table whenever a 7-d vector is mentioned, the entries always correspond to the physics shower parameters in the order *time - x - y - z - energy - zenith - azimuth.*

Table C.1: Configuration parameters of the Gulliver main module I3ShowerFitter

Parameter	Default value	Description
SeedService	(required)	Name of the seed service in the SeaTray script.
ParametrizationService	(required)	Name of the parametrization service in the SeaTray script.
MinimizerService	(required)	Name of the minimizer service in the SeaTray script.
LikelihoodService	(required)	Name of the likelihood service in the SeaTray script.
StoragePolicy	"AllFits"	Defines how the output is written to the frame in case of more seeds have been provided by the seed service (see appendix A.2.1).
FitOutput	*the name of this module*	Naming prefix for all results that are written to the frame.
DoNotWriteFitParams	False	If true, no Gulliver fit parameters (**I3LogLikelihoodFitParams**) will be written to the frame.
DoNotWriteCutParams	False	If true, no **I3ShowerFitterCutParams** will be written to the frame.
WriteOutSeeds	False	If true, the module also writes out the incoming seed(s) from the seed service to the frame.
ConvertFitResultFrom-ThetaPhi	False	Some likelihood services return the fitted direction in *theta* and *phi* instead of *azimuth* and *zenith*. If so, set this to true to correct the values.
EventSelection	""	Name of an optional bool in the frame that defines whether a fit should be done at all.

Table C.2: Configuration parameters of the service I3ShowerSeedService

Parameter	Default value	Description
TimeSeedType	"FirstTriggered"	Defines how the time is set for the first basic seed. See table C.3 for more possible options.
VertexSeedType	"CenterOf-Amplitude"	Defines how the vertex is set for the first basic seed. See table C.4 for more possible options.
EnergySeedType	"Fit"	Defines how the energy is set for the first basic seed. See table C.6 for more possible options.
DirectionSeedType	"Horizontal"	Defines how the direction is set for the first basic seed. See table C.5 for more possible options.
NumberOfSeeds	1	How many seeds should be created? Note: For more than one seed an additional random service is required!
TimeShift	0	If > 0 the time of the first seed will be shifted for the alternative seeds by this value (randomly to + and -).
VertexShift	0	If > 0 the vertex will be shifted by this value in random directions for the alternative seeds.
LogEnergyShift	0	If > 0 the logarithmic energy will be shifted by this value randomly to + and - for the alternative seeds.
DirectionShift	0	If > 0 the direction will be shifted by this value in random directions for the alternative seeds.
InputParticle	""	Only needed if one of the *SeedTypes* above is set to the option *InputParticle*.
SkipInputParticle-FitStatusCheck	False	Forces the service to return a seed, even if the fit status of the (optional) *InputParticle* is not *OK*.
InputPulses	""	May be required depending on what has been set as *SeedTypes*. See also tables C.3 - C.6.
AvoidNAN	False	If true, the module will replace a NAN value if it occurs in one of the shower parameters during the seed creation by a 0.
MCTree	"AntMCTree"	Name of the **I3MCTree** in the frame. Required only if one of the *SeedTypes* is set to option *MC*.
MCAdditionalParams	AntMCAdditional Parameters"	Name of the **I3AntMCAdditional-Params** in the frame. Required only if *EnergySeedType* is set to option *MC* (for bjorken_y).

Table C.3: Possible options for TimeSeedType

Option	Description
FirstTriggered	Takes the time of the first triggered hit from hit map in *Input-Pulses*.
BiggestTriggered	Takes the time of the biggest triggered hit from hit map in *InputPulses*.
First	Takes the time of the first hit from hit map in *InputPulses*.
Biggest	Takes the time of the biggest hit from hit map in *InputPulses*.
InputParticle	Takes the time from an existing **I3Particle** from the frame as set in *InputParticle*, for example a previously done pre-fit.
MC	Takes the time from the Monte-Carlo primary particle.
NAN	Sets the seed for the time to NAN. (If so, the start value for the fit could be created from the boundaries in the **I3ShowerParametrization**. (See appendix A.2.3))

Table C.4: Possible options for VertexSeedType

Option	Description
DetectorCenter	Takes the center of the detector as it is defined in the geometry.
CenterOfAmplitude	Takes the center of gravity of the hits' amplitudes in hit map *InputPulses*.
InputParticle	Takes the vertex from an existing **I3Particle** from the frame as set in *InputParticle*, for example a previously done pre-fit.
MC	Takes the vertex from the Monte-Carlo primary particle.
NAN	Sets the seed for the vertex components to NAN. (If so, the start value for the fit could be created from the boundaries in the **I3ShowerParametrization**. (See appendix A.2.3))

Table C.5: Possible options for DirectionSeedType

Option	Description
Upgoing	Sets the zenith to 180° and the azimuth to 180°.
Horizontal	Sets the zenith to 90° and the azimuth to 180°.
InputParticle	Takes the direction from an existing **I3Particle** from the frame as set in *InputParticle*, for example a previously done pre-fit.
MC	Takes the direction from the Monte-Carlo primary particle.
NAN	Sets the seed for the direction components to NAN. (If so, the start value for the fit could be created from the boundaries in the **I3ShowerParametrization**. (See appendix A.2.3))

Table C.6: Possible options for EnergySeedType

Option	Description
Fit	Takes the energy from the result of a hard-coded rough correlation fit between the shower energy and the total charge (without noise) of the event. See appendix A.2.2 for a detailed description. The total charge is evaluated from the hit map in *InputPulses*.
Low	Sets the energy to 100 GeV.
Middle	Sets the energy to 100 TeV.
High	Sets the energy to 100 PeV.
InputParticle	Takes the energy from an existing **I3Particle** from the frame as set in *InputParticle*, for example a previously done pre-fit.
MC	Takes the energy from the Monte-Carlo primary particle.
NAN	Sets the seed for the energy to NAN. (If so, the start value for the fit could be created from the boundaries in the **I3ShowerParametrization**. (See appendix A.2.3))

Table C.7: Configuration parameters of the service I3ShowerParametrizationService

Parameter	Default value	Description
StepsizeVector	(required)	A 7-d vector to define the step sizes for the single physics shower parameters. If one entry is 0, this parameter will be kept fixed during the fit.
AdjustUpperIntervalVector	NAN for all entries	A 7-d vector to define the upper limit of the fit range adjustment around the start value. If one entry is NAN, no adjustment will be done for this parameter and the corresponding entry in *UltimateUpperBoundVector* is taken. See also figure A.4.
AdjustLowerIntervalVector	NAN for all entries	A 7-d vector to define the lower limit of the fit range adjustment around the start value. If one entry is NAN, no adjustment will be done for this parameter and the corresponding entry in *UltimateLowerBoundVector* is taken. See also figure A.4.
UltimateUpperBoundVector	NAN for all entries	A 7-d vector to define the absolute maximum upper limits for the fit parameters. If one entry is NAN and no corresponding entry has been set to the *AdjustUpperIntervalVector*, the fit will be unlimited in positive direction for this parameter. See also figure A.4.
UltimateLowerBoundVector	NAN for all entries	A 7-d vector to define the absolute minimum lower limits for the fit parameters. If one entry is NAN and no corresponding entry has been set to the *AdjustLowerIntervalVector*, the fit will be unlimited in negative direction for this parameter. See also figure A.4.
LimitToCanVolume	False	If true, the *UltimateUpperBoundVector* and *UltimateLowerBoundVector* entries for the 3 space coordinates will be set to the can volume (detector size + can).
Can	[55 m, 55 m, 55 m]	A 3-d vector to define the extension of the can (x, y, z). These values will be added to the detector extensions in each direction to get the can volume.
StartVector	NAN for all entries	A 7-d vector to define start values for the fit. If for one parameter a value is set (i.e. not NAN) the parametrization will override the seed from the seed service for this parameter!

C.2 Parameters of the Dusj shower reconstruction project

Table C.8 lists all arguments of the standard Python function **addDusjShowerReconstruction** that was used to perform the shower reconstruction.

Table C.9 lists the configuration parameters, their default values and a brief description for the ARS hit selection to identify hits from direct photons (see chapter 6.1.1). The tables C.10 - C.12 list the configuration parameters for the **I3DusjShowerIdentifier** hit selection that was introduced in chapter 6.1.2.

Table C.13 lists the configuration parameters of the **I3DusjShowerVertexPDF** likelihood service for the vertex and interaction time reconstruction (see chapter 6.2.1), table C.14 those of the **I3DusjShowerEnergyDirectionPDF** service for the reconstruction of the shower energy and the neutrino direction (see chapter 6.2.2).

Finally, table C.15 lists the configuration parameters of the **I3DusjShowerCutValuesCollector**, as introduced in chapter 6.3. The cut parameters that can be stored in this container class are listed in appendix C.2.1.

The configuration of further tools to perform cuts on these cut values is given in appendix C.2.2, to use the RDF classification in C.2.3, and to create new Dusj PDF tables in C.2.4.

Table C.8: Arguments of the Python function addDusjShowerReconstruction

Argument	Default value	Description
inputpulses	(required)	Name of the **I3RecoPulseSeriesMap** containing the detected hits in the frame.
outputprefix	"DusjShowerReco"	Prefix that will be used for all output results written to the frame.
applyminconstraints	True	Turns on/off the **I3Minimum-ConstraintsFilter** that discards events where the number of selected shower hits, the number of fired OMs or the number of hit strings with signal hits is below a certain threshold. The configuration of this event filter is done at the beginning of the Python function. Here also one can choose whether not passing events should be removed or just flagged with an **I3Bool** that is written to the frame.
cleanuplevel	1	(0) Each intermediate result will be kept in the frame, (1) Intermediate results will be deleted.
discardfailedfits	False	If true, all events where the reconstruction failed for what reason ever will be discarded. Otherwise they will be kept and marked with a bad fit status.
applyeventclassification	True	Turns on/off the random decision forest event classification for muon/shower discrimination.
rdffile	"resources/rdf/RDF_RBRv2_Line12.rdf"	Name and path of the rdf file containing the random decision forest. (See chapter 6.4)
donotinstallrandomservice	False	Can be used to prevent the function from installing a second random service when one is already installed somewhere else in the Python script.

Table C.9: Configuration parameters of the hit selection I3RemovePulsesAfterARSDeadTime

Parameter	Default value	Description
ARSDeadTime	250 ns	Dead time span of one ARS chip.
RemoveAlsoPulsesFrom SecondARS	False	If true, hits from the second fired ARS (around 40 ns after the first one) will also be removed.

Table C.10: Input/Output configuration parameters of the hit selection I3DusjShowerIdentifier

Parameter	Default value	Description
InputPulses	(required)	Name of the input **I3RecoPulseSeriesMap** in the frame.
SeedParticle	""	Optional seed particle (from a pre-fit vertex reconstruction) that can be used to identify the shower hits. The module will try to find its own vertex and compare whether this own or the seed particle yields a better chi-square.
OutputPulses	"ShowerPulses"	Name of the output **I3RecoPulseSeriesMap** with the shower hits. Note: If *FindBiggestShowerOnly* is set to false, the module may find more than one shower vertex. In this case the hits are written in separate maps to the frame, named *[OutputPulses]_2, [OutputPulses]_3...*
WriteOutVertex	True	If true the result(s) of the internal vertex fit routine will be written to the frame.
OutputVertex	"ShowerIdentifier Vertex"	Name of the output **I3Particle** that contains the pre-fit vertex. Note: If *FindBiggestShowerOnly* is set to false, the module may find more than one shower vertex. In this case the vertices are named *[OutputVertex]_2, [OutputVertex]_3...*
WriteOutReduced ChiSquare	True	If true the reduced chi-squares of the pre-fits will be written as **I3Double** to the frame
OutputChiSquare	"ShowerIdentifier ReducedChiSquare"	Name of the output **I3Double** that contains the reduced chi-square. Note: If *FindBiggestShowerOnly* is set to false, the module may find more than one shower vertex. In this case this values are named *[OutputChiSquare]_2, [OutputChiSquare]_3...*
PrintLevel	0	Level of printed logs. 0: No logs, 1: Rough info about the shower after each step, 2: Detailed info about the shower and its hits after each step.

Table C.11: Steering configuration parameters of the hit selection I3DusjShowerIdentifier

Parameter	Default value	Description
FindBiggestShowerOnly	True	If true, the module writes out just one shower (the "biggest" - the one identified from the most coincidences).
EventContainsShowerOnly	True	If true, the module skips the muon filter and will not remove events. The reduced chi-square can be written to the frame to perform cuts later on.
DoNotWriteEmpty PulseMaps	False	If true, in events where no shower was found nothing will be written to frame. By default an empty hit map and vertex particle will be written out.

Table C.12: Internal configuration parameters of the hit selection I3DusjShowerIdentifier

Parameter	Default value	Description
ShowerThreshold	1.2 pe	Charge threshold of a hit to be declared as big hit.
CoincidenceWindow	20.0 ns	Time span where big hits are regarded as coincident.
CoincidenceLevel	2	Number of big hits that are required on one storey within the *CoincidenceWindow* to be a coincidence.
MinimumNumberOf Coincidences	1	Minimum number of coincidences of big hits to be declared as a shower.
ShowerResolution	70 m	Showers, where the earliest coincidences of each are closer than this parameter, are merged to one shower.
TimeSteplength	1 ns	Steplength for the interaction time scan fit.
PositionSteplength	5 m	Steplength for the vertex position scan fit.
ScanIterations	7	Number of attempts to improve the vertex position with the scan fit.
TimeTolerance	80 ns	Maximum allowed time difference for the time of a hit from the expected arrival time (time residual) to be declared as shower signal hit.
DistanceToCoincidence	50 m	Maximum allowed distance for a hit to the next coincidence to be declared as a shower signal hit.
MinimumNumberOfHits	5	Minimum number of found shower hits for one vertex to be kept.
ChiSquareCut	1000.0	Maximum allowed reduced chi-square for an event to be kept as shower. Only used if *EventContainsShowerOnly* is set to False.

Table C.13: Configuration parameters of the likelihood service I3DusjShowerVertexPDF

Parameter	Default value	Description
InputPulses	(required)	The input **I3RecoPulseSeriesMap** containing the selected shower signal hits. Note that this service requires a very pure signal hit sample. So use the **I3DusjShowerIdentifier** hit selection (see chapter 6.1.2) to remove optical background hits.
PDFTableFile	"resources/ root/DusjVertexPDFTable_ directlight.root"	The name and path of the .root file containing the PDF table.
UseInterpolation	True	Uses the ROOT bilinear interpolation for TH2 histograms during the readout of the table.
PDFThreshold	10^{-8}	Minimum allowed pdf value. It will be returned if a table entry is smaller or outside the range.
Smoothness	0	Smooths the histogram landscape n times (using the ROOT TH2D method Smooth).
ClipThreshold	1.0	All bins with contents higher than *ClipThreshold* will be clipped to this value to remove high peaks that might occur in regions of low statistics. Afterwards the table will be normalised again to 1.
ApplyWaterAbsorption	False	Applies an exponentially (with distance from the vertex) decreasing factor to the probabilities. By default this decrease is not applied and all distances have the same weight.
IncludeNotFiredOMs	False	Takes also OMs where no hit has been recorded into account when evaluating the likelihood. Increases cpu-time by a factor of about 10!
NotFiredOMsWeight	1.0	Weight that will be applied to pdf values coming from not fired OMs.
InputOMConditionMap	"OMCondition"	Name of the **I3OMConditionMap** in the frame. (Needed only if *IncludeNotFiredOMs* is set to true)
WaterAbsorptionLength	60 m	Water absorption length to evaluate the light attenuation (needed only if *ApplyWaterAbsorption* or *IncludeNotFiredOMs* is set to true).
WriteOutUsedTable	""	Writes out the used table that might have been modified (smoothed and clipped) by this service into a new file. For test and check purpose.

Table C.14: Configuration parameters of the likelihood service I3DusjShowerEnergyDirectionPDF

Parameter	Default value	Description
InputPulses	(required)	The input **I3RecoPulseSeriesMap** containing the selected shower signal hits. Note that this service requires a very pure signal hit sample. So use the **I3DusjShowerIdentifier** hit selection (see chapter 6.1.2) to remove optical background hits.
PDFTableFile	"resources/root/ DusjEnergyDirec-tionPDFTable_ directlight.root"	The name and path of the .root file containing the PDF table.
UseInterpolation	True	Uses the ROOT trilinear interpolation for TH3 histograms during the readout of the table.
PDFThreshold	10^{-10}	Minimum allowed pdf value. It will be returned if a table entry is smaller or outside the range.
Smoothness	0	Smooths the histogram landscape n times (using the ROOT TH3D method Smooth).
ClipThreshold	1.0	All bins with contents higher than *ClipThreshold* will be clipped to this value to remove high peaks that might occur in regions of low statistics. Afterwards the table will be normalised again to 1.
WeightingMode	0	Defines the weighting of the single pdf values. (0) Auto select: The service chooses the correct weighting that is consistent with the weighting mode that was chosen during the generation of the PDF table. (1) Photon-based. (2) Hit-based
VertexChargeMode	0	Defines the way the *total vertex charge* is calculated. (0) Auto select: The service chooses the correct calculation that is consistent with the way it was done during the generation of the PDF table. (1) Isotropic light emission. (2) Pure Cherenkov light emission.
LogEnergyMin	2.0	Forces a lower limit for the log energy axis, even if the table contains lower entries.
LogEnergyMax	9.0	Forces an upper limit for the log energy axis, even if the table contains higher entries.
WriteOutUsedTable	""	Writes out the used table that might have been modified (smoothed and clipped) by this service into a new file. For test and check purpose.

Table C.15: Configuration parameters of the cut parameters collector I3DusjShower-CutValuesCollector

Parameter	Default value	Description
ShowerIdentifier-ReducedChiSquare	””	Name of the **I3Double** containing the reduced chi-square from the hit selection in the frame.
ShowerIdentifier-Vertex	””	Name of the **I3Particle** containing the vertex and time estimation of the hit selection in the frame.
PrefitPulses	””	Name of the **I3RecoPulseSeriesMap** containing the hits that have been used for the pre-fit in the frame.
PrefitResult	””	Name of the **I3Particle** containing the result of the pre-fit in the frame.
PrefitVertex-ConvergencePosition	””	Name of the **I3ShowerFitterCutParams** class containing the convergence positions for the vertex pre-fit in the frame. (See appendix A.2.1.2)
PrefitTime-ConvergencePosition	””	Name of the **I3ShowerFitterCutParams** class containing the convergence position for the interaction time pre-fit in the frame. (See appendix A.2.1.2)
FitPulses	””	Name of the **I3RecoPulseSeriesMap** containing the hits that have been used for all main fit parts in the frame.
FitResult	””	Name of the **I3Particle** containing the final result of all main fit parts in the frame.
FitVertex-ConvergencePosition	””	Name of the **I3ShowerFitterCutParams** class containing the convergence positions for the vertex main fit in the frame. (See appendix A.2.1.2)
FitTime-ConvergencePosition	””	Name of the **I3ShowerFitterCutParams** class containing the convergence position for the interaction time main fit in the frame. (See appendix A.2.1.2)
FitEnergy-ConvergencePosition	””	Name of the **I3ShowerFitterCutParams** class containing the convergence position for the energy main fit in the frame. (See appendix A.2.1.2)
FitDirection-ConvergencePosition	””	Name of the **I3ShowerFitterCutParams** class containing the convergence positions for the direction main fit in the frame. (See appendix A.2.1.2)
GulliverFitParams	[]	A list of strings, naming the **I3LogLikelihood-FitParams** containers from all Gulliver fits (no matter whether pre-fit or main fit) in the frame. Each fit will contribute four parameters to the output map. (see appendix A.2.1.1)
OutputMap	”Dusj-ShowerReco-CutValues”	Name of the output **I3MapStringDouble** that will be written to the frame.

C.2.1 Possible cut parameters that are stored in the I3DusjShower-CutValues container

This sections gives an overview of all potential cut parameters that can be stored in the container created by the **I3DusjShowerCutValuesCollector**, as introduced in chapter 6.3. The parameters can be used for quality and purity cuts. The tables C.16 - C.18 list the parameters that have a fixed name, whereas table C.19 lists a set of additional parameters that can be added for each Gulliver maximum likelihood fit.

Table C.16: Parameters from an optional pre-fit than can be written out by the I3DusjShowerCutValuesCollector (not used in the Dusj default reconstruction)

Parameter	Description
PrefitConvergence-PositionTime	Convergence position for interaction time of a Gulliver pre-fit as defined in appendix A.2.1.2.
PrefitConvergence-PositionX	Convergence position for x of a Gulliver pre-fit as defined in appendix A.2.1.2.
PrefitConvergence-PositionY	Convergence position for y of a Gulliver pre-fit as defined in appendix A.2.1.2.
PrefitConvergence-PositionZ	Convergence position for z of a Gulliver pre-fit as defined in appendix A.2.1.2.
PrefitTotalCharge	Summated charge from all hits that have been used for the pre-fit.
PrefitNumberOfStrings	Number of strings that are hit by the hits that have been used for the pre-fit.
PrefitVerticalDistance-ToDetectorCenter	z-distance of the pre-fit vertex from the detector center.
PrefitHorizontalDistance-ToDetectorCenter	xy-distance of the pre-fit vertex from the detector center.
PrefitTimeResidual-ChiSquare	Chi-square from used shower hits with respect to the pre-fit vertex as evaluated from equation (6.13).

Table C.17: Parameters from the hit selection than can be written out by the I3DusjShowerCutValuesCollector

Parameter	Description
ShowerIdentifier-ReducedChiSquare	Reduced chi-square from selected shower hits with respect to the internal vertex estimation of the **I3DusjShowerIdentifier** as described in equation (6.2).
ShowerIdentifier-VerticalDistance-ToDetectorCenter	z-distance of the internal vertex estimation of the **I3DusjShowerIdentifier** from the detector center.
ShowerIdentifier-HorizontalDistance-ToDetectorCenter	xy-distance of the internal vertex estimation of the **I3DusjShowerIdentifier** from the detector center.

Table C.18: Parameters from the main fit than can be written out by the I3DusjShower-CutValuesCollector

Parameter	Description
FitConvergence-PositionTime	Convergence position for interaction time of a Gulliver fit as described in appendix A.2.1.2.
FitConvergencePositionX	Convergence position for x of a Gulliver fit as described in appendix A.2.1.2.
FitConvergencePositionY	Convergence position for y of a Gulliver fit as described in appendix A.2.1.2.
FitConvergencePositionZ	Convergence position for z of a Gulliver fit as described in appendix A.2.1.2.
FitConvergence-PositionEnergy	Convergence position for shower energy of a Gulliver fit as described in appendix A.2.1.2.
FitConvergence-PositionZenith	Convergence position for zenith of a Gulliver fit as described in appendix A.2.1.2.
FitConvergence-PositionAzimuth	Convergence position for azimuth of a Gulliver fit as described in appendix A.2.1.2.
FitTotalCharge	Summated charge from all hits that have been used for the main fit.
FitNumberOfStrings	Number of strings that are hit by the hits that have been used for the main fit.
FitVerticalDistance-ToDetectorCenter	z-distance of the main fit vertex from the detector center.
FitHorizontalDistance-ToDetectorCenter	xy-distance of the main fit vertex from the detector center.
FitTimeResidual-ChiSquare	Chi-square from used shower hits with respect to the main fit vertex as evaluated from equation (6.13).
FitQuadrupoleMoment	Quadrupole moment of the used shower hits with respect to the main fit result. (See also table 6.1 in chapter 6.3.)

Table C.19: Parameters than can be written out by the I3DusjShowerCutValuesCollector for each Gulliver maximum likelihood fit

Parameter	Description
[NameOfTheFit]-LogLikelihood	Final minimum log-likelihood value that belongs the the fit result.
[NameOfTheFit]-ReducedLogLikelihood	Reduced final log-likelihood value as evaluated from equation (6.6) in chapter 6.2.
[NameOfTheFit]-DegreesOfFreedom	Degrees of freedom of the fit as evaluated from equation (6.7) in chapter 6.2.
[NameOfTheFit]-MinimizerCalls	Number of minimizer calls during the fit routine.

C.2.2   Module and class to perform cuts on the Dusj cut parameters

This section lists the methods of the Python classes **DusjShowerCuts** (table C.20) and **DusjCutValuesConfigfileReader** (table C.21) that can be used to easily perform cuts on the parameters stored in the container class as created by the **I3DusjShower-CutValuesCollector**. Table C.22 lists the configuration parameters of the SeaTray wrapper module for this class. The functionality of these cut tools is explained in appendix B.3.1.

Table C.20: Methods of the Python class DusjShowerCuts

Constructor **DusjShowerCuts(*configfilename*)**: Initializes the cutter class. Parameter *configfilename* sets the name of the .dcv configuration file that contains the allowed parameter ranges.

LoadConfigfile(*configfilename*): Loads a .dcv configuration file into the class.

DoesEventPass(*frame,   dusjcontainer="DusjShowerRecoCutValues",   skippa-rameters=[], ignorenans=False*): Gets the Dusj cut parameter container out of the frame and returns *True*, if the event passes the cuts, and *False*, if not. The arguments follow those from table C.22.

PrintReaderInfo(): Print the information provided by the configuration file reader class (see table C.21).

IsReady(): A method to check whether the module is ready to process frames. Returns a bool.

Reset(): Resets the class.

Table C.21: Methods of the Python helper class DusjCutValuesConfigfileReader

---

Constructor **DusjCutValuesConfigfileReader(*filename=' '*)**: Initializes the class and optionally opens a .dcv configuration file.

OpenConfigfile(*filename*): Opens a .dcv configuration file and reads in all allowed ranges that are specified in this file.

HasParameter(*parametername*): Checks whether the configuration file has an entry for this parameter and returns a bool.

GetAllowedParameterRange(*parametername*) :   Returns a 2-tuple containing [min,max] of the allowed range for this parameter.

GetFileName(): Returns the name of the currently loaded .dcv configuration file.

GetNumberOfParameters(): Returns the number of parameters defined in the currently loaded .dcv configuration file.

IsReady(): Checks whether the read-in of the parameter ranges from the file was successful and the class is ready to provide the ranges. Returns a bool.

Reset(): Resets the class.

PrintInfo(): Prints information about the configured parameters in the file.

Table C.22: Configuration parameters of the cutter module I3ApplyDusjShowerCuts

Parameter	Default value	Description
InputCutValues	"DusjShowerReco-CutValues"	Name of the input **I3MapStringDouble** that stores the cut values.
InputConfigFile	"resources/files/ DusjShowerDe-faultCutVal-ues.dcv"	Name and path of the input .dcv file, where the information is stored how to cut on the values.
DiscardEvents	False	If true, events that don't pass the cut will be removed from the stream. If false, events will be kept but an **I3Bool** will be written to the frame containing the information whether the event would have passed or not and/or the fit status will be marked with *InsufficientQuality*.
DecisionName	DusjShowerReco-CutsPassed"	Name of the **I3Bool** that will be written to the frame, if *DiscardEvents* is set to False.
InputFitResult	""	The name of the fit result that will be flagged with a fit status *InsufficientQuality*.
IgnoreNANs	False	By default events where at least one of the cut parameters is NAN, will not pass the cuts. Use this option to allow them to pass.
SkipParameters	[]	A Python list of parameter names that are to be excluded from the cuts.

C.2.3   Parameters and tools of the RDF classification

This section gives configuration tables for the RDF muon/shower classification tool that was introduced in chapter 6.4.

Table C.23 lists all arguments of the Python function **addDusjCutValuesRDF-Classification** that can be used to add the classification to a SeaTray script. Table C.24 lists the methods of the Python class **DusjCutValuesRDFFeatureExtract** that converts the physics data into RDF feature values, table C.25 the configuration of the SeaTray wrapper module for this class. Finally, the arguments of the Python function **CreateFeatureDataTables** to create feature data tables for the training of new forests is given in table C.26.

Table C.23: Arguments of the Python function addDusjCutValuesRDFClassification

Argument	Default value	Description
cutvaluescontainer	"DusjShowerReco-CutValues"	Name of the **I3MapStringDouble** that stores the evaluated Dusj cut parameters in the frame.
useparameters	[list with the 5 parameters introduced in chapter 6.4]	A list with the Dusj cut parameters that are to be used as features for the classification.
rdffile	"resources/rdf/-RDF_RBRv2-_Line12.rdf"	Name and path of the file containing the trained forest.
outputprefix	"DusjShowerReco-RDF"	Prefix that will be added to all outputs of this function.

Table C.24: Methods of the Python class DusjCutValuesRDFFeatureExtract

Constructor **DusjCutValuesRDFFeatureExtract(*useparameters=[]*)**: Initializes the extractor class. Parameter *useparameters* expects a list that specifies the names of the Dusj cut parameters that will be read out. (default = [], means all that are found in the first frame are used)

ExtractFeatures(*frame,   dusjcontainer="DusjShowerRecoCutValues",   fitresult="DusjShowerRecoReconstructionResult*): Gets the Dusj cut values container out of the frame and returns a list containing the parameters, specified in the constructor as *useparameters*. An optional check on the *fitresult* is done. If the fit status is not *OK* no features will be returned. If no *fitresult* is specified each frame will be included.

GetNumberOfEvaluatedFrames(): Returns the number of evaluated frames.

PrintInfo(): Print some information on the current status of the class.

IsReady(): A method to check whether the module is ready to process frames. Returns a bool.

Table C.25: Configuration parameters of the feature extract module I3DusjCutValues-RDFFeatureExtract

Parameter	Default value	Description
InputCutValues	"DusjShowerReco-CutValues"	Name of the input **I3MapStringDouble** Dusj cut values container in the frame.
UseParameters	[]	A list that specifies the names of the Dusj cut values that will be read out. If empty, all parameters that are found in the first frame are used.
FeatureVectorName	"DusjShowerReco-RDFFeatures"	Name of the output feature vector in the frame.

Table C.26: Arguments of the Python function CreateFeatureDataTables

Argument	Default value	Description
inputfiles	[]	A list of files in .i3 format that contain the Dusj cut values container and that all represent one event class.
outputfile	""	Output .dat-file that stores the selected features in an ascii format for the RDF training.
classnumber	-1	Integer that will be used as ID for this event class.
classname	""	Name that will be assigned to this event class.
dusjcontainer	"DusjShowerReco CutValues"	Name of the **I3MapStringDouble** Dusj cut values container in the frame.
fitresult	"DusjShowerReco ReconstructionRe-sult"	Name of the **I3Particle** containing the fit result in the frame (to skip events with bad fit status). If no fitresult is specified each frame will be included.
useparameters	[]	A list that specifies the names of Dusj cut parameters that will be used as features. [] means all that are found in the first frame are used.
precedingcuts	""	Optional name of a .dcv (see appendix B.3.1) file to perform an additional cut on the Dusj cut parameters before extracting the features. Events that do not pass these cuts will not be filled into the feature table.
logenergymin	NAN	Optional cut on the fit energy. All events with a lower energy will be removed before training.
eventfrequency	1	Just take each i-th event.

C.2.4   Parameters and tools to create new Dusj PDF tables

This section gives configuration tables for the tools to create new Dusj PDF Tables. For a detailed manual how to do so, see appendix B.5.

Table C.27 lists the configuration parameters of the Python script **InstallData-FromEventFile.py** that is used to extract the relevant information from an .evt Monte-Carlo file and convert it into the .dusj format. Table C.28 lists the methods of the Python class **DusjFileReader** that is used to read in the created .dusj files. Table C.29 holds the methods of the Python class **RandomizeOMSaturations** that provides random values for the charge saturation of the ANTARES OMs, table C.30 the configuration of the corresponding SeaTray wrapper module that applies the randomized saturation values to a set of hits. Finally the configuration of the two Python functions **BuildDusjVertexPDFTable.py** and **BuildDusjEnergyDirectionPDFTable.py** that are used to create the PDF tables from a set of .dusj files is given in the tables C.31 and C.32, respectively.

Table C.27: Configuration parameters of the Python script InstallDataFromEvtFile.py

Argument	Default value	Description
-i inputfile	(required)	Name and path of the input .evt file.
-o outputfile	(default from *inputfile* using suffix .dusj)	Name and path of the output .dusj file.
-d detectorfile	(required)	Name and path of the detector .det file that was used for the Monte-Carlo simulation.
-O omparam	(required)	Angular acceptance parametrization of the optical module that was used for the Monte-Carlo simulation.
-a arsintegrationtime	40 ns	Integration time span of the ARS in the optical module.
-x arsdeadtime	250 ns	Dead time span of the ARS after data taking.
-v vertextype	"vertex"	Defines the definition of the vertex that will be used for the evaluation of the relevant data. *vertex* means the true Monte-Carlo interaction vertex, *cog* means the center of gravity from all given shower hits' amplitudes. (see also appendix B.5.1)
-s saturationtable	"resources/root/ OMCal_run_30000 _to_55000.root"	Name and path of the .root file containing the distribution of the OM charge saturation that will be applied to the hits. (See appendix B.5.1.2 for more information.)
-n nevents	0	Limits the number of events that will be processed (Just for test purpose. To build reliable PDF tables all .dusj files should be created with this option set to 0, which means all available events are taken).

Table C.28: Methods of the Python class DusjFileReader

Constructor **DusjFileReader(*filename=' '*)**: Initializes the class and optionally opens a .dusj file.

OpenDusjFile(*filename*): Opens a .dusj file without making consistency checks to previous processed files.

OpenAndCheckNewDusjFile(*filename*): Opens a new .dusj file and makes consistency checks to the previous processed files.

GetHeaderInfo(): Returns a Python dict containing the information stored in the header of the .dusj file.

GetAdditionalInfo(): Returns a Python dict containing the additional information stored in the .dusj file.

GetFileName(): Returns the name of the currently loaded .dusj file.

IsOpen(): Tells, whether the reader is ready to provide data.

GetDataLine(): Returns a 7-tuple with the content of the next value line in the .dusj file. The tuple contains (counter, omdistance, arrivaltime, emissionangle, pulsecharge, angularefficiency, showerenergy).

GetLastPhotonNumber(): Returns the number of the last hit accessed via *GetDataLine*.

GetOMDistanceRange(): Returns a 2-tuple containing the minimum and maximum omdistance that occurred in the already read out lines.

GetArrivalTimeRange(): Returns a 2-tuple containing the minimum and maximum arrivaltime that occurred in the already read out lines.

GetEmissionAngleRange(): Returns a 2-tuple containing the minimum and maximum emissionangle that occurred in the already read out lines.

GetPulseChargeRange(): Returns a 2-tuple containing the minimum and maximum pulsecharge that occurred in the already read out lines.

GetAngularEfficiencyRange(): Returns a 2-tuple containing the minimum and maximum angularefficiency that occurred in the already read out lines.

GetShowerEnergyRange(): Returns a 2-tuple containing the minimum and maximum showerenergy that occurred in the already read out lines.

Reset(): Resets the class.

PrintInfo(): Prints information about the current status of the class.

Table C.29: Methods of the Python class RandomizeOMSaturations

---

Constructor **RandomizeOMSaturations(*rootfilename, histname="cal_OM_saturations_good_ARS"*)**: Initialized the class, opens the .root file and retrieves the table (by default the one with the good ARS).

LoadRootFile(*filename, histname='cal_OM_saturations_good_ARS'*): Opens the .root file and retrieves the table.

GetRandomSaturation(): Returns a random number following the distributions of the table.

IsReady(): Tells whether the class is ready to return random numbers.

CloseRootFile(): Closes the active .root file.

Test(*nevents=100000, drawtest=False*): Performs a self-check to show that the randomization is correct. Here the method *GetRandomSaturation* is called *nevents* times. In the end the discrepancy from the expectations from the table is listed and optional the result is drawn in a canvas.

Table C.30: Configuration parameters of the Python module I3RandomizeOMSaturations

Parameter	Default value	Description
InputPulses	””	Name of the input **I3RecoPulse-SeriesMap** containing the original hit sample.
OutputPulses	””	Name of the output **I3RecoPulse-SeriesMap** with the randomly clipped hit sample.
SaturationTable	”resources/root/ OMCal‿ run‿30000 ‿to‿55000.root”	Name of the .root file containing the saturation distribution table.
TableName	”cal‿OM‿saturations ‿good‿ARS”	Name of the saturation distribution table in the .root file.

Table C.31: Configuration parameters of the Python script BuildDusjVertexPDFTable.py

Argument	Default value	Description
-i inputfile	(required)	Name(s) and path(s) of the .dusj input-file(s). More files have to be separated by comma. Wild card ∗ is also allowed.
-o outputfile	DusjVertexPDF Table+*time*.root	Name and path of the output .root file.
-t timesmearing	0.0	Sigma of a Gaussian smearing in ns that can be applied to the arrival time values.
-d distancesmearing	0.0	Sigma of a Gaussian smearing in m that can be applied to the distance values.
-T timebinning	300	Number of bins along the arrival time axis.
-D distancebinning	300	Number of bins along the OM distance axis.
-L forcelimits	””	Limits the table axes manually. If this parameter is not set, the limits will be chosen when flushing the buffer for the first time. To force limits, set this parameter like -L timemin,timemax,distmin,distmax.
-b bufferlength	1.000.000	Number of lines that will be read in before the limits for the histogram will be fixed.

Table C.32: Configuration parameters of the Python script BuildDusjEnergyDirectionPDFTable.py

Argument	Default value	Description
-i inputfile	(required)	Name(s) and path(s) of the .dusj input-file(s). More files have to be separated by comma. Wild-card $*$ is also allowed.
-o outputfile	DusjEnergy DirectionPDF Table+*time*.root	Name and path of the output .root file.
-e energysmearing	0.0	Sigma of a Gaussian smearing that can be applied to the log shower energy values.
-c chargesmearing	0.0	Sigma of a Gaussian smearing in pe that can be applied to the hit charge values.
-a anglesmearing	0.0	Sigma of a Gaussian smearing in deg that can be applied to the emission angle values.
-d distancesmearing	0.0	Sigma of a Gaussian smearing in m that can be applied to the OM distance values.
-y angularefficiency-smearing	0.0	Sigma of a Gaussian smearing that can be applied to the angular acceptance values.
-E energybinning	50	Number of bins along the log shower energy axis.
-C chargebinning	50	Number of bins along the log total vertex charge axis.
-A anglebinning	100	Number of bins along the emission angle axis.
-V minenergybincoverage	0.5	Minimum percentage of bins with entries in one energy bin plane to be taken into account in the normalization.
-v vertexchargemode	"isotropic"	Defines the way the total vertex charge is evaluated. Possible is *isotropic* or *cerenkov*. (See chapter 6.2.2 for more information) .
-W applychargeweights	False	If true, each entry will be weighted with the evaluated *initial hit charge* at the vertex. (See chapter 6.2.2 for more information) .
-w waterabsorptionlength	60 m	Absorption length in water.
-L forcelimits	""	Limits the table axes manually. If this parameter is not set, the limits will be chosen when flushing the buffer for the first time. To force limits, set this parameter like -L logEmin,logEmax,chargemin,chargemax, anglemin,anglemax.
-b bufferlength	1.000.000	Number of lines that will be read in before the limits for the histogram will be fixed.

Appendix D

Run list for the diffuse flux analysis

D.1   List of selected runs

This section lists all run numbers that have been used for the diffuse flux analysis. As basis all runs where a RBR v2 simulation was available were chosen. See chapter 8 for more details. For the burn sample analysis all runs with a run number ending with 0 were chosen, whereas for the final analysis of the full data set, the remaining ones, except for the burn sample runs, have been used. Single runs that have been removed from the sample are listed in appendix D.2.

- Runs used in the burn sample analysis:

  25700, 25720, 25730, 25800, 25880, 25920, 25930, 25990, 26010, 26030, 26110, 26160, 26190, 26230, 26270, 26340, 26470,
  26480, 26540, 26640, 26660, 26710, 26720, 26770, 26800, 26810, 26820, 26830, 26870, 26920, 26940, 26970, 27080, 27090,
  27100, 27130, 27170, 27180, 27230, 27270, 27290, 27440, 27460, 27470, 27550, 27580, 27620, 27640, 27660, 27720, 27750,
  27760, 27830, 27890, 27900, 27980, 27990, 28070, 28110, 28280, 28340, 28350, 28450, 28460, 28510, 28570, 28620, 28630,
  28650, 28720, 28730, 28770, 28780, 28790, 28850, 28860, 28870, 28950, 28970, 28980, 28990, 29040, 29050, 29060, 29100,
  29110, 29120, 29160, 29180, 29190, 29220, 29250, 29270, 29280, 29320, 29330, 29350, 29360, 29370, 29420, 29440, 29480,
  29490, 29500, 29540, 29580, 29600, 29740, 29760, 29790, 29810, 29820, 29830, 29840, 29910, 29920, 29980, 30020, 30030,
  30060, 30070, 30080, 30090, 30100, 30110, 30120, 30140, 30150, 30160, 30170, 30210, 30220, 30240, 30310, 30320, 30340,
  30370, 30380, 30390, 30410, 30430, 30440, 30450, 30460, 30580, 30590, 30610, 30670, 30710, 30720, 30730, 30880, 30950,
  30970, 31000, 31010, 31020, 31030, 31040, 31070, 31080, 31120, 31130, 31160, 31170, 31230, 31280, 31360, 31680, 31690,
  31700, 31920, 31970, 32080, 32090, 32100, 32110, 32150, 32160, 32170, 32260, 32290, 32340, 32350, 32360, 32400, 32430,
  32450, 32460, 32470, 32490, 32570, 32580, 32600, 32700, 32710, 32740, 32760, 32770, 32830, 32850, 32880, 32900, 32970,
  32990, 33010, 33060, 33110, 33210, 33230, 33290, 33300, 33310, 33320, 33380, 33390, 33500, 33530, 33570, 33590, 33600,
  33630, 33660, 33700, 34350, 34360, 34400, 34420, 34470, 34490, 34550, 34560, 34580, 34600, 34610, 34630, 34640, 34650,
  34660, 34670, 34740, 34780, 34790, 34800, 34860, 34880, 34890, 34930, 34960, 35000, 35060, 35160, 35170, 35180, 35190,
  35200, 35240, 35250, 35300, 35330, 35340, 35360, 35370, 35470, 35480, 35490, 35520, 35530, 35550, 35580, 35630, 35640,
  35700, 35710, 35730, 35740, 35750, 35790, 35800, 35880, 35890, 35900, 35910, 35930, 36000, 36070, 36110, 36160, 36210,
  36220, 36260, 36280, 36300, 36360, 36380, 36420, 36430, 36450, 36480, 36500, 36570, 36590, 36740, 36750, 36840, 36850,
  36860, 36870, 36900, 36930, 36940, 36950, 36960, 36970, 37070, 37090, 37130, 37150, 37220, 37230, 37280, 37300, 37320,
  37330, 37340, 37350, 37420, 37430, 37440, 37450, 37470, 37620, 37630, 37650, 37670, 37720, 37770, 37780, 37990, 38060,
  38070, 38080, 38090, 38100, 38110, 38170, 38180, 38190, 38200, 38230, 38260, 38290, 38400, 38410, 38440, 38450, 38470,
  38480, 38500, 38520, 38540, 38560, 38590, 38600, 38610, 38620, 38640, 38650, 38690, 38700, 38720, 38750, 38760, 38770,
  38780, 38790, 38800, 38810, 38830, 38840, 38850, 38900, 38940, 38960, 38980, 38990, 39000, 39030, 39040, 39060, 39080,
  39090, 39120, 39150, 39180, 39220, 39240, 39250, 39260, 39360, 39400, 39410, 39420, 39430, 39460, 39570, 39580, 39590,
  39620, 39640, 39680, 39700, 39760, 40150, 40160, 40220, 40480, 40530, 40660, 40690, 40710, 40770, 40780, 40790, 40870,
  40880, 40910, 40920, 40930, 41270, 41310, 41320, 41350, 41370, 41390, 41400, 41410, 41430, 41440, 41450, 41540, 41550,
  41560, 41580, 41610, 41630, 41690, 41740, 41780, 41810, 41830, 41850, 41870, 41940, 41950, 41980, 42020, 42050, 42090,
  42190, 42320, 42420, 42500, 42530, 42550, 42580, 42640, 42750, 42810, 42860, 42900, 42950, 42990, 43010, 43040, 43050,
  43140, 43180, 43240, 43250, 43350, 43390, 43450, 43480, 43540, 43600, 43610, 43620, 43710, 43760, 43800, 43860, 43890,
  43930, 43940, 44010, 44020, 44040, 44060, 45110, 45140, 45150, 45210, 45250, 45290, 45430, 45440, 45470, 45540, 45620,
  45630, 45650, 45660, 45670, 45700, 45710, 45730, 45750, 45780, 45790, 45800, 45820, 45860, 45920, 45940, 45960, 46020,
  46030, 46040, 46050, 46120, 46130, 46140, 46150, 46170, 46200, 46230, 46310, 46420, 46430, 46460, 46480, 46500, 46510,
  46540, 46570, 46610, 46620, 46640, 46650, 46660, 46670, 46700, 46710, 46750, 46770, 46820, 46890, 46970, 47070, 47120,
  47210, 47250, 47260, 47580, 47610, 47660, 47670, 47710, 47730, 47790, 47830, 47840, 47870, 47900, 47990, 48070, 48120,
  48140, 48190, 48280, 48370, 48380, 48490, 48520, 48950, 48970, 49240, 49290, 49310, 49350, 49360, 49420, 49450, 49500,
  49640, 49670, 49690, 49710, 49770, 49780, 49790, 49810, 49850, 49860, 49870, 49900, 49980, 50030, 50080, 50230, 50330,
  50340, 50390, 50400, 50440, 50610, 50650, 50700, 50740, 50850, 50880, 50960, 50990, 51040, 51050, 51070, 51110, 51130,
  51140, 51160, 51230, 51260, 51290, 51320, 51330, 51370, 51390, 51460, 51480, 51550, 51580, 51600, 51630, 51690, 51700,
  51710, 51720, 51740, 51780, 51800, 51810, 51820, 51840, 51850, 51870, 52220, 52240, 52250, 52260, 52280, 52290, 52330,
  52340, 52350, 52370, 52430, 52460, 52530, 52550, 52570, 52580, 52590, 52610, 52640, 52710, 52750, 52790, 52840, 52850,
  52920, 52930, 52950, 53000, 53050, 53060, 53070, 53080, 53110, 53140, 53220, 53230, 53240, 53270, 53280, 53290, 53300,
  53350, 53410, 53420, 53450, 53460, 53490, 53500, 53510, 53520, 53550, 53570, 53580, 53600, 53610, 53620, 53660, 53670,

53680, 53690, 53700, 53710, 53730, 53760, 53770, 53820, 53830, 53860, 53900, 53910, 53930, 53940, 53950, 53960, 53980, 54050, 54060, 54100, 54110, 54140, 54150, 54210, 54220, 54250, 54260, 54290, 54300, 54320, 54330, 54350, 54370, 54390, 54410, 54420, 54510, 54580, 54610, 54630, 54640, 54680, 54690, 54700, 54710, 54720, 54730, 54740, 54760, 54820, 54840, 54850, 54860, 54890, 54900, 54910, 54940, 54950, 54980, 55010, 55020, 55030, 55040, 55050, 55080, 55090, 55110, 55180, 55190, 55210, 55230, 55240, 55330, 55360, 55670, 55720, 55760, 55810, 55820, 55830, 55850, 55870, 55890, 55900, 55920, 55950, 55990, 56010, 56200, 56220, 56250, 56350, 56390, 56420, 56440, 56450, 56570, 56600, 56610, 56670, 56680, 56690, 56700, 56710, 56730, 56740, 56760, 56800, 57060, 57110, 57130, 57240, 57250, 57260, 57280, 57310, 57320, 57350, 57360, 57370, 57380, 57400, 57410, 57420, 57440, 57470, 57480, 57500, 57520, 57560, 57580, 57590, 57610, 57650, 57660, 57690, 57700, 57710, 57720, 57820, 57920, 57930, 58030, 58050, 58080, 58090, 58110, 58130, 58140, 58150, 58170, 58180, 58200, 58210, 58220, 58240, 58260, 58280, 58290, 58300, 58310, 58370, 58420, 58430, 58440, 58460, 58480, 58490, 58500, 58510, 58540, 58550, 58560, 58570, 58590, 58620, 58640, 58650, 58660, 58670, 58690, 58710, 58730, 58770, 58790, 58810, 58830, 58890, 58900, 58940, 58950, 58960, 58980, 58990, 59020, 59040, 59080, 59090, 59110, 59150, 59170, 59180, 59190, 59200, 59220, 59240, 59260, 59320, 59330, 59370, 59380, 59390, 59430, 59450, 59460, 59500, 59540, 59550, 59570, 59580, 59590, 59600, 59620, 59640, 59660, 59670, 59690, 59710, 59770, 59810, 59840, 59860, 59870, 59880, 59890, 59900, 59910, 59930, 59960, 59990, 60020, 60030, 60050, 60060, 60070, 60100, 60110, 60120, 60130, 60150, 60170, 60220, 60240, 60260, 60290, 60300, 60310, 60320, 60380, 60390, 60410, 60420, 60440, 60460, 60490, 60500, 60520, 60570, 60590, 60600, 60610, 60690, 60720, 60730, 60740, 60780, 60800, 60820, 60840, 60850, 60870, 60880, 60910, 60930, 60940, 60970, 60990, 61010, 61020, 61030, 61040, 61050, 61060, 61070, 61080, 61090, 61100, 61140, 61150, 61160, 61180, 61210, 61220, 61290, 61320, 61330, 61390, 61410, 61440, 61450, 61460, 61470, 61480, 61530, 61560, 61590, 61620, 61710, 61730, 61740, 61750, 61760, 61770, 61800, 61830, 61840, 61850, 61880, 61900, 61920, 61930, 61960, 61980, 61990, 62030, 62050, 62080, 62100, 62110, 62130, 62140, 62150, 62170, 62180, 62230, 62240, 62250, 62260, 62270, 62290, 62300, 62310, 62340, 62370, 62380, 62390, 62400, 62410, 62420, 62440, 62450, 62460, 62500, 62560, 62570, 62610, 62670, 62720, 62730, 62780, 62800, 62930, 63030, 63060, 63070, 63080, 63120, 63150, 63210, 63220, 63230, 63330, 63340, 63350, 63380, 63390, 63400, 63550, 63740, 63770, 64090, 64100, 64110, 64130, 64140, 64150, 64200, 64400, 64430, 64440, 64450, 64500, 64600, 64630, 64640, 64680, 64690, 64750, 64760, 64810, 64890, 64900, 64910, 64920, 64930, 64940, 64960, 64990, 65000, 65010, 65030, 65050, 65100, 65120, 65140, 65150, 65160, 65180, 65220, 65280, 65310, 65350, 65360, 65390, 65400, 65410, 65440, 65480, 65500, 65520, 65530, 65540, 65550, 65570, 65590, 65600, 65610, 65620, 65630, 65640, 65660, 65680, 65690, 65710, 65730, 65740, 65760, 65770, 65780, 65790, 65860, 65870, 65890, 65900, 65910, 65930, 65940, 65990, 66020, 66060, 66090, 66100, 66120, 66140, 66170, 66200, 66250, 66260, 66280, 66300, 66310, 66320, 66330, 66340, 66380, 66390, 66400, 66420, 66450, 66470, 66480, 66510, 66530, 66540, 66550, 66580, 66590, 66630, 66640, 66660, 66680, 66700, 66720, 66730, 66760, 66770, 66790, 66800, 66870, 66950, 66960, 66970, 66980, 67000, 67010, 67100, 67130, 67140, 67150, 67190, 67200, 67210, 67220, 67250, 67270, 67280, 67300, 67310, 67330, 67350, 67360, 67380, 67420, 67440, 67450, 67480, 67490, 67510, 67520, 67540, 67580, 67590, 67630, 67640, 67750, 67770, 67790, 67830, 67850, 68140, 68160, 68170

- Runs used in the full sample analysis:

25689, 25691, 25705, 25706, 25707, 25713, 25714, 25715, 25716, 25717, 25719, 25721, 25722, 25723, 25724, 25725, 25728, 25729, 25731, 25863, 25864, 25872, 25892, 25893, 25895, 25905, 25921, 25922, 25923, 25926, 25927, 25928, 25931, 25932, 25933, 25934, 25935, 25937, 25947, 25953, 25954, 25955, 25958, 25964, 25965, 25972, 25986, 25988, 25991, 26062, 26087, 26129, 26131, 26132, 26133, 26134, 26135, 26144, 26159, 26161, 26165, 26227, 26228, 26238, 26248, 26265, 26267, 26269, 26271, 26272, 26273, 26274, 26275, 26276, 26277, 26281, 26283, 26331, 26333, 26334, 26335, 26345, 26355, 26361, 26363, 26364, 26389, 26395, 26396, 26397, 26398, 26405, 26406, 26407, 26408, 26413, 26461, 26462, 26463, 26465, 26469, 26471, 26483, 26484, 26485, 26487, 26509, 26528, 26534, 26535, 26536, 26537, 26538, 26539, 26541, 26542, 26543, 26544, 26545, 26546, 26592, 26593, 26594, 26606, 26633, 26637, 26638, 26647, 26676, 26677, 26684, 26702, 26703, 26704, 26713, 26714, 26715, 26716, 26718, 26719, 26721, 26723, 26726, 26769, 26795, 26797, 26801, 26802, 26803, 26804, 26805, 26806, 26807, 26808, 26809, 26811, 26812, 26813, 26814, 26815, 26816, 26817, 26818, 26819, 26821, 26823, 26824, 26825, 26826, 26827, 26828, 26829, 26831, 26832, 26833, 26834, 26864, 26865, 26866, 26867, 26868, 26869, 26871, 26872, 26873, 26874, 26875, 26876, 26877, 26878, 26879, 26891, 26893, 26894, 26895, 26896, 26897, 26898, 26899, 26902, 26903, 26904, 26905, 26916, 26917, 26918, 26919, 26936, 26937, 26938, 26939, 26956, 26957, 26958, 26959, 26963, 26964, 26965, 26967, 26968, 26971, 26974, 26978, 26979, 26982, 26983, 26984, 26987, 26994, 26995, 26998, 27002, 27003, 27004, 27008, 27009, 27013, 27015, 27081, 27091, 27092, 27094, 27095, 27143, 27153, 27162, 27163, 27164, 27165, 27169, 27172, 27173, 27174, 27175, 27176, 27177, 27179, 27182, 27185, 27186, 27216, 27217, 27218, 27226, 27227, 27228, 27229, 27231, 27232, 27233, 27235, 27244, 27246, 27248, 27249, 27271, 27272, 27289, 27291, 27292, 27293, 27294, 27296, 27297, 27351, 27352, 27353, 27379, 27403, 27404, 27405, 27406, 27407, 27408, 27413, 27424, 27425, 27426, 27427, 27429, 27458, 27461, 27462, 27463, 27464, 27465, 27467, 27468, 27469, 27471, 27501, 27502, 27504, 27505, 27549, 27551, 27558, 27565, 27566, 27567, 27569, 27571, 27572, 27573, 27574, 27575, 27576, 27577, 27578, 27579, 27581, 27616, 27617, 27618, 27622, 27623, 27624, 27625, 27626, 27627, 27632, 27633, 27634, 27635, 27638, 27641, 27642, 27644, 27646, 27647, 27648, 27649, 27657, 27658, 27659, 27667, 27668, 27669, 27721, 27722, 27723, 27724, 27726, 27727, 27728, 27729, 27742, 27743, 27744, 27745, 27746, 27747, 27748, 27749, 27751, 27752, 27753, 27754, 27755, 27756, 27757, 27758, 27759, 27761, 27762, 27763, 27764, 27808, 27812, 27813, 27814, 27815, 27822, 27824, 27825, 27826, 27827, 27828, 27829, 27831, 27832, 27853, 27871, 27872, 27874, 27875, 27877, 27883, 27887, 27889, 27891, 27892, 27893, 27894, 27895, 27896, 27897, 27898, 27899, 27941, 27946, 27952, 27953, 27954, 27963, 27979, 27981, 27982, 27984, 27988, 27991, 28007, 28034, 28035, 28037, 28044, 28058, 28061, 28062, 28063, 28064, 28065, 28066, 28067, 28068, 28069, 28071, 28106, 28109, 28111, 28114, 28119, 28131, 28132, 28133, 28143, 28148, 28161, 28162, 28163, 28182, 28211, 28224, 28225, 28226, 28233, 28235, 28236, 28237, 28238, 28239, 28241, 28242, 28243, 28244, 28246, 28247, 28278, 28281, 28285, 28303, 28304, 28305, 28306, 28312, 28315, 28316, 28317, 28319, 28327, 28334, 28335, 28336, 28337, 28341, 28342, 28343, 28344, 28345, 28346, 28347, 28348, 28349, 28351, 28352, 28354, 28386, 28387, 28388, 28389, 28395, 28401, 28402, 28404, 28421, 28422, 28432, 28433, 28434, 28441, 28442, 28443, 28444, 28445, 28446, 28448, 28449, 28451, 28452, 28453, 28454, 28456, 28457, 28458, 28487, 28494, 28495, 28496, 28497, 28503, 28507, 28508, 28509, 28512, 28542, 28552, 28553, 28554, 28563, 28566, 28567, 28568, 28569, 28583, 28584, 28585, 28586, 28613, 28615, 28616, 28617, 28618, 28619, 28621, 28622, 28623, 28624, 28625, 28628, 28629, 28631, 28632, 28642, 28643, 28644, 28645, 28647, 28648, 28649, 28651, 28652, 28653, 28654, 28655, 28681, 28686, 28687, 28688, 28702, 28711, 28712, 28713, 28714, 28715, 28716, 28717, 28718, 28719, 28721, 28722, 28723, 28724, 28726, 28727, 28728, 28729, 28731, 28732, 28733, 28734, 28735, 28736, 28737, 28738, 28761, 28762, 28764, 28765, 28766, 28767, 28768, 28769, 28771, 28772, 28774, 28775, 28776, 28777, 28782, 28783, 28784, 28785, 28786, 28787, 28788, 28789, 28791, 28792, 28793, 28794, 28795, 28796, 28797, 28798, 28801, 28802, 28803, 28804, 28832, 28833, 28834, 28835, 28836, 28839, 28841, 28842, 28844, 28845, 28846, 28847, 28848, 28849, 28851, 28852, 28853, 28854, 28856, 28857, 28858, 28859, 28861, 28862, 28863, 28864, 28865, 28866, 28867, 28868, 28869, 28871, 28872, 28873, 28874, 28913, 28948, 28949, 28952, 28953, 28954, 28955, 28956, 28957, 28958, 28966, 28967, 28968, 28969, 28971, 28972, 28973, 28974, 28975, 28979, 28981, 28982, 28983, 28984, 28985, 28986, 28987, 28988, 28989, 28991, 28992, 28993, 28994, 28995, 29022, 29023, 29024, 29025, 29026, 29027, 29028, 29029, 29035, 29036, 29037, 29038, 29039, 29041, 29042, 29043, 29044, 29045, 29047, 29048, 29049, 29051, 29054, 29055, 29056, 29057, 29058, 29059, 29061, 29062, 29063, 29064, 29065, 29066, 29067, 29068, 29069, 29091, 29092, 29093, 29094, 29096, 29097, 29098, 29099, 29101, 29103, 29104, 29105, 29106, 29107, 29108, 29109, 29111, 29112, 29113, 29114, 29115, 29116, 29117, 29118, 29119, 29121, 29122, 29123, 29124, 29125, 29126, 29127, 29128, 29129, 29152, 29153, 29154, 29155, 29156, 29157, 29158, 29159, 29161, 29162, 29165, 29172, 29173, 29174, 29175, 29176, 29177, 29178, 29179, 29181, 29183, 29186, 29187, 29188, 29189, 29191, 29192, 29193, 29194, 29197, 29213, 29214, 29215, 29216, 29217, 29218, 29219, 29221, 29222, 29223, 29224, 29246, 29247, 29251, 29252, 29253, 29254, 29255, 29256, 29257, 29258, 29259, 29261, 29262, 29263, 29264, 29265, 29266, 29267, 29271, 29272, 29273, 29274, 29275, 29276, 29277, 29278, 29279, 29281, 29282, 29283, 29284, 29285, 29286, 29287, 29288, 29292, 29317, 29318, 29319, 29321, 29322, 29323, 29324, 29325, 29327, 29328, 29329, 29335, 29338, 29339, 29341, 29343, 29359, 29361, 29362, 29363, 29364, 29365, 29366, 29367, 29368, 29369, 29411, 29413, 29414, 29417, 29419, 29421,

29422, 29423, 29424, 29426, 29433, 29434, 29435, 29436, 29437, 29438, 29439, 29441, 29448, 29472, 29473, 29474, 29476,
29477, 29478, 29481, 29483, 29484, 29485, 29487, 29488, 29538, 29539, 29541, 29542, 29543, 29547, 29549, 29551, 29552,
29553, 29554, 29557, 29558, 29559, 29561, 29562, 29563, 29564, 29566, 29567, 29581, 29582, 29594, 29595, 29596, 29599,
29604, 29605, 29606, 29623, 29624, 29625, 29626, 29643, 29646, 29657, 29658, 29659, 29664, 29678, 29688, 29693, 29695,
29697, 29698, 29716, 29722, 29728, 29733, 29751, 29752, 29753, 29754, 29755, 29756, 29757, 29758, 29759, 29761, 29762,
29763, 29764, 29788, 29789, 29791, 29802, 29803, 29804, 29805, 29806, 29807, 29808, 29809, 29812, 29813, 29814, 29815,
29816, 29817, 29818, 29819, 29821, 29822, 29823, 29825, 29826, 29827, 29829, 29831, 29832, 29833, 29835, 29836, 29837,
29838, 29839, 29869, 29871, 29872, 29873, 29874, 29877, 29891, 29892, 29895, 29903, 29904, 29905, 29906, 29907, 29908,
29909, 29911, 29912, 29913, 29914, 29915, 29916, 29917, 29918, 29919, 29921, 29922, 29923, 29924, 29925, 29926, 29963,
29968, 29969, 29971, 29978, 29979, 29981, 29982, 29993, 30017, 30018, 30021, 30023, 30024, 30025, 30026, 30027, 30028,
30029, 30031, 30032, 30033, 30034, 30035, 30036, 30059, 30061, 30062, 30063, 30064, 30065, 30066, 30067, 30068, 30069,
30071, 30072, 30073, 30074, 30075, 30076, 30077, 30078, 30079, 30081, 30082, 30083, 30084, 30085, 30086, 30087, 30088,
30089, 30091, 30092, 30093, 30094, 30095, 30097, 30098, 30099, 30101, 30102, 30103, 30104, 30105, 30106, 30107, 30108,
30109, 30111, 30112, 30113, 30114, 30115, 30116, 30117, 30118, 30141, 30142, 30143, 30144, 30145, 30146, 30147, 30148,
30149, 30151, 30152, 30153, 30154, 30155, 30156, 30157, 30158, 30159, 30161, 30162, 30163, 30164, 30165, 30166, 30167,
30169, 30171, 30172, 30173, 30174, 30175, 30176, 30177, 30203, 30205, 30206, 30207, 30208, 30209, 30211, 30212, 30213,
30215, 30216, 30217, 30218, 30219, 30221, 30222, 30223, 30224, 30225, 30232, 30233, 30234, 30235, 30236, 30237, 30238,
30239, 30241, 30242, 30243, 30244, 30307, 30308, 30309, 30311, 30312, 30313, 30314, 30315, 30316, 30317, 30318, 30319,
30321, 30322, 30324, 30326, 30327, 30328, 30329, 30332, 30333, 30335, 30336, 30337, 30339, 30341, 30343, 30344, 30345,
30346, 30369, 30371, 30372, 30373, 30374, 30375, 30376, 30377, 30378, 30379, 30381, 30384, 30385, 30386, 30387, 30388,
30389, 30391, 30392, 30393, 30394, 30395, 30396, 30397, 30398, 30399, 30401, 30402, 30407, 30408, 30409, 30416, 30417,
30422, 30423, 30424, 30427, 30428, 30429, 30431, 30433, 30434, 30437, 30438, 30441, 30442, 30449, 30452, 30453, 30454,
30455, 30457, 30459, 30508, 30514, 30521, 30526, 30529, 30533, 30538, 30541, 30545, 30551, 30555, 30557, 30561, 30563,
30568, 30571, 30575, 30577, 30583, 30586, 30592, 30593, 30598, 30599, 30601, 30604, 30606, 30614, 30618, 30623, 30624,
30626, 30629, 30633, 30642, 30654, 30662, 30678, 30706, 30711, 30712, 30713, 30714, 30715, 30716, 30717, 30718, 30719,
30721, 30722, 30723, 30724, 30725, 30726, 30727, 30728, 30729, 30784, 30785, 30787, 30789, 30792, 30793, 30795, 30799,
30801, 30802, 30804, 30806, 30872, 30873, 30876, 30881, 30883, 30885, 30887, 30889, 30891, 30892, 30894, 30896, 30897,
30942, 30944, 30946, 30947, 30952, 30953, 30955, 30956, 30959, 30961, 30963, 30964, 30967, 30969, 30972, 30974, 30977,
30979, 30981, 30983, 30986, 30987, 30989, 30992, 30995, 30997, 30998, 31003, 31005, 31006, 31008, 31011, 31013, 31016,
31017, 31022, 31024, 31025, 31027, 31029, 31033, 31035, 31036, 31038, 31042, 31044, 31046, 31048, 31049, 31051, 31053,
31055, 31057, 31061, 31062, 31065, 31067, 31069, 31072, 31074, 31075, 31078, 31082, 31083, 31085, 31087, 31091, 31094,
31096, 31098, 31099, 31101, 31104, 31105, 31107, 31109, 31111, 31112, 31115, 31117, 31118, 31122, 31123, 31125, 31128,
31132, 31134, 31136, 31137, 31139, 31141, 31144, 31145, 31147, 31149, 31152, 31154, 31164, 31165, 31167, 31169, 31172,
31176, 31207, 31209, 31211, 31212, 31219, 31221, 31226, 31228, 31232, 31234, 31235, 31237, 31247, 31275, 31277, 31282,
31283, 31285, 31287, 31312, 31314, 31316, 31318, 31355, 31357, 31359, 31362, 31365, 31368, 31374, 31675, 31678, 31682,
31683, 31685, 31687, 31695, 31697, 31698, 31702, 31704, 31706, 31708, 31709, 31712, 31714, 31716, 31718, 31719, 31721,
31723, 31724, 31728, 31731, 31732, 31734, 31736, 31783, 31785, 31786, 31788, 31794, 31797, 31803, 31807, 31811, 31813,
31823, 31834, 31835, 31837, 31839, 31841, 31849, 31863, 31871, 31873, 31875, 31877, 31879, 31888, 31893, 31896, 31897,
31899, 31901, 31903, 31905, 31907, 31911, 31913, 31915, 31916, 31918, 31958, 31962, 31963, 31965, 31966, 31968, 31975,
31979, 31987, 31988, 31992, 31999, 32008, 32009, 32011, 32013, 32015, 32021, 32023, 32028, 32029, 32031, 32034, 32039,
32049, 32064, 32077, 32078, 32082, 32083, 32086, 32088, 32091, 32093, 32095, 32096, 32098, 32102, 32103, 32105, 32107,
32109, 32165, 32167, 32168, 32173, 32176, 32177, 32179, 32181, 32183, 32185, 32187, 32189, 32233, 32239, 32241, 32243,
32244, 32246, 32248, 32252, 32258, 32262, 32263, 32265, 32267, 32269, 32271, 32273, 32275, 32276, 32278, 32281, 32283,
32284, 32286, 32288, 32292, 32294, 32338, 32343, 32344, 32346, 32348, 32354, 32356, 32359, 32381, 32387, 32397, 32399,
32402, 32404, 32411, 32423, 32436, 32437, 32439, 32441, 32442, 32445, 32447, 32452, 32454, 32455, 32458, 32462, 32463,
32468, 32472, 32474, 32475, 32478, 32479, 32482, 32485, 32486, 32488, 32491, 32525, 32529, 32531, 32533, 32535, 32571,
32576, 32578, 32582, 32584, 32588, 32597, 32599, 32602, 32604, 32606, 32611, 32617, 32621, 32622, 32624, 32626, 32628,
32629, 32632, 32634, 32636, 32637, 32639, 32641, 32644, 32645, 32647, 32649, 32651, 32652, 32655, 32657, 32659, 32704,
32706, 32708, 32742, 32743, 32745, 32747, 32749, 32751, 32753, 32755, 32757, 32762, 32767, 32769, 32771, 32772, 32773,
32775, 32778, 32781, 32784, 32786, 32789, 32815, 32817, 32821, 32823, 32826, 32828, 32833, 32835, 32848, 32852,
32855, 32858, 32875, 32889, 32895, 32897, 32901, 32904, 32942, 32954, 32958, 32961, 32978, 32984, 32986, 32989, 32993,
32995, 32998, 33002, 33003, 33005, 33008, 33036, 33038, 33039, 33041, 33046, 33047, 33049, 33053, 33056, 33058, 33062,
33064, 33067, 33069, 33071, 33075, 33076, 33079, 33081, 33083, 33094, 33102, 33111, 33113, 33115, 33117, 33134, 33161,
33172, 33173, 33176, 33178, 33186, 33194, 33215, 33217, 33219, 33222, 33223, 33225, 33227, 33231, 33234, 33236, 33238,
33239, 33241, 33243, 33246, 33247, 33249, 33251, 33281, 33284, 33285, 33288, 33296, 33307, 33308, 33312, 33314, 33316,
33321, 33323, 33325, 33327, 33328, 33331, 33338, 33341, 33343, 33345, 33346, 33349, 33351, 33353, 33355, 33357, 33359,
33362, 33364, 33365, 33367, 33369, 33371, 33373, 33375, 33377, 33379, 33382, 33385, 33387, 33389, 33429, 33431, 33433,
33435, 33436, 33439, 33444, 33447, 33449, 33451, 33452, 33454, 33459, 33461, 33463, 33464, 33466, 33468, 33471, 33472,
33474, 33476, 33478, 33479, 33482, 33484, 33486, 33487, 33491, 33494, 33496, 33499, 33502, 33505, 33507, 33509, 33511,
33513, 33515, 33516, 33518, 33521, 33523, 33525, 33527, 33529, 33559, 33563, 33565, 33567, 33568, 33573, 33584, 33585,
33587, 33588, 33592, 33595, 33596, 33598, 33611, 33613, 33615, 33617, 33618, 33621, 33623, 33624, 33626, 33628, 33632,
33634, 33636, 33638, 33639, 33641, 33644, 33647, 33651, 33653, 33654, 33656, 33658, 33668, 33695, 33697, 33698, 33702,
33705, 33706, 33709, 33711, 33713, 33714, 33716, 33718, 33721, 33722, 33724, 33726, 33728, 33729, 33738, 33746, 33748,
33749, 33751, 33754, 33756, 34346, 34348, 34352, 34355, 34356, 34358, 34362, 34363, 34385, 34386, 34388, 34389,
34394, 34395, 34396, 34397, 34398, 34399, 34401, 34403, 34405, 34407, 34414, 34416, 34417, 34419, 34422, 34423, 34425,
34426, 34427, 34432, 34433, 34439, 34443, 34444, 34445, 34448, 34451, 34452, 34454, 34455, 34457, 34458, 34459, 34462,
34465, 34466, 34467, 34469, 34473, 34474, 34481, 34486, 34487, 34489, 34491, 34493, 34494, 34496, 34497, 34498, 34502,
34521, 34522, 34549, 34551, 34552, 34553, 34554, 34561, 34562, 34563, 34564, 34565, 34566, 34571, 34572, 34573, 34574,
34575, 34576, 34577, 34579, 34583, 34588, 34598, 34601, 34603, 34604, 34605, 34608, 34609, 34616, 34621, 34622, 34625,
34626, 34628, 34632, 34633, 34635, 34636, 34639, 34642, 34643, 34644, 34646, 34647, 34649, 34656, 34658, 34661, 34669,
34672, 34673, 34675, 34678, 34679, 34685, 34687, 34688, 34692, 34695, 34703, 34708, 34711, 34712, 34718, 34719, 34721,
34723, 34724, 34726, 34734, 34742, 34744, 34745, 34747, 34748, 34754, 34756, 34771, 34773, 34775, 34781, 34783,
34785, 34786, 34789, 34792, 34793, 34796, 34798, 34801, 34806, 34808, 34809, 34813, 34819, 34821, 34832, 34834, 34835,
34841, 34843, 34845, 34846, 34848, 34851, 34853, 34856, 34862, 34864, 34866, 34867, 34869, 34871, 34873, 34877, 34878,
34882, 34883, 34888, 34892, 34896, 34898, 34899, 34906, 34907, 34909, 34912, 34913, 34915, 34917, 34919, 34921,
34927, 34928, 34931, 34933, 34935, 34937, 34938, 34941, 34942, 34944, 34945, 34947, 34953, 34955, 34957, 34959, 34961,
34963, 34964, 34968, 34969, 34971, 34974, 34976, 35002, 35003, 35057, 35061, 35063, 35064, 35068, 35069, 35071, 35073,
35074, 35151, 35153, 35155, 35158, 35159, 35161, 35162, 35163, 35164, 35166, 35168, 35172, 35173, 35175, 35176, 35178,
35179, 35193, 35195, 35196, 35198, 35199, 35201, 35202, 35203, 35236, 35238, 35242, 35243, 35244, 35246, 35247, 35248,
35253, 35261, 35264, 35277, 35285, 35288, 35289, 35291, 35292, 35293, 35294, 35296, 35304, 35306, 35308, 35309, 35311,
35312, 35314, 35316, 35318, 35319, 35321, 35322, 35325, 35327, 35328, 35332, 35333, 35335, 35336, 35337, 35339, 35342,
35343, 35346, 35348, 35349, 35351, 35353, 35354, 35355, 35357, 35359, 35362, 35363, 35368, 35372, 35374, 35375, 35377,
35472, 35473, 35475, 35476, 35477, 35479, 35483, 35484, 35485, 35488, 35491, 35493, 35495, 35496, 35498, 35501, 35503,
35504, 35506, 35511, 35512, 35513, 35515, 35517, 35519, 35521, 35523, 35529, 35532, 35534, 35535, 35539, 35541, 35543,
35545, 35548, 35551, 35553, 35555, 35557, 35559, 35561, 35562, 35563, 35565, 35567, 35569, 35571, 35573, 35575, 35577,
35579, 35582, 35583, 35584, 35627, 35632, 35633, 35635, 35636, 35639, 35651, 35653, 35656, 35658, 35659, 35661, 35662,
35663, 35665, 35666, 35668, 35671, 35672, 35674, 35678, 35681, 35683, 35685, 35686, 35689, 35691, 35696, 35698, 35702,
35704, 35706, 35707, 35709, 35712, 35716, 35717, 35719, 35721, 35723, 35724, 35726, 35728, 35732, 35734, 35735, 35737,
35741, 35743, 35744, 35746, 35748, 35751, 35753, 35754, 35756, 35758, 35777, 35779, 35781, 35783, 35785, 35788, 35793,
35795, 35797, 35798, 35799, 35802, 35838, 35843, 35846, 35849, 35851, 35852, 35853, 35855, 35856, 35858, 35863, 35864,
35872, 35873, 35875, 35876, 35878, 35881, 35884, 35885, 35886, 35887, 35889, 35891, 35892, 35894, 35896, 35897, 35899,

35901, 35902, 35904, 35905, 35906, 35907, 35908, 35911, 35912, 35914, 35916, 35917, 35919, 35921, 35923, 35924, 35926,
35927, 35929, 35932, 35933, 35935, 35936, 35937, 35939, 35941, 35942, 35944, 35948, 35953, 35954, 35956, 35958, 35959,
35962, 35963, 35964, 35966, 35968, 35969, 35971, 35972, 35975, 35976, 35977, 35979, 35981, 35983, 35984, 35985, 35987,
35989, 35991, 35992, 35993, 35996, 35997, 35999, 36002, 36029, 36071, 36072, 36075, 36076, 36079, 36088, 36091, 36093,
36095, 36097, 36099, 36101, 36103, 36104, 36107, 36108, 36112, 36113, 36119, 36123, 36124, 36128, 36139, 36149, 36151,
36153, 36155, 36156, 36157, 36159, 36161, 36163, 36165, 36168, 36176, 36189, 36198, 36202, 36205, 36209, 36212, 36213,
36215, 36218, 36221, 36223, 36225, 36227, 36229, 36232, 36234, 36238, 36244, 36254, 36255, 36256, 36258, 36259, 36262,
36263, 36264, 36267, 36268, 36269, 36271, 36272, 36273, 36275, 36276, 36277, 36279, 36281, 36283, 36284, 36285, 36287,
36288, 36289, 36291, 36294, 36297, 36298, 36302, 36303, 36305, 36306, 36309, 36315, 36352, 36359, 36362, 36364, 36366,
36367, 36369, 36371, 36372, 36373, 36375, 36385, 36386, 36389, 36392, 36394, 36396, 36401, 36403, 36406, 36409, 36411,
36413, 36417, 36418, 36422, 36424, 36426, 36428, 36431, 36434, 36435, 36436, 36438, 36439, 36442, 36443, 36444, 36446,
36448, 36452, 36453, 36456, 36458, 36459, 36461, 36466, 36467, 36469, 36471, 36473, 36474, 36475, 36477, 36478, 36481,
36483, 36484, 36485, 36488, 36489, 36491, 36492, 36494, 36495, 36497, 36498, 36501, 36502, 36505, 36506, 36507, 36509,
36511, 36512, 36514, 36516, 36517, 36519, 36532, 36534, 36543, 36548, 36549, 36551, 36552, 36555, 36556, 36557, 36572,
36576, 36577, 36582, 36587, 36592, 36593, 36594, 36596, 36598, 36599, 36603, 36605, 36607, 36623, 36624, 36663, 36724,
36725, 36734, 36736, 36738, 36742, 36745, 36747, 36749, 36752, 36755, 36759, 36761, 36763, 36772, 36775, 36776, 36783,
36785, 36786, 36787, 36789, 36791, 36808, 36809, 36812, 36813, 36814, 36815, 36816, 36817, 36818, 36825, 36826, 36832,
36835, 36836, 36837, 36838, 36853, 36858, 36862, 36863, 36865, 36867, 36869, 36872, 36874, 36877, 36879, 36881, 36883,
36885, 36887, 36889, 36891, 36892, 36893, 36895, 36897, 36898, 36901, 36903, 36904, 36906, 36907, 36908, 36911, 36914,
36915, 36918, 36922, 36923, 36925, 36926, 36927, 36929, 36932, 36934, 36935, 36938, 36939, 36942, 36943, 36945, 36947,
36948, 36951, 36953, 36956, 36957, 36958, 36961, 36963, 36964, 36966, 36968, 36973, 36975, 36978, 37015, 37016, 37018,
37019, 37021, 37024, 37025, 37026, 37028, 37029, 37031, 37033, 37035, 37037, 37044, 37045, 37047, 37049, 37051, 37053,
37055, 37057, 37061, 37064, 37065, 37068, 37072, 37073, 37075, 37076, 37078, 37081, 37082, 37084, 37085, 37091, 37093,
37095, 37096, 37098, 37099, 37103, 37104, 37105, 37107, 37108, 37109, 37111, 37112, 37114, 37115, 37118, 37119, 37121,
37123, 37125, 37128, 37132, 37134, 37137, 37139, 37141, 37142, 37144, 37146, 37147, 37149, 37151, 37153, 37155, 37158,
37159, 37161, 37163, 37165, 37167, 37169, 37171, 37176, 37209, 37211, 37213, 37215, 37217, 37218, 37222, 37224, 37226,
37228, 37231, 37234, 37236, 37238, 37239, 37241, 37242, 37246, 37248, 37249, 37251, 37252, 37253, 37255, 37257, 37259,
37261, 37263, 37266, 37268, 37271, 37272, 37276, 37281, 37283, 37284, 37285, 37287, 37289, 37291, 37292, 37293, 37296,
37297, 37301, 37302, 37304, 37305, 37307, 37308, 37309, 37312, 37313, 37314, 37316, 37317, 37319, 37321, 37323, 37324,
37327, 37328, 37331, 37332, 37334, 37335, 37337, 37339, 37342, 37344, 37346, 37348, 37349, 37352, 37353, 37389, 37391,
37393, 37395, 37397, 37399, 37402, 37404, 37407, 37409, 37412, 37415, 37417, 37419, 37423, 37424, 37426, 37428, 37432,
37434, 37436, 37437, 37439, 37442, 37443, 37445, 37447, 37448, 37452, 37454, 37455, 37456, 37458, 37459, 37461, 37462,
37463, 37465, 37466, 37468, 37471, 37473, 37474, 37475, 37592, 37593, 37595, 37597, 37599, 37601, 37603, 37605,
37607, 37608, 37611, 37614, 37615, 37616, 37618, 37619, 37622, 37623, 37625, 37626, 37628, 37631, 37632, 37634, 37635,
37637, 37638, 37639, 37642, 37643, 37644, 37651, 37653, 37655, 37656, 37658, 37659, 37662, 37664, 37668, 37672, 37673,
37675, 37678, 37679, 37682, 37683, 37685, 37687, 37688, 37689, 37701, 37712, 37714, 37716, 37717, 37719, 37722, 37723,
37731, 37732, 37733, 37735, 37736, 37738, 37739, 37741, 37744, 37746, 37751, 37752, 37753, 37755, 37757, 37759, 37761,
37763, 37764, 37765, 37767, 37768, 37771, 37772, 37774, 37777, 37779, 37782, 37783, 37785, 37788, 37789, 37791,
37871, 37873, 37874, 37876, 37877, 37878, 37879, 37915, 37929, 37988, 37992, 37993, 37994, 37996, 37997, 37999, 38002,
38004, 38007, 38009, 38011, 38045, 38052, 38054, 38056, 38058, 38063, 38065, 38067, 38072, 38074, 38075, 38076, 38078,
38082, 38084, 38086, 38088, 38093, 38095, 38097, 38099, 38102, 38104, 38106, 38108, 38112, 38113, 38115, 38117, 38118,
38119, 38121, 38122, 38123, 38125, 38126, 38128, 38129, 38131, 38133, 38152, 38153, 38155, 38156, 38157, 38158, 38159,
38161, 38162, 38163, 38168, 38172, 38173, 38175, 38176, 38177, 38179, 38182, 38183, 38185, 38187, 38188, 38193, 38195,
38196, 38197, 38199, 38202, 38204, 38205, 38207, 38208, 38209, 38211, 38212, 38213, 38215, 38216, 38218, 38223, 38225,
38227, 38228, 38233, 38241, 38242, 38244, 38249, 38251, 38252, 38253, 38255, 38257, 38258, 38261, 38263, 38264, 38265,
38285, 38287, 38289, 38292, 38293, 38294, 38296, 38298, 38299, 38329, 38331, 38332, 38363, 38365, 38391, 38397, 38398,
38402, 38403, 38404, 38406, 38407, 38421, 38423, 38424, 38426, 38427, 38429, 38431, 38432, 38435, 38438, 38442, 38443,
38445, 38447, 38448, 38451, 38461, 38463, 38465, 38466, 38467, 38472, 38474, 38475, 38477, 38478, 38481, 38485, 38486,
38488, 38489, 38491, 38492, 38493, 38495, 38496, 38502, 38503, 38504, 38506, 38511, 38512, 38515, 38517, 38518, 38519,
38521, 38523, 38524, 38526, 38527, 38529, 38533, 38534, 38536, 38537, 38539, 38542, 38543, 38546, 38548, 38549, 38551,
38552, 38554, 38555, 38557, 38558, 38562, 38569, 38571, 38572, 38574, 38575, 38577, 38578, 38581, 38582, 38583, 38585,
38586, 38588, 38589, 38592, 38593, 38596, 38597, 38599, 38601, 38603, 38604, 38606, 38607, 38611, 38612, 38614, 38615,
38617, 38618, 38621, 38623, 38625, 38626, 38628, 38629, 38631, 38632, 38634, 38635, 38636, 38639, 38641, 38643, 38645,
38646, 38647, 38649, 38652, 38654, 38656, 38658, 38659, 38661, 38663, 38664, 38665, 38667, 38668, 38671, 38674, 38685,
38687, 38688, 38691, 38692, 38695, 38696, 38697, 38699, 38702, 38703, 38711, 38712, 38716, 38717, 38719, 38722, 38723,
38724, 38726, 38727, 38738, 38739, 38741, 38742, 38744, 38745, 38747, 38748, 38752, 38753, 38755, 38756, 38757, 38759,
38762, 38765, 38766, 38771, 38773, 38774, 38783, 38784, 38787, 38788, 38791, 38793, 38795, 38796, 38799, 38801, 38803,
38805, 38806, 38807, 38809, 38813, 38814, 38823, 38824, 38829, 38833, 38834, 38835, 38837, 38838, 38841,
38843, 38844, 38847, 38849, 38852, 38853, 38855, 38856, 38869, 38899, 38902, 38903, 38905, 38906, 38908, 38909, 38913,
38917, 38918, 38925, 38926, 38928, 38929, 38931, 38932, 38934, 38936, 38938, 38941, 38943, 38944, 38946, 38947, 38949,
38951, 38953, 38954, 38955, 38957, 38961, 38962, 38965, 38966, 38968, 38969, 38971, 38972, 38974, 38975, 38977,
38978, 38982, 38983, 38985, 38986, 38988, 38989, 38992, 38994, 38996, 38997, 38999, 39001, 39003, 39004, 39006, 39008,
39015, 39021, 39022, 39025, 39028, 39031, 39033, 39034, 39036, 39037, 39038, 39042, 39044, 39045, 39047, 39048, 39049,
39051, 39052, 39054, 39056, 39057, 39059, 39062, 39063, 39065, 39066, 39067, 39069, 39071, 39072, 39074, 39076, 39078,
39079, 39082, 39083, 39085, 39086, 39087, 39091, 39095, 39099, 39101, 39102, 39104, 39105, 39106, 39108, 39109, 39111,
39112, 39114, 39116, 39117, 39119, 39122, 39124, 39125, 39127, 39128, 39131, 39133, 39134, 39144, 39147, 39151, 39153,
39154, 39155, 39157, 39158, 39159, 39161, 39168, 39169, 39181, 39182, 39184, 39196, 39197, 39199, 39204, 39205, 39207,
39209, 39211, 39212, 39214, 39215, 39217, 39218, 39221, 39223, 39225, 39227, 39228, 39229, 39231, 39232, 39234, 39235,
39237, 39238, 39242, 39244, 39246, 39247, 39249, 39254, 39255, 39257, 39259, 39262, 39263, 39265, 39266, 39273, 39307,
39313, 39319, 39321, 39324, 39327, 39331, 39339, 39341, 39342, 39345, 39349, 39351, 39357, 39362, 39364, 39365, 39369,
39372, 39373, 39377, 39379, 39381, 39382, 39384, 39387, 39389, 39391, 39393, 39395, 39398, 39425, 39427, 39432, 39438,
39442, 39453, 39456, 39458, 39462, 39464, 39466, 39469, 39564, 39567, 39569, 39573, 39575, 39581, 39583, 39586,
39589, 39603, 39609, 39617, 39623, 39625, 39627, 39629, 39631, 39633, 39636, 39638, 39642, 39644, 39647, 39649, 39652,
39662, 39669, 39671, 39673, 39675, 39677, 39682, 39683, 39685, 39689, 39702, 39705, 39707, 39711, 39712, 39713, 39717,
39718, 39723, 39725, 39726, 39727, 39728, 39729, 39757, 39762, 39763, 39765, 39772, 39774, 39775, 40098, 40111, 40119,
40152, 40154, 40155, 40157, 40161, 40167, 40169, 40171, 40177, 40179, 40189, 40191, 40195, 40197, 40199, 40205, 40206,
40213, 40216, 40218, 40221, 40223, 40225, 40227, 40229, 40231, 40233, 40238, 40453, 40473, 40475, 40478, 40483, 40494,
40507, 40509, 40516, 40545, 40553, 40555, 40591, 40594, 40603, 40606, 40608, 40616, 40618, 40623, 40647, 40649, 40653,
40655, 40657, 40659, 40663, 40664, 40666, 40668, 40669, 40672, 40675, 40676, 40677, 40678, 40681, 40682, 40684, 40686,
40688, 40691, 40695, 40697, 40698, 40705, 40706, 40707, 40709, 40712, 40713, 40714, 40716, 40717, 40718, 40719, 40721,
40722, 40741, 40751, 40753, 40756, 40758, 40762, 40763, 40765, 40766, 40768, 40772, 40775, 40777, 40783, 40784, 40786,
40788, 40793, 40795, 40799, 40803, 40804, 40805, 40808, 40809, 40841, 40848, 40859, 40867, 40872, 40879, 40884, 40908,
40912, 40913, 40916, 40917, 40922, 40924, 40926, 40944, 40957, 40959, 40962, 40964, 40966, 40967, 40969, 41005, 41009,
41014, 41089, 41092, 41094, 41096, 41161, 41164, 41166, 41168, 41171, 41173, 41175, 41177, 41192, 41194, 41196, 41198,
41201, 41203, 41204, 41206, 41208, 41209, 41212, 41214, 41215, 41217, 41222, 41224, 41226, 41228, 41231, 41233, 41234,
41237, 41247, 41249, 41251, 41252, 41254, 41257, 41259, 41261, 41262, 41265, 41268, 41279, 41281, 41283, 41285, 41287,
41289, 41292, 41295, 41301, 41303, 41305, 41308, 41313, 41314, 41316, 41318, 41321, 41352, 41353, 41355, 41365, 41367,
41369, 41373, 41374, 41376, 41377, 41381, 41384, 41385, 41388, 41391, 41393, 41395, 41397, 41399, 41402, 41403, 41404,
41406, 41408, 41411, 41416, 41417, 41418, 41421, 41423, 41424, 41426, 41428, 41429, 41431, 41433, 41434, 41435, 41437,
41439, 41441, 41442, 41444, 41445, 41446, 41449, 41452, 41453, 41455, 41469, 41481, 41482, 41483, 41484, 41486, 41487,
41488, 41489, 41491, 41492, 41494, 41496, 41498, 41524, 41528, 41534, 41536, 41538, 41543, 41546, 41548, 41552, 41555,

41557, 41563, 41567, 41569, 41578, 41582, 41584, 41586, 41591, 41597, 41605, 41608, 41612, 41614, 41626, 41628, 41631,
41632, 41633, 41634, 41635, 41661, 41662, 41665, 41666, 41673, 41675, 41677, 41679, 41684, 41691, 41692, 41694, 41696,
41697, 41699, 41702, 41703, 41706, 41711, 41712, 41714, 41715, 41717, 41719, 41722, 41724, 41727, 41729, 41731, 41733,
41737, 41742, 41744, 41769, 41781, 41784, 41787, 41789, 41803, 41808, 41812, 41815, 41822, 41826, 41828, 41835, 41836,
41839, 41842, 41844, 41845, 41847, 41852, 41854, 41886, 41899, 41913, 41937, 41939, 41944, 41947, 41952, 41971, 41973,
41975, 41977, 41982, 41984, 41986, 41988, 41991, 41993, 41995, 41996, 41998, 42001, 42003, 42005, 42032, 42035, 42038,
42042, 42045, 42047, 42053, 42056, 42059, 42062, 42064, 42066, 42069, 42072, 42074, 42076, 42086, 42088, 42091, 42096,
42102, 42109, 42111, 42114, 42116, 42117, 42119, 42121, 42129, 42132, 42135, 42137, 42161, 42174, 42178, 42181, 42185,
42187, 42198, 42208, 42264, 42323, 42326, 42359, 42362, 42365, 42369, 42373, 42376, 42379, 42381, 42407, 42412, 42415,
42417, 42425, 42477, 42482, 42494, 42497, 42502, 42504, 42515, 42518, 42521, 42523, 42526, 42528, 42533, 42536, 42541,
42543, 42545, 42547, 42554, 42577, 42585, 42588, 42592, 42594, 42597, 42602, 42606, 42609, 42612, 42616, 42623, 42625,
42628, 42631, 42634, 42638, 42643, 42646, 42649, 42652, 42655, 42658, 42661, 42668, 42671, 42676, 42679, 42682, 42686,
42689, 42692, 42695, 42698, 42753, 42756, 42758, 42765, 42771, 42777, 42781, 42785, 42792, 42796, 42799, 42804, 42811,
42813, 42815, 42819, 42821, 42825, 42829, 42831, 42835, 42838, 42842, 42851, 42856, 42863, 42866, 42889, 42893, 42897,
42906, 42909, 42912, 42922, 42926, 42932, 42936, 42941, 42944, 42954, 42959, 42962, 42964, 42967, 42971, 42973, 42976,
42983, 42986, 42994, 42997, 43003, 43007, 43015, 43019, 43022, 43026, 43031, 43034, 43046, 43059, 43062, 43066, 43069,
43073, 43078, 43081, 43086, 43091, 43098, 43101, 43105, 43108, 43112, 43115, 43118, 43122, 43128, 43132, 43144, 43148,
43155, 43158, 43161, 43164, 43169, 43173, 43176, 43183, 43185, 43191, 43199, 43219, 43222, 43226, 43229, 43234, 43237,
43242, 43245, 43253, 43256, 43258, 43262, 43265, 43269, 43271, 43274, 43282, 43285, 43288, 43316, 43321, 43325, 43328,
43333, 43336, 43343, 43347, 43353, 43359, 43362, 43366, 43372, 43376, 43379, 43385, 43396, 43442, 43457, 43462, 43466,
43472, 43476, 43487, 43491, 43495, 43508, 43512, 43516, 43521, 43525, 43534, 43546, 43551, 43555, 43563, 43568, 43574,
43584, 43587, 43591, 43596, 43606, 43612, 43615, 43624, 43627, 43629, 43632, 43634, 43639, 43646, 43649, 43653, 43657,
43663, 43666, 43669, 43673, 43678, 43681, 43689, 43692, 43695, 43698, 43701, 43705, 43713, 43716, 43719, 43722, 43725,
43728, 43731, 43734, 43737, 43741, 43743, 43745, 43748, 43751, 43758, 43764, 43769, 43773, 43776, 43778, 43782, 43787,
43796, 43806, 43812, 43817, 43823, 43826, 43831, 43834, 43837, 43842, 43846, 43849, 43852, 43855, 43866, 43869, 43872,
43875, 43878, 43882, 43885, 43888, 43893, 43899, 43902, 43905, 43911, 43922, 43925, 43932, 43936, 43959, 43964, 43969,
43974, 43978, 43981, 43984, 43987, 43991, 43999, 44003, 44007, 44013, 44016, 44018, 44025, 44029, 44037, 44042, 44045,
44049, 44053, 44056, 44064, 44072, 44075, 44078, 44081, 44083, 44087, 44089, 44098, 44105, 44107, 44108, 44109, 44112,
44115, 44118, 44121, 44124, 44129, 44137, 44141, 44146, 44149, 44152, 44156, 44159, 44165, 44169, 44174, 44177, 44182,
44184, 44188, 44193, 44195, 44199, 44203, 44207, 44214, 44218, 44221, 44225, 44228, 44234, 44241, 44266, 44268,
44271, 44274, 44277, 44281, 44285, 44289, 44293, 44296, 44298, 44304, 44307, 44311, 44315, 44322, 44328, 45054, 45058,
45061, 45065, 45069, 45071, 45102, 45105, 45108, 45112, 45116, 45128, 45134, 45138, 45142, 45145, 45147, 45165, 45168,
45169, 45172, 45173, 45174, 45176, 45177, 45179, 45181, 45183, 45185, 45188, 45191, 45193, 45196, 45197, 45199, 45202,
45212, 45214, 45218, 45222, 45225, 45227, 45229, 45232, 45234, 45238, 45243, 45248, 45252, 45254, 45256, 45259, 45265,
45267, 45271, 45274, 45275, 45277, 45279, 45287, 45291, 45295, 45326, 45332, 45338, 45342, 45349, 45354, 45356, 45367,
45385, 45388, 45391, 45393, 45397, 45408, 45412, 45418, 45419, 45424, 45431, 45435, 45438, 45442, 45444, 45446, 45448,
45468, 45472, 45474, 45477, 45479, 45485, 45487, 45489, 45495, 45503, 45506, 45509, 45511, 45516, 45521, 45523, 45527,
45529, 45533, 45536, 45538, 45546, 45551, 45553, 45557, 45561, 45563, 45565, 45567, 45573, 45575, 45577, 45586, 45589,
45592, 45595, 45598, 45601, 45617, 45626, 45628, 45632, 45635, 45639, 45641, 45643, 45648, 45653, 45655, 45658, 45663,
45665, 45668, 45681, 45683, 45685, 45687, 45689, 45692, 45695, 45697, 45701, 45703, 45705, 45707, 45714, 45717, 45719,
45721, 45724, 45726, 45728, 45746, 45749, 45753, 45755, 45757, 45759, 45761, 45766, 45768, 45771, 45773, 45775, 45776,
45778, 45784, 45788, 45795, 45797, 45802, 45804, 45807, 45812, 45814, 45816, 45818, 45822, 45825, 45827, 45829, 45831,
45833, 45835, 45838, 45841, 45843, 45845, 45848, 45851, 45853, 45855, 45858, 45862, 45864, 45867, 45869, 45871, 45873,
45875, 45877, 45879, 45881, 45884, 45905, 45909, 45912, 45915, 45918, 45924, 45931, 45933, 45936, 45938, 45942, 45944,
45946, 45952, 45956, 45958, 45962, 45964, 45966, 45971, 45976, 45978, 45981, 45983, 45985, 45987, 45991, 45994, 45996,
45998, 46001, 46003, 46006, 46009, 46011, 46014, 46016, 46018, 46022, 46026, 46027, 46033, 46036, 46039, 46043, 46045,
46048, 46052, 46054, 46092, 46094, 46097, 46099, 46101, 46102, 46104, 46106, 46109, 46112, 46118, 46122, 46124, 46126,
46127, 46129, 46133, 46135, 46137, 46139, 46141, 46143, 46145, 46147, 46153, 46159, 46165, 46167, 46169, 46173, 46175,
46177, 46181, 46183, 46193, 46195, 46197, 46202, 46207, 46211, 46213, 46215, 46217, 46219, 46225, 46228, 46233, 46241,
46324, 46341, 46353, 46356, 46362, 46367, 46369, 46383, 46388, 46389, 46392, 46394, 46396, 46399, 46401, 46404, 46406,
46407, 46409, 46411, 46413, 46415, 46418, 46422, 46423, 46425, 46428, 46432, 46434, 46438, 46442, 46449, 46451, 46453,
46455, 46457, 46462, 46464, 46468, 46469, 46472, 46474, 46475, 46478, 46482, 46485, 46487, 46489, 46492, 46494, 46498,
46502, 46505, 46507, 46512, 46514, 46516, 46518, 46521, 46523, 46525, 46527, 46529, 46531, 46533, 46536, 46538, 46542,
46544, 46546, 46549, 46551, 46554, 46556, 46558, 46559, 46561, 46563, 46564, 46567, 46572, 46574, 46576, 46584, 46586,
46591, 46593, 46595, 46597, 46599, 46601, 46602, 46604, 46605, 46607, 46611, 46613, 46615, 46616, 46618, 46621, 46623,
46624, 46626, 46628, 46631, 46633, 46635, 46638, 46642, 46646, 46653, 46665, 46667, 46673, 46676, 46684, 46687, 46689,
46692, 46694, 46696, 46698, 46702, 46704, 46707, 46712, 46714, 46716, 46718, 46721, 46724, 46726, 46729, 46731, 46733,
46736, 46745, 46747, 46752, 46754, 46756, 46763, 46765, 46768, 46772, 46774, 46777, 46807, 46823, 46825, 46827, 46831,
46834, 46838, 46852, 46855, 46858, 46861, 46863, 46865, 46867, 46869, 46872, 46874, 46876, 46878, 46879, 46881, 46883,
46885, 46887, 46892, 46893, 46895, 46896, 46898, 46899, 46901, 46903, 46905, 46908, 46909, 46911, 46913, 46916, 46918,
46921, 46924, 46949, 46953, 46955, 46957, 46959, 46962, 46964, 46966, 46968, 46972, 46974, 46977, 46982, 47012, 47016,
47025, 47039, 47042, 47044, 47053, 47058, 47061, 47066, 47076, 47082, 47125, 47135, 47146, 47214, 47218, 47223, 47228,
47235, 47236, 47238, 47241, 47244, 47246, 47247, 47249, 47253, 47254, 47255, 47256, 47257, 47259, 47261, 47263, 47536,
47538, 47568, 47573, 47574, 47575, 47577, 47591, 47594, 47596, 47599, 47601, 47603, 47612, 47629, 47634, 47662, 47665,
47667, 47672, 47674, 47676, 47679, 47682, 47685, 47686, 47688, 47692, 47694, 47706, 47708, 47713, 47716, 47719, 47733,
47735, 47738, 47749, 47785, 47788, 47792, 47794, 47795, 47797, 47799, 47801, 47833, 47835, 47836, 47838, 47843, 47846,
47859, 47861, 47862, 47865, 47866, 47868, 47873, 47874, 47878, 47879, 47882, 47883, 47891, 47893, 47895, 47897, 47898,
47943, 47947, 47949, 47951, 47952, 47969, 47973, 47975, 47992, 47994, 47997, 48043, 48059, 48064, 48072, 48074, 48075,
48077, 48084, 48092, 48094, 48095, 48097, 48116, 48141, 48143, 48145, 48146, 48148, 48179, 48181, 48182, 48184,
48186, 48188, 48276, 48282, 48347, 48366, 48368, 48372, 48384, 48411, 48461, 48463, 48465, 48466, 48468, 48471, 48472,
48474, 48476, 48478, 48482, 48484, 48487, 48488, 48492, 48494, 48495, 48512, 48514, 48515, 48517, 48518, 48521, 48522,
48524, 48525, 48527, 48529, 48532, 48534, 48536, 48904, 48909, 48929, 48931, 48932, 48934, 48937, 48939, 48943,
48945, 48947, 48953, 48956, 48958, 48959, 48961, 48963, 48964, 48966, 48968, 48972, 48975, 48978, 49225, 49227, 49229,
49231, 49233, 49236, 49238, 49241, 49243, 49245, 49246, 49249, 49251, 49255, 49257, 49259, 49262, 49263, 49283, 49284,
49287, 49288, 49293, 49295, 49298, 49301, 49303, 49304, 49308, 49312, 49333, 49336, 49339, 49341, 49344, 49346, 49358,
49362, 49366, 49369, 49372, 49375, 49388, 49393, 49395, 49396, 49398, 49401, 49403, 49407, 49409, 49411, 49413, 49415,
49417, 49422, 49425, 49427, 49429, 49431, 49435, 49437, 49441, 49447, 49452, 49455, 49457, 49459, 49461, 49464, 49474,
49478, 49489, 49493, 49495, 49497, 49504, 49508, 49515, 49516, 49518, 49522, 49581, 49584, 49586, 49588, 49591, 49593,
49596, 49598, 49601, 49604, 49606, 49608, 49613, 49617, 49619, 49621, 49624, 49627, 49633, 49643, 49658, 49661, 49663,
49667, 49672, 49674, 49677, 49683, 49693, 49699, 49701, 49703, 49706, 49708, 49709, 49712, 49715, 49722, 49725, 49728,
49731, 49733, 49737, 49743, 49745, 49749, 49755, 49757, 49759, 49773, 49775, 49777, 49783, 49787, 49792, 49795, 49798,
49801, 49803, 49805, 49808, 49813, 49815, 49818, 49821, 49824, 49826, 49831, 49858, 49863, 49866, 49872, 49897, 49902,
49906, 49908, 49911, 49914, 49932, 49942, 49945, 49948, 49951, 49954, 49958, 49983, 49986, 49989, 49995, 50002, 50012,
50016, 50018, 50021, 50023, 50026, 50028, 50032, 50035, 50037, 50038, 50043, 50046, 50049, 50053, 50055, 50057, 50061,
50073, 50075, 50078, 50082, 50086, 50088, 50115, 50159, 50162, 50164, 50166, 50175, 50198, 50204, 50207, 50209, 50211,
50216, 50218, 50221, 50225, 50227, 50232, 50236, 50238, 50241, 50244, 50247, 50249, 50253, 50255, 50258, 50263, 50273,
50292, 50316, 50317, 50321, 50323, 50325, 50328, 50331, 50335, 50337, 50339, 50344, 50346, 50348, 50351, 50355, 50359,
50361, 50377, 50379, 50383, 50386, 50388, 50391, 50392, 50394, 50396, 50397, 50398, 50399, 50402, 50405, 50407, 50411,
50416, 50419, 50422, 50426, 50429, 50434, 50435, 50436, 50437, 50443, 50449, 50451, 50453, 50457, 50459, 50461, 50626,
50634, 50635, 50638, 50641, 50645, 50648, 50654, 50658, 50661, 50663, 50666, 50669, 50671, 50675, 50677, 50679, 50684,
50685, 50687, 50689, 50692, 50695, 50698, 50709, 50724, 50729, 50731, 50736, 50738, 50744, 50746, 50749, 50753, 50756,

50761, 50764, 50767, 50771, 50776, 50779, 50782, 50785, 50789, 50792, 50796, 50802, 50821, 50824, 50826, 50829, 50832,
50834, 50837, 50839, 50843, 50845, 50848, 50854, 50859, 50861, 50863, 50867, 50869, 50872, 50874, 50877, 50878, 50882,
50884, 50887, 50889, 50891, 50897, 50901, 50914, 50937, 50941, 50943, 50947, 50949, 50951, 50955, 50958, 50964, 50967,
50969, 50972, 50976, 50978, 50981, 50983, 50986, 50993, 50995, 50999, 51002, 51003, 51005, 51007, 51009, 51011, 51013,
51014, 51017, 51019, 51022, 51024, 51025, 51033, 51037, 51039, 51052, 51055, 51057, 51061, 51063, 51067, 51072, 51077,
51079, 51083, 51085, 51088, 51092, 51094, 51097, 51101, 51104, 51107, 51113, 51116, 51118, 51122, 51124, 51127, 51132,
51133, 51136, 51138, 51144, 51146, 51149, 51152, 51154, 51156, 51158, 51162, 51163, 51165, 51166, 51168, 51169, 51172,
51174, 51175, 51177, 51179, 51199, 51207, 51216, 51222, 51223, 51225, 51226, 51228, 51232, 51234, 51235, 51237, 51238,
51241, 51242, 51245, 51246, 51251, 51252, 51254, 51256, 51257, 51261, 51263, 51264, 51266, 51268, 51271, 51273, 51274,
51276, 51278, 51285, 51292, 51295, 51299, 51301, 51305, 51312, 51315, 51323, 51326, 51327, 51332, 51334, 51336, 51337,
51339, 51341, 51343, 51345, 51348, 51354, 51358, 51359, 51362, 51367, 51373, 51375, 51379, 51382, 51384, 51387, 51393,
51396, 51399, 51403, 51406, 51409, 51411, 51413, 51415, 51423, 51435, 51441, 51443, 51445, 51447, 51449, 51451, 51452,
51455, 51456, 51463, 51471, 51474, 51477, 51483, 51485, 51488, 51493, 51497, 51499, 51503, 51506, 51511, 51514, 51529,
51531, 51536, 51538, 51541, 51544, 51547, 51553, 51555, 51558, 51559, 51561, 51564, 51566, 51568, 51572, 51574, 51576,
51578, 51582, 51584, 51586, 51588, 51591, 51594, 51596, 51598, 51603, 51605, 51607, 51609, 51614, 51616, 51632, 51634,
51636, 51638, 51641, 51645, 51648, 51657, 51669, 51672, 51677, 51681, 51684, 51686, 51692, 51695, 51697, 51702, 51704,
51705, 51708, 51715, 51717, 51722, 51724, 51727, 51729, 51731, 51733, 51736, 51742, 51745, 51747, 51751, 51755, 51757,
51761, 51763, 51765, 51768, 51771, 51773, 51776, 51778, 51784, 51786, 51789, 51792, 51794, 51797, 51803, 51806, 51813,
51815, 51825, 51828, 51834, 51835, 51838, 51842, 51844, 51846, 51848, 51853, 51855, 51857, 51859, 51861, 51863, 51865,
51868, 51872, 51876, 51879, 51881, 51883, 51885, 51886, 51889, 51892, 51897, 51899, 51901, 51903, 51905, 51906, 51908,
51909, 51912, 51914, 51916, 51917, 51919, 51921, 51923, 51924, 51926, 51929, 51931, 51933, 51934, 51936, 51938, 51941,
51943, 51964, 51965, 51967, 51969, 51971, 51975, 51977, 51979, 51983, 51984, 51986, 51988, 51989, 51991, 51993, 51994,
51997, 51999, 52001, 52002, 52004, 52006, 52007, 52009, 52011, 52013, 52015, 52017, 52019, 52021, 52023, 52025, 52026,
52028, 52031, 52032, 52034, 52038, 52041, 52043, 52044, 52046, 52048, 52051, 52053, 52055, 52057, 52059, 52062, 52064,
52066, 52068, 52071, 52073, 52075, 52077, 52079, 52081, 52083, 52085, 52087, 52089, 52092, 52096, 52098, 52101, 52103,
52105, 52108, 52112, 52114, 52116, 52119, 52123, 52125, 52128, 52131, 52133, 52136, 52138, 52139, 52142, 52145, 52147,
52149, 52151, 52155, 52157, 52159, 52162, 52164, 52166, 52169, 52171, 52174, 52178, 52179, 52182, 52184, 52186, 52187,
52189, 52191, 52193, 52195, 52197, 52199, 52201, 52202, 52204, 52206, 52208, 52209, 52212, 52216, 52242, 52244, 52246,
52247, 52252, 52254, 52258, 52261, 52263, 52265, 52268, 52269, 52271, 52273, 52274, 52276, 52278, 52282, 52284, 52285,
52287, 52288, 52292, 52293, 52295, 52297, 52298, 52301, 52302, 52305, 52307, 52309, 52312, 52314, 52316, 52319, 52321,
52323, 52326, 52328, 52332, 52335, 52337, 52338, 52341, 52343, 52345, 52347, 52353, 52356, 52359, 52361, 52363, 52365,
52366, 52368, 52371, 52376, 52377, 52393, 52395, 52397, 52399, 52401, 52403, 52404, 52406, 52408, 52409, 52411, 52413,
52414, 52417, 52419, 52421, 52423, 52425, 52426, 52428, 52433, 52435, 52437, 52439, 52441, 52442, 52444, 52447, 52449,
52451, 52453, 52455, 52456, 52458, 52463, 52465, 52467, 52469, 52471, 52473, 52475, 52478, 52479, 52481, 52483, 52485,
52487, 52489, 52491, 52493, 52495, 52497, 52499, 52502, 52504, 52506, 52509, 52511, 52513, 52515, 52517, 52518, 52521,
52523, 52526, 52528, 52532, 52533, 52535, 52537, 52539, 52542, 52545, 52547, 52553, 52555, 52557, 52563, 52565, 52568,
52573, 52575, 52578, 52583, 52585, 52587, 52592, 52596, 52599, 52601, 52603, 52605, 52608, 52612, 52615, 52617, 52619,
52621, 52623, 52626, 52628, 52629, 52631, 52634, 52636, 52638, 52642, 52644, 52646, 52649, 52652, 52654, 52656, 52659,
52662, 52664, 52666, 52668, 52671, 52673, 52676, 52678, 52679, 52681, 52685, 52687, 52689, 52705, 52707, 52712, 52713,
52715, 52717, 52719, 52721, 52732, 52733, 52735, 52737, 52739, 52741, 52742, 52752, 52754, 52756, 52758, 52759, 52761,
52764, 52767, 52769, 52771, 52772, 52774, 52776, 52779, 52781, 52783, 52784, 52786, 52788, 52799, 52824, 52826, 52827,
52829, 52831, 52832, 52835, 52837, 52838, 52843, 52845, 52848, 52853, 52922, 52924, 52928, 52932, 52934, 52935, 52937,
52941, 52943, 52945, 52947, 52949, 52952, 52956, 52959, 52961, 52963, 52965, 52967, 52969, 52971, 52972, 52975, 52977,
52979, 52981, 52983, 52985, 52987, 52989, 52992, 52994, 52996, 52998, 53005, 53007, 53008, 53009, 53014, 53016, 53019,
53021, 53025, 53027, 53028, 53032, 53034, 53037, 53039, 53041, 53044, 53045, 53047, 53049, 53052, 53054, 53055, 53057,
53059, 53062, 53066, 53068, 53072, 53075, 53077, 53079, 53082, 53084, 53085, 53089, 53091, 53093, 53097, 53099, 53102,
53103, 53105, 53107, 53109, 53112, 53116, 53118, 53119, 53144, 53148, 53151, 53153, 53154, 53156, 53158, 53159, 53161,
53162, 53164, 53166, 53169, 53171, 53173, 53175, 53177, 53179, 53181, 53212, 53214, 53216, 53218, 53223, 53224, 53226,
53229, 53232, 53234, 53235, 53237, 53238, 53241, 53243, 53245, 53246, 53248, 53249, 53251, 53253, 53254, 53256, 53257,
53259, 53261, 53262, 53264, 53265, 53267, 53269, 53272, 53274, 53275, 53277, 53279, 53282, 53284, 53285, 53287, 53288,
53292, 53293, 53295, 53297, 53298, 53302, 53303, 53305, 53306, 53308, 53352, 53353, 53355, 53356, 53358, 53359, 53361,
53363, 53364, 53365, 53367, 53368, 53371, 53373, 53374, 53376, 53378, 53379, 53381, 53383, 53384, 53408, 53412, 53413,
53415, 53417, 53418, 53422, 53423, 53425, 53427, 53428, 53431, 53433, 53434, 53436, 53438, 53439, 53441, 53443, 53445,
53446, 53448, 53451, 53453, 53455, 53456, 53458, 53461, 53463, 53465, 53466, 53467, 53469, 53471, 53472, 53474, 53476,
53477, 53479, 53481, 53482, 53484, 53486, 53489, 53492, 53495, 53497, 53498, 53502, 53503, 53505, 53507, 53512,
53514, 53516, 53517, 53519, 53522, 53523, 53525, 53527, 53528, 53531, 53533, 53534, 53536, 53537, 53539, 53541, 53543,
53545, 53547, 53548, 53552, 53553, 53555, 53557, 53559, 53561, 53563, 53565, 53568, 53571, 53573, 53575, 53576, 53578,
53581, 53583, 53584, 53586, 53588, 53589, 53592, 53594, 53595, 53597, 53601, 53603, 53605, 53607, 53608, 53612, 53613,
53615, 53617, 53618, 53622, 53623, 53625, 53627, 53628, 53631, 53633, 53635, 53637, 53639, 53641, 53642, 53644, 53646,
53647, 53649, 53651, 53654, 53656, 53657, 53662, 53664, 53665, 53667, 53669, 53672, 53674, 53675, 53677, 53679, 53682,
53683, 53685, 53687, 53688, 53692, 53693, 53695, 53696, 53698, 53701, 53703, 53704, 53706, 53707, 53708, 53712, 53714,
53715, 53718, 53719, 53721, 53722, 53724, 53726, 53728, 53732, 53734, 53736, 53739, 53741, 53743, 53745, 53747, 53749,
53751, 53753, 53755, 53756, 53758, 53762, 53764, 53766, 53768, 53772, 53773, 53777, 53779, 53781, 53783, 53785, 53787,
53804, 53806, 53808, 53809, 53811, 53813, 53814, 53818, 53819, 53822, 53823, 53825, 53826, 53828, 53832, 53834, 53836,
53854, 53856, 53857, 53859, 53862, 53863, 53865, 53866, 53868, 53869, 53901, 53903, 53904, 53905, 53907, 53909, 53912,
53914, 53916, 53917, 53919, 53926, 53927, 53928, 53932, 53933, 53935, 53937, 53938, 53942, 53943, 53945, 53948, 53952,
53953, 53955, 53957, 53958, 53962, 53963, 53964, 53966, 53968, 53969, 53971, 53973, 53974, 53976, 53977, 53983, 53986,
53988, 53997, 53999, 54001, 54003, 54005, 54007, 54011, 54027, 54029, 54031, 54033, 54034, 54036, 54037, 54039, 54041,
54042, 54043, 54045, 54047, 54049, 54052, 54053, 54054, 54056, 54057, 54059, 54062, 54063, 54065, 54066, 54088, 54089,
54091, 54093, 54094, 54096, 54097, 54099, 54102, 54103, 54105, 54107, 54108, 54111, 54113, 54115, 54116, 54118, 54119,
54121, 54123, 54124, 54125, 54127, 54129, 54131, 54133, 54135, 54136, 54138, 54142, 54144, 54146, 54148, 54152, 54154,
54156, 54158, 54161, 54163, 54165, 54167, 54169, 54171, 54175, 54177, 54179, 54181, 54182, 54184, 54186, 54188,
54189, 54191, 54193, 54194, 54196, 54198, 54199, 54201, 54202, 54204, 54205, 54207, 54209, 54212, 54213, 54215, 54217,
54218, 54222, 54224, 54226, 54228, 54229, 54231, 54233, 54234, 54236, 54237, 54239, 54241, 54242, 54244, 54246, 54247,
54249, 54252, 54253, 54257, 54258, 54261, 54263, 54265, 54266, 54268, 54269, 54271, 54272, 54275, 54277, 54279, 54281,
54283, 54284, 54286, 54287, 54289, 54292, 54294, 54295, 54297, 54298, 54301, 54303, 54305, 54306, 54309, 54311, 54312,
54314, 54315, 54317, 54319, 54322, 54323, 54325, 54326, 54328, 54331, 54333, 54334, 54336, 54337, 54339, 54341, 54342,
54344, 54345, 54347, 54348, 54351, 54365, 54366, 54368, 54371, 54373, 54374, 54376, 54378, 54379, 54381, 54382, 54384,
54385, 54387, 54388, 54391, 54393, 54394, 54396, 54397, 54399, 54401, 54403, 54405, 54406, 54408, 54412, 54414, 54415,
54417, 54418, 54421, 54423, 54425, 54426, 54428, 54429, 54431, 54434, 54436, 54437, 54439, 54441, 54443, 54445, 54447,
54449, 54451, 54453, 54454, 54456, 54457, 54459, 54461, 54462, 54464, 54465, 54473, 54475, 54476, 54478, 54479, 54481,
54483, 54485, 54486, 54488, 54491, 54493, 54495, 54497, 54498, 54501, 54502, 54504, 54506, 54508, 54514, 54517, 54519,
54521, 54523, 54525, 54527, 54529, 54536, 54546, 54549, 54573, 54575, 54576, 54578, 54582, 54584, 54586, 54588, 54606,
54608, 54612, 54614, 54616, 54618, 54619, 54621, 54623, 54624, 54626, 54627, 54629, 54632, 54634, 54635, 54637, 54638,
54642, 54644, 54646, 54648, 54649, 54651, 54653, 54654, 54656, 54658, 54671, 54673, 54675, 54676, 54678, 54681, 54683,
54685, 54686, 54692, 54693, 54695, 54697, 54698, 54702, 54703, 54705, 54707, 54708, 54712, 54714, 54715, 54717, 54719,
54722, 54724, 54725, 54727, 54732, 54733, 54738, 54742, 54744, 54745, 54747, 54749, 54751, 54752, 54754, 54756, 54758,
54761, 54763, 54765, 54767, 54769, 54771, 54772, 54774, 54776, 54778, 54779, 54781, 54783, 54785, 54786, 54788, 54789,
54791, 54793, 54795, 54796, 54798, 54799, 54801, 54802, 54804, 54805, 54807, 54809, 54811, 54812, 54814, 54818, 54822,
54824, 54826, 54827, 54829, 54831, 54832, 54834, 54837, 54838, 54842, 54844, 54846, 54849, 54852, 54856, 54857, 54859,
54862, 54864, 54866, 54868, 54869, 54871, 54872, 54874, 54876, 54877, 54881, 54885, 54887, 54889, 54893, 54895, 54897,

54898, 54902, 54903, 54905, 54906, 54908, 54914, 54916, 54917, 54919, 54921, 54922, 54924, 54925, 54927, 54928, 54929, 54931, 54933, 54935, 54937, 54938, 54942, 54943, 54945, 54947, 54948, 54952, 54953, 54967, 54969, 54971, 54972, 54974, 54975, 54977, 54978, 54982, 55001, 55003, 55004, 55006, 55008, 55012, 55014, 55016, 55018, 55021, 55024, 55025, 55028, 55032, 55033, 55035, 55037, 55038, 55042, 55043, 55045, 55047, 55048, 55052, 55054, 55055, 55057, 55059, 55061, 55062, 55069, 55071, 55073, 55074, 55076, 55078, 55081, 55083, 55085, 55086, 55088, 55092, 55093, 55095, 55097, 55099, 55101, 55103, 55105, 55106, 55108, 55112, 55114, 55115, 55117, 55119, 55121, 55124, 55126, 55142, 55144, 55146, 55147, 55149, 55151, 55152, 55154, 55157, 55167, 55173, 55176, 55177, 55178, 55182, 55183, 55185, 55188, 55192, 55193, 55195, 55197, 55199, 55201, 55203, 55208, 55212, 55213, 55217, 55219, 55221, 55222, 55224, 55226, 55228, 55232, 55233, 55235, 55237, 55251, 55253, 55309, 55311, 55313, 55315, 55317, 55319, 55321, 55323, 55325, 55326, 55328, 55332, 55334, 55335, 55337, 55593, 55595, 55617, 55619, 55626, 55642, 55644, 55646, 55648, 55649, 55651, 55653, 55655, 55657, 55659, 55661, 55663, 55666, 55668, 55672, 55674, 55676, 55681, 55683, 55685, 55687, 55689, 55691, 55693, 55695, 55697, 55699, 55701, 55703, 55705, 55707, 55709, 55712, 55714, 55716, 55718, 55722, 55726, 55728, 55729, 55731, 55733, 55734, 55736, 55737, 55739, 55741, 55743, 55744, 55746, 55748, 55749, 55751, 55753, 55754, 55757, 55759, 55762, 55763, 55765, 55812, 55813, 55815, 55817, 55818, 55821, 55823, 55828, 55832, 55836, 55837, 55839, 55841, 55842, 55843, 55844, 55846, 55847, 55848, 55849, 55851, 55852, 55854, 55855, 55856, 55857, 55858, 55859, 55863, 55868, 55871, 55873, 55875, 55877, 55879, 55881, 55883, 55886, 55888, 55892, 55894, 55896, 55898, 55904, 55906, 55908, 55909, 55912, 55914, 55916, 55922, 55923, 55925, 55927, 55929, 55931, 55933, 55935, 55936, 55941, 55943, 55945, 55947, 55948, 55951, 55953, 55955, 55957, 55959, 55964, 55971, 55972, 55986, 55988, 55993, 56058, 56059, 56062, 56063, 56065, 56067, 56069, 56071, 56073, 56075, 56077, 56079, 56081, 56083, 56084, 56086, 56087, 56089, 56091, 56093, 56095, 56097, 56099, 56101, 56103, 56105, 56107, 56109, 56111, 56113, 56116, 56118, 56123, 56125, 56127, 56129, 56131, 56132, 56134, 56135, 56157, 56165, 56171, 56179, 56186, 56192, 56207, 56213, 56228, 56235, 56242, 56256, 56264, 56271, 56277, 56284, 56291, 56297, 56304, 56312, 56318, 56326, 56347, 56353, 56356, 56358, 56363, 56368, 56372, 56376, 56381, 56386, 56393, 56395, 56396, 56397, 56399, 56403, 56414, 56416, 56417, 56419, 56422, 56423, 56424, 56426, 56427, 56429, 56431, 56433, 56436, 56437, 56438, 56444, 56446, 56447, 56449, 56516, 56517, 56521, 56522, 56535, 56536, 56541, 56542, 56552, 56554, 56555, 56556, 56558, 56559, 56561, 56562, 56564, 56565, 56567, 56568, 56571, 56573, 56574, 56575, 56577, 56578, 56579, 56581, 56582, 56589, 56591, 56592, 56594, 56596, 56597, 56599, 56602, 56604, 56605, 56606, 56608, 56609, 56612, 56613, 56615, 56616, 56617, 56618, 56619, 56623, 56631, 56633, 56642, 56672, 56674, 56675, 56677, 56679, 56682, 56683, 56685, 56686, 56688, 56689, 56692, 56694, 56697, 56699, 56703, 56706, 56708, 56711, 56713, 56715, 56716, 56718, 56719, 56721, 56722, 56725, 56728, 56732, 56734, 56736, 56737, 56739, 56742, 56743, 56745, 56746, 56749, 56751, 56754, 56755, 56756, 56758, 56761, 56794, 56796, 56797, 56798, 56802, 56804, 56805, 56807, 56828, 56829, 56832, 56834, 56836, 56839, 56841, 56842, 56844, 56845, 56855, 57053, 57056, 57057, 57059, 57067, 57101, 57119, 57123, 57127, 57132, 57134, 57136, 57138, 57139, 57141, 57143, 57212, 57218, 57221, 57235, 57242, 57244, 57246, 57249, 57252, 57254, 57256, 57258, 57266, 57268, 57269, 57271, 57272, 57274, 57275, 57276, 57278, 57279, 57282, 57284, 57285, 57287, 57289, 57291, 57293, 57295, 57297, 57299, 57302, 57304, 57306, 57308, 57311, 57313, 57314, 57316, 57317, 57319, 57321, 57323, 57324, 57326, 57327, 57329, 57331, 57332, 57334, 57336, 57338, 57339, 57341, 57342, 57344, 57346, 57348, 57352, 57354, 57356, 57358, 57362, 57364, 57372, 57374, 57376, 57378, 57382, 57384, 57386, 57388, 57391, 57392, 57394, 57396, 57398, 57402, 57403, 57408, 57411, 57413, 57415, 57417, 57419, 57422, 57424, 57426, 57427, 57429, 57431, 57433, 57435, 57436, 57438, 57442, 57444, 57446, 57447, 57449, 57451, 57452, 57454, 57461, 57462, 57464, 57466, 57468, 57472, 57474, 57476, 57478, 57482, 57484, 57486, 57488, 57489, 57491, 57493, 57495, 57498, 57502, 57504, 57506, 57509, 57511, 57513, 57515, 57517, 57519, 57522, 57524, 57526, 57528, 57542, 57544, 57546, 57547, 57549, 57551, 57553, 57555, 57557, 57558, 57564, 57566, 57567, 57569, 57571, 57572, 57574, 57576, 57582, 57584, 57588, 57592, 57594, 57595, 57597, 57599, 57601, 57604, 57606, 57608, 57614, 57615, 57617, 57619, 57621, 57629, 57631, 57633, 57635, 57637, 57639, 57641, 57642, 57644, 57646, 57648, 57652, 57654, 57656, 57658, 57662, 57668, 57671, 57676, 57678, 57679, 57681, 57682, 57684, 57686, 57687, 57689, 57692, 57694, 57695, 57697, 57698, 57703, 57705, 57706, 57708, 57711, 57713, 57715, 57717, 57718, 57722, 57728, 57729, 57731, 57733, 57734, 57766, 57767, 57769, 57771, 57772, 57774, 57775, 57777, 57779, 57784, 57786, 57788, 57789, 57792, 57795, 57797, 57799, 57801, 57803, 57805, 57809, 57811, 57813, 57815, 57817, 57818, 57822, 57824, 57826, 57829, 57831, 57833, 57835, 57837, 57839, 57841, 57846, 57848, 57849, 57851, 57855, 57857, 57859, 57861, 57863, 57865, 57866, 57873, 57875, 57877, 57879, 57881, 57883, 57885, 57887, 57889, 57891, 57893, 57899, 57901, 57903, 57905, 57907, 57909, 57911, 57913, 57914, 57916, 57918, 57922, 57924, 57926, 57928, 57932, 57933, 57935, 57937, 57957, 58024, 58032, 58034, 58035, 58038, 58039, 58041, 58043, 58045, 58047, 58052, 58053, 58054, 58057, 58058, 58059, 58061, 58063, 58065, 58067, 58069, 58071, 58072, 58074, 58077, 58078, 58081, 58083, 58084, 58086, 58087, 58088, 58091, 58093, 58094, 58095, 58097, 58101, 58102, 58104, 58106, 58108, 58112, 58114, 58115, 58117, 58118, 58121, 58123, 58124, 58132, 58134, 58136, 58138, 58142, 58143, 58145, 58147, 58149, 58152, 58154, 58156, 58163, 58165, 58166, 58168, 58172, 58174, 58176, 58178, 58182, 58184, 58185, 58187, 58189, 58191, 58193, 58195, 58197, 58199, 58202, 58204, 58206, 58208, 58212, 58214, 58216, 58218, 58221, 58223, 58225, 58227, 58229, 58231, 58233, 58235, 58239, 58242, 58244, 58245, 58247, 58249, 58251, 58252, 58254, 58256, 58258, 58262, 58264, 58265, 58269, 58271, 58273, 58275, 58277, 58278, 58282, 58283, 58288, 58292, 58294, 58295, 58297, 58299, 58302, 58305, 58308, 58309, 58312, 58314, 58315, 58317, 58318, 58319, 58321, 58322, 58324, 58325, 58327, 58329, 58331, 58334, 58361, 58363, 58365, 58368, 58372, 58374, 58376, 58378, 58379, 58381, 58383, 58385, 58387, 58389, 58391, 58393, 58395, 58397, 58399, 58401, 58403, 58405, 58407, 58409, 58411, 58413, 58415, 58417, 58418, 58422, 58424, 58426, 58428, 58432, 58434, 58436, 58438, 58441, 58449, 58451, 58453, 58455, 58457, 58458, 58462, 58464, 58466, 58467, 58469, 58472, 58474, 58476, 58478, 58482, 58483, 58485, 58487, 58488, 58491, 58493, 58495, 58496, 58498, 58502, 58504, 58506, 58508, 58512, 58513, 58515, 58517, 58519, 58521, 58522, 58524, 58525, 58527, 58528, 58529, 58531, 58532, 58534, 58536, 58538, 58542, 58545, 58547, 58549, 58552, 58554, 58555, 58556, 58558, 58562, 58563, 58565, 58566, 58568, 58572, 58573, 58575, 58577, 58583, 58585, 58586, 58588, 58595, 58596, 58598, 58599, 58601, 58602, 58604, 58606, 58612, 58616, 58617, 58619, 58622, 58624, 58625, 58627, 58629, 58631, 58633, 58636, 58638, 58642, 58644, 58646, 58648, 58652, 58654, 58656, 58658, 58662, 58663, 58664, 58666, 58667, 58669, 58672, 58674, 58675, 58677, 58679, 58681, 58683, 58684, 58686, 58688, 58692, 58693, 58695, 58697, 58699, 58701, 58702, 58704, 58706, 58708, 58713, 58715, 58717, 58719, 58721, 58727, 58729, 58732, 58734, 58736, 58753, 58761, 58762, 58764, 58766, 58768, 58772, 58775, 58778, 58781, 58782, 58784, 58785, 58787, 58792, 58794, 58795, 58797, 58799, 58801, 58802, 58804, 58806, 58808, 58812, 58814, 58815, 58817, 58819, 58821, 58823, 58825, 58826, 58828, 58832, 58833, 58835, 58837, 58847, 58849, 58854, 58859, 58881, 58882, 58883, 58884, 58885, 58886, 58887, 58888, 58892, 58894, 58896, 58898, 58902, 58904, 58906, 58908, 58909, 58911, 58913, 58915, 58917, 58919, 58921, 58923, 58925, 58927, 58929, 58931, 58933, 58935, 58937, 58939, 58942, 58944, 58946, 58948, 58952, 58958, 58962, 58964, 58966, 58967, 58969, 58973, 58975, 58977, 58982, 58984, 58986, 58988, 58992, 58998, 59007, 59012, 59014, 59016, 59018, 59022, 59028, 59029, 59032, 59034, 59036, 59042, 59044, 59046, 59048, 59049, 59051, 59053, 59055, 59057, 59059, 59061, 59064, 59065, 59067, 59069, 59071, 59073, 59075, 59077, 59079, 59082, 59084, 59086, 59088, 59092, 59094, 59096, 59097, 59103, 59105, 59107, 59109, 59112, 59114, 59116, 59118, 59119, 59121, 59124, 59125, 59127, 59129, 59131, 59132, 59134, 59136, 59138, 59139, 59141, 59143, 59145, 59146, 59148, 59152, 59153, 59155, 59157, 59159, 59163, 59165, 59166, 59168, 59172, 59174, 59176, 59179, 59182, 59184, 59188, 59192, 59194, 59196, 59198, 59202, 59203, 59205, 59207, 59209, 59211, 59213, 59215, 59217, 59218, 59222, 59224, 59226, 59232, 59234, 59236, 59238, 59242, 59243, 59245, 59247, 59249, 59251, 59253, 59255, 59256, 59258, 59262, 59264, 59266, 59268, 59269, 59271, 59273, 59275, 59277, 59279, 59282, 59284, 59286, 59287, 59289, 59291, 59293, 59295, 59299, 59301, 59302, 59313, 59314, 59316, 59318, 59322, 59323, 59325, 59327, 59329, 59332, 59334, 59336, 59338, 59341, 59342, 59344, 59346, 59348, 59354, 59356, 59359, 59361, 59362, 59364, 59366, 59368, 59372, 59374, 59376, 59378, 59382, 59384, 59386, 59388, 59417, 59419, 59421, 59423, 59425, 59428, 59432, 59434, 59435, 59437, 59439, 59441, 59443, 59445, 59447, 59448, 59451, 59453, 59456, 59458, 59462, 59464, 59466, 59467, 59469, 59471, 59472, 59474, 59476, 59477, 59479, 59481, 59483, 59485, 59486, 59487, 59489, 59491, 59492, 59494, 59496, 59501, 59503, 59509, 59511, 59512, 59515, 59517, 59519, 59521, 59523, 59525, 59527, 59529, 59532, 59535, 59536, 59538, 59542, 59544, 59546, 59552, 59555, 59557, 59559, 59561, 59563, 59565, 59567, 59572, 59574, 59576, 59578, 59582, 59583, 59585, 59587, 59589, 59592, 59594, 59596, 59598, 59601, 59605, 59607, 59609, 59611, 59613, 59615, 59617, 59619, 59622, 59623, 59625, 59627, 59629, 59631, 59633, 59642, 59644, 59646, 59647, 59649, 59651, 59653, 59654, 59656, 59658, 59661, 59663, 59664, 59666, 59668, 59672, 59674, 59677, 59679, 59681, 59682, 59684, 59688, 59692, 59694, 59696, 59698, 59699, 59701, 59702, 59704, 59705, 59707, 59709, 59712, 59714, 59716, 59736, 59738, 59739, 59741, 59743, 59745, 59747, 59749, 59751, 59753, 59778, 59782, 59785, 59787, 59789, 59793, 59795, 59797, 59799, 59802, 59803, 59813,

59816, 59829, 59831, 59832, 59834, 59836, 59838, 59842, 59843, 59847, 59851, 59853, 59855, 59857, 59862, 59864, 59866,
59868, 59872, 59874, 59876, 59878, 59882, 59884, 59886, 59888, 59892, 59894, 59896, 59898, 59904, 59906, 59908, 59912,
59914, 59916, 59919, 59921, 59923, 59924, 59926, 59928, 59931, 59933, 59939, 59941, 59942, 59944, 59946, 59947, 59949,
59951, 59953, 59954, 59955, 59957, 59959, 59962, 59964, 59965, 59967, 59969, 59971, 59972, 59974, 59976, 59978, 59979,
59981, 59983, 59985, 59987, 59988, 59992, 59995, 59996, 59998, 59999, 60001, 60005, 60007, 60009, 60011, 60013,
60014, 60016, 60018, 60022, 60024, 60026, 60028, 60031, 60033, 60035, 60037, 60039, 60041, 60043, 60045, 60047, 60049,
60052, 60054, 60056, 60058, 60062, 60071, 60073, 60074, 60077, 60079, 60082, 60084, 60087, 60089, 60091, 60093,
60095, 60097, 60098, 60101, 60103, 60104, 60106, 60108, 60112, 60114, 60116, 60118, 60122, 60124, 60125, 60127, 60129,
60132, 60133, 60135, 60136, 60138, 60139, 60141, 60142, 60144, 60146, 60147, 60149, 60152, 60153, 60155, 60156, 60158,
60159, 60161, 60163, 60164, 60166, 60167, 60168, 60172, 60175, 60177, 60179, 60181, 60183, 60185, 60187, 60189, 60191,
60193, 60195, 60201, 60203, 60205, 60207, 60209, 60211, 60213, 60215, 60216, 60218, 60222, 60224, 60226, 60228, 60231,
60233, 60235, 60237, 60238, 60241, 60242, 60244, 60245, 60247, 60248, 60249, 60251, 60253, 60254, 60256, 60257, 60262,
60263, 60265, 60267, 60269, 60272, 60274, 60275, 60281, 60283, 60284, 60286, 60288, 60292, 60294, 60296, 60298, 60302,
60303, 60305, 60306, 60308, 60311, 60313, 60315, 60316, 60319, 60322, 60324, 60325, 60327, 60329, 60331, 60332, 60334,
60336, 60337, 60339, 60341, 60342, 60344, 60346, 60347, 60349, 60351, 60352, 60354, 60356, 60357, 60359, 60361, 60362,
60364, 60366, 60367, 60369, 60371, 60373, 60374, 60376, 60378, 60382, 60383, 60385, 60387, 60388, 60392, 60393, 60396,
60398, 60399, 60401, 60403, 60405, 60407, 60409, 60412, 60414, 60416, 60418, 60421, 60423, 60425, 60426, 60428, 60429,
60431, 60433, 60435, 60436, 60438, 60441, 60443, 60444, 60446, 60448, 60449, 60451, 60453, 60455, 60456, 60458, 60461,
60463, 60465, 60466, 60468, 60471, 60473, 60474, 60478, 60481, 60483, 60484, 60489, 60492, 60494, 60495,
60497, 60499, 60502, 60503, 60505, 60508, 60511, 60512, 60514, 60516, 60517, 60519, 60522, 60524, 60525, 60527, 60533,
60535, 60536, 60538, 60539, 60541, 60543, 60544, 60546, 60548, 60549, 60551, 60553, 60554, 60556, 60557, 60559, 60561,
60562, 60564, 60565, 60567, 60568, 60571, 60573, 60574, 60576, 60578, 60579, 60581, 60582, 60583, 60585, 60586, 60587,
60589, 60592, 60593, 60594, 60596, 60597, 60599, 60601, 60603, 60604, 60606, 60608, 60614, 60615, 60617, 60619, 60621,
60622, 60624, 60625, 60627, 60629, 60631, 60633, 60635, 60637, 60639, 60671, 60673, 60675, 60677, 60679, 60685, 60686,
60688, 60691, 60693, 60695, 60696, 60698, 60699, 60701, 60703, 60704, 60706, 60708, 60709, 60711, 60712, 60714, 60715,
60717, 60719, 60722, 60723, 60725, 60727, 60728, 60731, 60733, 60735, 60736, 60738, 60741, 60743, 60746, 60747, 60749,
60751, 60752, 60754, 60756, 60758, 60759, 60761, 60763, 60766, 60767, 60771, 60775, 60776, 60779, 60782, 60783, 60785,
60786, 60789, 60791, 60792, 60794, 60796, 60798, 60801, 60803, 60805, 60806, 60808, 60814, 60815, 60818, 60821, 60823,
60824, 60826, 60827, 60829, 60831, 60832, 60834, 60835, 60837, 60838, 60842, 60843, 60845, 60847, 60848, 60852, 60853,
60855, 60856, 60858, 60859, 60861, 60862, 60864, 60865, 60867, 60869, 60872, 60873, 60875, 60877, 60878, 60881, 60883,
60884, 60886, 60888, 60889, 60891, 60894, 60896, 60897, 60899, 60901, 60903, 60905, 60907, 60909, 60913, 60915, 60916,
60918, 60919, 60921, 60922, 60924, 60925, 60927, 60928, 60932, 60934, 60936, 60938, 60941, 60943, 60946, 60948, 60949,
60951, 60953, 60954, 60956, 60958, 60959, 60965, 60967, 60969, 60972, 60974, 60976, 60977, 60979, 60982, 60984, 60986,
60989, 60992, 60994, 60995, 60997, 60999, 61003, 61005, 61006, 61008, 61011, 61013, 61015, 61017, 61018, 61022, 61023,
61025, 61027, 61028, 61032, 61033, 61035, 61037, 61038, 61042, 61043, 61045, 61047, 61048, 61052, 61053, 61055, 61057,
61058, 61062, 61063, 61065, 61066, 61069, 61072, 61074, 61075, 61077, 61082, 61083, 61085, 61087, 61088, 61092,
61093, 61095, 61097, 61098, 61103, 61104, 61113, 61114, 61116, 61118, 61119, 61121, 61123, 61124, 61126, 61127, 61129,
61131, 61133, 61134, 61137, 61139, 61142, 61143, 61145, 61147, 61154, 61155, 61157, 61158, 61161, 61163, 61165,
61167, 61169, 61171, 61173, 61176, 61178, 61182, 61184, 61186, 61187, 61189, 61191, 61193, 61194, 61196, 61198, 61201,
61203, 61208, 61212, 61214, 61216, 61218, 61223, 61225, 61226, 61229, 61231, 61233, 61235, 61237, 61239, 61241, 61251,
61254, 61255, 61257, 61259, 61261, 61263, 61265, 61269, 61271, 61273, 61275, 61277, 61279, 61281, 61284, 61286, 61288,
61292, 61294, 61296, 61298, 61301, 61303, 61305, 61307, 61309, 61311, 61313, 61315, 61317, 61318, 61322, 61324, 61326,
61328, 61332, 61333, 61337, 61339, 61341, 61343, 61345, 61347, 61349, 61351, 61353, 61355, 61357, 61359, 61361, 61363,
61365, 61367, 61373, 61375, 61377, 61379, 61381, 61383, 61385, 61387, 61389, 61392, 61393, 61396, 61398, 61399, 61401,
61402, 61406, 61408, 61411, 61413, 61415, 61416, 61419, 61421, 61423, 61424, 61426, 61428, 61429, 61431, 61433, 61434,
61436, 61438, 61441, 61443, 61447, 61449, 61452, 61454, 61455, 61457, 61459, 61462, 61464, 61466, 61468, 61471, 61474,
61476, 61478, 61481, 61483, 61485, 61486, 61489, 61496, 61497, 61499, 61501, 61502, 61504, 61507, 61522, 61524, 61525,
61527, 61529, 61532, 61534, 61536, 61537, 61539, 61542, 61544, 61546, 61548, 61549, 61551, 61553, 61555, 61556, 61558,
61562, 61563, 61565, 61567, 61569, 61571, 61572, 61574, 61576, 61578, 61579, 61581, 61583, 61585, 61586, 61588, 61592,
61594, 61595, 61598, 61606, 61608, 61609, 61611, 61613, 61615, 61618, 61622, 61624, 61625, 61627, 61629, 61631,
61632, 61634, 61636, 61638, 61641, 61642, 61644, 61646, 61648, 61649, 61651, 61653, 61654, 61656, 61662, 61664, 61665,
61667, 61669, 61671, 61672, 61674, 61675, 61677, 61679, 61681, 61682, 61684, 61686, 61687, 61689, 61691, 61693, 61694,
61696, 61698, 61699, 61701, 61703, 61706, 61707, 61709, 61712, 61713, 61716, 61718, 61719, 61721, 61725, 61727, 61728,
61729, 61732, 61734, 61736, 61738, 61742, 61744, 61748, 61752, 61754, 61756, 61758, 61762, 61764, 61766, 61768, 61772,
61775, 61777, 61779, 61781, 61783, 61785, 61787, 61789, 61796, 61801, 61803, 61805, 61806, 61808, 61809, 61811,
61813, 61814, 61816, 61817, 61819, 61821, 61822, 61824, 61825, 61827, 61828, 61832, 61833, 61835, 61837, 61838, 61842,
61843, 61845, 61847, 61848, 61852, 61853, 61855, 61856, 61858, 61859, 61861, 61863, 61864, 61866, 61868, 61869, 61871,
61872, 61874, 61875, 61877, 61879, 61882, 61884, 61886, 61887, 61889, 61891, 61892, 61894, 61896, 61898, 61902, 61904,
61908, 61909, 61911, 61913, 61915, 61917, 61919, 61922, 61924, 61926, 61928, 61931, 61933, 61935, 61941, 61943, 61945,
61947, 61949, 61951, 61952, 61954, 61956, 61958, 61962, 61964, 61966, 61969, 61971, 61973, 61975, 61976, 61978, 61982,
61984, 61986, 61988, 61989, 61992, 61993, 61996, 61997, 61999, 62001, 62002, 62004, 62006, 62008, 62009, 62011, 62013,
62015, 62017, 62019, 62021, 62022, 62024, 62026, 62028, 62032, 62033, 62035, 62037, 62039, 62041, 62043, 62044, 62046,
62048, 62052, 62054, 62056, 62057, 62059, 62061, 62072, 62074, 62076, 62078, 62083, 62085, 62087, 62089, 62091, 62093,
62095, 62096, 62098, 62102, 62104, 62108, 62112, 62113, 62117, 62119, 62121, 62123, 62124, 62127, 62128,
62132, 62134, 62135, 62137, 62139, 62143, 62145, 62152, 62153, 62155, 62157, 62159, 62161, 62163, 62165, 62166, 62168,
62172, 62174, 62176, 62178, 62182, 62184, 62187, 62189, 62191, 62192, 62228, 62232, 62234, 62236, 62238, 62241, 62243,
62245, 62247, 62249, 62252, 62254, 62256, 62258, 62261, 62263, 62265, 62267, 62269, 62272, 62274, 62276, 62277, 62279,
62281, 62283, 62285, 62286, 62288, 62291, 62293, 62295, 62297, 62298, 62302, 62303, 62305, 62307, 62309, 62312, 62314,
62315, 62317, 62319, 62321, 62322, 62324, 62326, 62328, 62329, 62331, 62334, 62336, 62338, 62342, 62344, 62345, 62347,
62349, 62351, 62352, 62354, 62355, 62357, 62359, 62369, 62372, 62374, 62376, 62378, 62382, 62384, 62386, 62388, 62392,
62394, 62396, 62398, 62402, 62404, 62406, 62408, 62412, 62414, 62416, 62418, 62422, 62424, 62426, 62429, 62432, 62434,
62436, 62438, 62442, 62444, 62446, 62448, 62452, 62454, 62456, 62462, 62464, 62466, 62468, 62475, 62477, 62479,
62484, 62486, 62488, 62489, 62491, 62498, 62502, 62505, 62506, 62508, 62509, 62511, 62513, 62515, 62517, 62523, 62525,
62527, 62529, 62531, 62533, 62535, 62537, 62539, 62541, 62543, 62545, 62547, 62549, 62551, 62553, 62554, 62556, 62559,
62562, 62565, 62566, 62568, 62572, 62579, 62581, 62583, 62585, 62587, 62589, 62596, 62599, 62601, 62602, 62612,
62614, 62616, 62623, 62625, 62629, 62631, 62632, 62634, 62636, 62638, 62642, 62644, 62645, 62647, 62649, 62651, 62653,
62655, 62657, 62659, 62661, 62663, 62668, 62672, 62675, 62677, 62679, 62681, 62683, 62687, 62689, 62693, 62695, 62697,
62699, 62701, 62703, 62705, 62707, 62714, 62716, 62718, 62722, 62724, 62726, 62728, 62745, 62747, 62749, 62751, 62753,
62755, 62757, 62759, 62766, 62773, 62782, 62784, 62786, 62788, 62789, 62791, 62794, 62796, 62798, 62802, 62804, 62805,
62807, 62811, 62812, 62815, 62817, 62819, 62821, 62822, 62824, 62826, 62827, 62829, 62831, 62832, 62834, 62836, 62838,
62839, 62841, 62843, 62844, 62846, 62849, 62855, 62857, 62859, 62862, 62863, 62865, 62867, 62869, 62872, 62875, 62877,
62879, 62881, 62883, 62885, 62887, 62891, 62895, 62897, 62899, 62901, 62902, 62906, 62908, 62911, 62913, 62915, 62917,
62919, 62921, 62922, 62924, 62926, 62931, 62933, 62935, 62937, 62939, 62941, 62943, 62945, 62947, 62949, 62951, 62953,
62955, 62957, 62959, 62962, 62964, 62966, 62968, 62969, 62971, 62973, 62975, 62977, 62983, 62985, 62987, 62989, 62991,
62993, 62995, 62997, 62999, 63001, 63003, 63007, 63009, 63011, 63013, 63015, 63017, 63019, 63021, 63024, 63026, 63028,
63032, 63033, 63035, 63037, 63039, 63041, 63043, 63045, 63047, 63049, 63051, 63054, 63056, 63058, 63062, 63064, 63066,
63068, 63072, 63074, 63076, 63078, 63082, 63083, 63085, 63087, 63089, 63091, 63093, 63095, 63097, 63099, 63101, 63107,
63109, 63111, 63113, 63115, 63118, 63152, 63168, 63178, 63204, 63206, 63208, 63213, 63218, 63222, 63224, 63226, 63228,
63241, 63243, 63245, 63247, 63249, 63261, 63263, 63265, 63267, 63269, 63271, 63273, 63275, 63277, 63279, 63281,
63283, 63285, 63287, 63289, 63291, 63293, 63296, 63326, 63328, 63332, 63334, 63336, 63338, 63342, 63343, 63344, 63345,
63346, 63348, 63352, 63353, 63355, 63361, 63363, 63365, 63367, 63369, 63371, 63373, 63375, 63377, 63379, 63382, 63384,

63387, 63388, 63392, 63393, 63395, 63396, 63398, 63402, 63404, 63405, 63407, 63409, 63411, 63413, 63415, 63417, 63419,
63421, 63423, 63425, 63427, 63436, 63519, 63521, 63523, 63525, 63527, 63529, 63531, 63532, 63534, 63536, 63538, 63539,
63541, 63542, 63543, 63544, 63545, 63547, 63548, 63552, 63554, 63555, 63579, 63735, 63736, 63738, 63742, 63744, 63745,
63747, 63749, 63766, 63768, 63772, 63773, 63842, 64027, 64028, 64074, 64076, 64077, 64079, 64081, 64083, 64085, 64087,
64088, 64092, 64094, 64096, 64098, 64101, 64113, 64114, 64116, 64117, 64119, 64121, 64123, 64124, 64126, 64128, 64132,
64133, 64135, 64136, 64138, 64142, 64144, 64146, 64148, 64151, 64153, 64155, 64157, 64159, 64161, 64162, 64166, 64168,
64178, 64192, 64194, 64196, 64198, 64202, 64264, 64267, 64272, 64277, 64278, 64295, 64296, 64305, 64334, 64367, 64403,
64404, 64406, 64408, 64409, 64411, 64413, 64415, 64417, 64419, 64423, 64424, 64426, 64428, 64432, 64434, 64436, 64437,
64439, 64442, 64444, 64446, 64448, 64454, 64455, 64489, 64491, 64493, 64495, 64497, 64499, 64502, 64503, 64548, 64558,
64574, 64576, 64577, 64584, 64592, 64602, 64604, 64606, 64608, 64609, 64611, 64613, 64615, 64616, 64618, 64619, 64623,
64624, 64626, 64627, 64629, 64632, 64634, 64636, 64637, 64638, 64641, 64642, 64654, 64658, 64659, 64661, 64662, 64665,
64666, 64668, 64669, 64671, 64674, 64675, 64676, 64678, 64682, 64683, 64688, 64692, 64694, 64695, 64717, 64718, 64725,
64735, 64736, 64737, 64738, 64739, 64741, 64743, 64744, 64746, 64748, 64751, 64753, 64755, 64756, 64758, 64772, 64773,
64776, 64782, 64791, 64793, 64795, 64797, 64799, 64801, 64803, 64805, 64807, 64808, 64877, 64879, 64882, 64884, 64887,
64889, 64892, 64894, 64895, 64897, 64898, 64902, 64903, 64905, 64907, 64908, 64911, 64913, 64914, 64915, 64917, 64918,
64921, 64923, 64924, 64926, 64927, 64929, 64933, 64935, 64937, 64938, 64942, 64944, 64946, 64947, 64951, 64952, 64954,
64956, 64958, 64961, 64963, 64965, 64967, 64969, 64971, 64972, 64974, 64976, 64978, 64979, 64981, 64983, 64984, 64986,
64987, 64989, 64992, 64993, 64994, 64996, 64997, 64999, 65002, 65004, 65005, 65007, 65008, 65011, 65013, 65015, 65016,
65018, 65019, 65021, 65022, 65024, 65025, 65027, 65028, 65031, 65033, 65034, 65041, 65047, 65048, 65052, 65054, 65055,
65057, 65059, 65061, 65063, 65064, 65066, 65068, 65069, 65071, 65072, 65073, 65074, 65076, 65077, 65088, 65091, 65094,
65095, 65109, 65118, 65119, 65122, 65123, 65125, 65126, 65133, 65135, 65136, 65138, 65139, 65145, 65146, 65148, 65149,
65152, 65153, 65154, 65176, 65177, 65178, 65181, 65183, 65184, 65185, 65187, 65188, 65189, 65191, 65192, 65193, 65195,
65196, 65198, 65199, 65201, 65203, 65205, 65211, 65212, 65214, 65215, 65217, 65221, 65223, 65224, 65226, 65228, 65229,
65231, 65233, 65234, 65236, 65238, 65239, 65241, 65243, 65244, 65246, 65247, 65249, 65251, 65252, 65254, 65256, 65258,
65259, 65261, 65263, 65265, 65266, 65268, 65269, 65271, 65273, 65274, 65276, 65278, 65281, 65283, 65284, 65286, 65288,
65289, 65291, 65292, 65294, 65295, 65296, 65298, 65299, 65311, 65313, 65315, 65317, 65319, 65321, 65323, 65325, 65326,
65328, 65329, 65331, 65332, 65333, 65335, 65336, 65338, 65339, 65341, 65342, 65344, 65345, 65346, 65347, 65349, 65351,
65352, 65353, 65355, 65356, 65357, 65358, 65365, 65366, 65368, 65369, 65371, 65372, 65374, 65376, 65378, 65379, 65381,
65383, 65384, 65386, 65388, 65393, 65396, 65398, 65402, 65404, 65406, 65407, 65412, 65414, 65415, 65417, 65419, 65421,
65423, 65425, 65427, 65428, 65434, 65436, 65438, 65441, 65443, 65445, 65447, 65449, 65453, 65457, 65459, 65461, 65462,
65464, 65465, 65467, 65469, 65471, 65472, 65474, 65475, 65477, 65478, 65482, 65484, 65485, 65487, 65489, 65491, 65493,
65494, 65495, 65497, 65499, 65502, 65503, 65505, 65506, 65508, 65509, 65511, 65512, 65518, 65521, 65523, 65525, 65527,
65528, 65531, 65533, 65535, 65537, 65539, 65542, 65544, 65545, 65547, 65548, 65551, 65552, 65554, 65555, 65556, 65558,
65559, 65561, 65563, 65565, 65566, 65568, 65572, 65573, 65575, 65577, 65579, 65581, 65583, 65585, 65587, 65588, 65592,
65593, 65595, 65597, 65598, 65602, 65603, 65605, 65607, 65609, 65612, 65613, 65615, 65617, 65619, 65622, 65624, 65625,
65627, 65628, 65632, 65633, 65635, 65637, 65638, 65642, 65643, 65645, 65647, 65649, 65651, 65652, 65654, 65656, 65658,
65661, 65667, 65669, 65671, 65673, 65675, 65676, 65678, 65682, 65684, 65685, 65688, 65691, 65693, 65694, 65696, 65698,
65699, 65701, 65702, 65704, 65706, 65707, 65708, 65712, 65713, 65715, 65716, 65718, 65719, 65721, 65722, 65724, 65726,
65727, 65729, 65732, 65737, 65742, 65743, 65745, 65747, 65748, 65751, 65752, 65754, 65755, 65757, 65758, 65762, 65764,
65765, 65767, 65768, 65771, 65773, 65774, 65776, 65777, 65779, 65782, 65784, 65786, 65787, 65789, 65792, 65793, 65795,
65796, 65798, 65799, 65801, 65802, 65803, 65805, 65806, 65808, 65809, 65811, 65813, 65814, 65816, 65817, 65819, 65821,
65854, 65856, 65858, 65862, 65864, 65865, 65867, 65869, 65872, 65874, 65875, 65877, 65879, 65881, 65882, 65884, 65885,
65887, 65888, 65892, 65894, 65896, 65898, 65901, 65903, 65905, 65907, 65908, 65911, 65913, 65915, 65917, 65919, 65921,
65922, 65924, 65926, 65928, 65932, 65933, 65935, 65937, 65939, 65942, 65943, 65945, 65947, 65949, 65951, 65954, 65955,
65956, 65958, 65961, 65963, 65965, 65967, 65969, 65971, 65973, 65975, 65981, 65982, 65984, 65986, 65987, 65989, 65992,
65993, 65995, 65997, 65999, 66001, 66002, 66004, 66006, 66007, 66009, 66011, 66013, 66014, 66016, 66018, 66022, 66024,
66025, 66027, 66029, 66031, 66033, 66035, 66041, 66044, 66048, 66051, 66055, 66058, 66062, 66064, 66065, 66067, 66069,
66071, 66073, 66075, 66077, 66079, 66081, 66083, 66085, 66087, 66089, 66092, 66093, 66095, 66097, 66098, 66101, 66103,
66105, 66107, 66114, 66115, 66117, 66119, 66122, 66124, 66125, 66127, 66129, 66131, 66132, 66134, 66135, 66137, 66139,
66142, 66144, 66146, 66153, 66154, 66155, 66159, 66161, 66163, 66164, 66166, 66168, 66171, 66173, 66176, 66177, 66183,
66185, 66187, 66189, 66191, 66193, 66195, 66197, 66199, 66202, 66204, 66206, 66208, 66209, 66211, 66213, 66215, 66216,
66219, 66221, 66222, 66224, 66226, 66232, 66233, 66235, 66237, 66239, 66241, 66242, 66244, 66246, 66248, 66251, 66253,
66255, 66257, 66258, 66262, 66264, 66266, 66267, 66269, 66271, 66273, 66277, 66278, 66282, 66284, 66286, 66287, 66289,
66291, 66293, 66295, 66297, 66299, 66304, 66306, 66308, 66312, 66314, 66316, 66318, 66322, 66324, 66326, 66328, 66332,
66334, 66336, 66338, 66339, 66341, 66343, 66345, 66347, 66349, 66351, 66353, 66359, 66361, 66362, 66364, 66365, 66367,
66369, 66371, 66373, 66375, 66378, 66382, 66384, 66386, 66388, 66392, 66402, 66404, 66406, 66407, 66409, 66411, 66413,
66414, 66416, 66418, 66421, 66423, 66425, 66426, 66428, 66432, 66434, 66435, 66437, 66439, 66441, 66443, 66445, 66446,
66448, 66452, 66454, 66457, 66459, 66461, 66462, 66464, 66466, 66468, 66472, 66474, 66476, 66478, 66482, 66484, 66491,
66493, 66495, 66497, 66499, 66501, 66502, 66504, 66506, 66508, 66512, 66514, 66515, 66517, 66519, 66522, 66524, 66526,
66528, 66532, 66534, 66536, 66538, 66541, 66543, 66544, 66546, 66548, 66552, 66554, 66555, 66557, 66558, 66562, 66563,
66565, 66568, 66569, 66571, 66573, 66575, 66577, 66578, 66581, 66583, 66585, 66587, 66589, 66592, 66594, 66596, 66598,
66599, 66602, 66604, 66606, 66608, 66614, 66616, 66617, 66619, 66621, 66622, 66624, 66626, 66628, 66632, 66634, 66636,
66638, 66642, 66643, 66645, 66647, 66649, 66651, 66653, 66654, 66658, 66662, 66664, 66665, 66667, 66669, 66671, 66673,
66675, 66677, 66678, 66682, 66684, 66686, 66687, 66689, 66691, 66693, 66694, 66696, 66698, 66701, 66703, 66705, 66707,
66709, 66711, 66713, 66714, 66716, 66718, 66722, 66724, 66726, 66728, 66732, 66733, 66735, 66737, 66743, 66745, 66749,
66751, 66752, 66754, 66756, 66758, 66762, 66763, 66765, 66768, 66772, 66774, 66776, 66778, 66779, 66781, 66783, 66785,
66786, 66788, 66792, 66793, 66795, 66797, 66798, 66804, 66805, 66807, 66809, 66811, 66812, 66814, 66816, 66818, 66821,
66823, 66825, 66827, 66829, 66831, 66832, 66834, 66836, 66838, 66839, 66841, 66843, 66844, 66846, 66847, 66849, 66851,
66853, 66855, 66857, 66859, 66861, 66862, 66864, 66866, 66867, 66869, 66871, 66873, 66875, 66877, 66878, 66884, 66886,
66888, 66892, 66894, 66896, 66898, 66899, 66901, 66903, 66909, 66911, 66913, 66915, 66917, 66919, 66923, 66925, 66934,
66936, 66938, 66939, 66941, 66943, 66944, 66946, 66947, 66949, 66952, 66953, 66955, 66957, 66958, 66961, 66963, 66965,
66967, 66969, 66975, 66978, 66983, 66985, 66987, 66989, 66991, 66993, 66995, 66996, 66998, 67002, 67004, 67006, 67008,
67012, 67013, 67015, 67017, 67019, 67021, 67023, 67025, 67027, 67029, 67035, 67037, 67039, 67041, 67043, 67045, 67047,
67049, 67051, 67053, 67055, 67057, 67059, 67062, 67063, 67065, 67067, 67069, 67071, 67073, 67075, 67077, 67079, 67081,
67082, 67084, 67086, 67088, 67089, 67091, 67093, 67098, 67102, 67104, 67106, 67108, 67109, 67111, 67113, 67115, 67117,
67119, 67121, 67122, 67124, 67126, 67128, 67132, 67133, 67135, 67136, 67138, 67141, 67143, 67145, 67146, 67148, 67156,
67185, 67187, 67189, 67192, 67194, 67196, 67198, 67202, 67206, 67208, 67212, 67213, 67215, 67217, 67219, 67222, 67224,
67226, 67228, 67229, 67231, 67234, 67236, 67237, 67239, 67242, 67244, 67248, 67252, 67253, 67255, 67257, 67259, 67261,
67263, 67266, 67269, 67272, 67274, 67276, 67277, 67279, 67282, 67284, 67286, 67288, 67289, 67291, 67292, 67294, 67295,
67297, 67298, 67301, 67306, 67307, 67312, 67313, 67315, 67317, 67323, 67325, 67327, 67328, 67331, 67333, 67335, 67336,
67338, 67339, 67341, 67342, 67343, 67345, 67347, 67348, 67352, 67353, 67355, 67357, 67359, 67362, 67364, 67366, 67367,
67369, 67371, 67372, 67374, 67375, 67377, 67379, 67382, 67384, 67385, 67387, 67389, 67391, 67392, 67394, 67396, 67397,
67399, 67401, 67403, 67406, 67409, 67414, 67418, 67421, 67423, 67425, 67428, 67429, 67431, 67433, 67434, 67436, 67438,
67442, 67444, 67446, 67448, 67452, 67461, 67463, 67465, 67473, 67475, 67477, 67478, 67482, 67484, 67488, 67492, 67493,
67495, 67497, 67499, 67501, 67502, 67504, 67507, 67509, 67512, 67514, 67516, 67518, 67522, 67523, 67525, 67527, 67529,
67531, 67533, 67535, 67537, 67539, 67542, 67544, 67545, 67547, 67549, 67551, 67553, 67554, 67556, 67561, 67562, 67564,
67566, 67568, 67571, 67573, 67575, 67576, 67578, 67582, 67583, 67585, 67586, 67588, 67592, 67594, 67596, 67597, 67605,
67607, 67609, 67611, 67613, 67615, 67617, 67619, 67622, 67627, 67628, 67632, 67634, 67637, 67638, 67639, 67641, 67645,
67647, 67649, 67651, 67653, 67656, 67657, 67659, 67661, 67663, 67667, 67669, 67671, 67673, 67675, 67677, 67679,
67681, 67683, 67685, 67687, 67689, 67691, 67692, 67694, 67696, 67698, 67701, 67703, 67705, 67706, 67715, 67717, 67719,
67721, 67723, 67725, 67727, 67729, 67733, 67735, 67737, 67739, 67741, 67743, 67745, 67747, 67749, 67752, 67754, 67756,

67757, 67759, 67761, 67765, 67767, 67768, 67772, 67774, 67775, 67777, 67779, 67783, 67785, 67787, 67792, 67793, 67795,
67797, 67799, 67804, 67805, 67807, 67809, 67811, 67812, 67814, 67816, 67817, 67819, 67821, 67822, 67824, 67826, 67828,
67832, 67833, 67835, 67837, 67838, 67844, 67846, 67848, 67852, 67854, 67856, 67858, 67863, 67865, 67867, 67869, 67871,
67873, 67875, 67877, 67879, 67881, 67883, 67885, 67887, 67889, 67891, 67893, 67895, 67897, 67899, 67901, 67903, 68138,
68142, 68143, 68145, 68147, 68149, 68151, 68152, 68154, 68156, 68158, 68162, 68164, 68166, 68168

D.2   List of excluded runs

This section lists all run numbers that have been excluded from the analysis of the
burn sample and the full sample.

- Runs, for which the processing of the RBR failed:

  30993, 32033, 34759, 38672, 41687, 47876, 48941, 54879, 55827, 56763, 58099, 58131, 58237, 58304, 58366, 58759, 58971,
  59038, 59498, 59603, 59686, 59849, 60003, 60068, 60788, 60912, 61206, 61267, 61395, 61491, 61541, 61704, 61715, 61720,
  61723, 61746

- Runs, for which the data processing failed:

  36387, 38347, 38348, 38349, 38351, 38352, 41298, 41668, 41671, 42511, 44070, 45098, 45118, 45126, 45130, 45132, 45137,
  45246, 45261, 45263, 45269, 45281, 45283, 45285, 45294, 45330, 45334, 45352, 45358, 45361, 45363, 45371, 45373, 45374,
  45377, 45379, 45381, 45383, 45389, 45395, 45399, 45400, 45403, 45405, 45410, 45414, 45416, 45422, 45426, 45428, 45433,
  45450, 45466, 45481, 45484, 45491, 45493, 45497, 45500, 45504, 45513, 45518, 45525, 45531, 45542, 45544, 45548, 45555,
  45559, 45569, 45571, 45579, 45581, 45583, 45607, 45616, 45622, 45646, 45715, 46360, 47712, 54255, 55755, 56727, 56752,
  56831, 56837, 58779, 58788, 60486, 60944, 62081, 67095

- Runs, for which the MUPAGE simulation was empty after the reconstruction
  step:

  26503, 26506, 29622, 30688, 46483, 57587, 63557, 64026, 64649, 64893

- Sparking runs (confirmed and suspicious):

  30658, 31309, 33608, 33610, 34663, 34665, 35467, 36600, 36666, 36670, 36689, 38347, 38348, 38349, 38351, 38352, 38353,
  38355, 38357, 38482, 39192, 41668, 41671, 42507, 42509, 42511, 42513, 42746, 42915, 42919, 43196, 43202, 43206, 43210,
  43215, 43684, 43996, 44030, 44035, 44070, 45242, 46980, 51036, 52675, 53508, 53851, 54512, 55259, 56457, 63718, 64452,
  64457, 65532, 66037, 66039, 66042, 66046, 66049, 66053

- Runs that are marked as *SCAN*:

  34370, 29182, 29196, 29867, 30814, 30815, 30816, 30818, 30820, 30821, 30823, 30825, 30826, 30829, 30832, 30835, 30841,
  30842, 30843, 30853, 30855, 30857, 30858, 30861, 30863, 30864, 30866, 30867, 30870, 31256, 31261, 31263, 31264, 31266,
  31269, 31270, 31381, 31383, 31385, 31387, 31388, 31394, 31399, 31401, 31404, 31405, 31407, 31409, 31413, 31414, 31415,
  31417, 31418, 31424, 31426, 31427, 31430, 31432, 31434, 31435, 31436, 31438, 31440, 31443, 31444, 31446, 31448, 31449,
  31451, 31454, 31478, 31479, 31481, 31483, 31485, 31490, 31493, 31496, 31505, 31508, 31509, 31511, 31513, 31515, 31516,
  31519, 31520, 31522, 31523, 31524, 31527, 31528, 31530, 31532, 31534, 31536, 31538, 31540, 31542, 31543, 31550, 31552,
  31554, 31566, 31579, 31581, 31584, 31586, 31587, 31589, 31591, 31592, 31595, 31612, 31614, 31615, 31617, 31619, 31641,
  31644, 31646, 31648, 31650, 31651, 31654, 31657, 31662, 31664, 31729, 32592, 32594, 32712, 32727, 33126, 33131, 33292,
  33757, 33758, 33763, 33764, 33766, 33768, 33770, 33772, 33773, 33776, 33785, 33798, 33805, 33806, 33809, 33810, 33812,
  33814, 33815, 33817, 33818, 33821, 33823, 33824, 33826, 33828, 33829, 33832, 33834, 33862, 33865, 33866, 33868, 33869,
  33871, 33873, 33875, 33878, 33880, 33883, 33885, 33886, 33888, 33889, 33891, 33893, 33896, 33897, 33899, 33902, 33903,
  33905, 33906, 33909, 33911, 33912, 33914, 33916, 33918, 33920, 33921, 33924, 33926, 33927, 33929, 33931, 33932, 33934,
  33935, 33938, 33940, 33941, 33943, 33944, 33946, 33948, 33950, 33952, 33954, 33956, 33958, 33960, 33961, 33965, 33967,
  33969, 33970, 33972, 34007, 34011, 34012, 34014, 34016, 34017, 34019, 34021, 34026, 34031, 34033, 34041, 34045, 34046,
  34048, 34050, 34052, 34062, 34064, 34074, 34075, 34077, 34080, 34082, 34083, 34085, 34087, 34088, 34091, 34092, 34094,
  34096, 34097, 34099, 34100, 34102, 34105, 34106, 34108, 34109, 34111, 34113, 34114, 34117, 34118, 34122, 34124, 34125,
  34127, 34128, 34130, 34131, 34133, 34136, 34137, 34139, 34140, 34142, 34145, 34146, 34149, 34151, 34152, 34182, 34183,
  34191, 34192, 34194, 34195, 34197, 34204, 34208, 34209, 34211, 34212, 34214, 34217, 34222, 34230, 34242, 34243, 34245,
  34246, 34248, 34250, 34252, 34254, 34255, 34257, 34259, 34261, 34262, 34264, 34265, 34268, 34270, 34272, 34273, 34275,
  34276, 34278, 34281, 34282, 34284, 34285, 34287, 34289, 34291, 34365, 34366, 34368, 34370, 34371, 34374, 34375, 34378,
  34978, 34980, 34981, 34983, 34984, 34986, 34988, 34990, 34996, 34998, 34999, 35006, 35007, 35008, 35011, 35016, 35019,
  35021, 35022, 35024, 35026, 35028, 35030, 35031, 35033, 35037, 35038, 35040, 35041, 35044, 35049, 35052, 35053, 35054,
  35056, 35058, 35413, 35417, 35419, 35420, 35421, 35422, 35423, 35424, 35425, 35426, 35427, 35428, 35430, 35431, 35432,
  35433, 35434, 35435, 35436, 35437, 35438, 35439, 35441, 35442, 35443, 35444, 35445, 35446, 35447, 35448, 35449, 35451,
  35452, 35453, 35454, 35455, 35456, 35459, 35460, 35465, 35466, 37131, 37298, 38730, 38731, 38733, 38734,
  38736, 38737, 38859, 38860, 38862, 38863, 38864, 38865, 38866, 38867, 38868, 41361, 41364, 41530, 41572, 42099, 42101,
  42213, 42215, 42218, 42222, 42224, 42226, 42230, 42233, 42236, 42239, 42242, 42244, 42248, 42250, 42252, 42254, 42259,
  42260, 42261, 42266, 42267, 42269, 42271, 42272, 42274, 42277, 42278, 42279, 42280, 42283, 42285, 42286, 42290, 42292,
  42296, 42298, 42300, 42303, 42305, 42309, 42311, 42314, 42316, 42318, 42328, 42329, 42334, 42337, 42341, 42344, 42349,

42350, 42353, 42355, 42358, 42408, 42423, 42432, 42433, 42438, 42445, 42451, 42453, 42455, 42456, 42458, 42460, 42462, 42464, 42467, 42469, 42473, 42475, 64368, 64369, 64370, 64373, 64643, 64724, 64730, 64732, 64780, 64783, 64785, 64787, 64789, 64811, 64814, 64816, 64817, 64818, 64820, 64822, 64824, 64826, 64828, 64830, 64833, 64836, 64838, 64840, 64842, 64844, 64846, 64848, 64861, 64863, 64864, 64867, 64869, 64872, 64875, 65078, 65092, 65093, 65096, 65098, 65099, 65101, 65104, 65106, 65110, 65112, 65114, 65115, 65116, 65117, 65141, 65143, 67781, 67802, 67861, 68361, 68363, 68364, 68366, 68368, 68370, 68372, 68374, 68376, 68522, 68524, 68527, 68542

- Runs that are marked as *PRELIM*:

  49689, 44334, 44338, 44340, 44344, 44348, 44353, 44356, 44358, 44361, 44364, 44367, 44372, 44375, 44378, 44383, 44391, 44395, 44400, 44404, 44407, 44412, 44415, 44419, 44421, 44423, 44426, 44428, 44431, 44434, 44437, 44440, 44443, 44450, 44454, 44461, 44472, 44473, 44477, 44480, 44482, 44485, 44487, 44491, 44493, 44497, 44499, 44502, 44513, 44529, 44532, 44535, 44539, 44544, 44556, 44560, 44564, 44566, 44568, 44574, 44577, 44580, 44583, 44585, 44588, 44593, 44596, 44598, 44602, 44605, 44608, 44611, 44614, 44617, 44620, 44623, 44627, 44633, 44637, 44640, 44644, 44648, 44653, 44656, 44658, 44662, 44664, 44666, 44670, 44675, 44693, 44778, 44782, 44784, 44786, 44787, 44790, 44792, 44794, 44824, 44833, 44835, 44840, 44860, 45000, 45030, 45040, 45050, 49609, 49629, 49631, 49634, 49660, 49669, 49685, 49689, 49696, 49740, 49741, 49764, 49766, 49833, 49853, 49991, 50063, 50064, 50065, 50066, 50068, 50069, 50070, 50071, 50072, 51549, 51552, 51589, 52856, 52861, 52862, 52863, 52864, 52865, 52866, 52867, 52869, 52870, 52871, 52873, 52874, 52875, 52876, 52877, 52878, 52879, 52880, 52881, 52882, 52883, 52884, 52885, 52886, 52887, 52890, 52894, 52895, 52896, 52897, 52899, 52901, 52903, 52905, 52907, 52909, 52910, 52911, 52912, 52914, 52916, 52917, 52918, 52938, 52954, 53003, 53011, 53031, 53042, 53064, 53087, 53094, 53100, 53113, 53122, 53126, 53127, 53131, 53135, 66394, 66396, 66398, 66399, 66560, 66656, 66747, 66767, 67204, 67247, 67304, 67417, 67487, 67559, 67599, 67625, 67643, 67713, 67731, 67763

- Runs with a quality basic parameter of 0:

  25682, 25683, 25684, 25685, 25686, 25687, 25690, 25693, 25694, 25695, 25703, 25712, 25718, 25726, 25746, 25918, 25925, 25929, 25936, 25952, 25956, 25957, 25966, 25975, 26016, 26017, 26018, 26019, 26038, 26058, 26063, 26064, 26065, 26068, 26072, 26073, 26074, 26076, 26077, 26078, 26079, 26081, 26085, 26086, 26127, 26128, 26136, 26264, 26332, 26409, 26410, 26411, 26412, 26414, 26415, 26416, 26472, 26493, 26503, 26506, 26590, 26678, 26722, 26724, 26725, 26763, 26776, 26782, 26790, 26791, 26796, 26798, 26799, 26822, 26921, 26935, 26980, 26996, 26997, 26999, 27000, 27001, 27005, 27010, 27011, 27012, 27014, 27079, 27178, 27181, 27183, 27184, 27214, 27215, 27237, 27503, 27568, 27570, 27629, 27631, 27637, 27661, 27662, 27663, 27664, 27666, 27670, 27700, 27765, 27810, 27955, 27958, 27999, 28072, 28103, 28104, 28151, 28154, 28160, 28223, 28232, 28234, 28240, 28353, 28406, 28462, 28514, 28539, 28540, 28545, 28547, 28550, 28551, 28565, 28571, 28572, 28614, 28626, 28627, 28646, 28773, 28778, 28779, 28781, 28799, 28843, 28855, 28951, 29030, 29095, 29102, 29164, 29260, 29316, 29536, 29550, 29560, 29565, 29622, 29696, 29824, 29828, 29834, 29894, 29901, 30204, 30331, 30400, 30547, 30595, 30596, 30607, 30647, 30688, 30709, 30797, 30814, 30820, 30835, 30843, 30853, 30858, 30878, 30975, 30984, 31059, 31413, 31414, 31418, 31496, 31538, 31566, 31579, 31641, 31643, 31693, 31694, 31727, 31791, 31816, 31821, 31880, 31882, 31883, 31885, 31972, 31993, 32016, 32351, 32362, 33334, 33561, 33646, 33772, 33818, 33893, 33931, 33972, 34050, 34052, 34062, 34064, 34067, 34074, 34077, 34105, 34114, 34200, 34214, 34259, 34353, 34379, 34392, 34409, 34413, 34480, 34484, 34500, 34513, 34518, 34557, 34567, 34578, 34696, 34701, 34794, 34811, 34885, 34977, 35024, 35075, 35147, 35150, 35182, 35297, 35466, 35467, 35469, 35500, 35673, 35715, 35759, 35762, 35764, 35765, 35767, 35768, 35769, 35771, 35773, 35945, 36005, 36080, 36236, 36252, 36559, 36571, 36581, 36744, 36765, 36806, 36822, 36829, 37012, 37067, 37288, 37646, 37747, 37748, 37750, 37967, 38043, 38220, 38238, 38269, 38271, 38366, 38471, 38531, 38714, 38737, 38816, 38859, 38860, 38862, 38863, 38864, 38865, 38866, 38867, 38868, 39024, 39135, 39145, 39174, 39192, 39195, 39201, 39272, 39347, 39350, 39376, 39595, 39714, 39715, 39730, 39736, 39737, 39738, 39739, 39740, 39767, 39776, 40109, 40172, 40176, 40182, 40236, 40511, 40515, 40544, 40546, 40597, 40679, 40723, 40800, 40801, 40802, 41013, 41122, 41163, 41379, 41413, 41479, 41562, 41575, 41577, 41637, 41638, 41639, 41640, 41641, 41642, 41643, 41644, 41645, 41646, 41647, 41649, 41650, 41651, 41652, 41653, 41654, 41655, 41656, 41657, 41658, 41659, 41660, 41669, 41685, 41700, 41708, 41739, 41799, 41861, 42101, 42122, 42207, 42236, 42265, 42328, 42448, 42673, 42740, 42744, 43188, 43803, 43908, 43920, 43921, 43977, 44231, 44326, 44472, 44593, 44627, 44784, 44786, 44794, 44976, 44996, 45003, 45049, 45184, 45245, 45336, 45672, 46206, 46237, 46483, 46844, 47047, 47609, 47680, 47745, 47765, 47963, 47979, 48065, 48192, 48196, 48204, 48206, 48208, 48217, 48318, 48329, 48375, 48408, 48413, 48497, 48499, 48500, 48502, 48504, 48506, 48558, 48680, 48711, 48717, 48718, 48754, 48758, 48759, 48760, 48762, 48763, 48802, 48905, 48924, 49083, 49198, 49212, 49267, 49270, 49439, 49646, 49649, 49651, 49653, 49656, 49680, 49752, 49766, 49837, 50065, 50066, 50070, 50151, 50154, 50220, 50319, 50447, 50633, 51074, 51824, 51830, 52094, 52118, 52723, 52727, 52791, 52795, 52797, 52855, 52856, 52881, 52883, 52911, 52912, 52926, 53011, 53074, 53775, 53816, 54009, 54274, 54736, 54816, 54882, 54911, 55155, 55204, 55205, 55206, 55238, 55597, 55601, 55665, 55724, 55833, 55835, 55861, 55864, 55867, 55985, 56009, 56333, 56337, 56340, 56341, 56343, 56344, 56434, 56441, 56443, 56452, 56702, 56705, 56724, 56821, 56826, 56849, 56850, 56851, 56852, 57106, 57125, 57301, 57497, 57612, 57782, 57853, 57868, 58076, 58129, 58589, 58592, 58593, 58613, 58754, 58758, 58850, 58852, 58855, 58857, 58860, 58863, 58866, 58870, 58872, 58874, 58996, 59062, 59186, 59280, 59297, 59514, 59554, 59569, 59780, 59791, 59819, 59821, 59823, 59825, 59827, 59846, 59902, 60081, 60259, 60476, 60612, 60769, 60773, 61994, 62142, 62147, 62148, 62333, 62470, 62473, 62493, 62503, 62591, 62592, 62593, 62594, 62604, 62606, 62608, 62620, 62627, 62665, 62685, 62691, 62731, 62734, 62737, 62739, 62742, 62793, 62809, 62814, 62893, 62904, 62990, 63052, 63211, 63476, 63557, 64026, 64164, 64170, 64172, 64174, 64176, 64274, 64276, 64286, 64368, 64369, 64370, 64373, 64399, 64421, 64601, 64621, 64645, 64647, 64648, 64649, 64651, 64656, 64672, 64679, 64697, 64700, 64705, 64707, 64727, 64729, 64730, 64732, 64734, 64861, 64864, 64867, 64869, 64872, 64875, 64932, 65036, 65078, 65092, 65093, 65096, 65098, 65099, 65101, 65104, 65106, 65110, 65112, 65114, 65115, 65141, 65144, 65202, 65218, 65687, 66148, 66150, 66151, 66157, 66179, 66275, 66377, 66430, 66456, 66874, 66890, 67097, 67454, 67456, 68220, 68612, 68614, 68616, 68620, 68623, 68625, 68627, 68629, 68631, 68634, 68637

Appendix E

Data cards for the Pole 1.0 program

This section holds the data cards that have been used to run the Pole 1.0 [16] FORTRAN-77 [125] program to include systematic uncertainties into the upper limit calculations for the burn sample (chapter 13.1) and the full sample (chapter 14.1).

E.1   Data card for the burn sample

```
1  ! Burn sample Data card for Pole 1.0
2  ! hbfile dictionary
3  of test.hb
4  ! skip diagnostic histograms
5  ft 0
6  ! flux factor
7  ff 1.
8  ! confidence level
9  ll 0.90
10 ! do not read nobs/bg from file
11 fi 0
12 ! no inputfile needed
13 fn nofile
14 ! write to file
15 fo burnsample.out
16 ! max signal events
17 rf 50.0
18 ! stepwidth for signal events
19 sw 0.05
20 ! do not apply conditioning
21 no 0
22 ! apply Feldman-Cousins likelihood ordering
23 fc 1
24 ! expected background events
25 bg 0.52
26 ! observed events
27 nm 1
28 ! cc
29 cc 0
30 ! background uncertainty
```

```
31  bu  0
32  pb  1
33  !  relative  signal  efficiency  uncertainty
34  eu  0.29
35  pu  1
36  !  relative  background  efficiency  uncertainty
37  eb  0.42
38  pe  1
```

E.2   Data card for the full sample

```
 1  !Full sample Data card for Pole 1.0
 2  !  hbfile  dictionary
 3  of  test.hb
 4  !  skip  diagnostic  histograms
 5  ft  0
 6  !  flux  factor
 7  ff  1.
 8  !  confidence  level
 9  ll  0.90
10  !  do  not  read  nobs/bg  from  file
11  fi  0
12  !  no  inputfile  needed
13  fn  nofile
14  !  write  to  file
15  fo  fullsample.out
16  !  max  signal  events
17  rf  200.0
18  !  stepwidth  for  signal  events
19  sw  0.2
20  !  do  not  apply  conditioning
21  no  0
22  !  apply  Feldman−Cousins  likelihood  ordering
23  fc  1
24  !  expected  background  events
25  bg  4.92
26  !  observed  events
27  nm  8
28  !  cc
29  cc  0
30  !  background  uncertainty
31  bu  0
32  pb  1
33  !  relative  signal  efficiency  uncertainty
34  eu  0.29
35  pu  1
36  !  relative  background  efficiency  uncertainty
37  eb  0.42
38  pe  1
```

List of Figures

List of Tables

Abbreviations

1D_MIXED	ANTARES trigger algorithm
3D_SCAN	ANTARES trigger algorithm
^{40}K	Potassium-40 atom
AGN	Active galactic nucleus
AMANDA	Former neutrino telescope at the South pole
ANT	Prefix for ANTARES
ANTARES	Astronomy with a Neutrino Telescope and Abyss environmental RESearch
arccos	Arc cosine
ARS	Analogue ring sampler
AVC	Amplitude-to-voltage converter
BAIKAL	Neutrino telescope in Lake Baikal
BBFit	Track and shower vertex reconstruction tool in ANTARES
BRB II	Becker-Biermann-Rhode neutrino flux
cal	Calibration
CC	Charged current (interaction)
cog	Center of gravity
CPU	Central processing unit
C++	Programming language
CTEQ6	Parton distribution function tables
DAQ	Data acquisition system
dcv	Dusj cut values (file format)
det	File format of the ANTARES detector file
DIS	Deep inelastic scattering
DQ	Data quality parameter
em	electromagnetic
eV	electron volt
evt	File format of the ANTARES Monte-Carlo simulation
FR II	Fanaroff-Riley Class II radio galaxy
GEANT	Monte-Carlo generator for particle physics
GEASIM	Simulation software in ANTARES for light propagation and particle showers
GENHEN	Neutrino generator software in ANTARES
GeV	Giga-electron volt (10^9 eV)

GPS	Global positioning system
GRB	Gamma ray burst
GSL	GNU Scientific library (Software package)
HEMAS	Monte-Carlo generator for cosmic ray interactions
Hz	Hertz (counts per second)
i3	File format of the SeaTray framework
IC22	IceCube with 22 strings
IC40	IceCube with 40 strings
IC59	IceCube with 59 strings
ID	Identification number
IMB	IrvineMichiganBrookhaven (detector)
Int	Integer number
JETSET	Monte-Carlo generator for hadronisation
keV	Kilo-electron volt (10^3 eV)
kHz	Kilohertz (10^3 Hz)
KM3	Simulation software in ANTARES for light propagation
KM3NeT	Cubic kilometre neutrino telescope
L1	Hits that passed the ANTARES trigger level 1
L2	Hits that passed the ANTARES trigger level 2
LEPTO	Monte-Carlo generator for deep inelastic lepton nucleon scattering
LLH	Likelihood
LogL	Logarithmic likelihood
MACRO	Cosmic ray experiment at Gran Sasso
MC	Monte-Carlo
MeV	Mega-electron volt (10^6 eV)
MHz	Megahertz (10^6 Hz)
Mpc	Mega-parsec ($3.26 \cdot 10^6$ light years)
MPR	Mannheim-Protheroe-Rachen neutrino flux
MRF	Model rejection factor
MUPAGE	Muon generator software in ANTARES
MUSIC	Monte-Carlo generator for muon propagation
μs	Micro second
NAN	Not a number
NC	Neutral current (interaction)
Ndof	Number of degrees of freedom
Nmini	Number of minimizer calls
ns	Nano second
OM	Optical module
OPA	One particle approximation
PDF	Probability density function
pe	Photo electron

PeV	Peta-electron volt (10^{15} eV)
PhD	Doctoral degree
PMT	Photomultiplier
PRELIM	Tag to mark preliminary ANTARES data taking run setups
prod11	Name of a shower Monte-Carlo production
py	Python file format
PYTHIA	Monte-Carlo generator for hadronisation
RBR	Run-by-run Monte-Carlo simulation (version 2)
RDF	Random decision forest
rLogL	Reduced logarithmic likelihood
ROOT	Software framework provided by CERN
RSQ	Monte-Carlo generator for resonant and quasi-elastic scattering
SCAN	Tag to mark incomplete ANTARES data taking run setups
SVN	Subversion version control software
T2	ANTARES trigger algorithm
T3	ANTARES trigger algorithm
TeV	Tera-electron volt (10^{12} eV)
TH1	1-dimensional histogram in ROOT
TH2D	2-dimensional histogram with double precision in ROOT
TH3D	3-dimensional histogram with double precision in ROOT
TQ	ANTARES trigger algorithm
TVC	Time-to-voltage converter
VLLH	Reduced vertex likelihood
w.e.	Water equivalent ($= 10^6 \, \mathrm{kg} \cdot \mathrm{m}^2$)

Bibliography

[1] M. Ageron et al. ANTARES: The first undersea neutrino telescope. *Nucl. Inst. and Meth. A*, 656(1):11–38, 2011.

[2] P. A. Cherenkov. Visible radiation produced by electrons moving in a medium with velocities exceeding that of light. *Phys. Rev.*, 52:378–379, 1937.

[3] T. DeYoung. Neutrino astronomy with IceCube. *Mod. Phys. Lett. A*, 24(20):1543–1557, 2009.

[4] The IceCube Collaboration. Evidence for high-energy extraterrestrial neutrinos at the IceCube detector. *Science*, 342(6161), 2013.

[5] G. J. Feldman et al. Unified approach to the classical statistical analysis of small signals. *Phys. Rev. D*, 57:3873–3889, 1998.

[6] C. Kopper et al. A software framework for KM3NeT. Proceedings of the ICRC 2009 conference, Available online at `http://icrc2009.uni.lodz.pl/proc/pdf/icrc0476.pdf`.

[7] J. A. Aguilar et al. A fast algorithm for muon track reconstruction and its application to the ANTARES neutrino telescope. *Astropart. Phys.*, 34(9):652–662, 2011.

[8] Q. D. Hasankiadeh. *Reconstruction of neutrino-induced showers with ANTARES*. PhD thesis, Rijksuniversiteit Groningen, 2013. Available online at `http://dissertations.ub.rug.nl/faculties/science/2013/q.dorosti.hasankiade/`.

[9] G. D. Barr et al. Three-dimensional calculation of atmospheric neutrinos. *Phys. Rev. D*, 70:023006, 2004.

[10] R. Enberg et al. Prompt neutrino fluxes from atmospheric charm. *Phys. Rev. D*, 78:043005, 2008.

[11] R. Abbasi et al. First search for atmospheric and extraterrestrial neutrino-induced cascades with the IceCube detector. *Phys. Rev. D*, 84:072001, 2011.

[12] M. G. Aartsen et al. Search for neutrino-induced particle showers with IceCube-40. *submitted to Phys. Rev. D*, 2013. Available online at `http://arxiv.org/abs/1312.0104`.

[13] M. G. Aartsen et al. The IceCube neutrino observatory Part II: Atmospheric and diffuse UHE neutrino searches of all flavors. Version 3, Proceedings of the ICRC 2013 conference, Available online at `http://arxiv.org/abs/1309.7003`.

[14] G. C. Hill et al. Unbiased cut selection for optimal upper limits in neutrino detectors: The model rejection potential technique. *Astropart. Phys.*, 19(3):393–402, 2003.

[15] J. Conrad et al. Including systematic uncertainties in confidence interval construction for Poisson statistics. *Phys. Rev. D*, 67:012002, 2003.

[16] J. Conrad. A program for confidence interval calculations for a Poisson process with background including systematic uncertainties: POLE 1.0. *Comp. Phys. Comm.*, 158(2):117–123, 2004.

[17] M. G. Aartsen et al. Observation of high-energy astrophysical neutrinos in three years of IceCube data. *submitted to Phys. Rev. Lett.*, 2014. Available online at `http://arxiv.org/abs/1405.5303`.

[18] A. Avrorin et al. Search for a diffuse flux of high-energy neutrinos with the Baikal neutrino telescope NT200. Proceedings of the ICRC 2009 conference, Available online at `http://arxiv.org/abs/0909.5562`.

[19] A. Achterberg et al. Multiyear search for a diffuse flux of muon neutrinos with AMANDA-II. *Phys. Rev. D*, 76:042008, 2007.

[20] R. Abbasi et al. Search for neutrino-induced cascades with five years of AMANDA data. *Astropart. Phys.*, 34(6):420–430, 2011.

[21] M. Ackermann et al. Search for ultra-high-energy neutrinos with AMANDA-II. *Astrophys. J.*, 675(2):1014, 2008.

[22] R. Abbasi et al. Search for a diffuse flux of astrophysical muon neutrinos with the IceCube 40-string detector. *Phys. Rev. D*, 84:082001, 2011.

[23] M. G. Aartsen et al. Search for a diffuse flux of astrophysical muon neutrinos with the IceCube 59-string configuration. *submitted to Phys. Rev. D*, 2013. Available online at `http://arxiv.org/abs/1311.7048`.

[24] J. A. Aguilar et al. Search for a diffuse flux of high-energy ν_μ with the ANTARES neutrino telescope. *Phys. Lett. B*, 696(1-2):16–22, 2011.

[25] The ANTARES collaboration. ICRC 2013 proceedings. Available online at `http://arxiv.org/abs/1312.4308`.

[26] C. L. Cowan et al. Detection of the free neutrino: a confirmation. *Science*, 124(3212):103–104, 1956.

[27] R. Davis et al. Search for neutrinos from the Sun. *Phys. Rev. Lett.*, 20:1205–1209, 1968.

[28] I. A. Belolaptikov et al. The BAIKAL underwater neutrino telescope: Design, performance, and first results. *Astropart. Phys.*, 7(3):263–282, 1997.

[29] R. Wischnewski. The AMANDA-II neutrino telescope. Proceedings of the TAUP2001 conference, Available online at `http://arxiv.org/abs/astro-ph/0204268`.

[30] S. Adrián-Martínez et al. Search for cosmic neutrino point sources with four years of data from the ANTARES telescope. *Astrophys. J.*, 760(1):53, 2012.

[31] M. G. Aartsen et al. Search for time-independent neutrino emission from astrophysical sources with 3 years of IceCube data. *submitted to ApJ*, 2013. Version 2, Available online at `http://arxiv.org/abs/1307.6669`.

[32] M. G. Aartsen et al. The IceCube neutrino observatory Part I: Point source searches. Version 2, Proceedings of the ICRC 2013 conference, Available online at `http://arxiv.org/abs/1309.6979`.

[33] The IceCube collaboration. The IceCube neutrino observatory II: All sky searches: Atmospheric, diffuse and EHE. Version 2, Proceedings of the ICRC 2011 conference, Available online at `http://arxiv.org/abs/1111.2736`.

[34] M. G. Aartsen et al. First observation of PeV-energy neutrinos with IceCube. *Phys. Rev. Lett.*, 111:021103, 2013.

[35] The ANTARES Collaboration. ANTARES proposal - A deep sea telescope for high energy neutrinos, 1999. Available online ate `http://antares.in2p3.fr/Publications/index.html`.

[36] B. Hartmann. *Reconstruction of neutrino-induced hadronic and electromagnetic showers with the ANTARES experiment.* PhD thesis, University of Erlangen-Nürnberg, 2006. Available online at `http://arxiv.org/abs/astro-ph/0606697`.

[37] C. Grupen. *Astroparticle physics.* Springer-Verlag Berlin Heidelberg New-York, 2005.

[38] K. Hirata et al. Observation of a neutrino burst from the supernova SN1987A. *Phys. Rev. Lett.*, 58:1490–1493, 1987.

[39] R. M. Bionta et al. Observation of a neutrino burst in coincidence with supernova 1987A in the Large Magellanic Cloud. *Phys. Rev. Lett.*, 58:1494–1496, 1987.

[40] E. N. Alexeyev et al. Detection of the neutrino signal from SN 1987A in the LMC using the INR Baksan underground scintillation telescope. *Phys. Lett. B*, 205(23):209–214, 1988.

[41] J. Blümer et al. Cosmic rays from the knee to the highest energies. *Prog. Part. Nucl. Phys.*, 63(2):293–338, 2009.

[42] T. K. Gaisser. *Cosmic rays and particle physics*. Cambridge University Press, 1990.

[43] K. Nakamura et al. *Particle Physics booklet*. Particle data group at LBNL and CERN, 2010.

[44] H. Athar et al. The intrinsic and oscillated astrophysical neutrino flavor ratios. *Mod. Phys. Lett. A*, 21:1049–1066, 2006.

[45] V. S. Berezinsky et al. *Astrophysics of cosmic rays*. North Holland, 1990.

[46] M. Su et al. Giant gamma-ray bubbles from Fermi-LAT: Active galactic nucleus activity or bipolar galactic wind? *Astrophys. J.*, 724(2):1044, 2010.

[47] S. Adrián-Martínez et al. A search for neutrino emission from the Fermi bubbles with the ANTARES telescope. *Eur. Phys. J. C*, 74(2):1434–6044, 2014.

[48] C. Distefano et al. Neutrino flux predictions for known galactic microquasars. *Astrophys. J.*, 575(1):378, 2002.

[49] S. Adrián-Martínez et al. First search for neutrinos in correlation with gamma-ray bursts with the ANTARES neutrino telescope. *JCAP*, 2013(03):006, 2013.

[50] S. Adrián-Martínez et al. Search for muon neutrinos from gamma-ray bursts with the ANTARES neutrino telescope using 2008 to 2011 data. *A&A*, 559:A9, 2013.

[51] R. Abbasi et al. An absence of neutrinos associated with cosmic-ray acceleration in γ-ray bursts. *Nature*, 484:351–354, 2012.

[52] E. Waxman et al. High energy neutrinos from astrophysical sources: An upper bound. *Phys. Rev. D*, 59:023002, 1998.

[53] J. Bahcall et al. High energy astrophysical neutrinos: The upper bound is robust. *Phys. Rev. D*, 64:023002, 2001.

[54] K. Mannheim et al. Cosmic ray bound for models of extragalactic neutrino production. *Phys. Rev. D*, 63:023003, 2000.

[55] K. Mannheim. High-energy neutrinos from extragalactic jets. *Astropart. Phys.*, 3(3):295–302, 1995.

[56] F. W. Stecker. Note on high-energy neutrinos from active galactic nuclei cores. *Phys. Rev. D*, 72:107301, 2005.

[57] J. K. Becker et al. The diffuse neutrino flux from FR-II radio galaxies and blazars: A source property based estimate. *Astropart. Phys.*, 23(4):355–368, 2005.

[58] The KM3NeT Collaboration. KM3NeT - Technical design report for a deep-sea research infrastructure in the Mediterranean Sea incorporating a very large volume neutrino telescope. Available online at `http://www.km3net.org/TDR/TDRKM3NeT.pdf`, 2008.

[59] P. Amram et al. The ANTARES optical module. *Nucl. Inst. and Meth. A*, 484(1-3):369–383, 2002.

[60] S. Adrián-Martínez et al. The positioning system of the ANTARES Neutrino Telescope. *JINST*, 7(T08002), 2012.

[61] The ANTARES Collaboration. Technical design report of the ANTARES $0.1\,\mathrm{km}^3$ project, Version 1.0, 2001. Available online at `http://antares.in2p3.fr/Publications/TDR/v1r0/`.

[62] The ANTARES Collaboration. Experiment documentation. Website. Available online at `http://antares.in2p3.fr/`.

[63] F. Folger. Reconstruction of neutrino induced hadronic showers with the ANTARES neutrino telescope. Diploma thesis, University of Erlangen-Nürnberg, 2009. Available online at `http://www.ecap.nat.uni-erlangen.de/publications/pub/2009_Folger_Diplom.pdf`.

[64] M. Ageron et al. ANTARES: The first undersea neutrino telescope, 2011. Version 2, Available online at `http://arxiv.org/abs/1104.1607`.

[65] J. A. Formaggio et al. From eV to EeV: Neutrino cross-sections across energy scales. *Rev. Mod. Phys.*, 84:1307–1341, 2012.

[66] R. Abbasi et al. Search for ultrahigh-energy tau neutrinos with IceCube. *Phys. Rev. D*, 86:022005, 2012.

[67] S. L. Glashow. Resonant scattering of antineutrinos. *Phys. Rev.*, 118:316–317, 1960.

[68] A. Bhattacharya et al. The Glashow resonance at IceCube: signatures, event rates and pp vs. pγ interactions. *JCAP*, 2011(10):017, 2011.

[69] J. A. Formaggio et al. From eV to EeV: Neutrino cross-sections across energy scales, 2013. Available online at `http://arxiv.org/abs/1305.7513`.

[70] J. A. Aguilar et al. The data acquisition system for the ANTARES neutrino telescope. *Nucl. Inst. and Meth. A*, 570(1):107–116, 2007.

[71] J. A. Aguilar et al. Performance of the front-end electronics of the ANTARES neutrino telescope. *Nucl. Inst. and Meth. A*, 622(1):59–73, 2010.

[72] J. A. Aguilar et al. Time calibration of the ANTARES neutrino telescope. *Astropart. Phys.*, 34(7):539–549, 2011.

[73] M. De Jong. The ANTARES trigger software. ANTARES internal note ANTARES-SOFT-2005-005, 2005.

[74] S. Escoffier. Performance of the T3 triggers on MC data. ANTARES internal note ANTARES-SOFT-2008-009, 2008.

[75] G. deVries-Uiterweerd. *Signal and background in the underwater neutrino telescope ANTARES*. PhD thesis, Utrecht University, the Netherlands, 2007.

[76] R. Abbasi at al. Measurement of the atmospheric neutrino energy spectrum from 100 GeV to 400 TeV with IceCube. *Phys. Rev. D*, 83:012001, 2011.

[77] M. Honda et al. Calculation of atmospheric neutrino flux using the interaction model calibrated with atmospheric muon data. *Phys. Rev. D*, 75:043006, 2007.

[78] S. Adrián-Martínez et al. Measurement of the atmospheric ν_μ energy spectrum from 100 GeV to 200 TeV with the ANTARES telescope. *Eur. Phys. J. C*, 73(10):1434–6044, 2013.

[79] M. G. Aartsen et al. Measurement of the atmospheric ν_e flux in IceCube. *Phys. Rev. Lett.*, 110:151105, 2013.

[80] T. Montaruli et al. NeutrinoFlux service for IceTray. Website. Available online at `http://icecube.wisc.edu/~tmontaruli/neutrinoflux/NeutrinoFlux.html`.

[81] T. Montaruli et al. The NeutrinoFlux C++ class: a service for fluxes for weighting. Website. Available online at `http://icecube.wisc.edu/~tmontaruli/neutrinoflux/NeutrinoFlux_Teresa.html`.

[82] A. Schuhkraft. A view of prompt atmospheric neutrinos with IceCube. *Nucl. Phys. B - Proceedings Supplements*, 237-238(0):266–268, 2013. Proceedings of the Neutrino Oscillation Workshop.

[83] Y. Becherini et al. A parameterisation of single and multiple muons in the deep water or ice, 2005. Available online at `http://arxiv.org/abs/hep-ph/0507228`.

[84] CNRS/CC-IN2P3. Centre de Calcul IN2P3/CNRS. Website. Available online at `http://cc.in2p3.fr/`.

[85] C. Rivière. Run-by-run Monte Carlo simulation for ANTARES: v2. ANTARES internal note ANTARES-PHYS-2012-001, 2012. Version 6.

[86] D. J. L. Bailey. Genhen v5r1: Software Documentation. ANTARES internal note ANTARES-SOFT-2002-004, 2002.

[87] A. L'Abbate et al. GENHEN v6: ANTARES neutrino generator extension to all neutrino flavors and inclusion of propagation through the earth. ANTARES internal note ANTARES-SOFT-2004-010, 2004.

[88] K. Kuzmin et al. GENHEN v6r3: Implementation of the Glashow resonance and of the MUSIC transport code. ANTARES internal note ANTARES-SOFT-2004-012, 2004.

[89] G. Ingelman et al. LEPTO 6.5 - A Monte Carlo generator for deep inelastic lepton-nucleon scattering. *Comp. Phys. Comm.*, 101(1-2):108–134, 1997.

[90] G. D. Barr. *The separation of signals and background in a nucleon decay experiment.* PhD thesis, University of Oxford, 1987.

[91] J. Pumplin et al. . New generation of parton distributions with uncertainties from global QCD analysis. *JHEP*, 2002(07):012, 2002.

[92] T. Sjöstrand. High-energy physics event generation with PYTHIA 5.7 and JET-SET 7.4. *Comp. Phys. Comm.*, 82(1):74–89, 1994.

[93] P. Antonioli et al. A three-dimensional code for muon propagation through the rock: MUSIC. *Astropart. Phys.*, 7(4):357–368, 1997.

[94] L. Core. *Search of an ultra high energy neutrino diffuse flux with the ANTARES telescope.* PhD thesis, Aix-Marseille Université, 2013. Available online at `http://antares.in2p3.fr/internal/dokuwiki/lib/exe/fetch.php?id=ultra_high_energy_neutrino_diffuse_flux&cache=cache&media=wiki:finale_version.pdf`.

[95] G. Carminati et al. Atmospheric MUons from PArametric formulas: a fast GEnerator for neutrino telescopes (MUPAGE). *Comp. Phys. Comm.*, 179(12):915–923, 2008.

[96] M. Bazzotti et al. An update of the generator of atmospheric muons from parametric formulas (MUPAGE). *Comp. Phys. Comm.*, 181(4):835–836, 2010.

[97] Y. Becherini et al. A parameterisation of single and multiple muons in the deep water or ice. *Astropart. Phys.*, 25(1):1–13, 2006.

[98] C. Forti et al. Simulation of atmospheric cascades and deep underground muons. *Phys. Rev. D*, 42:3668–3689, 1990.

[99] M. Ambrosio et al. High energy cosmic ray physics with underground muons in MACRO. I. Analysis methods and experimental results. *Phys. Rev. D*, 56(3):1407–1417, 1997.

[100] M. Ambrosio et al. High energy cosmic ray physics with underground muons in MACRO. II. Primary spectra and composition. *Phys. Rev. D*, 56(3):1418–1436, 1997.

[101] D. J. L. Bailey. KM3 v2r1: User guide. ANTARES internal note ANTARES-SOFT-2002-006, 2002.

[102] C. W. James. KM3 release v4r3. ANTARES internal note ANTARES-SOFT-2012-003, 2012.

[103] C. W. James. KM3 release v4r4. ANTARES internal note ANTARES-SOFT-2012-007, 2012.

[104] CERN Geneva, Switzerland. GEANT - Detector description and simulation tool. Manual, 1993. Available online at `http://wwwasdoc.web.cern.ch/wwwasdoc/pdfdir/geant.pdf`.

[105] S. Navas. A comparison between GEASIM and KM3 generators. ANTARES internal note ANTARES-SOFT-1999-002, 1999.

[106] M. Dentler. Investigation of the One-Particle Approximation in the ANTARES simulation package KM3. Bachelor thesis, University of Erlangen-Nürnberg, 2012. Available online at `http://www.ecap.physik.uni-erlangen.de/publications/pub/2012_Dentler_Bachelor.pdf`.

[107] M. De Jong. The TriggerEfficiency program. ANTARES internal note ANTARES-SOFT-2009-001, 2009.

[108] B. Stroustrup. *The C++ programming language, 4th edition*. Addison-Wesley Professional, 2013.

[109] Python Software Foundation. Python programming language. Website. Available online at `http://www.python.org`.

[110] D. Boersma. Gulliver. Website (protected). Available online at `https://wiki.icecube.wisc.edu/index.php/Gulliver`.

[111] The Apache Software Foundation. Apache Subversion. Website. Available online at `http://subversion.apache.org`.

[112] R. Auer. Reconstruction of hadronic cascades in large-scale neutrino telescopes. *Nucl. Inst. and Meth. A*, 602(1):84–87, 2009. Proceedings of the 3rd International Workshop on a Very Large Volume Neutrino Telescope for the Mediterranean Sea.

[113] The ROOT team. ROOT - A data analysis framework. Website. Available online at `http://root.cern.ch/`.

[114] S. Geißelsöder. Classification of events for the ANTARES neutrino detector. Master thesis, University of Erlangen-Nürnberg, 2011. Available online at `http://www.ecap.physik.uni-erlangen.de/publications/pub/2011_Geisselsoeder_Master.pdf`.

[115] D.J.L. Bailey. Calculating effective areas for neutrinos. ANTARES internal note ANTARES-PHYS-2001-011, 2001.

[116] F. Folger. Diffuse flux analysis using the Dusj shower reconstruction. ANTARES internal note ANTARES-PHYS-2013-012, 2013.

[117] F. Folger. Updates on the Dusj diffuse flux analysis. ANTARES internal note ANTARES-PHYS-2013-014, 2013.

[118] J. Schnabel. Private communication. ECAP, University of Erlangen-Nürnberg.

[119] The ANTARES data quality working group. Data quality flags. Internal website. Available online at `http://antares.in2p3.fr/internal/dokuwiki/doku.php?id=quality_flags`.

[120] T. DeYoung. IceTray: A software framework for IceCube, 2004. Proceedings of the CHEP 2004 conference, Available online at `http://www.chep2004.org`.

[121] F. Folger. The Dusj shower reconstruction project. ANTARES internal note ANTARES-SOFT-2013-003, 2013.

[122] J. A. Nelder et al. A simplex method for function minimization. *Comp. J.*, 7(4):308–313, 1965.

[123] Free Software Foundation. GSL - GNU Scientific Library. Website. Available online at `http://www.gnu.org/software/gsl/`.

[124] W. L. Goffe et al. Global optimization of statistical functions with simulated annealing. *Journal of Econometrics*, 60(1–2):65–99, 1994.

[125] American National Standards Institute. Programming language FORTRAN. Website. Available online at `http://www.fortran.com/fortran/F77_std/rjcnf.html`.

Acknowledgments

First of all I would like to thank Uli Katz and Gisela Anton for the opportunity to work on such an interesting topic and for their help and advice during the passed years.

Thomas Eberl, I want to thank for his supervision, his support, for proofreading my work and all the interesting discussions we had.

Many thanks also to the ANTARES group at ECAP, particularly to Klaus Geyer, Jutta Schnabel, Kathrin Roensch, Roland Richter and Andreas Spies, for their support and the pleasant working atmosphere. Also to Claudio Kopper and Ralf Auer, who once introduced me to the group and the topic of neutrino astronomy.

Further, I would like to express my gratitude to the ANTARES shower working group, Tommaso Chiarusi, Giulia DeBonis and Qader Dorosti Hasankiadeh, as well as to the ANTARES collaboration for the cooperation and fruitful meetings we had together.

Mirjam, thank you for your encouragements and that you were always there for me during the final, arduous phase of my work.

Finally, I would particularly like to thank my parents, who always have supported me and without their help it would not have been possible for me to realise this work.

Thank you.